

# DFENS: Diffusion chronometry using Finite Elements and Nested Sampling

Euan J. F. Mutch<sup>1,2</sup>, John MacLennan<sup>1</sup>, Oliver Shorttle<sup>1,3</sup>, John F. Rudge<sup>4</sup> &  
David A. Neave<sup>5</sup>

<sup>1</sup>Department of Earth Sciences, University of Cambridge, Downing Street, Cambridge, CB2 3EQ, United Kingdom

<sup>2</sup>Department of Geology, University of Maryland, 8000 Regents Dr, College Park, Maryland, 20742, United States

<sup>3</sup>Institute of Astronomy, University of Cambridge, Madingley Road, Cambridge, CB3 0HA, United Kingdom

<sup>4</sup>Bullard Laboratories, Department of Earth Sciences, University of Cambridge, Madingley Road, Cambridge CB3 0EZ, United Kingdom

<sup>5</sup>Department of Earth and Environmental Sciences, University of Manchester, Manchester, M13 9PL, United Kingdom

## Key Points:

- New diffusion chronometry method that combines finite elements and Bayesian statistics to robustly account for timescale uncertainties.
- Agreement between olivine and plagioclase chronometers when applied to samples from the Bárðarbunga volcanic system, Iceland.
- Magma mixing timescales prior to the Skuggafjöll eruption are estimated to be on the order of 1 year.

---

Corresponding author: Euan J. F. Mutch, [ejfmutch@umd.edu](mailto:ejfmutch@umd.edu)

## Abstract

In order to reconcile petrological and geophysical observations in the temporal domain, the uncertainties of diffusion timescales need to be rigorously assessed. Here we present a new diffusion chronometry method: Diffusion chronometry using Finite Elements and Nested Sampling (DFENS). This method combines a finite element numerical model with a nested sampling Bayesian inversion meaning the uncertainties of the parameters that contribute to diffusion timescale estimates can be rigorously assessed, and that observations from multiple elements can be used to better constrain a single timescale. By accounting for the covariance in uncertainty structure in the diffusion parameters, estimates on timescale uncertainties can be reduced by a factor of 2 over assuming that these parameters are independent of each other. We applied the DFENS method to the products of the Skuggafjöll eruption from the Bárðarbunga volcanic system in Iceland, which contains zoned macrocrysts of olivine and plagioclase that record a shared magmatic history. Olivine and plagioclase provide consistent pre-eruptive mixing and mush disaggregation timescales of less than 1 year. The DFENS method goes some way to improving our ability to rigorously address the uncertainties of diffusion timescales, but efforts still need to be made to understand other systematic sources of uncertainty such as crystal morphology, appropriate choice of diffusion coefficients, growth, and the petrological context of diffusion timescales.

## Plain Language Summary

Diffusion acts to smooth out compositional changes in minerals, such as olivine and plagioclase, when they try to equilibrate with new magmatic environments. Modelling this diffusion process has proven to be a powerful tool for estimating the timescales of magmatic processes: an expanding field known as diffusion chronometry. This method, however, is typically associated with large errors due to uncertainties in physical parameters (e.g. temperature, pressure) and the experimentally derived diffusion coefficients. Here we present a new diffusion chronometry method called DFENS (Diffusion chronometry using Finite Elements and Nested Sampling). This method uses Bayesian statistics to account for all of the uncertainties in the physical and diffusion coefficient parameters, meaning the uncertainties in diffusion timescales can be robustly accounted for. We applied the DFENS method to olivine and plagioclase crystals from the Skuggafjöll eruption, Iceland. These minerals appear to have shared a common magmatic history. We found that the plagioclase and olivine crystals gave broadly consistent pre-eruptive residence timescales of less than 1 year. This could have important implications for volcanic hazard assessment and volcano monitoring in the Bárðarbunga volcanic system, Iceland.

## 1 Introduction

Diffusion chronometry has now emerged as an important method in quantitative petrology for constraining the timescales of magma residence, mixing and transport. It has been shown to play a key role in linking petrological processes to geophysical observations and volcanic monitoring data (Saunders et al., 2012; Rae et al., 2016; Pankhurst et al., 2018; Rasmussen et al., 2018; Costa et al., 2020). As a method, it can be used to estimate relative timescales and can thus be used to understand subvolcanic processes regardless of eruption age. Furthermore, mineral geospeedometers with different diffusivities can be used to track magmatic processes over different timescales, often within the same minerals and samples. Slower diffusing elements (e.g., Al-Cr interdiffusion in spinel; Sr in plagioclase) can provide information of long-term magma storage times on the order of hundreds to thousands of years (G. F. Zellmer et al., 1999; G. Zellmer et al., 2000; Cooper & Kent, 2014; Mutch, MacLennan, Holland, & Buisman, 2019), whilst faster diffusing species (e.g. Fe-Mg interdiffusion in olivine) can offer insight to processes operating days to weeks (Moore et al., 2014; Hartley et al., 2016; Lynn et al., 2017; Mutch,



MacLennan, Shorttle, et al., 2019), or even minutes to hours (e.g.,  $H^+$  diffusion in olivine) before eruption (Barth et al., 2019; Newcombe et al., 2020). However, the value of diffusion timescales is diminished without proper petrological context and the rigorous consideration of underlying uncertainties. In-depth petrological characterisation is required in order to determine whether the diffusion timescales can plausibly be linked to specific petrological processes, physical processes and ultimately volcano monitoring data. Petrological observations are also required to test whether assumptions about initial conditions, boundary conditions and intensive parameters are appropriate.

Linking magmatic processes to geophysical observations through time requires a robust treatment of the uncertainties associated with diffusion timescales. The Arrhenius relationship between temperature and elemental diffusivity means that uncertainties in temperature play a dominant role in controlling error estimates. Many diffusion studies account for the uncertainties of the methods used to estimate temperature such as phase equilibria geothermobarometers (Ruprecht & Plank, 2013), however the uncertainties in other intensive parameters that control diffusivity, as well as parameters in the diffusion coefficients themselves, are often not properly considered. Furthermore, the uncertainty structure associated with diffusion coefficients is correlated (Costa & Morgan, 2010). Here we present a Bayesian inversion method, known as DFENS (Diffusion chronometry using Finite Elements and Nested Sampling) for modelling diffusion of multiple elements for timescale estimation. DFENS combines a finite element numerical diffusion model with a Nested Sampling Bayesian inversion scheme, which can simultaneously account for observations from multiple diffusing elements and produces more robust uncertainty estimates by taking account of the covariance in uncertainty structure of the underlying diffusion coefficients.

Very few eruptions studied thus far contain multiple mineral phases that appear to have experienced common magmatic histories and can be independently used to estimate magmatic timescales and test the robustness of different mineral geospeedometers. In the plutonic record, Ca-in-olivine and Mg-in-plagioclase speedometers have shown consistent results when used to estimate the cooling rate of the lower oceanic crust (Faak & Gillis, 2016). However, in volcanic settings, complex crystal cargoes often make it difficult to compare different geospeedometers as different phases can record different magmatic histories (Chamberlain et al., 2014). The products of the Skuggafjöll eruption from the Bárðarbunga volcanic system, Iceland, contains macrocrysts of olivine and plagioclase that have been compositionally mapped in detail and appear to share a common history of long-term storage followed by rapid rim growth (Neave, MacLennan, Hartley, et al., 2014). Textural and microanalytical evidence indicates that these crystals provide a means of testing the consistency of olivine and plagioclase geospeedometers.

## 2 DFENS: a new diffusion chronometry method

### 2.1 Multi-element diffusion using the finite element method

Diffusion chronometry relies on solving some variant of Fick's second law through time from a set of pre-defined initial conditions until the model matches the observed compositional data. In many silicate minerals, the diffusivity of the elements of interest are often spatially variable. For example, Fe-Mg interdiffusion, Ni and Mn diffusion in olivine depend on forsterite content (Chakraborty, 1997; Petry et al., 2004; Dohmen et al., 2007; Dohmen & Chakraborty, 2007; Holzapfel et al., 2007; Spandler & O'Neill, 2010), whilst the diffusivities of trace elements in plagioclase (e.g., Mg, Sr, Ba) have been shown to depend on anorthite content (Cherniak & Watson, 1994; Van Orman et al., 2014). A spatially dependent version of Fick's second law (equation 1) is therefore required to model diffusion in most silicate minerals (Crank, 1979; Costa & Morgan, 2010):

$$\frac{\partial C}{\partial t} = \nabla \cdot (D \nabla C) \quad (1)$$

where  $C$  is the concentration of the element of interest,  $D$  is diffusivity,  $x$  is distance and  $t$  is time. Diffusive coupling between different trace elements can also create additional complexity (Costa et al., 2003; Tang et al., 2017). In the case of Mg diffusion in plagioclase, forms of the diffusion equation that account for the chemical potential of the Mg-component and coupling with the anorthite component need to be considered (Costa et al., 2003):

$$\frac{\partial C_{\text{Mg}}}{\partial t} = \nabla \left( D_{\text{Mg}} \nabla C - \frac{D_{\text{Mg}} C_{\text{Mg}}}{RT} A_{\text{Mg}} \nabla X_{\text{An}} \right) \quad (2)$$

where  $C_{\text{Mg}}$  is the composition of Mg,  $X_{\text{An}}$  is anorthite content (mole fraction),  $A_{\text{Mg}}$  is the slope of the Mg-in-plagioclase partitioning relationship, and  $D_{\text{Mg}}$  is the Mg-in-plagioclase diffusion coefficient. The complex diffusive behaviour in most silicate minerals, coupled with changing boundary conditions and diffusion coefficients imposed by continually changing intensive parameters in magmatic systems ( $P$ ,  $T$ ,  $f\text{O}_2$  etc.) makes it very difficult to solve diffusion timescale problems in igneous petrology using analytical solutions. This has led many studies to use numerical models to solve the diffusion equation using either finite-differences (Costa et al., 2008; Druitt et al., 2012; Moore et al., 2014) or finite elements (Mutch, MacLennan, Holland, & Buisman, 2019; Mutch, MacLennan, Shorttle, et al., 2019) that have been discretised in space and time.

The finite element method has emerged as a universal method for the solution of partial differential equations, like the diffusion equation. The power of the finite element method lies in its generality and flexibility allowing a wide range of partial differential equations to be solved within a common framework (Logg et al., 2012). A finite element is defined as a cell with a local function space ( $V$ ) and rules that describe the functions that operate in this space (Brenner & Scott, 2008; Logg et al., 2012). Together these cells form a mesh which defines a functional domain ( $\Omega$ ). These meshes can take a range of simple polygonal shapes such as intervals, triangles, quadrilaterals, tetrahedra or hexahedra, which makes it a more useful way to generate complex morphologies such as crystal forms than regular finite-difference methods (figure 1). Here we use the FEniCS Project (Logg et al., 2012; Alnæs et al., 2015) to solve equations 1 and 2. For this to happen, the unknown function (known as a trial function) needs to be discretised using the finite element method. This involves multiplying the trial function by a test function (usually represented as  $v$ ) and integrating. Second-order derivatives are typically (but not always) integrated by parts. This new form is known as the ‘variational form’ or ‘weak form’ and is supposed to hold for all  $v$  in some function space ( $V_x$ ). The trial function (defined as  $C$  here for composition) resides in a (possibly different) function space ( $V$ ). These function spaces are defined by the mesh and the type of finite elements. A derivation of the variational form for a time-dependent diffusion problem is included in the Supplementary Material. The variational form for diffusion equations with a spatially dependent diffusion coefficient, as is the case for olivine (equation 1) and spinel is:

$$\int_{\Omega} C^{k+1} v + \Delta t (D(C_{\text{mid}}) \nabla C_{\text{mid}}) \cdot \nabla v \, dx = \int_{\Omega} C^k v \, dx \quad (3)$$

where  $D(C_{\text{mid}})$  is the compositionally dependent diffusion coefficient. The variational form used in this study for the plagioclase diffusion equation (equation 2) is:

$$\int_{\Omega} C^{k+1} v + \Delta t \left( D \nabla C_{\text{mid}} - \frac{D A C_{\text{mid}}}{RT} \nabla X_{\text{An}} \right) \cdot \nabla v \, dx = \int_{\Omega} C^k v \, dx \quad (4)$$

where  $C_{\text{mid}}$ ,  $C^k$  and  $C^{k+1}$  are defined as the compositions at each time step. For solving time-dependent partial differential equations the time derivative needs to be discretised by a finite difference approximation, which yields a recursive set of stationary problems that can then be written in variational form. The type of time-stepping used in this study is defined by the  $\theta$  method (equation 5).

$$C_{\text{mid}} = \theta C^{k+1} + (1 - \theta) C^k \quad (5)$$

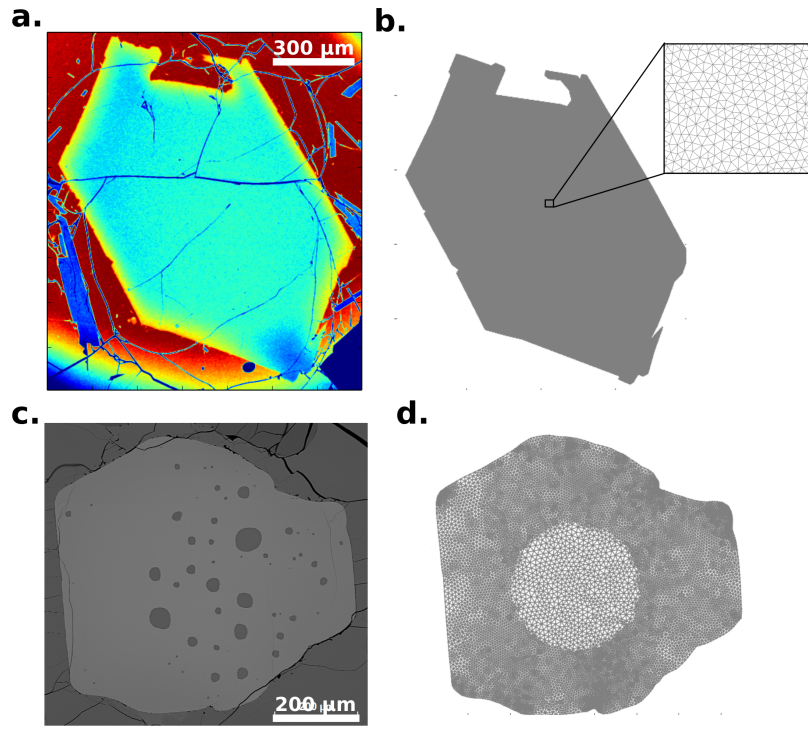


**Figure 1.** Comparison of crystal morphologies encountered in natural magmatic systems and the shapes that can be produced by 2D finite element meshes. **a** is a false colour BSE image of an olivine crystal from the Skuggafjöll eruption; the corresponding 2D finite element mesh is shown in **b**. The inset in **b** is a zoomed in section showing the individual cells in the triangular mesh. **c** is a BSE image of a spinel from Borgarhraun (Mutch, MacLennan, Holland, & Buisman, 2019) **d** is 2D finite element mesh of the crystal shown in **c**. The mesh shown in **d** has been refined at its edges (i.e. has a smaller mesh size) so that a more detailed solution can be captured in areas of interest, such as where diffusion is most likely to be operating. This means a balance can be made between spatial resolution and computational time.

where  $C_{mid}$  is the composition at the Crank-Nicholson time step,  $C^k$  is the composition at the current time step and  $C^{k+1}$  is the composition at the next time step.  $\theta = 0$  for a forward Euler time-stepping scheme (1<sup>st</sup> order),  $\theta = 1$  for a backward Euler time-stepping scheme (1<sup>st</sup> order), and  $\theta = 0.5$  for a Crank-Nicholson time stepping scheme (2<sup>nd</sup> order). The Crank-Nicholson scheme is both stable and accurate and therefore that scheme was used. The trial function and the test function use the same functional space defined based on the mesh and the type of finite element. Once the partial differential equation has been discretised and finite element functional spaces have been assigned, the FEniCS software uses direct LU solvers to solve the resulting algebraic systems. For non-linear equations like Fe-Mg interchange in olivine and Cr-Al interchange in spinel a Newton solver was used. In all cases in this study, linear Lagrange (Continuous Galerkin) finite elements were used to represent concentrations. The standard number of mesh points for a profile of length  $L$  was set to 300. The number of time steps in each realisation was kept constant at 300; the size of the time step was not kept constant. The numerical stability of the solution was assessed during each realisation using the Courant-Friedrichs-Lewy (CFL) condition:

$$\frac{\Delta t D}{(\Delta x)^2} < 0.5 \quad (6)$$

where  $\Delta t$  is the size of the time step and  $\Delta x$  is the mesh spacing. If the CFL value exceeded 0.5, the mesh was coarsened so that this criterion could be met. However, optimal standard time steps and mesh intervals were selected initially based on the expected diffusivities and observed length-scales of diffusion.

## 2.2 Accounting for the covariance in uncertainty structure in diffusion coefficients

Diffusion coefficient parameters are typically extracted using regressions through experimental data in  $\ln(D)$  versus  $1/T$  space. The slope and intercept of a linear regression are related to each other, which is critical when considering the uncertainties relating to the parameters that determine diffusion coefficients. This is particularly true for  $D_0$  and activation energy ( $E_a$ ), where higher values of  $D_0$  would need to be associated with higher values of  $E_a$  (figure 2). Taking account of this form of uncertainty in diffusion modelling requires an understanding of the covariance of all the parameters that go into the diffusion coefficients. This feature has somewhat been neglected by most diffusion modelling studies. One of the main foci of this work is the creation of new multiple linear regressions through the experimental data so that the uncertainty structure can be properly assessed with covariance matrices. These regressions and covariance matrices are presented below and in the Supplementary Material, along with new modelling methods that can account for the trade-offs between different parameters.

New multiple linear regressions through a compiled database of olivine diffusion experiments (Chakraborty, 1997; Petry et al., 2004; Dohmen et al., 2007; Dohmen & Chakraborty, 2007; Holzappel et al., 2007; Spandler & O'Neill, 2010) for Fe-Mg exchange (including a Global mechanism, which accounts for all diffusion data; and the TaMED mechanism, which accounts for diffusion experiments conducted at  $fO_2 > 10^{-10}$  Pa), Ni and Mn diffusion along the [001] axis for use in DFENS were first presented in the Supplementary Material of Mutch, MacLennan, Shorttle, et al. (2019). The least squares multiple linear regressions are expressed in the form shown in equation 7, with best fit parameters for each element presented in the Supplementary Material.

$$\ln D_{[001]}^{O,i} = a_i + b_i \ln fO_2 + c_i X_{Fe} + \frac{q_i + h_i P}{T} + j_i P + k_i \ln a_{SiO_2} \quad (7)$$

where  $a_i$ ,  $b_i$ ,  $c_i$ ,  $q_i$ ,  $h_i$ ,  $j_i$  and  $k_i$  are the best fit parameters from the regression for diffusing species  $i$ . Pressure ( $P$ ) is expressed in Pa,  $T$  in K and  $\ln fO_2$  in its native form (i.e.  $fO_2$  is in bars, a version where  $fO_2$  is in Pa is also available in the Supplementary Material).  $a_{SiO_2}$  is the activity of silica. Diffusive anisotropy is taken to be six times faster

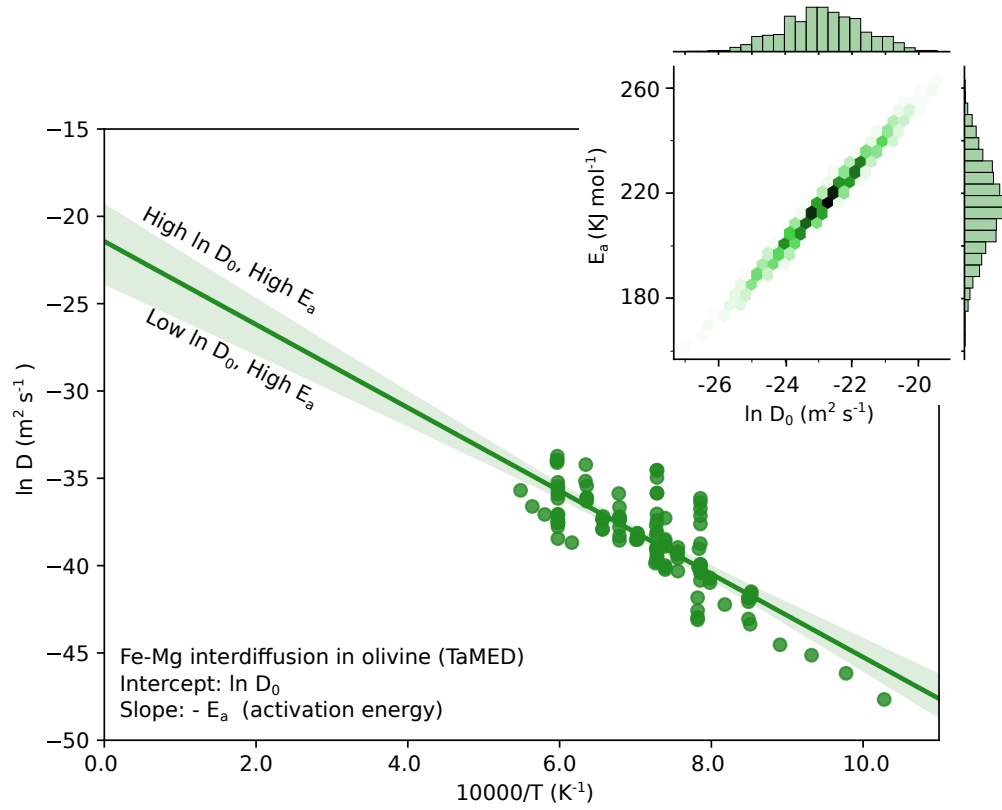


**Figure 2.** Arrhenius plot showing how  $D_0$  and  $E_a$  (activation energy) can be obtained by linear regression through diffusion experiments conducted at different temperatures. The experiments shown here are from the compilation made by Mutch, MacLennan, Shorttle, et al. (2019) for diffusion along [001] via the TaMED mechanism in olivine. The inset is a density plot showing the covariance between these two parameters. A higher slope ( $E_a$ ) will be associated with a higher intercept ( $\ln D_0$ ), which is an important factor to consider for error propagation.

along the [001] axis than the [010] and [100] axes for Fe-Mg and Mg (Chakraborty, 2010), and 10.7 times faster for Ni (Spandler & O'Neill, 2010). In this study, we do not account for any uncertainties in diffusive anisotropy.

The covariance matrices associated with the fitting parameters from these new regressions are shown in the Supplementary Material. They were created so that the uncertainty structure associated with the experimental fits can be rigorously explored. Fe-Mg diffusion experimental data was used to supplement Mn data in order to determine Mn's diffusive dependence on forsterite content. The regressions recover all of the experimental data within 0.5  $\log_{10}$  units and are consistent with previously been reported equations (Dohmen & Chakraborty, 2007; Chakraborty, 2010; Costa & Morgan, 2010). Separate regressions and covariance matrices for diffusion along [001] were derived for experimental datasets that were explicitly buffered for  $a_{\text{SiO}_2}$  (Zhukova et al., 2014; Jollands et al., 2016). The regressions and covariance matrices for Fe-Mg interdiffusion only use data from anhydrous experiments, and do not account for the effect of water on diffusivity (Hier-Majumder et al., 2005).

The multivariate linear regressions performed for trace element diffusion in plagioclase are presented using the form:

$$\ln D_i^{\text{Pl}} = a_i + b_i X_{\text{An}} + c_i \ln a_{\text{SiO}_2} + \frac{q_i}{T} \quad (8)$$

The regression parameters ( $a_i$ ,  $b_i$ ,  $c_i$  and  $q_i$  for diffusing species  $i$ ) are presented in the Supplementary Material. Given that the diffusive anisotropy of Mg in plagioclase is thought to be approximately a factor of 2 (Van Orman et al., 2014) and that no anisotropy has been reported for Sr (Cherniak & Watson, 1994), our regressions include all data regardless of crystallographic direction and do not account for any of the effects of anisotropy between the [010] and [001] directions. For Mg, the regression combines the datasets of Van Orman et al. (2014) and Faak et al. (2013). We consider the effects of anorthite content and  $a_{\text{SiO}_2}$  to be more important than diffusive anisotropy. Any uncertainty produced by ignoring anisotropy in the regression dataset would be incorporated into the corresponding covariance matrix, however this could introduce systematic error for profiles parallel to the main crystallographic directions.

### 2.3 Estimating uncertainties using Bayesian inference

Bayesian inference is a method of statistical inference in which Bayes' theorem is used to update the probability for a hypothesis (or model) as more information, or evidence, becomes available. It involves calculating a posterior probability (the probability of a hypothesis given the evidence) from a prior probability (the probability of the hypothesis before the evidence is observed) and a likelihood function based on a statistical model of the observed data. Bayes' theorem for model selection states (Feroz et al., 2009):

$$P(\theta|D, H_k) = \frac{P(D|\theta, H_k) \cdot P(\theta|H_k)}{P(D|H_k)} \quad (9)$$

where  $H$  is one hypothesis, or model, out of  $k$  competing hypotheses whose probability may be affected by the data ( $D$ ) and the set of parameters ( $\theta$ ).  $P(\theta|H_k) \equiv \pi(\theta)$  is the prior probability of the hypothesis ( $H_k$ ) before the evidence is observed.  $P(\theta|D, H_k) \equiv P(\theta)$  is the posterior probability distribution of the parameters.  $P(D|\theta, H_k) \equiv \mathcal{L}(\theta)$  is called the likelihood; it indicates the compatibility of the evidence with the given hypothesis.  $P(D|H) \equiv \mathcal{Z}$  is the Bayesian evidence. In model selection, the Bayesian evidence is the factor required to normalise the posterior over  $\theta$  (Feroz et al., 2009):

$$\mathcal{Z} = \int \mathcal{L}(\theta) \pi(\theta) d^N \theta \quad (10)$$

where  $N$  is the dimensionality of the parameter space. The Bayesian evidence inherently implements Occam's razor so that a simpler theory with a more compact parameter space



will have a larger evidence than a more complicated one, unless the latter is better at explaining the data (Feroz et al., 2009).

In the case of modelling diffusion in natural crystals: the evidence would be the compositional profiles measured across the crystals (or compositional maps in 2D) with associated analytical uncertainties. The prior probability would correspond to the probability density distribution of model parameters such as time, intensive parameters and diffusion coefficients. The likelihood function would therefore compare the misfit of the hypothesised diffusion model to the data. In the case of modelling multiple elements this would be exponentially related to the  $\chi^2$  misfit if the error is Gaussian. The maximum likelihood would have the best fit between the hypothesis diffusion model and all of the data. The prior distributions for the parameters that can go into the hypothesis models can be described using different functions; the main ones used in this study are log uniform priors, Gaussian priors and multivariate Gaussian priors. A uniform prior is a constant probability function, which means that all possible values are equally likely *a priori*. A log uniform prior is a uniform prior that is applied across a logarithmic domain. In the models used in this study, time was assigned a log uniform prior due to the exponential relationship between temperature and diffusivity. A Gaussian prior uses a Gaussian probability distribution as defined by the mean and standard deviation. Intensive parameters that have been independently estimated, such as temperature (T), pressure (P),  $fO_2$  and  $a_{SiO_2}$ , were assigned Gaussian priors using the independent estimate as the mean and the inherent uncertainty of the method as the standard deviation. It should also be noted that thermobarometric methods may also introduce correlation between intensive parameters. A multivariate Gaussian prior involves the generalisation of one dimensional Gaussian priors up to higher dimensions. This can account for any covariance in parameters (described by covariance matrices), which is the case for the parameters that contribute towards the diffusion coefficients such as activation energy ( $E_a$ ) and initial diffusivity ( $D_0$ ). A series of univariate Gaussians can be converted into a multivariate Gaussian using:

$$y = \lambda^{\frac{1}{2}} \phi x + \mu \quad (11)$$

where  $\lambda$  is a diagonal matrix of the eigenvalues of the covariance matrix,  $\phi$  is the matrix of eigenvectors from the covariance matrix,  $x$  is a one dimensional standard Gaussian distribution and  $\mu$  is a vector of the mean values of the Gaussian distributions. Using a Bayesian approach to diffusion modelling allows for observations from multiple elements in single or multiple phases to be considered simultaneously, whilst considering the covariance of all of the parameters in the diffusion coefficients offers a more robust way of accounting for uncertainties. This is critical when trying to reconcile geophysical and petrological observations in the temporal domain.

## 2.4 Nested sampling and the MultiNest algorithm

In order to integrate parameter estimation into the diffusion models, Monte Carlo methods were employed. Nested sampling (Skilling, 2004) is a type of Monte Carlo algorithm in which a fixed size of parameter vectors or “livepoints” are sorted by their likelihood. These points are randomly drawn from the prior distribution. The algorithm keeps drawing new points until one is found with a higher likelihood than the least likely point which is then removed (Buchner et al., 2014). This allows the algorithm to scan from the least probable to most probable zones. The MultiNest algorithm, which is used in this work, employs ellipsoidal nested sampling (Feroz et al., 2009, 2013; Buchner et al., 2014). Livepoints are drawn randomly from the prior distributions and are clustered into multi-dimensional ellipses. This form of clustering allows MultiNest to follow local maxima with ease meaning the parameter space can be efficiently explored which reduces the number of forward model runs required (Feroz et al., 2009, 2013; Buchner et al., 2014). The algorithm terminates once convergence of the marginal likelihood is attained (i.e., Bayesian evidence). A Python wrapper, PyMultiNest, has been developed (Buchner et

al., 2014), which allows efficient integration with the Python interface of FEniCS. Modelling in this study used MultiNest version 3.1, with each model using 400 livepoints in order to balance efficiency and accuracy. Once the algorithm terminates, PyMultiNest has the capability of plotting up two-dimensional marginalised posterior probability distributions so that the trade-offs between different parameters can be properly assessed (figure 3).

Once all of the posterior distributions have been generated, the median values of the parameters of interest, notably time and temperature, are used for further analyses. The median parameters may not necessarily be the same as the combination of parameters that produces the best fit. The mean was not used because it may be influenced by outliers. The mode was not used because it would involve discretising the posterior dataset. Figure 4 shows the covariance between activation energy and initial diffusivity for Fe-Mg exchange in olivine, and thus highlights the importance of including this into error propagation as it can reduce the size of the parameter space that is being explored. Accounting for covariance in diffusion parameters can improve the uncertainty estimates by a factor of 2-3. This is a significant reduction in timescale uncertainty, meaning diffusion timescales can be compared to other observations (e.g. geophysical observations) in the time domain with more confidence. Another benefit of MultiNest and PyMultiNest is that it can be programmed with a Message Passing Interface (MPI), meaning the same process can be run on multiple nodes and machines, making computation much more efficient. This currently requires high performance computing in order to complete models in a reasonable time. Supercomputer clusters would be required for more complex problems, such as using high resolution 3D meshes, to ensure convergence to a solution occurs in a reasonable timeframe. As an example, a Lenovo Thinkstation with an Intel XEON microprocessor could complete 10,000 1D olivine simulations in under 20 minutes when using 30 cores.

### 3 Application of DFENS to a petrologically well characterised system: The Skuggafjöll eruption, Bárðarbunga volcanic system

#### 3.1 The Skuggafjöll eruption, Bárðarbunga volcanic system

Bárðarbunga is a subglacial basaltic central volcano with a 70 km<sup>2</sup> caldera situated under the north western corner of the Vatnajökull ice cap in south eastern Iceland (Gudmundsson & Högnadóttir, 2007; Sigmundsson et al., 2015). The Bárðarbunga-Veiðivötn volcanic system comprises an extensive set of fissure swarms that have propagated up to 115 km to the southwest and 55 km to the north-northeast of Bárðarbunga central volcano (figure 5). It is the second largest volcanic system in the Eastern Volcanic Zone (EVZ), and elevated magmatic fluxes have been associated with the putative centre of the Iceland mantle plume (Gudmundsson & Högnadóttir, 2007; Jenkins et al., 2018). Within historical times alone, eruptions in the EVZ have accounted for approximately 82% (~ 71 km<sup>3</sup>) of the estimated eruptive volume on Iceland (Thordarson & Larsen, 2007). During this period of time the Bárðarbunga-Veiðivötn volcanic system erupted at least 24 times making it the second most active system in historical time and therefore an important target for hazard management (Larsen, 2002; Caracciolo et al., 2020). Most of these eruptions have taken place under the ice sheet with several generating large glacial floods, known as jökulhlaups, to the north (Thordarson & Larsen, 2007). The most recent Bárðarbunga-Holuhraun eruption in 2014-2015 serves as an additional reminder of the active nature of this volcanic system and the regional hazards that it can pose (Sigmundsson et al., 2015; Ágústsdóttir et al., 2016; Ilyinskaya et al., 2017).

Prior to the Holuhraun eruption, 13 days of seismicity that progressively propagated northeast from Bárðarbunga volcano along the Dyngjuháls fissure swarm was interpreted to represent the lateral propagation of magma (Sigmundsson et al., 2015; Ágústsdóttir et al., 2016). The eruption was accompanied by gradual caldera collapse, which



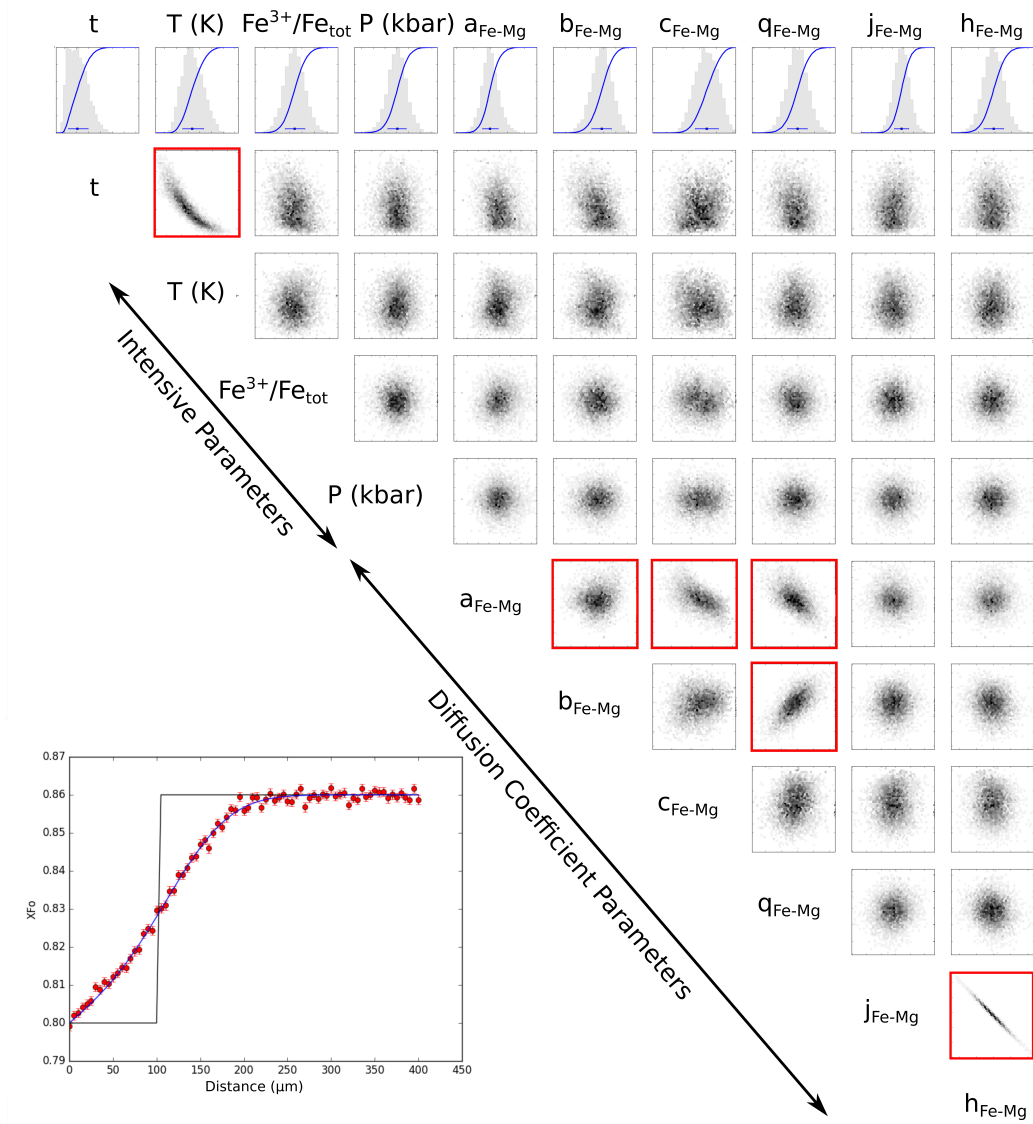


**Figure 3.** Posterior distributions generated by the DFENS method. Only Fe-Mg diffusion in olivine was modelled fitting a synthetic dataset generated using Skuggafjöll conditions (parallel to [100], using a time of 300 days, temperature of 1190 °C,  $\text{Fe}^{3+}/\text{Fe}_{\text{total}}$  of 0.15, pressure of 0.35 GPa, and a  $X_{\text{Fe}}$  uncertainty of  $\sim 0.01$ ). The profile data, initial conditions and model fits are shown in the bottom left corner. The top row shows marginal histograms and cumulative frequency distributions (blue curves) of the posteriors for each parameter (labelled at the top). The diffusion parameters for TaMED mechanism of Fe-Mg interdiffusion ( $a_{\text{Fe-Mg}}$ ,  $b_{\text{Fe-Mg}}$ ,  $c_{\text{Fe-Mg}}$ ,  $q_{\text{Fe-Mg}}$ ,  $j_{\text{Fe-Mg}}$  and  $h_{\text{Fe-Mg}}$ ) have been labelled as they have been presented in equation 7. The bottom nine rows show the trade-offs between each of these parameters in the form of density plots. Parameters which show systematic trade-offs have been highlighted with red boxes; which highlights the importance of including underlying covariance structures in the modelling. In this model, a total of 10 parameters were inverted for.

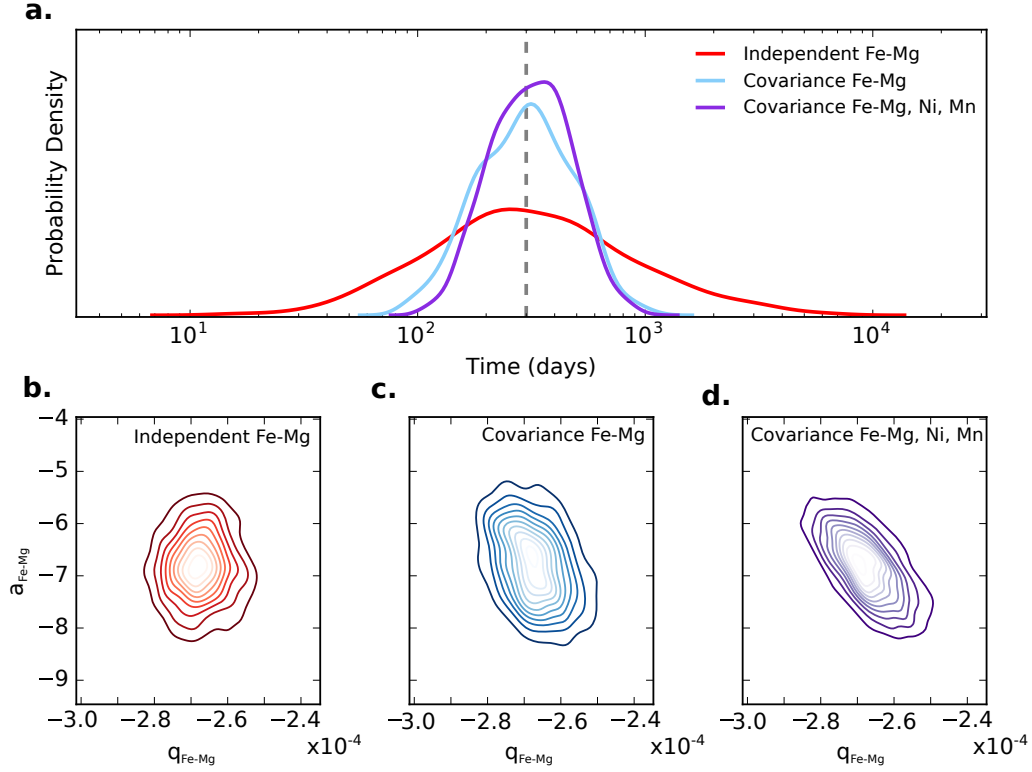


**Figure 4.** The effect of underlying covariance on the uncertainties of diffusion timescale estimates. **a** shows the posterior timescales distributions (kernel density estimates) for different olivine Bayesian inversion models using the DFENS method that were used to fit synthetic olivine profiles. The profiles were made parallel to [100] using a time of 300 days, temperature of 1190 °C,  $\text{Fe}^{3+}/\text{Fe}_{\text{total}}$  of 0.15 and pressure of 0.35 GPa, with additional noise added based on typical uncertainties from EPMA conditions used in this study ( $X_{\text{FeO}} \sim 0.01$ ,  $\text{Mn} \sim 36$  ppm,  $\text{Ni} \sim 36$  ppm). The grey line marks 300 days, which was used to produce the data. The red curve is a Fe-Mg diffusion model that assumes that the parameters that control the diffusion coefficient are independent. The blue curve is a Fe-Mg diffusion model that includes diffusion parameter covariance as defined by the covariance matrix shown in the Supplementary Material. The purple curve is a multi-element diffusion model (Fe-Mg, Ni, Mn) that also includes covariance structure. **b**, **c** and **d** are multivariate kernel density estimations showing the trade-off between posterior distributions in  $a_{\text{Fe-Mg}}$  (related to  $\ln D_0$ ) and  $q_{\text{Fe-Mg}}$  (related to the activation energy) for Fe-Mg interdiffusion. These plots have been colour-coded using the same scheme as in **a**. It is clear that models that include a covariance structure between the diffusion parameters are associated with much smaller uncertainties, by as much as a factor of 2-3.

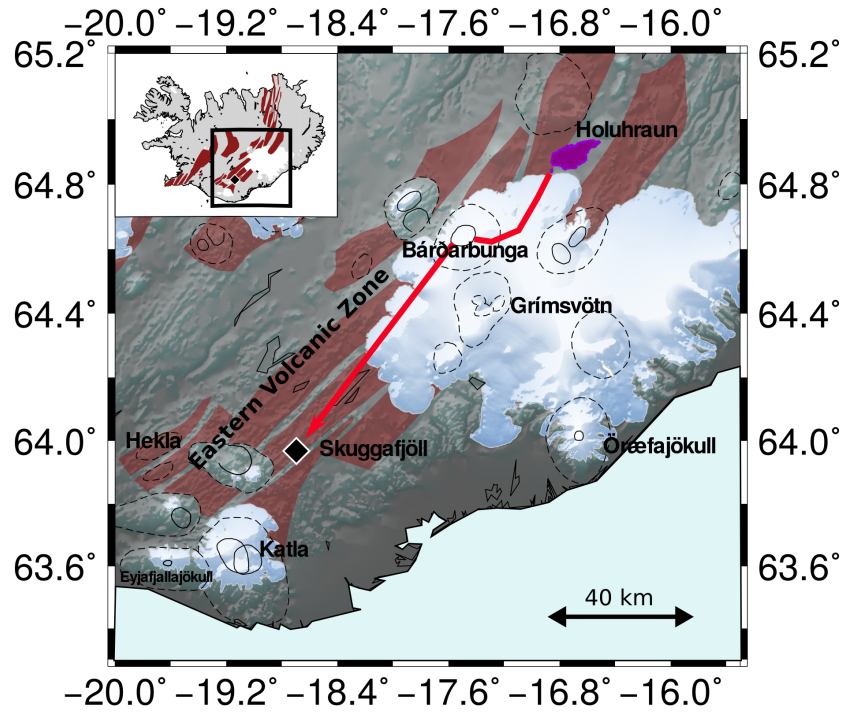


**Figure 5.** Map of the Eastern Volcanic Zone of Iceland (EVZ) showing the location of the Skuggafjöll eruption (black diamond) within the Bárðarbunga-Veiðivötn volcanic system. The most recent eruption in the Bárðarbunga system, the 2014-2015 Holuhraun eruption, is also shown in purple for reference. The dyke propagation pathways for each eruption are shown as red arrows. For Holuhraun the dyke propagation pathway was constrained using pre-eruptive seismicity (Sigmundsson et al., 2015; Ágústsson et al., 2016), whilst for Skuggafjöll a simple linear dyke pathway was assumed. The location of major central volcanoes is marked with their associated calderas (dashed lines). Major fissure swarms in the EVZ are shown in red (Thordarson & Larsen, 2007). Inset shows the location of the mapped region and Skuggafjöll with respect to the rest of Iceland.

supported the notion of lateral magma migration from the central volcano (Gudmundsson et al., 2016). The excellent coverage of geophysical monitoring methods of the Holuhraun eruption has provided a valuable insight into the timescales and mechanisms of dyke propagation and lateral magma flow during an Icelandic rifting event (Ágústsdóttir et al., 2016; Woods et al., 2018). These geophysical observations are now starting to be reconciled with geochemical observations in order to place real-time observations into a petrological framework (Halldórsson et al., 2018; Hartley et al., 2018; Bali et al., 2018). However, to develop effective forecasting strategies for volcanic eruptions and their associated hazards, studies into multiple eruptions from the same volcano or volcanic system are required. In this instance, looking for pre-eruptive signals prior to dyke propagation in the petrological record of older eruptions may help to focus current geophysical monitoring methods of Icelandic volcanoes.

The Bárðarbunga-Veiðivötn system is also believed to have been highly productive during the Holocene and Pleistocene with large fissure eruptions repeatedly taking place on the south-western Veiðivötn fissure swarm (Larsen, 1984). The Skuggafjöll eruption is one such example of Pleistocene activity in the Bárðarbunga-Veiðivötn system. Skuggafjöll is an 820 m high mountain that is part of a NE-SW striking hyaloclastite ridge situated between Vatnajökull and Mýrdalsjökull (Neave, MacLennan, Hartley, et al., 2014). It is composed of plagioclase ultraphyric basalts that transition from pillow lavas at the base to hyaloclastites halfway up the mountain. These characteristics indicate that Skuggafjöll was a subglacial eruption, and places a minimum eruption age of approximately 10 ka (Jakobsson & Gudmundsson, 2008; Neave, MacLennan, Hartley, et al., 2014). A minimum erupted volume of 0.2 km<sup>3</sup> was estimated for Skuggafjöll by Neave, MacLennan, Hartley, et al. (2014) assuming a cone shaped edifice with a basal radius of 1 km and height of 0.2 km; although this did not take into account any subsequent erosion or burial by later eruptions. In spite of the poor constraints on eruption age and erupted volume, the well constrained petrological history preserved in its crystal cargo can be used to gain important constraints on the timescales of pre-eruptive processes in the Bárðarbunga system and to test the performance of different mineral geospeedometers.

### 3.2 Petrology and sample description

All samples described by Neave, MacLennan, Hartley, et al. (2014) of the Skuggafjöll eruption are olivine (1-3 %), clinopyroxene (2-9 %), and plagioclase phyrlic (3-36 %) with macrocrysts of these phases occurring as single isolated crystals and within monomineralic and polymineralic glomerocrysts. Plagioclase and olivine are often intergrown in glomerocrysts with interstitial melt pockets, which is suggestive of sequestration in a crystal mush as opposed to being joined by synnuesis just before eruption. The habit of many of the coarser plagioclase macrocrysts is too equant to be the result of rapid crystallisation, and is likely to represent a deep mush origin (Holness, 2014).

Whole rock geochemical variation indicates significant crystal addition, particularly of plagioclase (Neave, MacLennan, Hartley, et al., 2014). Olivine macrocrysts range in size from 150 µm up to 4 mm, and are typically equant and subhedral. Clinopyroxene macrocrysts are 150 µm to 2.2 mm in size with equant and prismatic habits. The plagioclase macrocrysts show the largest range in observed crystal size and texture. They range in size from 150 µm up to 12 mm with large, low aspect ratio (> 600 µm size and length/width aspect ratios of 1.5) and small, high aspect ratio (< 600 µm and aspect ratios > 2) crystal populations present (Neave, MacLennan, Hartley, et al., 2014). Large plagioclase macrocryst cores show a range of melt inclusion textures from the absence of melt inclusions up to well-developed sieve textures. The presence of these defined crystal populations has been confirmed by crystal size distributions for each of the macrocryst phases, all of which show pronounced changes in gradient (Neave, MacLennan, Hartley, et al., 2014). The two crystal populations are also compositionally distinct; particularly for the cases of olivine and plagioclase. The coarser plagioclase and olivine macro-

crysts have a more primitive character with core compositions of  $\text{An}_{80-90}$  and  $\text{Fo}_{85-87}$  respectively. These crystal cores are surrounded by sharp, more evolved rims,  $\text{An}_{70-79}$  and  $\text{Fo}_{78-82}$ , that coincide with the compositions of the smaller macrocrysts and are in equilibrium with the matrix glass (Neave, MacLennan, Hartley, et al., 2014).

Melt inclusions from the primitive olivine and plagioclase macrocrysts show significant variation in their trace element compositions which is suggestive of crystallisation from a suite of unmixed primary mantle melts (MacLennan, 2008; Winpenny & MacLennan, 2011; Neave et al., 2013; Neave, MacLennan, Edmonds, & Thordarson, 2014). However, the major element composition of these melt inclusion suites combined with the fact that their average trace element compositions are near identical within uncertainty provides strong evidence to suggest that the olivine and plagioclase cores co-crystallised from the same range of primitive melts (Neave, MacLennan, Hartley, et al., 2014). The average incompatible trace element composition of the melt inclusions is also significantly more depleted than that of the matrix glass, which indicates that the more evolved rims and crystal population crystallised from distinct primary melt distributions (Neave, MacLennan, Hartley, et al., 2014). Clinopyroxene-liquid geobarometry based on equilibria between the matrix glass and the clinopyroxene macrocrysts suggest that most crystallisation took place at mid-crustal pressures ( $0.35 \pm 0.14$  GPa or  $11 \pm 4$  km depth) (Neave & Putirka, 2017).

All of the above observations have been interpreted by Neave, MacLennan, Hartley, et al. (2014) to be the result of two stages of crystallisation. The primitive macrocrysts cores crystallised from depleted primitive melts and were sequestered into a mineralogically stratified crystal mush pile in the mid-crust. Portions of non-cotectic mush were disaggregated and entrained into trace element enriched magma from which the more evolved rims and crystal assemblage grew at the three-phase gabbro eutectic. Transport and eruption at the surface must have occurred soon after given that the crystal rims are still relatively sharp. Modelling the diffusive re-equilibration between macrocryst cores and rims can provide a pre-eruptive timescale of the second stage of crystal growth and transport. The relatively simple petrological history that has been constrained by the in-depth work of Neave, MacLennan, Hartley, et al. (2014) makes Skuggafjöll an ideal eruption to develop, test and refine multi-element and multi-mineral diffusion modelling techniques.

### 3.3 Analytical methods

Individual olivine and plagioclase crystals were picked from crushed glassy pillow basalt rims collected from the lower sections of the Skuggafjöll eruptive stratigraphy (GR: 63°968'N, 18°695'W). These were then mounted in epoxy 1-inch rounds and polished using silicon carbide papers and Metprep diamond suspension down to 0.25  $\mu\text{m}$  grade.

#### 3.3.1 BSE imaging

The texture and zoning patterns of approximately 40 olivine crystals and 50 plagioclase crystals were assessed by back-scatter electron (BSE) microscopy using a FEI Quanta 650FEG SEM at the University of Cambridge. BSE images were typically collected using an accelerating voltage of 10-20 kV and a working distance of 13 mm. To try to minimise charging effects from cracks and vesicles, 10 images were collected with a scanning rate of 1  $\mu\text{s}$  and were integrated together with a drift correction. The brightness and contrast of collected images were adjusted using ImageJ image processing software in order to accentuate any zoning patterns.

To minimise potential sectioning problems and diffusion from multiple dimensions (Costa & Morgan, 2010), crystal sections that followed the criteria of Shea et al. (2015) underwent quantitative analysis. Compositional profiles were positioned on euhedral crys-

tal edges and in the centre of crystal faces or as far away from other crystal edges as possible.

### 3.3.2 EPMA

Compositional profiles of major and minor elements across selected olivine and plagioclase crystals were measured by electron probe microanalysis (wavelength dispersive X-ray spectroscopy, EPMA) using a Cameca SX100 with 5 wavelength dispersive spectrometers at the University of Cambridge. Calibration was carried using a mixture of natural and synthetic minerals and oxides. Instrument drift and measurement uncertainty was assessed by measuring secondary standards. For olivine analyses, an accelerating voltage of 20 kV was applied with a working current of 20 nA for major elements (Mg, Fe, Si) and 200 nA for minor and trace elements (Ni, Mn, Ca, Cr, Al). On peak count times of 20 s were used for major elements and 100-120 s for minor and trace elements, with half count times off peak. P was not measured routinely because the electron probe was operating without an LPET crystal (2 LIF arrangement). Plagioclase profiles were measured with an accelerating voltage of 15 kV and a working current of 10 nA for major (Ca, Al, Si, Na) and minor elements (Mg, Ti, K, Fe). On peak count times of 20 s were used for major elements and 90-110 s for minor and trace elements, with half count times off peak. For both sets of analyses, a spot size of 1  $\mu\text{m}$  was selected, with profile point spacing varying from 5  $\mu\text{m}$  (typically within 150  $\mu\text{m}$  of the crystal edge) and 20  $\mu\text{m}$  (distances exceeding 150  $\mu\text{m}$  from the edge). For plagioclase, the beam was not defocussed to account for any alkali or silica drift given that Na and K concentrations were typically low in high anorthite plagioclase (Humphreys et al., 2006). Instead, Na and K were measured at the start of the analytical cycle for only 10 s.

### 3.3.3 SIMS

Plagioclase trace element data were collected using a Cameca ims-4f and a Cameca 1270 Secondary Ion Mass Spectrometer (SIMS) at the Edinburgh Materials and Micro-Analysis Centre (EMMAC), University of Edinburgh. Spot analyses were made with a 3 nA  $^{16}\text{O}^-$  primary beam of 22 keV net impact energy focussed to approximately 15  $\mu\text{m}$ . This generated 10 keV positive secondary ions with 75 eV secondary (100 eV window). Spots were individually placed across crystals from rim to core. Elements measured by coarse spot analysis include (count times in seconds are in brackets):  $^{30}\text{Si}$  (2),  $^{26}\text{Mg}$  (5),  $^{42}\text{Ca}$  (2),  $^{47}\text{Ti}$  (5),  $^{88}\text{Sr}$  (5),  $^{138}\text{Ba}$  (5),  $^{39}\text{K}$  (5),  $^7\text{Li}$  (5),  $^{89}\text{Y}$  (5),  $^{140}\text{Ce}$  (5),  $^{139}\text{La}$  (5) and  $^{85}\text{Rb}$  (5). A 60  $\mu\text{m}$  image field is apertured to give about 20  $\mu\text{m}$  collection window. Coarse analyses were averaged over 10 cycles.  $^{30}\text{Si}$  (2),  $^{26}\text{Mg}$  (5),  $^{47}\text{Ti}$  (5) and  $^{88}\text{Sr}$  (5) were routinely measured using high resolution step scan analyses. Step scans (high resolution line scans) were collected by initially setting a line scan pre-sputter of 3.2 nA using 10  $\mu\text{m}$  steps. Step scan analyses were made with  $2.5 \times 10^{-11}$  nA primary beam focussed to approximately 2  $\mu\text{m}$ , with step spacing set to 2  $\mu\text{m}$ . There was no energy offset and 100 eV energy window was used. There were no losses due to field apertures as the spot size was much smaller than collection window. The scan position in the centre of line was positioned with scanning ion imaging of Na and Si. Electron multiplier ions counting was used and all data were dead-time corrected (51 ns dead time). An entrance slit of 100  $\mu\text{m}$  and exit slit of 400  $\mu\text{m}$  were used. The nominal mass resolution was approximately  $M/\Delta M$  2400. A combination of feldspar (SHF-1 and Lake county plagioclase) and glass standards (NIST610, and V, W, X borosilicate glasses) were used to access analytical precision and convert raw counts to ppm values. Trace element silicon ratios measured by SIMS were then corrected relative to Si measured by EPMA. Step scan data was then normalised to SIMS data in order to convert raw elemental ratios into concentrations. Prior to normalisation, SIMS, step scan and EPMA profiles were projected onto a single profile that was orientated perpendicular to the edge of the crystal. Distances of anal-



yses were corrected accordingly using  $\cos\theta$  where  $\theta$  is the angle between the measured profile and the perpendicular projection.

### 3.3.4 EBSD

Chemical diffusion of some major and minor elements in olivine has been shown to be strongly anisotropic. For example Fe-Mg interdiffusion along the [001] direction is typically 6 times greater than along the [100] and [010] axes (Chakraborty, 2010; Costa & Morgan, 2010). The lattice orientations of the studied olivine crystals were thus characterised using electron back-scatter diffraction. EBSD data with a resolution of 1-10  $\mu\text{m}$  were collected at the University of Cambridge with a Bruker e Flash HR EBSD detector equipped on the Quanta 650FEG SEM, operating at 20 kV and beam spot size 5.5, and a stage tilt of 70°. The detector resolution was 320 x 240 pixels, while working distance and sample to detector distance were 17-30 mm and 12-18 mm respectively. The data collection and indexing was performed with Bruker QUANTAX CrystAlign software (QUANTAX, 2010), using a Hough transform resolution of 60-70. Data were analysed using MTEX V4.0 (Bachmann et al., 2010), a freeware toolset for the commercial software package MATLAB (MATLAB, 2016).

## 3.4 Modelling Methods

### 3.4.1 Estimation of intensive parameters

The temperature of the carrier-liquid was estimated to be  $1190 \pm 30^\circ\text{C}$  by Neave, MacLennan, Hartley, et al. (2014) using the clinopyroxene-liquid thermometer from equation 33 of Putirka (2008), which was applied to second generation clinopyroxene macrocrysts that were in equilibrium with the glass. A pressure of  $0.35 \pm 0.14$  GPa was also estimated by (Neave & Putirka, 2017) using their recent clinopyroxene-liquid geobarometer. A  $\text{Fe}^{3+}/\text{Fe}_{\text{total}}$  (ferric iron content of the melt) value of  $0.15 \pm 0.02$ , representative of more enriched Icelandic basalts, was used (Shorttle et al., 2015); this value was then converted into an oxygen fugacity ( $f\text{O}_2$ ) using an average glass composition of Neave, MacLennan, Hartley, et al. (2014) and equation 7 of Kress and Carmichael (1991). The  $a_{\text{SiO}_2}$  ( $0.62 \pm 0.04$ ) of the Skuggafjöll magma was estimated using the same glass composition and the liquid's affinity for tridymite calculated in rhyolite-MELTSv1.02 (Gualda et al., 2012; Ghiorso & Sack, 1995).

### 3.4.2 Mg in plagioclase partitioning behaviour

Many plagioclase partitioning models have undergone recent scrutiny as in some cases they fail to properly replicate the partitioning behaviour observed in natural systems. This is believed to be in part due to experimental regressions using averaged analyses that may fail to account for disequilibrium, small scale zoning and analysis contamination (Nielsen et al., 2017). Furthermore, global partitioning relationships may smooth out subtle changes in plagioclase structure that could influence partitioning. This has led some studies to develop their own empirical partitioning relationships using crystals which are believed to show trace element pseudo-equilibrium (Moore et al., 2014). Here we adopt a similar empirical approach by using Skuggafjöll plagioclase macrocrysts with crystal faces defined by thin overgrowths. These thin rims are typically thinner than 20  $\mu\text{m}$  (in some instances being only 5  $\mu\text{m}$  thick) and are often associated with (010) faces, which have slower growth rates than (001) and (100) respectively (Holness, 2014; Muncill & Lasaga, 1988). The parts of the crystal cores that are adjacent to these rims will equilibrate fairly rapidly for Mg meaning these faces provide an excellent opportunity to constrain the partitioning behaviour of Mg in these types of systems at a given temperature. Rim and core compositional data measured 20  $\mu\text{m}$  of crystal edge were combined with experimental data (Bindeman et al., 1998; Bindeman & Davis, 2000) filtered above  $\text{An}_{60}$  to constrain a new empirical linear partitioning relationship applicable to basaltic

systems:

$$RT\ln K_{\text{Mg}} = -34.1(20)X_{\text{An}} - 17.4(16). \quad (12)$$

### 3.4.3 Olivine Initial conditions

Diffusion timescale estimates depend heavily on the assumed contributions of growth and diffusion, which is often expressed in the way that initial conditions are calculated. Compositional cross-plots of Al versus  $X_{\text{Fo}}$ , Ni and Mn in Skuggafjöll olivines (figure 6) show step-like patterns that indicate diffusive decoupling between the effectively immobile Al (Spandler & O'Neill, 2010) and the faster diffusing elements. The figure also shows a convex pattern between forsterite and Ni, which indicates that most profiles were dominated by diffusion (Costa et al., 2020). Mutch, MacLennan, Shorttle, et al. (2019) assumed the Al profiles can be used to track the compositional morphology of rapid crystal growth and can thus be used as a proxy for initial conditions for the other elements of interest. This approach also relies on the assumption that the concentration of each element is linearly related to each other during growth. We adopt the same approach here. Core and rim compositions of the Al and the elements of interest were selected. Rim compositions were at the edge of the crystal and the core composition were chosen based on where the profiles flattened out (accounting for analytical uncertainties). A rim zone was selected based on where Al starts to decrease rapidly (taking into account any variations in Al content in the core). A linear calibration curve was then made between the rim and core compositions for each element. Diffusion would cause any deviations from linearity. The linear calibration curve was then used to convert Al compositions in the rim zone into concentrations of the element of interest. Points outside the rim zone were assigned the core composition. Figures illustrating this concept are in the Supplementary Material.

As Phosphorus was not measured in most profiles, it was difficult to assess whether the Al profiles were controlled by growth rate. However, the fact that Al concentrations did not increase suggests that there was no enrichment associated with the establishment of a diffusive boundary layer (de Maisonneuve et al., 2016). Furthermore, the consistency in olivine rim compositions across all crystals ( $\sim 160$ -180 ppm) suggests that rim composition may have been controlled by the far field melt composition.

### 3.4.4 Plagioclase Initial Conditions

Plagioclase initial conditions were developed using the assumption of the instantaneous growth of a homogeneous rim with the same concentration as the outer edge in contact with the melt.  $X_{\text{An}}$  versus  $RT\ln K_{\text{Mg}}$  plots that have been colour coded for distance from the crystal edge show that Mg compositions measured in plagioclase cores are negatively correlated with  $X_{\text{An}}$  and form arrays that are subparallel to the partitioning relationship established in this study (figure 7). Crystal rims and cores that are close to the rim-core interface typically fall off these trends which suggests that diffusion was taking place. These patterns indicate that the plagioclase cores were equilibrated at a different set of P-T-X conditions (P-T-X 1) than those that were responsible for the rim (P-T-X 2), with points between the P-T-X arrays representing disequilibrium. Mg initial conditions were produced by combining equilibrated core Mg compositions at P-T-X 1 conditions with a homogeneous rim that was in equilibrium with the carrier liquid (i.e. there is a step in  $X_{\text{An}}$  and Mg rather than continuous variation). The higher  $RT\ln K_{\text{Mg}}$  values calculated for core compositions suggest that they need to be in equilibrium either at higher temperatures or with a more primitive melt than the final carrier liquid.



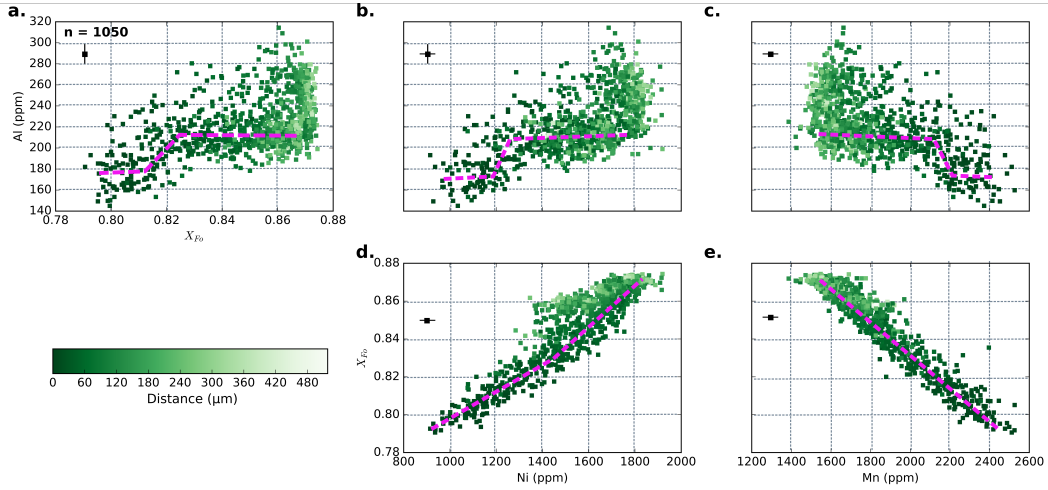


**Figure 6.** Compilation of olivine profile data collected by EPMA expressed as compositional cross-plots between the main elements typically used in olivine geospeedometry ( $X_{Fo}$ , Ni and Mn) and Al, an immobile trace element (Spandler & O’Neill, 2010) that we use as a proxy for growth. The upper row corresponds to cross-plots between Al and  $X_{Fo}$  (a), Ni (b) and Mn (c), whilst the lower row (d, e) has Ni versus  $X_{Fo}$  and Mn versus  $X_{Fo}$  cross-plots. All of the data have been colour-coded as a function of distance from the crystal edge. Cross-plots between Al and the elements of interest show a non-linear step-like distribution between rim and core compositions (purple lines) indicating diffusive decoupling. The large variability in Al content for forsteritic core compositions ( $X_{Fo} \sim 0.86-0.87$ ) may reflect intercrystalline or intracrystalline heterogeneity in Al that has not been diffusively re-equilibrated in the crystal mush pile (Thomson & MacLennan, 2012). The cross-plot between Mn and  $X_{Fo}$  shows a strong linear trend suggesting there has been very little diffusive decoupling between these two elements and that their diffusivities are similar. A subtle break in slope can be observed in the Ni versus  $X_{Fo}$  cross-plot, which is indicative of minor diffusive decoupling likely imposed by slight differences in elemental diffusivity. Typical analytical uncertainties are shown by the black point.

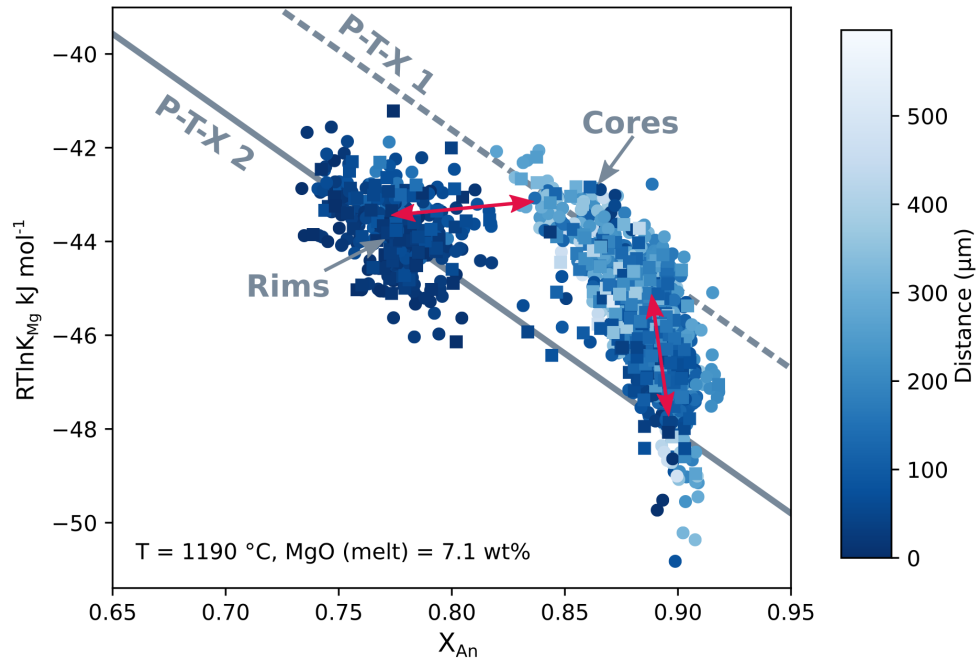


**Figure 7.** Calculated Mg partition coefficients ( $RT\ln K_{Mg}$ ) versus anorthite content for profiles collected by SIMS (squares) and EPMA (circles). Partition coefficients were calculated using the average concentration of the element in the glass and the estimated temperature of the carrier liquid (1190 °C) (Neave, MacLennan, Hartley, et al., 2014). Each point is colour-coded for the distance from the edge of the crystal. The grey lines are predictive partitioning models established for plagioclase at different sets of P-T-X conditions. The partitioning relationship is the one established in this study. The red arrows show data that may have been influenced by diffusion.

### 3.4.5 Diffusion modelling using Finite Elements and Nested Sampling (DFENS)

Magmatic timescales were estimated for measured olivine and plagioclase compositional profiles using the DFENS method outlined above. A fixed Dirichlet boundary condition ( $C = C_0$  on  $x = 0$ ) was maintained at the crystal edge and a no-flux Neumann boundary condition ( $\frac{\partial C}{\partial n} = 0$  on  $x = L$ ) was maintained in the crystal interior. Fe-Mg exchange was treated as nonlinear and was solved first at each time step using a Newton solver. Ni and Mn diffusion was treated as a linear problem and was solved at each time step using the corresponding Fe-Mg (forsterite) solution. Diffusion of Mg in plagioclase was modelled using the diffusion equation derived by Costa et al. (2003), which accounts for the variation of the chemical potential of the Mg-component (equation 2). In this instance, diffusion of Mg was also treated as a linear diffusion problem, but with diffusivity at each point in the mesh being controlled by the anorthite profile. The models assumed that there was a semi-infinite melt reservoir in which the elements of interest could diffuse into.

A log uniform prior was used for time (0-10,000 days). Independent Gaussian priors, set with  $1\sigma$  uncertainties, were used for intensive parameters including: temperature (T), pressure (P), ferric iron content of the melt ( $\text{Fe}^{3+}/\text{Fe}_{\text{total}}$ ), and the activity of  $\text{SiO}_2$  ( $a_{\text{SiO}_2}$ ). Multivariate Gaussian priors were used for coefficients in the diffusion equations which are controlled by their respective covariance matrices. In the case of plagioclase, a multivariate Gaussian prior was also used to define the A and B parameters of the Mg partitioning relationship (equation 12) that contributes to the diffusive flux. This was constrained using the covariance matrix of the regression shown in equation 12. The log likelihood function of the inversion employed a  $\chi^2$  misfit between the model and all measured observations which was weighted by their analytical uncertainties. The nested sampling Bayesian inversion was set with 400 livepoints, and the algorithm terminated once convergence of the marginal likelihood was attained.

## 4 Results

### 4.1 Olivine timescales

A total of 29 different olivine crystals were modelled using the DFENS method (e.g. figure 9). The inversion typically converged to short magmatic timescales with a median of all modelled olivine crystals being 146 days and 95 % of all retrieved timescales being shorter than 368 days (figure 8). Each crystal typically required 10,000 to 300,000 realisations in order to reach convergence. The median values for all of the realisations for each individual modelled crystal ranges from 56 to 323 days. All of the olivine models converged around similar temperature, pressure and  $f\text{O}_2$  conditions and are within the Gaussian priors used by the Bayesian inversion.

### 4.2 Plagioclase timescales

Many plagioclase crystals show evidence of uphill diffusion at the rim-core interface (figure 10). The median timescale of 23 plagioclase crystals modelled using the DFENS methodology was 203 days whilst 95 % quantile for all of the data was 1401 days. These plagioclase crystals were physically separate from the modelled olivine crystals. In spite of the median timescales of all plagioclase crystals being similar to those of the olivines, the medians of individual crystals spanned a much broader range (1-1323 days instead of 56-324 days). Figure 8 nevertheless shows that most of the plagioclase crystals are in excellent agreement with the olivines. However, approximately 25 % of crystals returned much shorter timescales than the olivines (0.2 - 6 days), whilst another 25 % of plagioclases returned considerably longer timescales (600 - 1323 days). The other intensive parameters, notably temperature, did vary more than those for olivine and in some instances

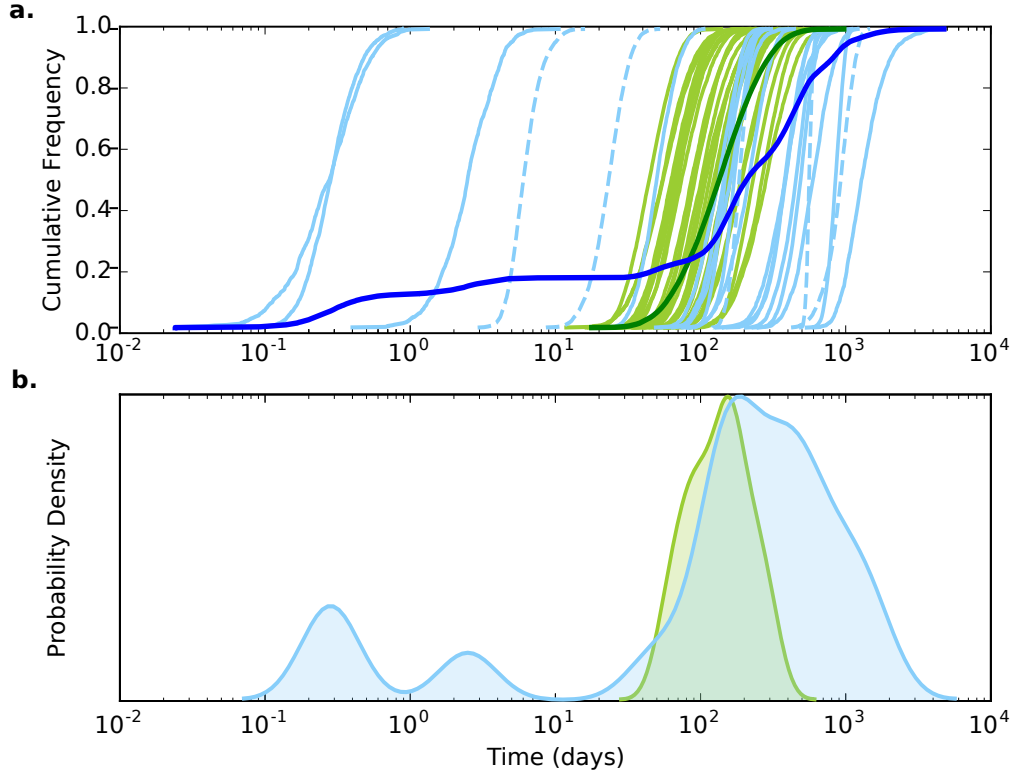


**Figure 8.** Maximum likelihood diffusion timescales for olivine (green) and plagioclase (blue) crystals modelled using the DFENS Bayesian inversion method. **a** shows cumulative frequency curves for each modelled crystal and combined cumulative frequency curve for each modelled phase in slightly darker colours. Dashed lines are model results that were eliminated based on some intensive parameters (e.g. temperature) converging outside their initial priors. **b** shows kernel density estimates (KDE) using the median timescales of the inversion result of each crystal. The bandwidth for each KDE was calculated using Silverman’s rule (Silverman, 2018). Plagioclase shows a much broader range in timescale estimates than olivine, however there is strong agreement between the two phases between 100 and 400 days.

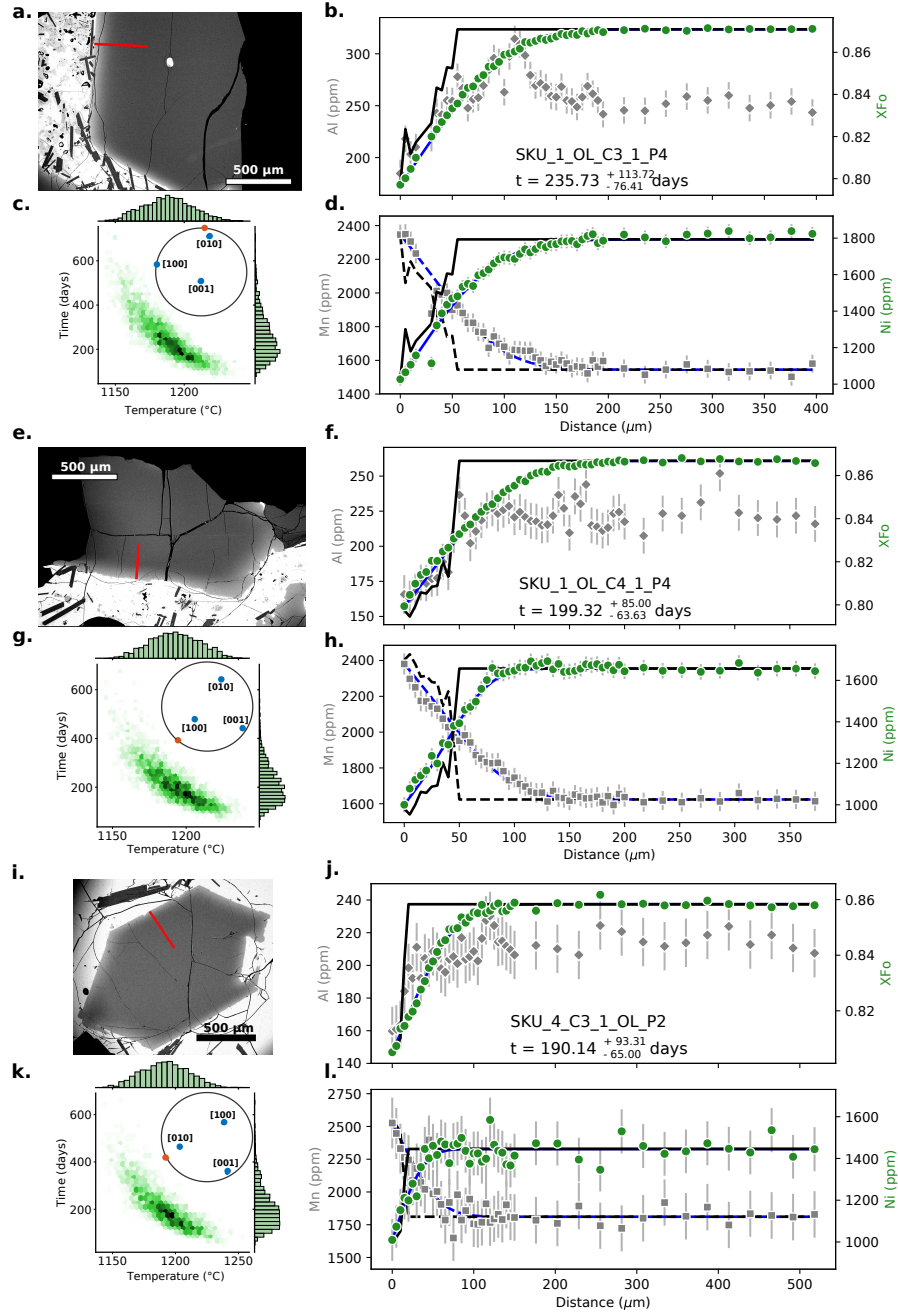


**Figure 9.** Compositional profiles and model results of Skuggafjöll olivine macrocrysts: SKU\_1\_OL\_C3\_P4 (a-d), SKU\_1\_OL\_C4\_1\_P4 (e-h) and SKU\_4\_C3\_1\_OL\_P2 (i-l). **a, e, i:** BSE images of olivine crystals showing the location of the EPMA profile (red line). **b, f, j:** forsterite (green circles) and Al (grey diamonds) compositional profiles. The Al profile is taken to be representative of crystal growth and was used as a proxy for initial conditions for each element (shown by black lines). **c, g, k:** Marginal plots showing posterior distributions of temperature and diffusion timescale from the DFENS Bayesian inversion and the trade-off between these two parameters. Inset is an equal area pole figure showing the orientation of the EPMA profile (red circle) with respect to the main crystallographic axes in olivine (labelled blue circles). **d, h, l:** Ni (green circles) and Mn (grey circles) compositional profiles. The blue lines in all profile plots are the minimised  $\chi^2$  misfit corresponding to the modelled maximum likelihood parameters estimated from the Bayesian inversion.

did converge outside of the original prior values. For example, plagioclase crystals that converged to shorter times typically converged to higher temperatures and vice versa; although there are some exceptions to this as well (e.g. HOR\_3\_C3\_P2). This could be due to the trade-offs between the trace element plagioclase partitioning relationships, which also controls the diffusive fluxes, and the other intensive parameters, most notably temperature.

## 5 Discussion

### 5.1 Consistency and inconsistency in timescale estimates

Overall there is good consistency between the timescale estimates obtained from olivine and plagioclase. Most crystals return timescales between 50 and 400 days, suggesting that rim growth took place less than a year prior to eruption. The general agreement between olivine and plagioclase timescales also suggests that the diffusion coefficients of these two separate phases are robust to the first order and that these geospeedometers are consistent within the uncertainties of the methods. It also confirms the interpretations of textural and petrographic observations that at least some of the crystals from both of these phases experienced a similar magmatic history. However, some of the plagioclase crystals record much shorter (0.2-6 days) and longer timescales (600 - 1479 days). These timescale disagreements could be rationalised in a number of ways.

### 5.2 Diffusion from multiple directions

Firstly, it seems that diffusion along a 1D plane may not be a valid assumption for some of the profiles measured. Efforts were made to try and position profiles in the centre of crystal faces in order to avoid merging diffusion fronts and multi-dimensional diffusional effects (Shea et al., 2015). However, some plagioclase SIMS profiles (e.g. HOR\_3\_C1\_P3, HOR\_3\_C2\_P1, SKU\_4\_C2\_P1) were positioned in inappropriate positions due to difficulties in observing crystal edges through the gold coat and the inability to properly correlate BSE maps to reflected light images. Therefore, it is likely that some of the anomalously long plagioclase timescales are partially the result of diffusion from directions different to the measured profile.

### 5.3 Improper fitting and misalignment of analytical profiles

Secondly, the plagioclase compositional data was collected using three different analytical methods; SIMS, EPMA and SIMS step scan. Each of these methods have their own associated spatial and compositional resolution. Na was not collected for the SIMS or step scan data meaning calculated anorthite contents were interpolated from EPMA profiles. Mismatches in profile alignment or the differences in spatial resolution may have introduced inconsistencies in calculated chemical potential gradients which may not have been properly fitted in the models. This may have been the case for the crystals that returned very short pre-eruptive residence times (e.g. SKU\_1\_C3\_P2, SKU\_4\_C2\_P1, SKU\_4\_C3\_P3; see Supplementary Material). These profile misalignments may also have led to misaligned initial conditions, which in turn may have been associated with poor model fits.

### 5.4 Sectioning effects

Thirdly, the assumption about the main chemical potential gradient being perpendicular to the measured compositional profile may not be true for all of the crystals. Costa and Morgan (2010) discuss that sectioning effects, in which the crystal zoning is at an angle to the surface on which the crystal is analysed, can act to increase the apparent thickness of crystal zoning and thus lead to overestimates in timescales. Given that all

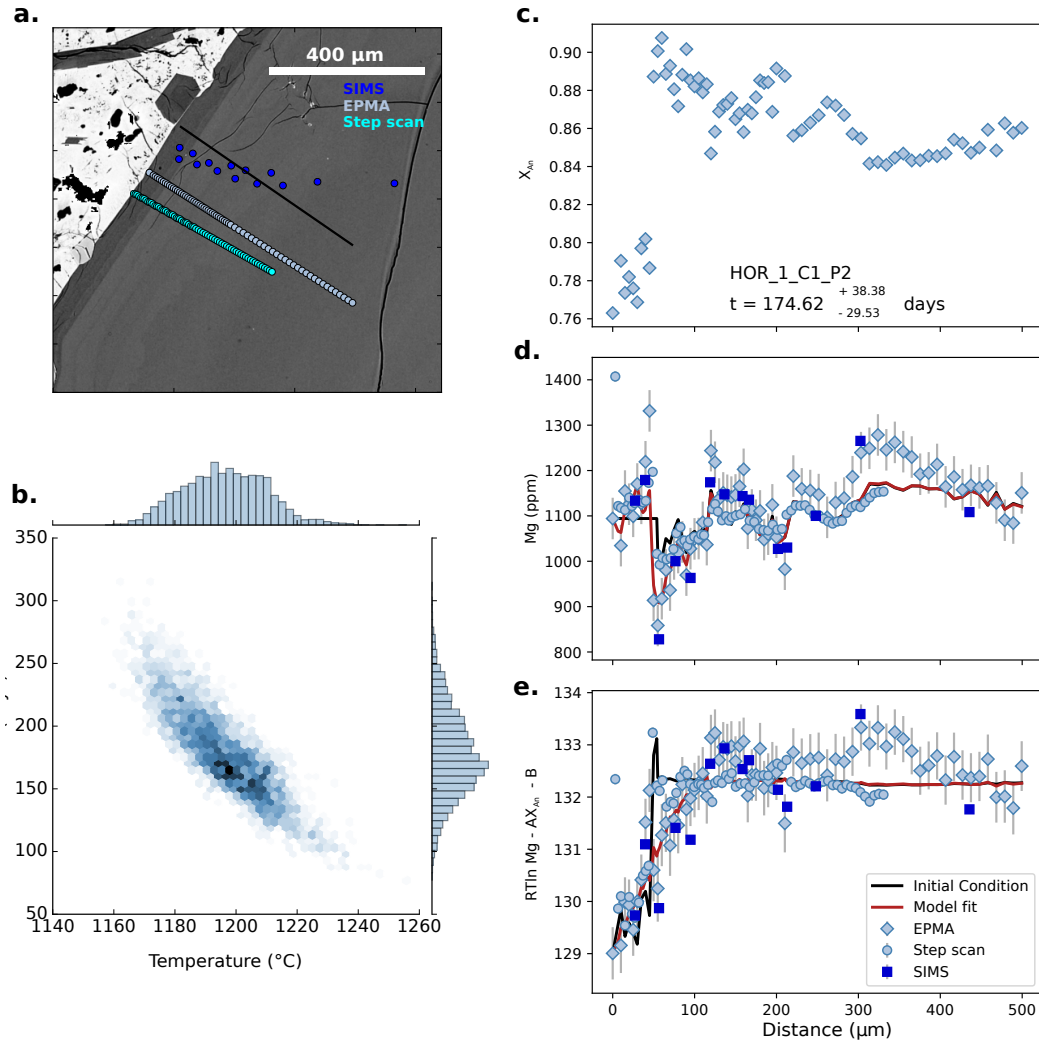


**Figure 10.** Plagioclase compositional data and diffusion model fits of crystal HOR\_1\_C1\_P2. **a** is a BSE image of the plagioclase crystal showing the location of coarse SIMS spot analyses (blue spots), EPMA traverse (light blue spots) and SIMS step scan analyses (cyan points). Points from each profile were projected onto the black line. **b**, Marginal plot showing the trade-off between temperature and time for the posterior distributions generated in the Bayesian inversion. **c**, Anorthite profile of plagioclase as measured by EPMA. **d**, Mg compositional profile with point shapes and colours marked by analytical method. Dark blue squares are SIMS coarse spot analyses, light blue circles are SIMS step scan analyses and light blue diamonds are EPMA analyses. The black line is the calculated initial conditions used in the modelling, and the red line is the model fit using the maximum likelihood of all of the parameters used in the Bayesian inversion. **e**, calculated activities of Mg in plagioclase using the most likely partitioning parameters estimated from the Bayesian inversion. Symbols and colours are the same as in **d**.



of the crystals are contained in glass chips and mounted in epoxy, it is difficult to assess the inclination of the crystal boundaries using conventional optical means (e.g. using a universal stage or looking for changes in birefringence) without resorting to polishing the samples down to thick section thickness. In the case of olivine, crystal morphology and zone thicknesses can be used as an effective way of filtering out inclined crystal boundaries (Shea et al., 2015). This can be more difficult for plagioclase as different crystal faces can grow at different rates. For example growth along [100] is faster than growth along [010] at different degrees of undercooling (Muncill & Lasaga, 1988; Higgins, 1996; Holness, 2014). Crystal profiles with longer timescales are often associated with thicker rims. This could, in part, be related to inclined crystal boundaries. X-ray tomography of crystals in the mounting medium may prove to be a useful method for identifying inclined crystal boundaries for use in diffusion studies.

## 5.5 Uncertainties in partitioning models

Fourthly, uncertainties in the partitioning relationships that control the chemical flux of trace elements in plagioclase can have a large impact on modelled timescales. These partitioning relationships have been established using experimental plagioclases that have been measured by SIMS, due to its high analytical precision. Profiles dominantly measured by EPMA will have more scatter associated with them and have a tendency to stretch relative changes in Mg content. Diffusion models that have used the SIMS-based partitioning relationships will end up returning longer times as they try to fit features that the partitioning relationship is not able to match. This was somewhat helped by the weighting of individual points in a  $\chi^2$  misfit. This issue can also be minimised in the Bayesian inversion by allowing the partitioning parameters to vary according to their covariance matrix, or in the case of profiles measured only by EPMA, use a relationship established by EPMA core data that is in equilibrium. However, in some cases the inversion converged to partitioning values and temperatures that may be deemed appropriate.

## 5.6 Magmatic origin

Finally, the discrepancies in timescales could be a real magmatic feature corresponding to multiple crystal populations. Texturally, all the plagioclase macrocrysts are very similar in that they have near homogeneous high An cores surrounded by sharp low An rims; this does make multiple magma storage regions unlikely, but does not preclude them. The plagioclase population does have subtle differences in trace element composition (e.g. Sr, Ba) in their cores, but these are not associated with different pre-eruptive residence timescales. There are some macrocrysts that do have extra An zones in their cores indicating that there is a more complex crystal history than that suggested by Neave, MacLennan, Hartley, et al. (2014). However, these crystals appear to have similar entrainment times to crystals with homogeneous cores. Incremental entrainment of crystal mush into the carrier liquid has been proposed as one mechanism for causing a range of observed timescales in basaltic fissure eruptions (Mutch, MacLennan, Shorttle, et al., 2019). This requires that the macrocrysts remain in contact with the magma for different periods of time. Injection of new magma has been invoked as a mechanism for initiating mixing and convection (Bergantz et al., 2015). Typical crystal residence times in the open convecting magma can be calculated following the method of Martin and Nokes (1989). This involves calculating a settling velocity for a spherical particle using Stokes' law:

$$v_s = \frac{g\Delta\rho a^2}{18\rho v_k} \quad (13)$$

where  $v_s$  is the settling velocity,  $\Delta\rho$  is the density contrast between the crystal and melt,  $a$  is crystal diameter,  $\rho$  is melt density and  $v_k$  is the kinematic viscosity of the melt. The settling velocity can then be combined with an exponential decay scheme to estimate the



residence time:

$$t_r = \ln 2h/v_s \quad (14)$$

where  $h$  is the thickness of the magma body. For a 10 m sill, a 2 mm diameter primitive plagioclase crystal ( $\text{An}_{89}$ ) with a density of  $2641 \text{ kg m}^{-3}$  would have a residence time of 160 days in a melt with a density of  $2704 \text{ kg m}^{-3}$  and a kinematic velocity of  $0.1 \text{ m s}^{-1}$ . A 1 mm diameter primitive olivine crystal ( $\text{Fo}_{86}$ ) of  $3285 \text{ kg m}^{-3}$  density would have a residence time of 70 days. Crystal and melt densities are from Neave, MacLennan, Hartley, et al. (2014), which were calculated at  $1190^\circ\text{C}$ . The kinematic velocity was the upper limit for basaltic magmas from Martin and Nokes (1989). For a 100 m sill, the residence times for the same plagioclase and olivine crystals would be 1500 days and 700 days. It therefore seems that residence in a 10 m sill would be sufficient to account for the median diffusion timescales, though thicker magma bodies ( $\sim 100 \text{ m}$ ) would potentially be required to account for the longest plagioclase residence times assuming no sectioning effects. Additional complexity may arise from the fact that in some instances plagioclase and olivine cores are touching meaning that there may be hindered settling or that some of these crystal clots are close to being neutrally buoyant. Incremental entrainment could account for minor variations in timescales once sectioning effects have been corrected for. The duration of the Skuggafjöll eruption is unknown, however given that many basaltic fissure eruptions occur over months (Thordarson & Larsen, 2007), then this is the timescale over which diffusion in the open liquid could have plausibly taken place. Alternatively, the Skuggafjöll eruption itself may have taken place at the end of a much longer period of eruptive activity, although this is difficult to determine. Crystals that retrieve very short times may have been entrained into the carrier liquid just before eruption, or may have been crystals entrained from mush horizons during potential lateral transport (Hartley et al., 2018).

Recent work by Lili et al. (2020) that combines timescale estimates from diffusion chronometry with fluid dynamical simulations of magma intruding into crystal mush has shown a wide distribution of timescales can be associated with a single intrusive event. Crystals positioned in different parts of the remobilised mush may evolve along different P-T-X trajectories at different times, which may make it difficult to retrieve consistent timescales if these different conditions are not known *a priori*. Lili et al. (2020) suggest that any delay between initial intrusion and when a diffusive response is recorded in the crystal cargo diminishes for longer magmatic residence times. This may explain some of the distribution in timescales observed in the measured Skuggafjöll olivine and plagioclase populations, however it may be subsumed by aforementioned effects associated with sectioning and model fitting.

## 5.7 Placing diffusion timescales into a petrogenetic context

The pre-eruptive timescales estimated in this study can be placed into the context of at least two phases of crystallisation from geochemically distinct magma batches as proposed by Neave, MacLennan, Hartley, et al. (2014) (figure 11). Primitive plagioclase and olivine macrocryst cores co-crystallised from primitive depleted melts at mid-crustal pressures ( $\sim 11 \text{ km}$  depth). Trace-element variability in olivine-hosted melt inclusions suggests that magma mixing was taking place concurrently with crystallisation. The morphology of olivine-plagioclase contacts in glomerocrysts suggests that these crystals were then sequestered in a crystal mush rather than being joined by synnuesis (Neave, MacLennan, Hartley, et al., 2014). Diffusive equilibration of Mg in plagioclase cores and forsterite in olivine crystal cores suggests that this storage must have lasted at least a few hundred years (Thomson & MacLennan, 2012; Cooper et al., 2016; Mutch, MacLennan, Holland, & Buisman, 2019). Following, this period of protracted mush storage and re-equilibration, the mush was then disturbed and disaggregated by a more evolved melt that had originally differentiated at depth. This injection event would have accompanied the second phase of crystallisation, and may have efficiently mixed with the host primitive magma

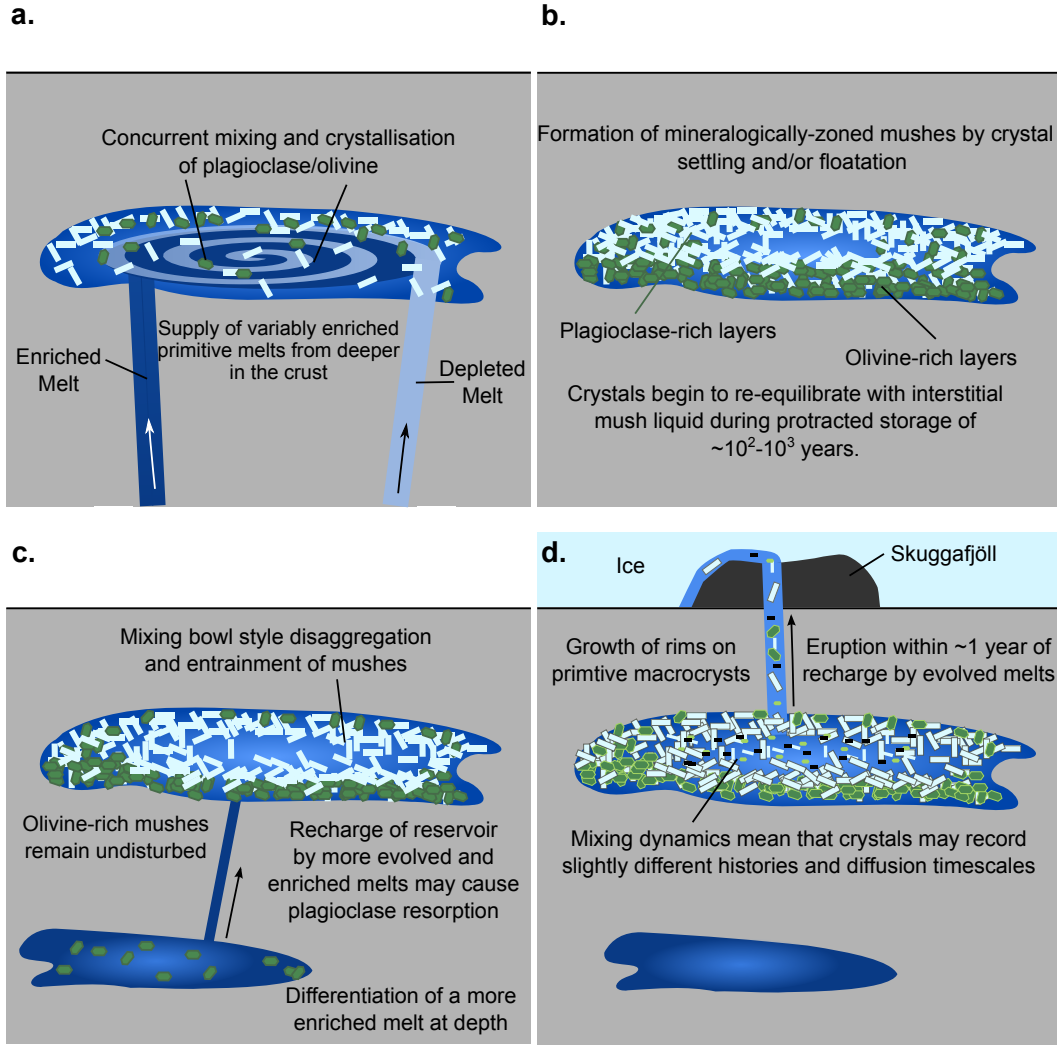


**Figure 11.** Schematic cartoon showing our proposed model for the petrogenesis of the Skuggafjöll magma, which involves 2 stages of crystallisation. **a** shows the crystallisation of the primitive macrocryst assemblage from geochemical variable melts (first stage of crystallisation). **b** shows the sequestration of these primitive macrocrysts in a crystal mush. The second stage of crystallisation is outlined in **c** and **d**. Recharge of the primitive mush with a more evolved and enriched magma (**c**), causes plagioclase dissolution and mush disaggregation, followed by the second stage of crystallisation prior to eruption (**d**). Diffusion chronometry using DFENS suggests this second phase of crystallisation and mixing took place approximately one year before eruption. Figure adapted from Neave, MacLennan, Hartley, et al. (2014).

if injection was rapid (Bergantz et al., 2015). The efficient mixing between the two liquids and the mush liquid for a long period of time could explain why no mush liquid component is observed when crystal addition is accounted for in the composition of whole rock samples (Neave, MacLennan, Hartley, et al., 2014). The entrainment of this mush into a now well mixed magma that is slightly colder will promote this rapid rim growth that is observed. Our diffusion timescales suggest that crystal residence in this newly mixed magma and transport to the surface took place approximately 1 year before eruption.

## 5.8 Comparison to 2014-2015 Holuhraun and implications for hazard management

The pre-eruptive timescale of final crystal entrainment and transport of the Skuggafjöll magma has been constrained here to take place approximately 100-400 days before the eruption. Seismicity detected prior to the Holuhraun eruption indicate that magma transport time took place over approximately 13 days. This is corroborated by diffusive hydration timescales of olivine-hosted melt inclusions which provide a minimum estimate of magma residence time of 1-12 days (Hartley et al., 2018). An in-depth diffusion chronometry study has yet to be published on magmatic zoning of Holuhraun macrocrysts so crystal entrainment and residence in the final magma prior to the initial dyke propagation event are still unknown.

It is unclear whether dyke propagation and magma migration prior to the Skuggafjöll eruption would occur over similar timescales to that of Holuhraun. The distance between Bárðarbunga central volcano and the Skuggafjöll eruption site is approximately 60 km assuming a linear propagation pathway. This distance is approximately 1.5 times the dyke propagation distance of Holuhraun suggesting the timescales for Skuggafjöll are likely to be similar. Sigmundsson et al. (2015) have suggested that underlying topography and its influence on gravitational potential energy can play a large role in controlling the orientation of the dyke. This is particularly prominent close to the central volcano where the topographic load is high, whilst regional tectonic stress fields play more of a major role on distal portions of the propagating dyke tip. As Skuggafjöll was erupted during the last glacial period, when there was additional loading of the crust by glacial ice, modern day topography may be ill-suited for predicting the dyke pathway leading to the eruption site. Regardless, any changes in dyke propagation path are likely to be minor as most of the pathway was distal from the central volcano and would thus be controlled by tectonic stresses, which is close to the down rift linear approximation. Any modification in transport time is therefore likely to come from the dyke stalling in the crust, which cannot be determined. Any lateral or vertical magma propagation to Skuggafjöll is unlikely to take more than a few weeks meaning most of the timescale recorded by the crystal cargo probably relates to magma residence and transport at depth.

Deeper seismicity (12-25 km depth) to the east of Bárðarbunga was detected up to 4 years before the Holuhraun eruption (Hudson et al., 2017), which could be interpreted as magma mixing and supply of melt from deep. The timescales and depths of this seismicity and those estimated from the crystal record of Skuggafjöll make for a tempting comparison given that they are fairly similar (i.e. deep activity recorded years before eruption). It could be speculated that these events refer to a common process (i.e. melt migration from deep followed by magma mixing and crystallisation), however the lack of geophysical observations prior to Skuggafjöll and lack of diffusion studies of Holuhraun mean that a model of magma emplacement and mixing months to years before eruption would require more multi-disciplinary observations in order for it to be applicable for forecasting basaltic fissure eruptions.

A further note of caution for comparison relates to differences in melt inclusion trace element compositions between the two eruptions. The composition of olivine-hosted Skuggafjöll melt inclusions (Neave, MacLennan, Edmonds, & Thordarson, 2014) is typically more depleted than that of Holuhraun and other eruptions from the Bárðarbunga system (Hartley et al., 2018). This is in spite of the fact that the whole rock compositions fall within the Bárðarbunga-Veiðivötn array. This may suggest that Skuggafjöll was sourced from a slightly different part of the system.

If consistent deep pre-eruptive magmatic behaviour can be shown for other case studies from the Bárðarbunga system, detecting deeper seismicity may be the strongest indicator that an eruption may be imminent within the following few years which may aid planning and hazard management in the area over this time period.

## 6 Conclusions

Diffusion chronometry applied to magmatic crystals plays a significant role in characterising the temporal evolution of volcanic plumbing systems and in reconciling geophysical and petrological observations. However, robust uncertainty propagation associated with this form of quantitative petrology has yet to be fully realised. A new Bayesian inversion method that combines a finite element numerical model with a nested sampling approach (DFENS) has been developed in order to achieve more robust uncertainty estimates, and to account for the observations from more than one element within a single phase. This method offers a promising way to account for multi-element diffusion timescales from different minerals to be adopted into a single framework. We applied the DFENS method to olivine and plagioclase macrocrysts with a shared magmatic history from the Skuggafjöll eruption to estimate the timescale between crystal entrainment and eruption. There is excellent agreement between both phases which return timescales on the order of hundreds of days; olivine had a median time across all crystals of 146 days and plagioclase had a median of 203 days. This first-order agreement should provide confidence that olivine and plagioclase diffusion coefficients have been calibrated appropriately, but also provides a decent check on the uncertainties of the method. Some plagioclase crystals converged to much longer timescales (400-1300 days); a discrepancy that can be resolved by accounting for sectioning and multi-dimensional effects, that weren't properly taken into consideration for the plagioclase analyses.

The estimated timescale of months to years for mush disaggregation and entrainment prior to the Skuggafjöll eruption are comparable to deep seismicity detected up to 4 years before the 2014-2015 Holuhraun eruption, which has been interpreted as melt migrating from deep (Hudson et al., 2017). If in both cases, magma transport by lateral dyke propagation accounts for 2-4 weeks of magma residence time, then a large portion of the recorded diffusion timescales is likely to occur at depth where magma mixing is taking place. If this consistent behaviour can be shown for other eruptions from the Bárðarbunga system, then detecting lower and mid-crustal seismicity may be a key precursor of basaltic fissure eruptions years before the event actually happens.

## Acknowledgments

This research was funded by a NERC studentship awarded to Euan J. F. Mutch (NE/L002507/1). We would like to thank Chris Richardson for helpful advice about FEniCS. We are grateful to Iris Buisman and Giulio Lampronti at the University of Cambridge for assistance with the EPMA and EBSD analyses respectively. We would also like to thank Richard Hinton (EMMAC) for assistance with SIMS analyses. Regression parameters, covariance matrices and supporting data are available in the Supplementary Material. Data will be also be uploaded to the National Geoscience Data Centre (NGDC), a NERC online repository, prior to acceptance. DFENS model codes are freely available in the Supplementary Material and at: <https://zenodo.org/badge/latestdoi/279905484> (DOI: 10.5281/zenodo.3948845).

## References

- Ágústsson, T., Woods, J., Greenfield, T., Green, R. G., White, R. S., Winder, T., ... Soosalu, H. (2016). Strike-slip faulting during the 2014 Bárðarbunga-Holuhraun dike intrusion, central Iceland. *Geophysical Research Letters*, 43(4), 1495–1503.
- Alnæs, M., Blechta, J., Hake, J., Johansson, A., Kehlet, B., Logg, A., ... Wells, G. N. (2015). The FEniCS project version 1.5. *Archive of Numerical Software*, 3(100), 9–23.
- Bachmann, F., Hielscher, R., & Schaefer, H. (2010). Texture analysis with MTEX—free and open source software toolbox. In *Solid state phenomena* (Vol. 160, pp.

- 63–68).
- Bali, E., Hartley, M., Halldórsson, S., Gudfinnsson, G., & Jakobsson, S. (2018). Melt inclusion constraints on volatile systematics and degassing history of the 2014–2015 Holuhraun eruption, Iceland. *Contributions to Mineralogy and Petrology*, 173(2), 9.
- Barth, A., Newcombe, M., Plank, T., Gonnermann, H., Hajimirza, S., Soto, G. J., ... Hauri, E. (2019). Magma decompression rate correlates with explosivity at basaltic volcanoes—Constraints from water diffusion in olivine. *Journal of Volcanology and Geothermal Research*, 387, 106664.
- Bergantz, G., Schleicher, J., & Burgisser, A. (2015). Open-system dynamics and mixing in magma mushes. *Nature Geoscience*, 8(10), 793.
- Bindeman, I. N., & Davis, A. M. (2000). Trace element partitioning between plagioclase and melt: investigation of dopant influence on partition behavior. *Geochimica et Cosmochimica Acta*, 64(16), 2863–2878.
- Bindeman, I. N., Davis, A. M., & Drake, M. J. (1998). Ion microprobe study of plagioclase-basalt partition experiments at natural concentration levels of trace elements. *Geochimica et Cosmochimica Acta*, 62(7), 1175–1193.
- Brenner, S. C., & Scott, L. R. (2008). Series: Texts in applied mathematics. *The mathematical theory of finite element methods*, 15.
- Buchner, J., Georgakakis, A., Nandra, K., Hsu, L., Rangel, C., Brightman, M., ... Kocevski, D. (2014). X-ray spectral modelling of the AGN obscuring region in the CDFS: Bayesian model selection and catalogue. *Astronomy & Astrophysics*, 564, A125.
- Caracciolo, A., Bali, E., Guðfinnsson, G. H., Kahl, M., Halldórsson, S. A., Hartley, M. E., & Gunnarsson, H. (2020). Temporal evolution of magma and crystal mush storage conditions in the Bárðarbunga-Veiðivötn volcanic system, Iceland. *Lithos*, 352, 105234.
- Chakraborty, S. (1997). Rates and mechanisms of Fe–Mg interdiffusion in olivine at 980–1300 °C. *Journal of Geophysical Research: Solid Earth*, 102(B6), 12317–12331.
- Chakraborty, S. (2010). Diffusion coefficients in olivine, wadsleyite and ringwoodite. *Reviews in mineralogy and geochemistry*, 72(1), 603–639.
- Chamberlain, K. J., Morgan, D. J., & Wilson, C. J. (2014). Timescales of mixing and mobilisation in the Bishop Tuff magma body: perspectives from diffusion chronometry. *Contributions to Mineralogy and Petrology*, 168(1), 1034.
- Cherniak, D. J., & Watson, E. B. (1994). A study of strontium diffusion in plagioclase using Rutherford backscattering spectroscopy. *Geochimica et Cosmochimica Acta*, 58(23), 5179–5190.
- Cooper, K. M., & Kent, A. J. (2014). Rapid remobilization of magmatic crystals kept in cold storage. *Nature*, 506(7489), 480.
- Cooper, K. M., Sims, K. W., Eiler, J. M., & Banerjee, N. (2016). Timescales of storage and recycling of crystal mush at Krafla Volcano, Iceland. *Contributions to Mineralogy and Petrology*, 171(6), 54.
- Costa, F., Chakraborty, S., & Dohmen, R. (2003). Diffusion coupling between trace and major elements and a model for calculation of magma residence times using plagioclase. *Geochimica et Cosmochimica Acta*, 67(12), 2189–2200.
- Costa, F., Dohmen, R., & Chakraborty, S. (2008). Time scales of magmatic processes from modeling the zoning patterns of crystals. *Reviews in Mineralogy and Geochemistry*, 69(1), 545–594.
- Costa, F., & Morgan, D. (2010). Time constraints from chemical equilibration in magmatic crystals. *Timescales of Magmatic Processes: From Core to Atmosphere*, 125–159.
- Costa, F., Shea, T., & Ubide, T. (2020). Diffusion chronometry and the timescales of magmatic processes. *Nature Reviews Earth & Environment*, 1–14.
- Crank, J. (1979). *The mathematics of diffusion*. Oxford university press.



- de Maisonneuve, C. B., Costa, F., Huber, C., Vonlanthen, P., Bachmann, O., & Dungan, M. A. (2016). How do olivines record magmatic events? Insights from major and trace element zoning. *Contributions to Mineralogy and Petrology*, 171(6), 56.
- Dohmen, R., Becker, H.-W., & Chakraborty, S. (2007). Fe–Mg diffusion in olivine I: experimental determination between 700 and 1,200 °C as a function of composition, crystal orientation and oxygen fugacity. *Physics and Chemistry of Minerals*, 34(6), 389–407.
- Dohmen, R., & Chakraborty, S. (2007). Fe–Mg diffusion in olivine II: point defect chemistry, change of diffusion mechanisms and a model for calculation of diffusion coefficients in natural olivine. *Physics and Chemistry of Minerals*, 34(6), 409–430.
- Druitt, T. H., Costa, F., Deloule, E., Dungan, M., & Scaillet, B. (2012). Decadal to monthly timescales of magma transfer and reservoir growth at a caldera volcano. *Nature*, 482(7383), 77.
- Faak, K., Chakraborty, S., & Coogan, L. A. (2013). Mg in plagioclase: Experimental calibration of a new geothermometer and diffusion coefficients. *Geochimica et Cosmochimica Acta*, 123, 195–217.
- Faak, K., & Gillis, K. M. (2016). Slow cooling of the lowermost oceanic crust at the fast-spreading East Pacific Rise. *Geology*, 44(2), 115–118.
- Feroz, F., Hobson, M., & Bridges, M. (2009). MultiNest: an efficient and robust Bayesian inference tool for cosmology and particle physics. *Monthly Notices of the Royal Astronomical Society*, 398(4), 1601–1614.
- Feroz, F., Hobson, M., Cameron, E., & Pettitt, A. (2013). Importance nested sampling and the MultiNest algorithm. *arXiv preprint arXiv:1306.2144*.
- Ghiorso, M. S., & Sack, R. O. (1995). Chemical mass transfer in magmatic processes IV. a revised and internally consistent thermodynamic model for the interpolation and extrapolation of liquid-solid equilibria in magmatic systems at elevated temperatures and pressures. *Contributions to Mineralogy and Petrology*, 119(2-3), 197–212.
- Gualda, G. A., Ghiorso, M. S., Lemons, R. V., & Carley, T. L. (2012). Rhyolite-MELTS: a modified calibration of melts optimized for silica-rich, fluid-bearing magmatic systems. *Journal of Petrology*, 53(5), 875–890.
- Gudmundsson, M. T., & Högnadóttir, T. (2007). Volcanic systems and calderas in the Vatnajökull region, central Iceland: Constraints on crustal structure from gravity data. *Journal of Geodynamics*, 43(1), 153–169.
- Gudmundsson, M. T., Jónsdóttir, K., Hooper, A., Holohan, E. P., Halldórsson, S. A., Ófeigsson, B. G., ... others (2016). Gradual caldera collapse at Bárðarbunga volcano, Iceland, regulated by lateral magma outflow. *Science*, 353(6296), aaf8988.
- Halldórsson, S. A., Bali, E., Hartley, M. E., Neave, D. A., Peate, D. W., Guðfinnsson, G. H., ... Thordarson, T. (2018, Jul 23). Petrology and geochemistry of the 2014–2015 Holuhraun eruption, central Iceland: compositional and mineralogical characteristics, temporal variability and magma storage. *Contributions to Mineralogy and Petrology*, 173(8), 64. Retrieved from <https://doi.org/10.1007/s00410-018-1487-9> doi: 10.1007/s00410-018-1487-9
- Hartley, M. E., Bali, E., MacLennan, J., Neave, D. A., & Halldórsson, S. A. (2018). Melt inclusion constraints on petrogenesis of the 2014–2015 Holuhraun eruption, Iceland. *Contributions to Mineralogy and Petrology*, 173(2), 10.
- Hartley, M. E., Morgan, D. J., MacLennan, J., Edmonds, M., & Thordarson, T. (2016). Tracking timescales of short-term precursors to large basaltic fissure eruptions through Fe–Mg diffusion in olivine. *Earth and Planetary Science Letters*, 439, 58–70.
- Hier-Majumder, S., Anderson, I. M., & Kohlstedt, D. L. (2005). Influence of protons on Fe–Mg interdiffusion in olivine. *Journal of Geophysical Research: Solid*

- 1033 *Earth*, 110(B2).
- 1034 Higgins, M. D. (1996). Magma dynamics beneath Kameni volcano, Thera, Greece, as  
1035 revealed by crystal size and shape measurements. *Journal of Volcanology and*  
1036 *Geothermal Research*, 70(1-2), 37–48.
- 1037 Holness, M. B. (2014). The effect of crystallization time on plagioclase grain shape  
1038 in dolerites. *Contributions to Mineralogy and Petrology*, 168(5), 1076.
- 1039 Holzapfel, C., Chakraborty, S., Rubie, D., & Frost, D. (2007). Effect of pressure on  
1040 Fe–Mg, Ni and Mn diffusion in  $(\text{Fe}_x\text{Mg}_{1-x})_2\text{SiO}_4$  olivine. *Physics of the Earth*  
1041 *and Planetary Interiors*, 162(3-4), 186–198.
- 1042 Hudson, T., White, R. S., Brisbourne, A., Greenfield, T., Ágústssdóttir, T., & Green,  
1043 R. G. (2017). Deep crustal melt plumbing of Bárðarbunga volcano, Iceland.  
1044 *Geophysical Research Letters*.
- 1045 Humphreys, M. C., Kearns, S. L., & Blundy, J. D. (2006). SIMS investigation  
1046 of electron-beam damage to hydrous, rhyolitic glasses: Implications for melt  
1047 inclusion analysis. *American Mineralogist*, 91(4), 667–679.
- 1048 Ilyinskaya, E., Schmidt, A., Mather, T. A., Pope, F. D., Witham, C., Baxter, P.,  
1049 ... others (2017). Understanding the environmental impacts of large fissure  
1050 eruptions: Aerosol and gas emissions from the 2014–2015 Holuhraun eruption  
1051 (Iceland). *Earth and Planetary Science Letters*, 472, 309–322.
- 1052 Jakobsson, S. P., & Gudmundsson, M. T. (2008). Subglacial and intraglacial vol-  
1053 canic formations in Iceland. *Jökull*, 58, 179–196.
- 1054 Jenkins, J., MacLennan, J., Green, R. G., Cottaar, S., Deuss, A., & White, R. S.  
1055 (2018). Crustal formation on a spreading ridge above a mantle plume: receiver  
1056 function imaging of the Icelandic crust. *Journal of Geophysical Research: Solid*  
1057 *Earth*, 123(6), 5190–5208.
- 1058 Jollands, M., Hermann, J., O'Neill, H. S. C., Spandler, C., & Padrón-Navarta, J.  
1059 (2016). Diffusion of Ti and some divalent cations in olivine as a function of  
1060 temperature, oxygen fugacity, chemical potentials and crystal orientation.  
1061 *Journal of petrology*, 57(10), 1983–2010.
- 1062 Kress, V. C., & Carmichael, I. S. (1991). The compressibility of silicate liquids  
1063 containing  $\text{Fe}_2\text{O}_3$  and the effect of composition, temperature, oxygen fugacity  
1064 and pressure on their redox states. *Contributions to Mineralogy and Petrology*,  
1065 108(1-2), 82–92.
- 1066 Larsen, G. (1984). Recent volcanic history of the Veidivötn fissure swarm, southern  
1067 Iceland—an approach to volcanic risk assessment. *Journal of Volcanology and*  
1068 *Geothermal Research*, 22(1-2), 33–58.
- 1069 Larsen, G. (2002). A brief overview of eruptions from ice-covered and ice-capped  
1070 volcanic systems in Iceland during the past 11 centuries: frequency, periodicity  
1071 and implications. *Geological Society, London, Special Publications*, 202(1),  
1072 81–90.
- 1073 Lili, C., Costa, F., & Bergantz, G. (2020). Linking fluid dynamics and olivine crys-  
1074 tal scale zoning during simulated magma intrusion. *Contributions to Mineral-*  
1075 *ogy and Petrology*, 175(6).
- 1076 Logg, A., Mardal, K.-A., Wells, G. N., et al. (2012). *Automated Solution of Dif-*  
1077 *ferential Equations by the Finite Element Method* (A. Logg, K.-A. Mardal, &  
1078 G. N. Wells, Eds.). Springer. doi: 10.1007/978-3-642-23099-8
- 1079 Lynn, K. J., Garcia, M. O., Shea, T., Costa, F., & Swanson, D. A. (2017).  
1080 Timescales of mixing and storage for Keanakāko ‘i Tephra magmas (1500–1820  
1081 ce), Kīlauea Volcano, Hawai ‘i. *Contributions to Mineralogy and Petrology*,  
1082 172(9), 76.
- 1083 MacLennan, J. (2008). Concurrent mixing and cooling of melts under Iceland. *Jour-*  
1084 *nal of Petrology*, 49(11), 1931–1953.
- 1085 Martin, D., & Nokes, R. (1989). A fluid-dynamical study of crystal settling in con-  
1086 vecting magmas. *Journal of Petrology*, 30(6), 1471–1500.
- 1087 MATLAB. (2016). *version 9.10.0 (r2016b)*. Natick, Massachusetts: The MathWorks

- 1088 Inc.
- 1089 Moore, A., Coogan, L., Costa, F., & Perfit, M. (2014). Primitive melt replenish-  
 1090 ment and crystal-mush disaggregation in the weeks preceding the 2005–2006  
 1091 eruption 9 50N, EPR. *Earth and Planetary Science Letters*, 403, 15–26.
- 1092 Muncill, G. E., & Lasaga, A. C. (1988). Crystal-growth kinetics of plagioclase in  
 1093 igneous systems: Isothermal H sub 2 O-saturated experiments and extension of  
 1094 a growth model to complex silicate melts. *American Mineralogist;(USA)*, 73.
- 1095 Mutch, E. J. F., MacLennan, J., Holland, T. J. B., & Buisman, I. (2019). Millennial  
 1096 storage of near-Moho magma. *Science*, 365(6450), 260–264.
- 1097 Mutch, E. J. F., MacLennan, J., Shorttle, O., Edmonds, M., & Rudge, J. F. (2019).  
 1098 Rapid transcrustal magma movement under Iceland. *Nature Geoscience*, 12(7),  
 1099 569–574.
- 1100 Neave, D. A., MacLennan, J., Edmonds, M., & Thordarson, T. (2014). Melt mixing  
 1101 causes negative correlation of trace element enrichment and CO<sub>2</sub> content prior  
 1102 to an Icelandic eruption. *Earth and Planetary Science Letters*, 400, 272–283.
- 1103 Neave, D. A., MacLennan, J., Hartley, M. E., Edmonds, M., & Thordarson, T.  
 1104 (2014). Crystal Storage and Transfer in Basaltic Systems: the Skug-  
 1105 gafjöll Eruption, Iceland. *Journal of Petrology*, 55(12), 2311–2346. Re-  
 1106 trieved from <http://dx.doi.org/10.1093/petrology/egu058> doi:  
 1107 10.1093/petrology/egu058
- 1108 Neave, D. A., Passmore, E., MacLennan, J., Fitton, G., & Thordarson, T. (2013).  
 1109 Crystal–melt relationships and the record of deep mixing and crystallization in  
 1110 the AD 1783 Laki Eruption, Iceland. *Journal of Petrology*, 54(8), 1661–1690.
- 1111 Neave, D. A., & Putirka, K. D. (2017). A new clinopyroxene-liquid barometer, and  
 1112 implications for magma storage pressures under Icelandic rift zones. *American*  
 1113 *Mineralogist*, 102(4), 777–794.
- 1114 Newcombe, M. E., Plank, T., Barth, A., Asimow, P., & Hauri, E. (2020). Water-  
 1115 in-olivine magma ascent chronometry: Every crystal is a clock. *Journal of Vol-*  
 1116 *canology and Geothermal Research*, 106872.
- 1117 Nielsen, R. L., Ustunisik, G., Weinsteiger, A. B., Tepley, F. J., Johnston, A. D., &  
 1118 Kent, A. J. (2017). Trace element partitioning between plagioclase and melt:  
 1119 An investigation of the impact of experimental and analytical procedures.  
 1120 *Geochemistry, Geophysics, Geosystems*, 18(9), 3359–3384.
- 1121 Pankhurst, M. J., Morgan, D. J., Thordarson, T., & Loughlin, S. C. (2018). Mag-  
 1122 matic crystal records in time, space, and process, causatively linked with  
 1123 volcanic unrest. *Earth and Planetary Science Letters*, 493, 231–241.
- 1124 Petry, C., Chakraborty, S., & Palme, H. (2004). Experimental determination of  
 1125 Ni diffusion coefficients in olivine and their dependence on temperature, com-  
 1126 position, oxygen fugacity, and crystallographic orientation. *Geochimica et*  
 1127 *Cosmochimica Acta*, 68(20), 4179–4188.
- 1128 Putirka, K. D. (2008). Thermometers and barometers for volcanic systems. *Reviews*  
 1129 *in mineralogy and geochemistry*, 69(1), 61–120.
- 1130 QUANTAX. (2010). *Crystalalign*. Berlin, Germany: Bruker Nano GmbH.
- 1131 Rae, A. S., Edmonds, M., MacLennan, J., Morgan, D., Houghton, B., Hartley, M. E.,  
 1132 & Sides, I. (2016). Time scales of magma transport and mixing at Kilauea  
 1133 volcano, Hawai‘i. *Geology*, 44(6), 463–466.
- 1134 Rasmussen, D. J., Plank, T. A., Roman, D. C., Power, J. A., Bodnar, R. J., &  
 1135 Hauri, E. H. (2018). When does eruption run-up begin? Multidisciplinary  
 1136 insight from the 1999 eruption of Shishaldin volcano. *Earth and Planetary*  
 1137 *Science Letters*, 486, 1–14.
- 1138 Ruprecht, P., & Plank, T. (2013). Feeding andesitic eruptions with a high-speed con-  
 1139 nection from the mantle. *Nature*, 500(7460), 68.
- 1140 Saunders, K., Blundy, J., Dohmen, R., & Cashman, K. (2012). Linking petrology  
 1141 and seismology at an active volcano. *Science*, 336(6084), 1023–1027.
- 1142 Shea, T., Costa, F., Krimer, D., & Hammer, J. E. (2015). Accuracy of timescales re-



- trieved from diffusion modeling in olivine: A 3D perspective. *American Mineralogist*, 100(10), 2026–2042.
- Shorttle, O., Moussallam, Y., Hartley, M. E., MacLennan, J., Edmonds, M., & Murtton, B. J. (2015). Fe-XANES analyses of Reykjanes Ridge basalts: Implications for oceanic crust’s role in the solid Earth oxygen cycle. *Earth and Planetary Science Letters*, 427, 272–285.
- Sigmundsson, F., Hooper, A., Hreinsdóttir, S., Vogfjörð, K. S., Ófeigsson, B. G., Heimisson, E. R., ... others (2015). Segmented lateral dyke growth in a rifting event at Bárðarbunga volcanic system, Iceland. *Nature*, 517(7533), 191.
- Silverman, B. W. (2018). *Density estimation for statistics and data analysis*. Routledge.
- Skilling, J. (2004). Nested sampling. In *Aip conference proceedings* (Vol. 735, pp. 395–405).
- Spandler, C., & O’Neill, H. S. C. (2010). Diffusion and partition coefficients of minor and trace elements in San Carlos olivine at 1,300 °C with some geochemical implications. *Contributions to Mineralogy and Petrology*, 159(6), 791–818.
- Tang, M., Rudnick, R. L., McDonough, W. F., Bose, M., & Goreva, Y. (2017). Multi-mode li diffusion in natural zircons: Evidence for diffusion in the presence of step-function concentration boundaries. *Earth and Planetary Science Letters*, 474, 110–119.
- Thomson, A., & MacLennan, J. (2012). The distribution of olivine compositions in Icelandic basalts and picrites. *Journal of Petrology*, 54(4), 745–768.
- Thordarson, T., & Larsen, G. (2007). Volcanism in Iceland in historical time: Volcano types, eruption styles and eruptive history. *Journal of Geodynamics*, 43(1), 118–152.
- Van Orman, J. A., Cherniak, D. J., & Kita, N. T. (2014). Magnesium diffusion in plagioclase: dependence on composition, and implications for thermal resetting of the  $^{26}\text{Al}$ – $^{26}\text{Mg}$  early solar system chronometer. *Earth and Planetary Science Letters*, 385, 79–88.
- Winpenny, B., & MacLennan, J. (2011). A partial record of mixing of mantle melts preserved in Icelandic phenocrysts. *Journal of Petrology*, 52(9), 1791–1812.
- Woods, J., Donaldson, C., White, R. S., Caudron, C., Brandsdóttir, B., Hudson, T. S., & Ágústssdóttir, T. (2018). Long-period seismicity reveals magma pathways above a laterally propagating dyke during the 2014–15 Bárðarbunga rifting event, Iceland. *Earth and Planetary Science Letters*, 490, 216–229.
- Zellmer, G., Turner, S., & Hawkesworth, C. (2000). Timescales of destructive plate margin magmatism: new insights from Santorini, Aegean volcanic arc. *Earth and Planetary Science Letters*, 174(3), 265–281.
- Zellmer, G. F., Blake, S., Vance, D., Hawkesworth, C., & Turner, S. (1999). Plagioclase residence times at two island arc volcanoes (Kameni Islands, Santorini, and Soufriere, St. Vincent) determined by Sr diffusion systematics. *Contributions to Mineralogy and Petrology*, 136(4), 345–357.
- Zhukova, I., O’Neill, H. S. C., Campbell, I. H., & Kilburn, M. R. (2014). The effect of silica activity on the diffusion of Ni and Co in olivine. *Contributions to Mineralogy and Petrology*, 168(2), 1029.

# Supporting Information for "DFENS: Diffusion chronometry using Finite Elements and Nested Sampling (NON-PEER REVIEW PREPRINT)"

Euan J. F. Mutch<sup>1,2</sup>, John MacLennan<sup>1</sup>, Oliver Shorttle<sup>1,3</sup>, John F. Rudge<sup>4</sup> &

David A. Neave<sup>5</sup>

<sup>1</sup>Department of Earth Sciences, University of Cambridge, Downing Street, Cambridge, CB2 3EQ, United Kingdom

<sup>2</sup>Department of Geology, University of Maryland, 8000 Regents Dr, College Park, Maryland, 20742, United States

<sup>3</sup>Institute of Astronomy, University of Cambridge, Madingley Road, Cambridge, CB3 0HA, United Kingdom

<sup>4</sup>Bullard Laboratories, Department of Earth Sciences, University of Cambridge, Madingley Road, Cambridge CB3 0EZ, United Kingdom

<sup>5</sup>Department of Earth and Environmental Sciences, University of Manchester, Manchester, M13 9PL, United Kingdom

## Contents of this file

1. Text S1
2. Figures S1 to S114
3. Tables S1 to S11

## Additional Supporting Information (Files uploaded separately)

1. Captions for Datasets S1 to S10

**Introduction** This document includes text and equations that describe the derivation of the weak form (variational form) used by FEniCS (Alnæs et al., 2015) when modelling the

different varieties of the diffusion equation in the finite element part of DFENS. This is followed by figures that support the findings in the main manuscript. These figures include: demonstrating the 3D capabilities of FEniCS (Alnæs et al., 2015) when applied to idealised olivine crystals, figures that assess the performance of the diffusion coefficient regressions used in this study, figures showing how the Mg-in-plagioclase partitioning relationship was obtained, figures showing how the initial conditions in olivine were obtained, figures that show profile fits and inversion results for olivine and plagioclase. Finally, there are tables that show the regression parameters and covariance matrices that have been derived and used in this study and in Mutch, MacLennan, Shorttle, Edmonds, and Rudge (2019). There are also tables showing the olivine and plagioclase timescale results, and the crystallographic angles used in the olivine diffusion modelling.

### **Text S1. Weak form derivation**

Here we provide an overview of deriving a variational form for a time-dependent diffusion problem, but more detail is available in Logg, Mardal, Wells, et al. (2012). Starting off with Fick's second law with a spatially independent diffusion coefficient.

$$\frac{\partial C}{\partial t} = D \nabla^2 C \text{ in } \Omega, \text{ for } t > 0 \quad (1)$$

$$C = C_0 \text{ on } \partial\Omega, \text{ for } t > 0 \quad (2)$$

$$C = I \text{ at } t = 0 \quad (3)$$

Here,  $C$  is concentration, which varies in space and time.  $D$  is the diffusion coefficient. The spatial domain is defined as  $\Omega$ , and  $\partial\Omega$  is the boundary of the spatial domain.  $C_0$  is the composition at the boundary as stated by a fixed (Dirichlet) boundary condition.  $I$  is the initial condition, which varies as a function of space only. For solving time-dependent partial differential equations the time derivative needs to be discretised by a

finite difference approximation, which yields a recursive set of stationary problems that can then be written in variational form. The type of time-stepping used in this study is defined by the  $\theta$  method (equation 4).

$$C_{mid} = \theta C^{k+1} + (1 - \theta) C^k \quad (4)$$

where  $C_{mid}$  is the composition at the Crank-Nicholson time step,  $C^k$  is the composition at the current time step and  $C^{k+1}$  is the composition at the next time step.  $\theta = 0$  for a forward Euler time-stepping scheme ( $1^{st}$  order),  $\theta = 1$  for a backward Euler time-stepping scheme ( $1^{st}$  order), and  $\theta = 0.5$  for a Crank-Nicholson time stepping scheme ( $2^{nd}$  order). The Crank-Nicholson scheme is both stable and accurate and therefore that scheme was used. Sampling the partial differential equation at some time as defined by  $C_{mid}$  would therefore look like:

$$\frac{\partial}{\partial t} C_{mid} = D \nabla^2 C_{mid} \quad (5)$$

The time-derivative can be approximated by a forward finite difference as:

$$\frac{\partial}{\partial t} C_{mid} \approx \frac{C^{k+1} - C^k}{\Delta t} \quad (6)$$

where  $\Delta t$  is the time discretisation parameter. Inserting (6) into (5) yields:

$$\frac{C^{k+1} - C^k}{\Delta t} = D \nabla^2 C_{mid} \quad (7)$$

which is the time-discrete version of (5). Rearranging (7) so that all of the  $C^{k+1}$  terms are on the left hand side yields:

$$C^0 = I \quad (8)$$

$$C^{k+1} - \Delta t D \nabla^2 C_{mid} = C^k, \quad k = 0, 1, 2, \dots \quad (9)$$

This shows that given an initial condition,  $I$ , concentrations at higher time steps (e.g.  $C^1, C^2$  etc.) can be solved for. The finite element method is used to solve equations (8)

and (9). This requires constructing the variational or weak forms of these equations, which involves multiplying by a test function  $v$  and integrating (whereby second derivatives are also integrated by parts). The variational form at  $t = 0$  looks like this:

$$\int_{\Omega} C^0 v \, dx = \int_{\Omega} I v \, dx \quad (10)$$

Multiplying by the test function and integrating for the other time steps looks like this:

$$\int_{\Omega} C^{k+1} v \, dx - \Delta t D \int_{\Omega} (\nabla^2 C_{mid}) v \, dx = \int_{\Omega} C^k v \, dx \quad (11)$$

This form assumes a constant  $D$  and  $\Delta t$  in space and time. Integration by parts of the second order derivatives produces:

$$\int_{\Omega} C^{k+1} v + \Delta t D \nabla C_{mid} \cdot \nabla v \, dx - \int_{\partial\Omega} \frac{\partial C}{\partial n} v \, ds = \int_{\Omega} C^k v \, dx \quad (12)$$

where  $\partial C / \partial n$  is the derivative of  $C$  in the outward normal direction of the boundary and  $ds$  refers to the integral being made on the edge of the mesh. The test function  $v \in V$  is required to vanish on parts of the boundary where  $C$  is known, which is the whole boundary in most cases. Consequently, the third term on the left hand side vanishes leaving:

$$\int_{\Omega} C^{k+1} v + \Delta t D \nabla C_{mid} \cdot \nabla v \, dx = \int_{\Omega} C^k v \, dx \quad (13)$$

This is the final variational form that is used by FEniCS to automatically solve the partial differential equation. The variational form for diffusion equations with a spatially dependent diffusion coefficient, as is the case for olivine and spinel is:

$$\int_{\Omega} C^{k+1} v + \Delta t (D(C_{mid}) \nabla C_{mid}) \cdot \nabla v \, dx = \int_{\Omega} C^k v \, dx \quad (14)$$

where  $D(C_{mid})$  is the compositionally dependent diffusion coefficient. The variational form used in this study for the plagioclase diffusion equation is:

$$\int_{\Omega} C^{k+1} v + \Delta t \left( D \nabla C_{mid} - \frac{D A C_{mid}}{RT} \nabla X_{An} \right) \cdot \nabla v \, dx = \int_{\Omega} C^k v \, dx \quad (15)$$

where  $X_{An}$  is the anorthite content in mole fraction. The trial function and the test function use the same functional space defined based on the mesh and the type of finite element. In all cases in this study, linear Lagrange (Continuous Galerkin) finite elements were used. Once the partial differential equation has been discretised and finite element functional spaces have been assigned, the FEniCS software uses direct LU solvers to solve the resulting algebraic systems. For non-linear equations like Fe-Mg interchange in olivine and Cr-Al interchange in spinel a Newton solver was used.

**Data Set S1. ds01.csv** Electron probe microanalysis (EPMA) profile data of olivine crystals used in this study. All compositional data is presented in parts per million (ppm). Standard deviations are averaged values of standard deviations from counting statistics and repeat measurements of secondary standards.

**Data Set S2. ds02.csv** Plagioclase compositional profiles used in this study, including SIMS, EPMA and step scan data. All compositional data is presented in parts per million (ppm). Standard deviations for EPMA analyses are averaged values of standard deviations from counting statistics and repeat measurements of secondary standards. Standard deviations for SIMS and step scan analyses are based on analytical precision of secondary standards.

**Data Set S3. ds03.csv** Angles between the EPMA profile and the main olivine crystallographic axes measured by electron backscatter diffraction (EBSD). 'angle100X' is the angle between the [100] crystallographic axis and the x direction of the EBSD map,



'angle100Y' is the angle between [100] crystallographic axis and the y direction of the EBSD map, and 'angle100Z' is the angle between the [100] crystallographic axis and the z direction in the EBSD map etc. 'angle100P' is the angle between the EPMA profile and the [100] crystallographic axis, 'angle010P' is the angle between the EPMA profile and the [010] crystallographic axis, and 'angle100P' is the angle between the EPMA profile and the [001] crystallographic axis. All angles are in degrees ( $^{\circ}$ ).

**Data Set S4. ds04.csv** Median timescales and  $1\sigma$  errors from the olivine crystals of this study. The +1 sigma (days) is the quantile value calculated at 0.841 (i.e.  $0.5 + (0.6826 / 2)$ ). The -1 sigma (days) is therefore the quantile calculated at approximately 0.158 (which is  $1 - 0.841$ ). This calculates the 1 sigma relative to the median and says that 68% of the times were between 7.57 and 20.09 around the median. The 2 sigma is basically the same but it is  $0.5 + (0.95/2)$ . The value quoted as the +1 sigma (error) is the difference between the upper 1 sigma quantile and the median. Likewise the -1 sigma (error) is the difference between the median and the lower 1 sigma quantile.

**Data Set S5. ds05.csv** Median timescales and  $1\sigma$  errors from the plagioclase crystals of this study. The +1 sigma (days) is the quantile value calculated at 0.841 (i.e.  $0.5 + (0.6826 / 2)$ ). The -1 sigma (days) is therefore the quantile calculated at approximately 0.158 (which is  $1 - 0.841$ ). This calculates the 1 sigma relative to the median and says that 68% of the times were between 7.57 and 20.09 around the median. The 2 sigma is basically the same but it is  $0.5 + (0.95/2)$ . The value quoted as the +1 sigma (error) is the difference between the upper 1 sigma quantile and the median. Likewise the -1 sigma (error) is the difference between the median and the lower 1 sigma quantile.

**Data Set S6. ds06.xlsx** Spreadsheet containing the regression parameters and covariance matrices used in this study and in Mutch et al. (2019). It contains excel versions of Supplementary Tables S1-S8.

**Data Set S7. DFENS\_Ol\_1D.py** Python wrapper script version of the olivine DFENS model (Fe-M, Ni and Mn). Can also be accessed at <https://zenodo.org/badge/latestdoi/279905484> (DOI: 10.5281/zenodo.3948845).

**Data Set S8. DFENS\_Plug\_1D.py** Python wrapper script version of the plagioclase DFENS model (Mg). Can also be accessed at <https://zenodo.org/badge/latestdoi/279905484> (DOI: 10.5281/zenodo.3948845).

**Data Set S9. pmc.py** Python script with PyMultiNest functions. Can also be accessed at <https://zenodo.org/badge/latestdoi/279905484> (DOI: 10.5281/zenodo.3948845).

**Data Set S10. KC\_fO2.py** Python script for calculating  $f\text{O}_2$  from  $\text{Fe}^{3+}/\text{Fe}_{\text{total}}$  using a rearranged version of equation 7 of Kress and Carmichael (1991). Can also be accessed at <https://zenodo.org/badge/latestdoi/279905484> (DOI: 10.5281/zenodo.3948845).

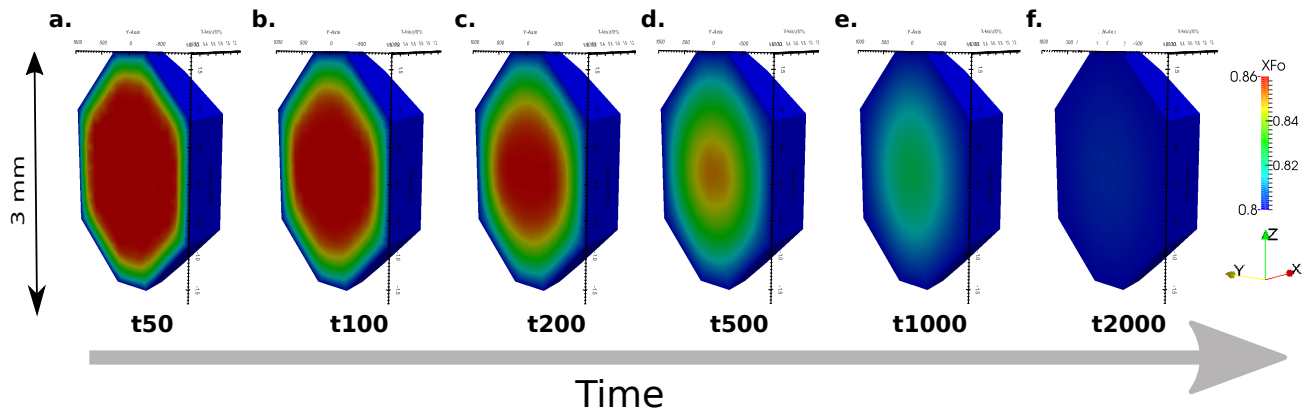


**Figure S1.** 3D olivine finite element diffusion model performed using FEniCS. The mesh was generated using an ideal olivine crystal shape as determined by the minimisation of surface energy. **a-f** are slices through the centre of the olivine which tracks the changing forsterite composition of the crystal through time. The notation t<sub>x</sub> corresponds to the time step in the model. E.g. **a** shows the model after 50 time steps. Each time step was 20 days. The model was run at 1190 °C, 0.36 GPa, and with a Fe<sup>3+</sup>/Fe<sub>total</sub> of 0.15 using the Skuggafjöll melt composition. Diffusive anisotropy is also incorporated into the model, which can be seen by the diffusion fronts moving faster parallel to the z axis in **a-c**.

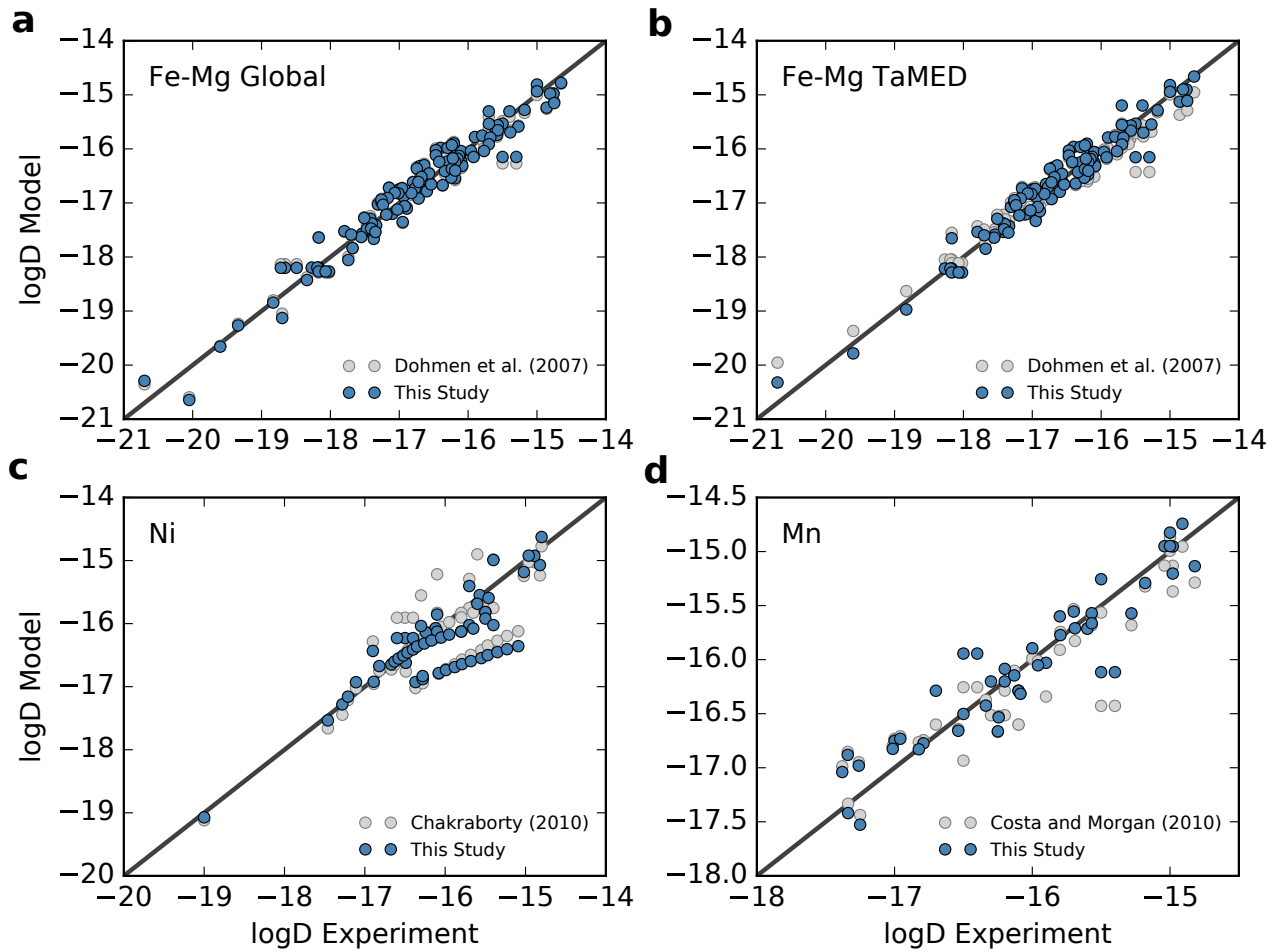


**Figure S2.** Plots from the supplementary material of Mutch et al. (2019) showing the model predictions of the DFENS olivine diffusion model multiple linear regressions (blue circles) and those of previous studies (Chakraborty, 2010; Dohmen et al., 2007; Dohmen & Chakraborty, 2007; Costa & Morgan, 2010) (grey circles) when applied to the calibrant experimental database. The black lines are 1:1 lines. **a**, Global Fe-Mg models **b**, TaMED mechanism for Fe-Mg exchange; **c**, Ni diffusion in olivine; **d**, Mn diffusion in olivine. The regressions of this study can retrieve the experimental diffusion coefficients within 0.5 log units, and are similar to diffusion equations of previous studies. In some cases, the models of this study outperforms the predictive power of previous calibrations, as is the case for Ni.

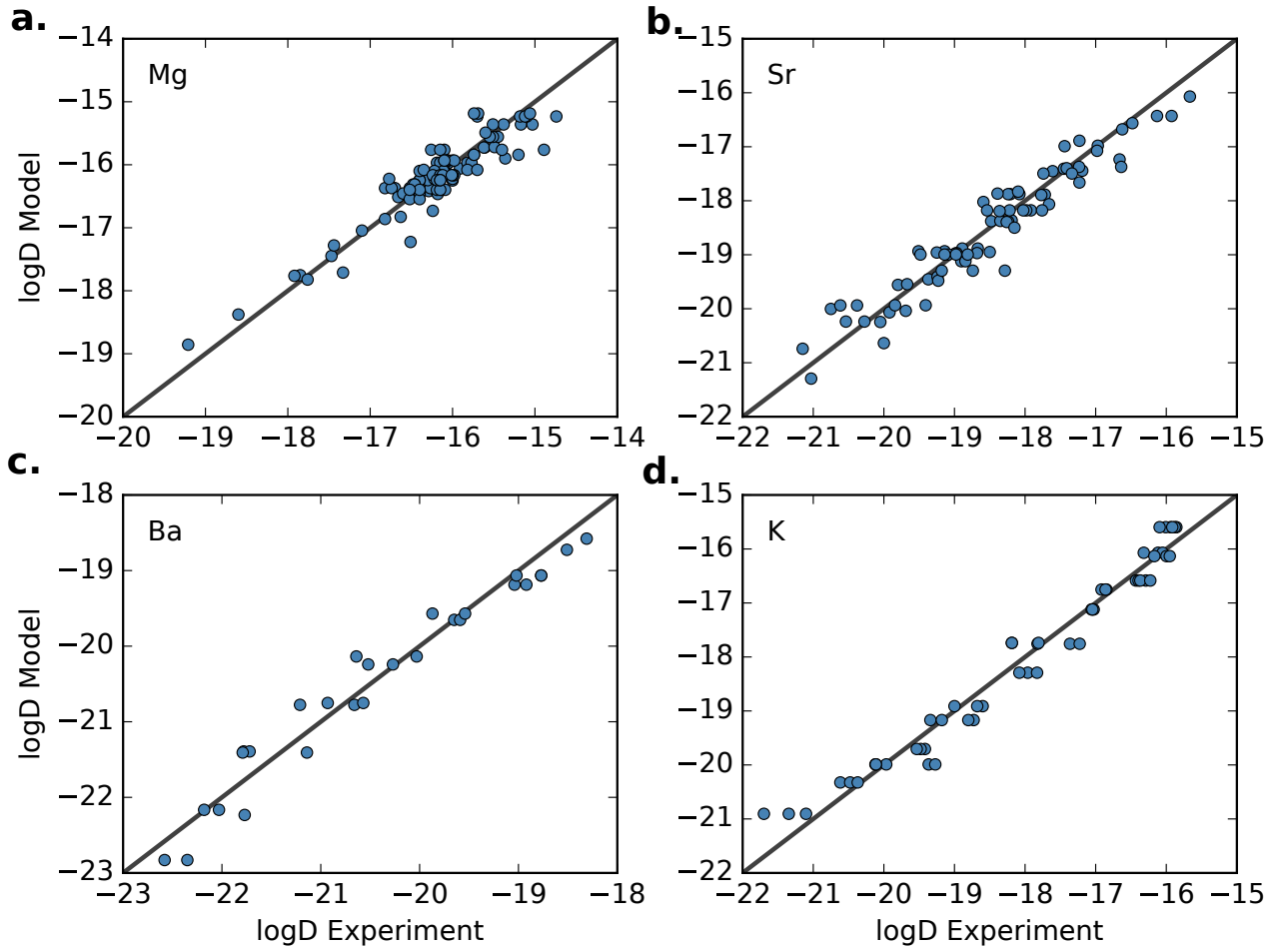


**Figure S3.** Plots showing the model predictions of this study's plagioclase model multiple linear regressions (blue circles) when applied to the calibrant experimental database that contains all available plagioclase diffusion data. **a**, Mg; **b**, Sr; **c**, Ba; **d**, K. The regressions of this study can retrieve the experimental diffusion coefficients within 0.5 log units.

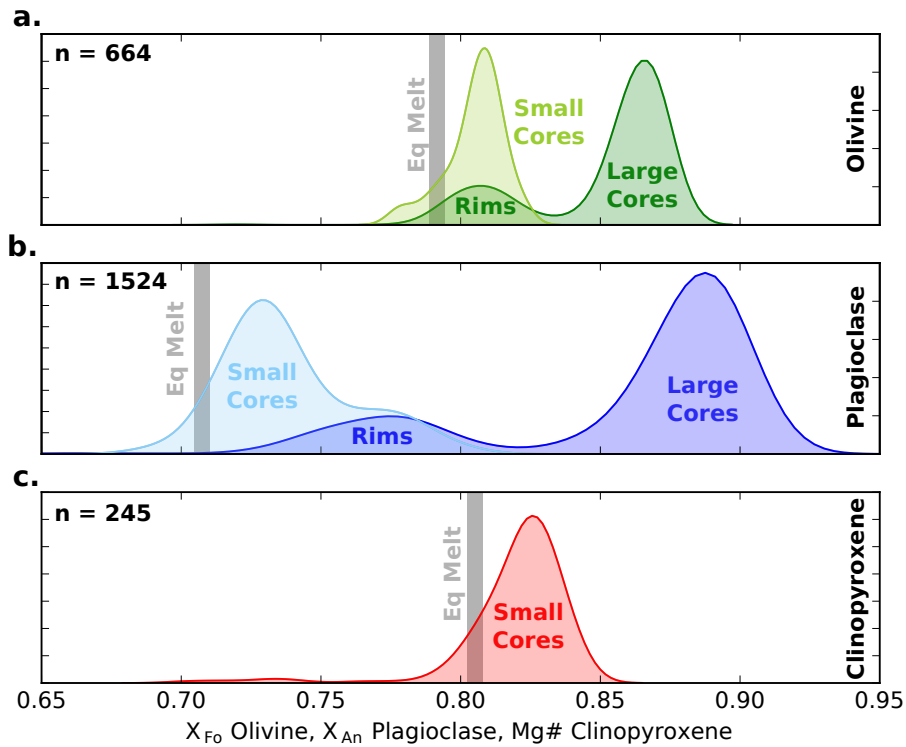


**Figure S4.** Summary of the major element characteristics of the main phases observed in the Skuggafjöll eruption. Each curve is a kernel density estimation (KDE) for olivine (a), plagioclase (b) and clinopyroxene (c) macrocrysts with the bandwidth estimated using Silverman's rule (Silverman, 1986). EPMA profile data collected from coarse olivine (dark green curve) and plagioclase (dark blue curve) macrocrysts were used to supplement data from Neave et al. (2014). The number of analyses (n) is shown in the top left corner for each phase. Compositions of small olivine, plagioclase and clinopyroxene macrocrysts collected by Neave et al. (2014) are shown for reference as light green, light blue and red curves respectively. The grey lines show phase compositions that were in equilibrium with the matrix glass as calculated by Neave et al. (2014). The coarse olivine and plagioclase macrocrysts show bimodal distributions in forsterite content ( $X_{Fo}$ ) and anorthite content ( $X_{An}$ ) as defined by their rim and core compositions respectively. The more evolved rim compositions of these coarse macrocrysts are similar to the core compositions of smaller macrocrysts which are close to equilibrium with the matrix glass. Clinopyroxene is unimodal and in near-equilibrium with the matrix glass (Neave et al., 2014).



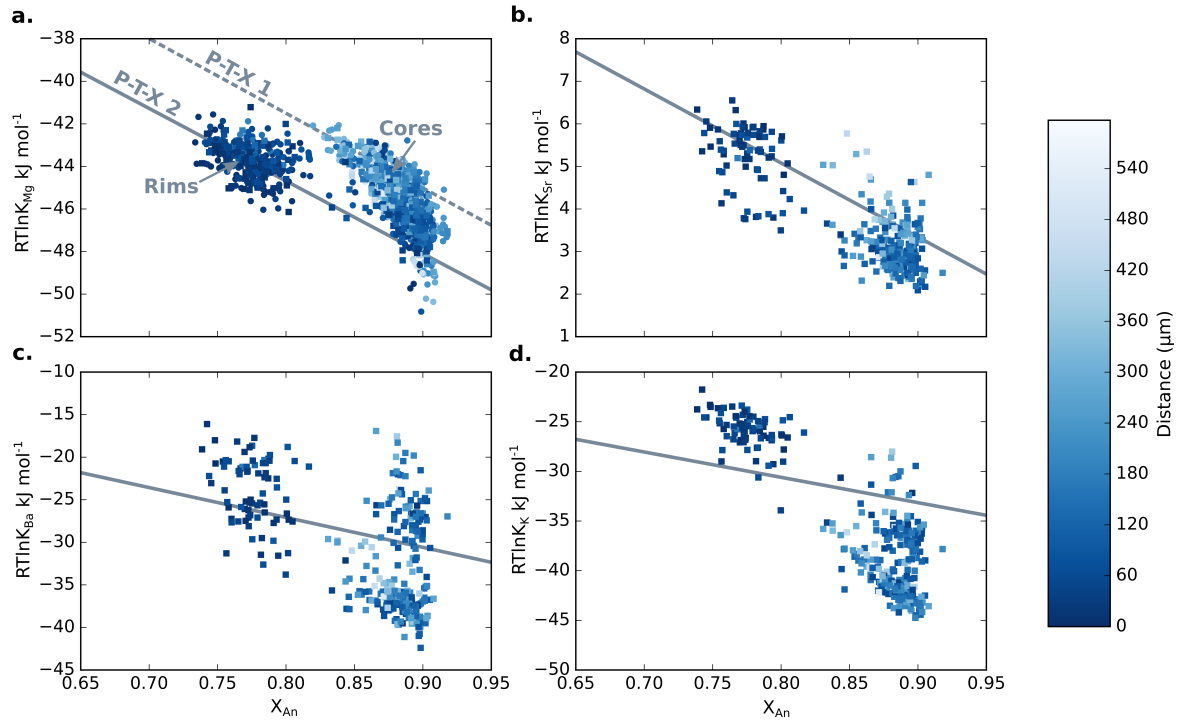


**Figure S5.** Calculated partition coefficients ( $RT\ln K$ ) versus anorthite content for plagioclase trace element profiles collected by SIMS (squares) and EPMA (circles). Partition coefficients for Mg (a), Sr (b), Ba (c) and K (d) are shown and were calculated using the average concentration of the element in the glass and the estimated temperature of the carrier liquid ( $1190^\circ\text{C}$ ) (Neave et al., 2014). Each point is colour-coded for the distance from the edge of the crystal. The grey lines are predictive partitioning models established for plagioclase: Mg uses the calibration of this study; Sr and Ba use Dohmen and Blundy (2014), and K uses Bindeman et al. (1998). The two lines in a represent equilibrium at two different P-T-X conditions.

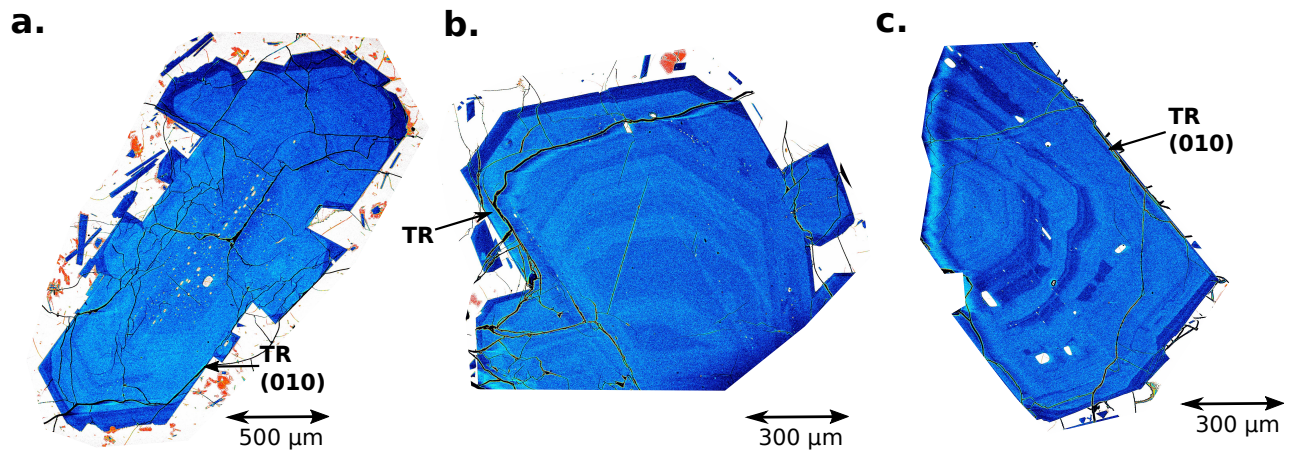


**Figure S6.** False coloured BSE images showing Skuggafjöll plagioclase macrocrysts with thin rims on potential (010) growth faces. Places with thin overgrowth rims are marked with TR. These thin rims are useful for constraining Mg partitioning relationships in calcic plagioclases. Thicker zones on other crystal faces could be due to faster growth rates or sectioning effects associated with inclined faces. **a** shows crystal HOR\_1\_C1\_11, **b** shows HOR\_1\_C1\_6, and **c** shows SKU\_4\_C3\_3.

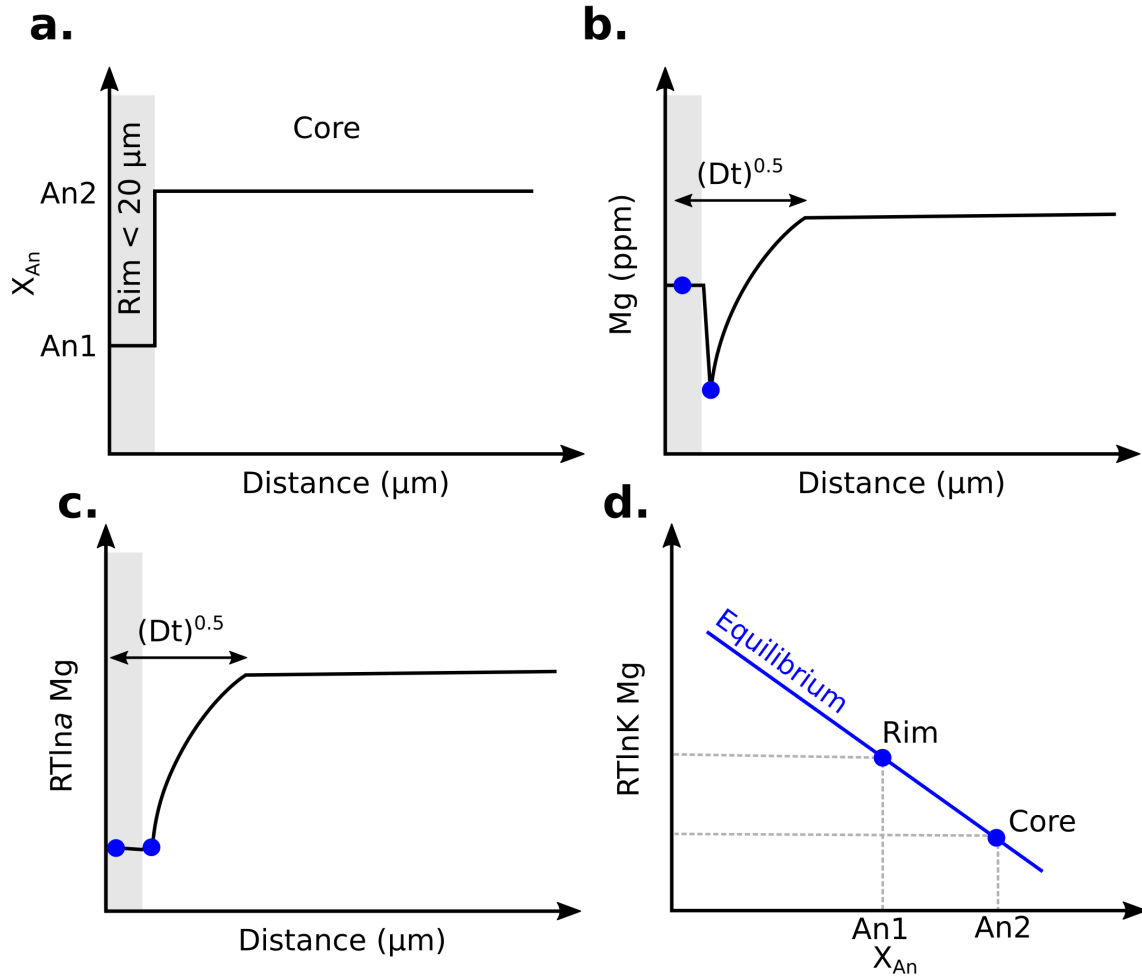


**Figure S7.** Schematic diagrams showing how thin rims on Skuggafjöll plagioclases can be used to constrain an empirical relationship for the partitioning of Mg in calcic plagioclases. **a** shows an anorthite profile for a simply zoned plagioclase crystal with a homogeneous core of composition labelled An<sub>2</sub> (this could be for example An<sub>90</sub>) surrounded by a thin rim of composition An<sub>1</sub> (e.g. An<sub>78</sub>). These overgrowth rims are very thin and can be less than 20 μm thick. This rim is marked by the grey region. **b** shows the corresponding Mg compositional profile where the thin rim has reached equilibrium and the diffusion front has progressed into the crystal core. If the timescale of diffusion is great enough then the outermost part of the core will also become equilibrated with the external conditions. The blue points highlight the regions that were targeted for analysis: a point in the rim, if thick enough, and a point in the core next to the rim. **c** shows what the Mg profile would look like when it is plotted up in activity space, which takes into account anorthite content. **d** shows how linear regression (blue line) can be used to constrain plagioclase-melt partitioning dependence on anorthite content provided the temperature and melt composition are well constrained, which is the case for Skuggafjöll.

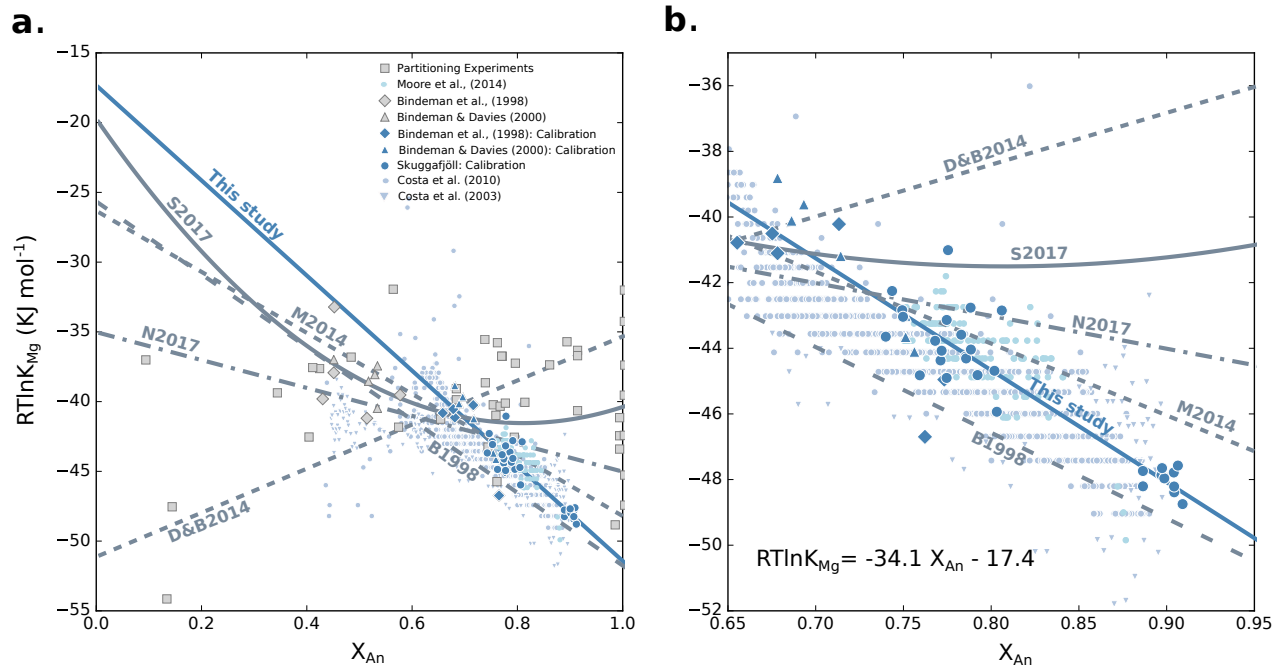


**Figure S8.** Predictive models for the partitioning dependence of Mg in plagioclase on anorthite content ( $X_{An}$ ). **a** shows the whole range of  $X_{An}$  contents, whilst **b** focuses in on  $X_{An}$  compositions applicable for mafic magmatism (e.g. Iceland or MORB). Each grey line corresponds to a different partitioning model: B1998, Bindeman et al. (1998); DI&B2014, Dohmen and Blundy (2014); M(2014), Moore et al. (2014); S(2017), Sun et al. (2017); and N2017, Nielsen et al. (2017). D&B2014 and S2017 models were calculated using a temperature of 1190 °C and pressure of 0.36 GPa. The blue line is the partitioning model of this study calibrated using Skuggafjöll SIMS data from crystal rims and equilibrated portions of crystal cores, and the experimental data of Bindeman et al. (1998) and Bindeman and Davis (2000) filtered above  $X_{An} = 0.60$ . The data used in this study's calibration are plotted in blue and regression parameters are included in **b**. Grey symbols are the main partitioning experiments used to calibrate previous models (Dohmen & Blundy, 2014; Bindeman et al., 1998; Bindeman & Davis, 2000; Sun et al., 2017; Miller et al., 2006; Fabbrizio et al., 2009; Tepley III et al., 2010; Aigner-Torres et al., 2007). The light blue points are natural plagioclase compositions, mostly from MORB samples, that have been interpreted to be equilibrated for Mg (Costa et al., 2003, 2010; Moore et al., 2014).

July 16, 2020, 11:34pm

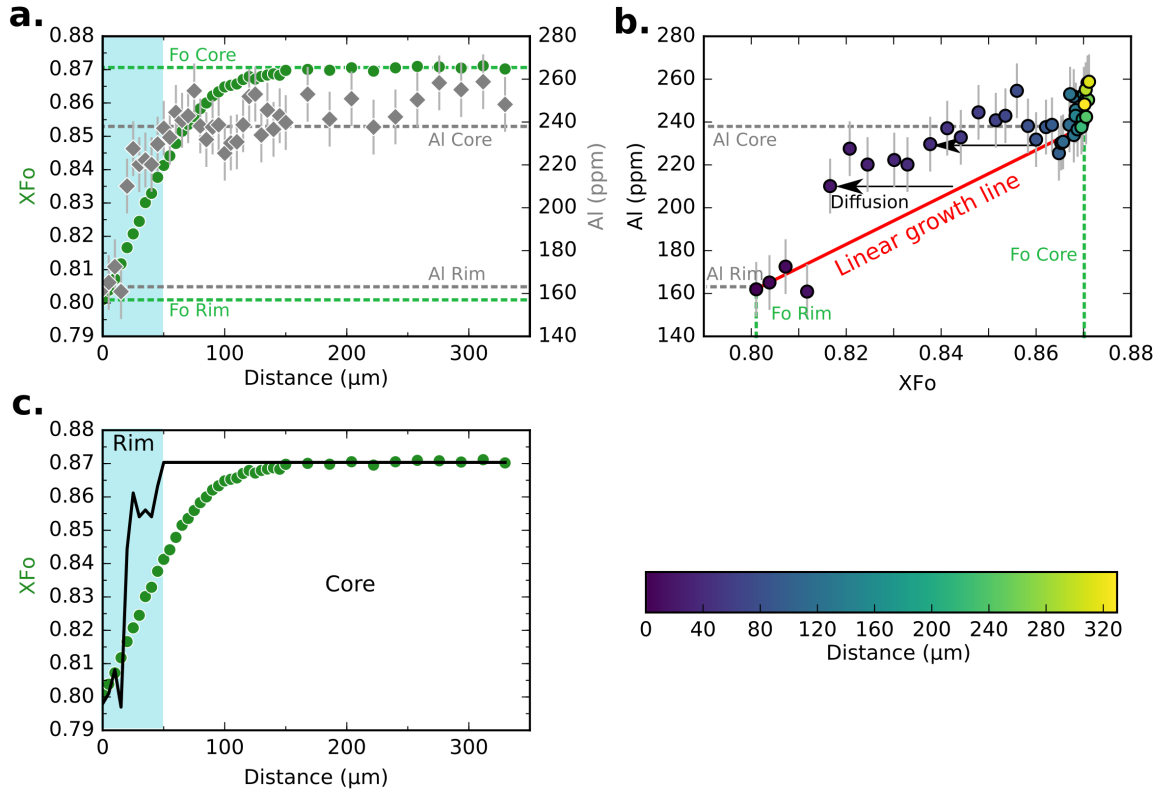


**Figure S9.** Plots showing how Al profiles were used to constrain the initial conditions for elemental diffusion modelling in sample HOR\_1\_OL\_C2\_P3 **a**, shows  $X_{Fo}$  (green points) and Al (grey diamonds) profiles. The position of the rim was determined by the place where Al content starts to decrease from a plateau (marked by the light blue region). The core and rim compositions for these two elements were then selected as shown by the green and grey dashed lines. Rim compositions were chosen at the edge of the crystal, and core compositions were selected based on where the profiles flatten out. **b**, shows these compositions plotted up in  $X_{Fo}$  vs. Al space with points being colour-coded based on distance. A linear regression between the picked rim and core compositions was then conducted (red line) and was used to represent growth. Deviation from this line was assumed to be due to diffusion, as shown by the arrows. **c**, shows these calculated initial conditions relative to the forsterite profile as a black line. Error bars are  $1\sigma$  uncertainties from repeat measurements of San Carlos olivine secondary standards.

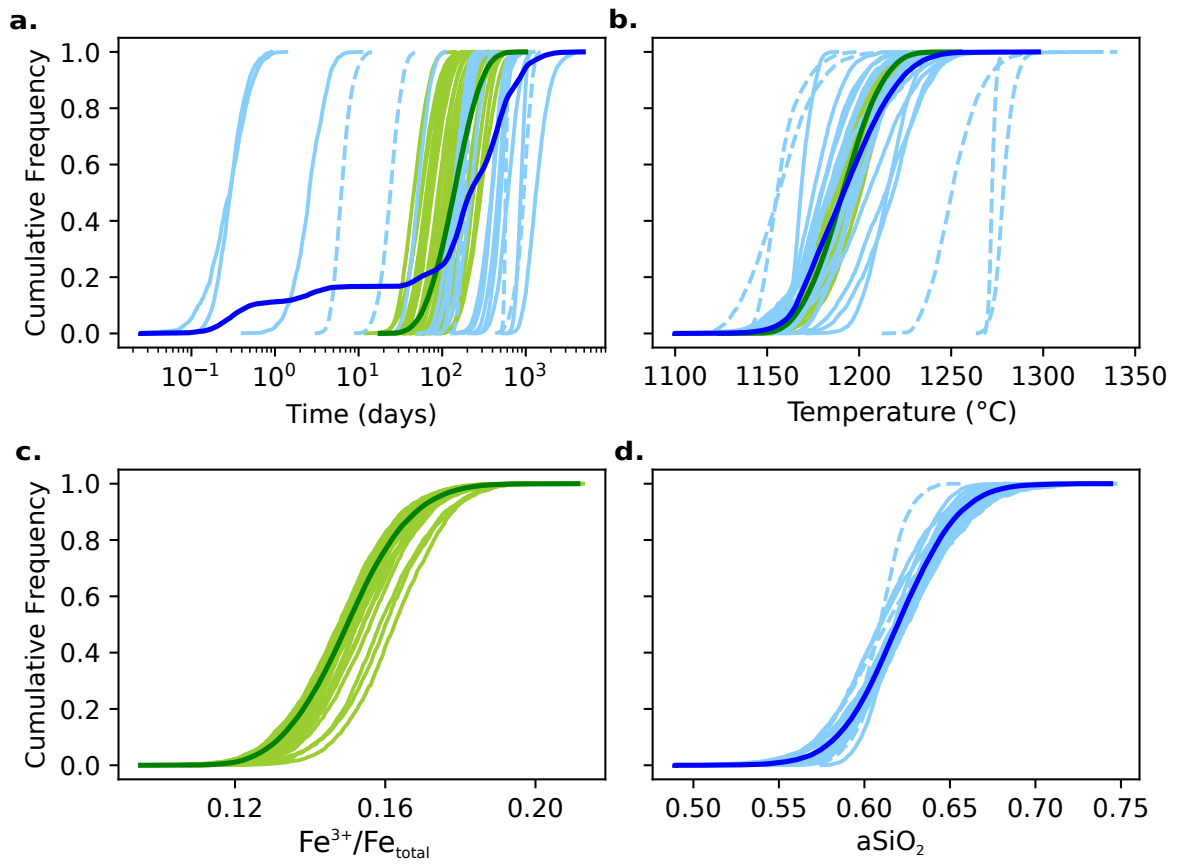


**Figure S10.** Maximum likelihood diffusion timescales and intensive parameters obtained from the DFENS Bayesian inversion method displayed as cumulative frequency curves. Green curves correspond to olivine inversions and blue curves to plagioclase inversions. Black lines are joint olivine-plagioclase models. Dashed lines are crystals in which the maximum likelihood temperature fell outside the  $1190 \pm 30^\circ\text{C}$  prior, meaning they were not incorporated into median values for all crystals. **a** shows estimated magmatic residence times. **b** shows magmatic temperatures. **c** shows the  $\text{Fe}^{3+}/\text{Fe}_{\text{total}}$  of the melt. **d** shows the  $a_{\text{SiO}_2}$  of the system.



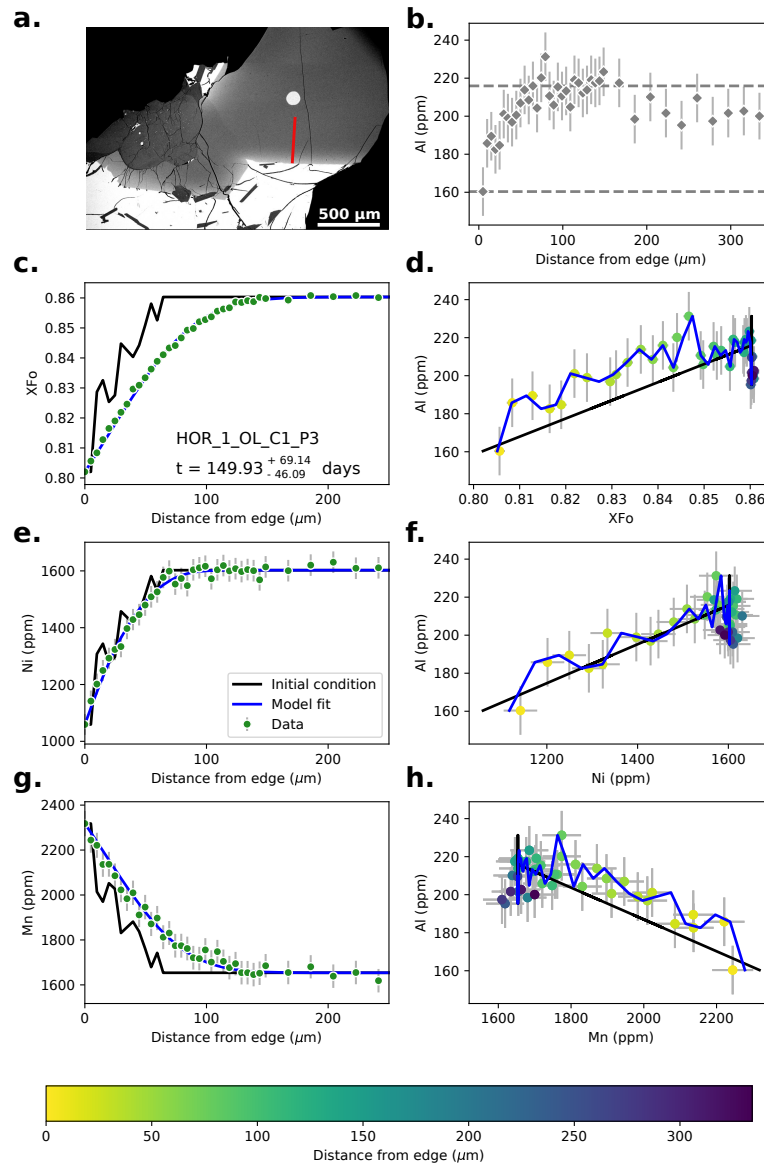


**Figure S11.** Data, initial conditions and model fits for sample HOR\_1\_OL\_C1\_P3. **a**, Backscattered electron (BSE) image of the analysed olivine crystal with the location of the EPMA profile (red line). **b**, EPMA profile of Al with selected rim and core compositions (dashed lines). **c**, EPMA profile of forsterite content ( $X_{Fo}$ ) shown in green. **d**,  $X_{Fo}$  vs. Al cross-plot. **e**, EPMA profile of Ni shown in green. **f**, Ni vs. Al cross-plot. **g**, EPMA profile of Mn shown in green. **h**, Mn vs. Al cross-plot. Blue curves in **c-h** are maximum likelihood best fit model curves from the Bayesian Inversion corresponding to the median time shown in **c**. The black lines and curves in **c-h** show the growth-controlled initial conditions based on a linear calibration between Al and the element of interest. All cross-plots have been colour-coded based on the distance from the edge of the crystal. Error bars are  $1\sigma$  uncertainties from repeat measurements of San Carlos olivine secondary standards.

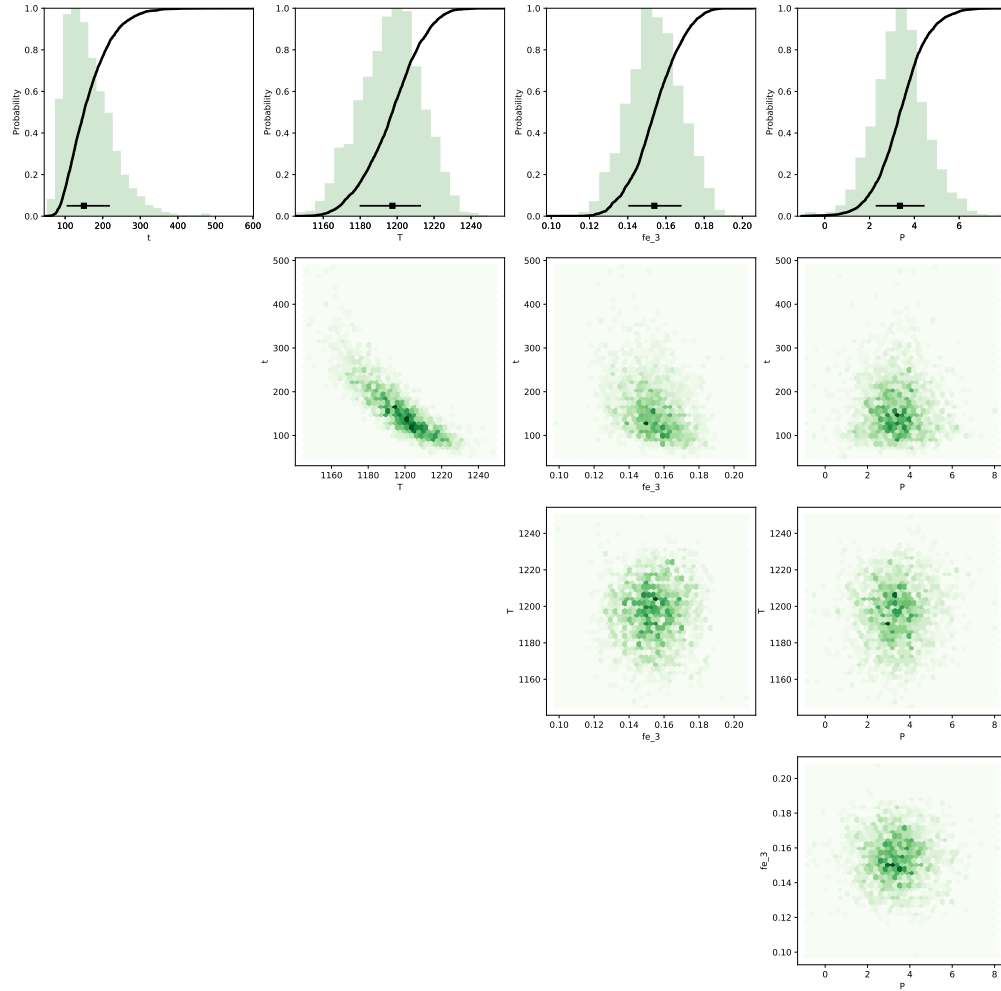


**Figure S12.** Bayesian inversion results for sample HOR\_1\_OL\_C1\_P3. Marginal plot showing the posterior distributions of the Nested Sampling Bayesian Inversion for the main intensive parameters:  $t$  is time (days),  $T$  is temperature ( $^{\circ}\text{C}$ ),  $fe\_3$  is ferric iron content of the melt and  $P$  is pressure (kbar). The top row shows histograms (green bars) and probability density functions (black curves) of the aforementioned intensive parameters. The black bar shows the median result and  $1\sigma$  standard deviation. The bottom three rows are density plots that show the trade offs between the different intensive parameters.

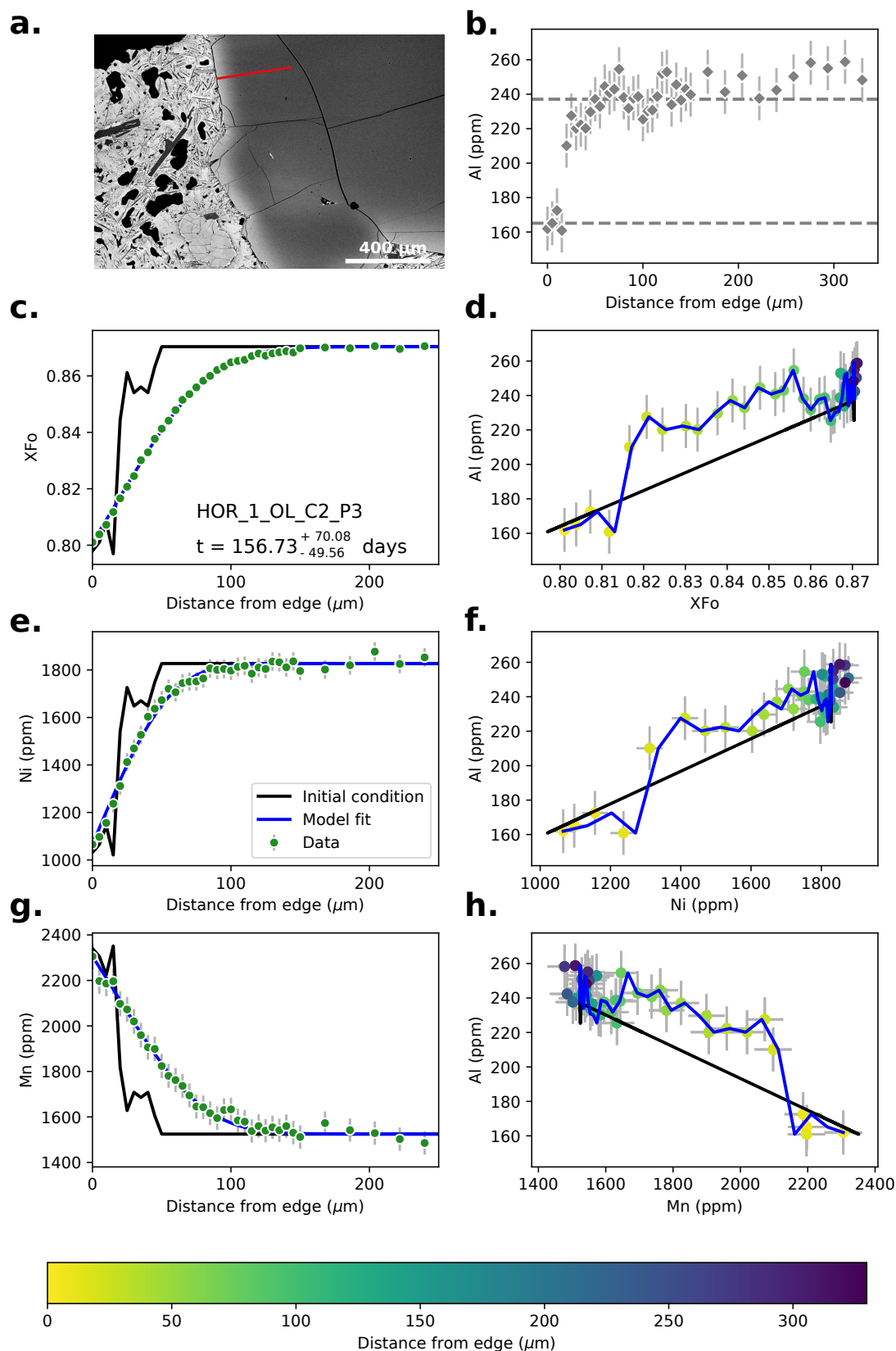


**Figure S13.** Data, initial conditions and model fits for sample HOR\_1\_OL\_C2\_P3. Caption the same as Supplementary Fig. S11.

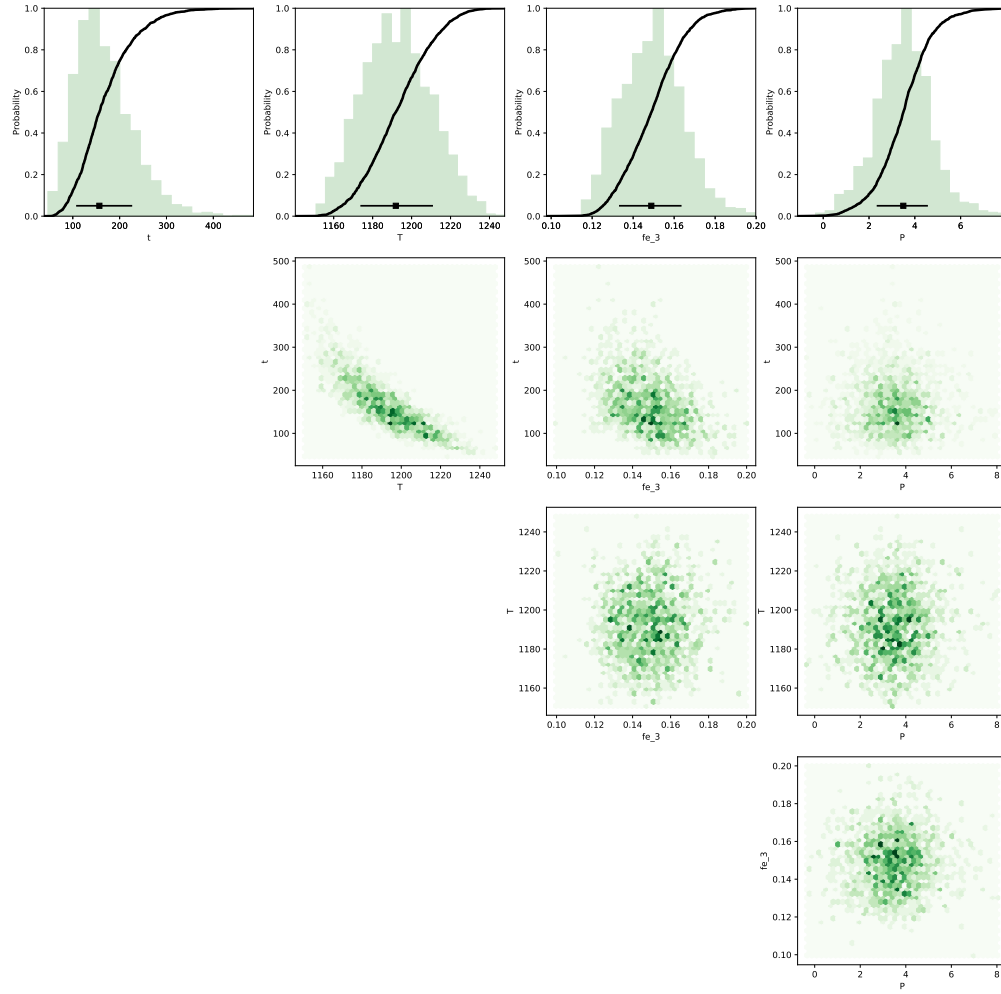


**Figure S14.** Bayesian inversion results for sample HOR\_1\_OL\_C2\_P3. Marginal plot showing the posterior distributions of the Nested Sampling Bayesian Inversion for the main intensive parameters:  $t$  is time (days),  $T$  is temperature ( $^{\circ}\text{C}$ ),  $fe\_3$  is ferric iron content of the melt and  $P$  is pressure (kbar). The top row shows histograms (green bars) and probability density functions (black curves) of the aforementioned intensive parameters. The black bar shows the median result and  $1\sigma$  standard deviation. The bottom three rows are density plots that show the trade offs between the different intensive parameters.

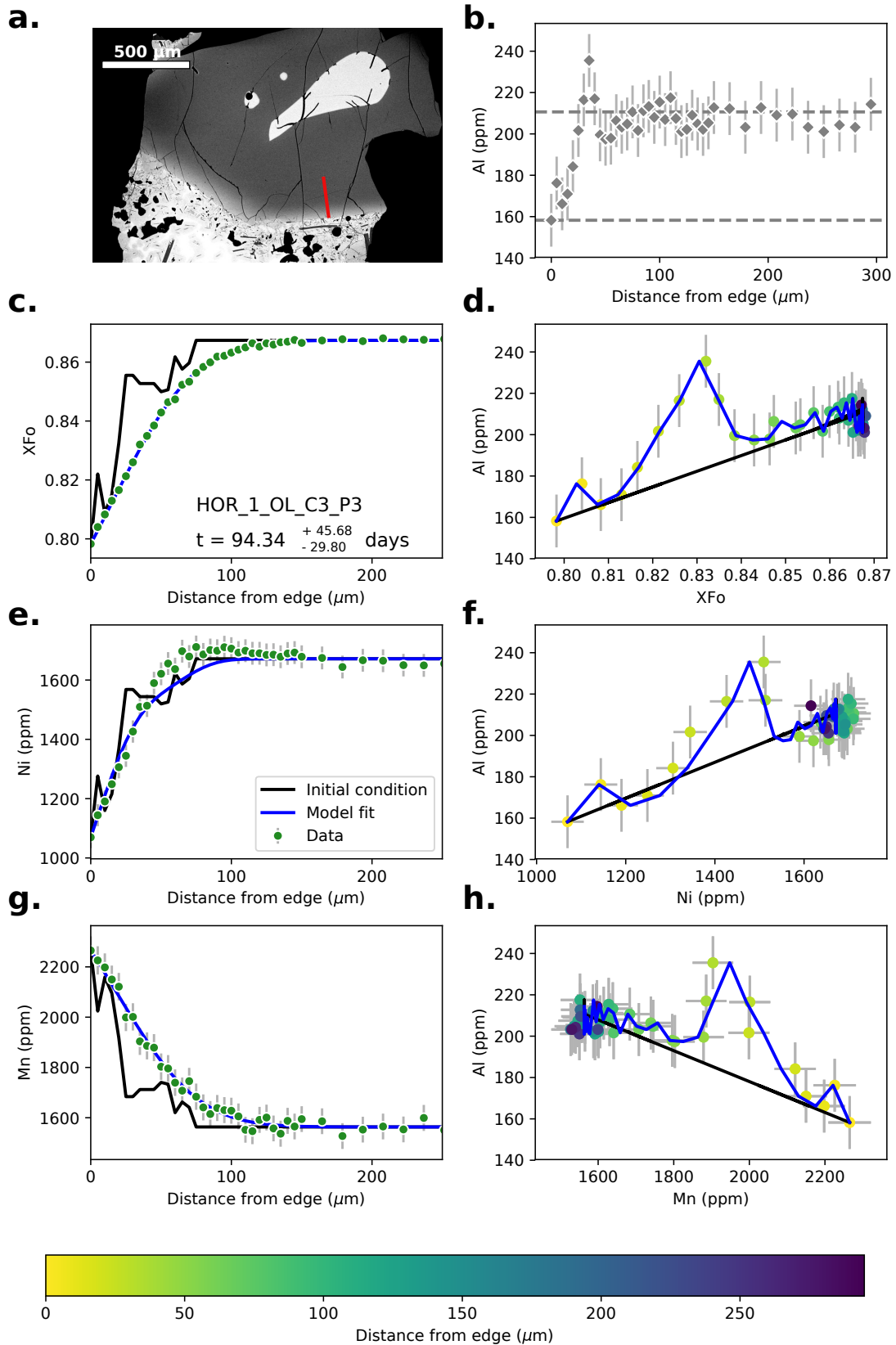


**Figure S15.** Data, initial conditions and model fits for sample HOR\_1\_OL\_C3\_P3. Caption the same as Supplementary Fig. S11.

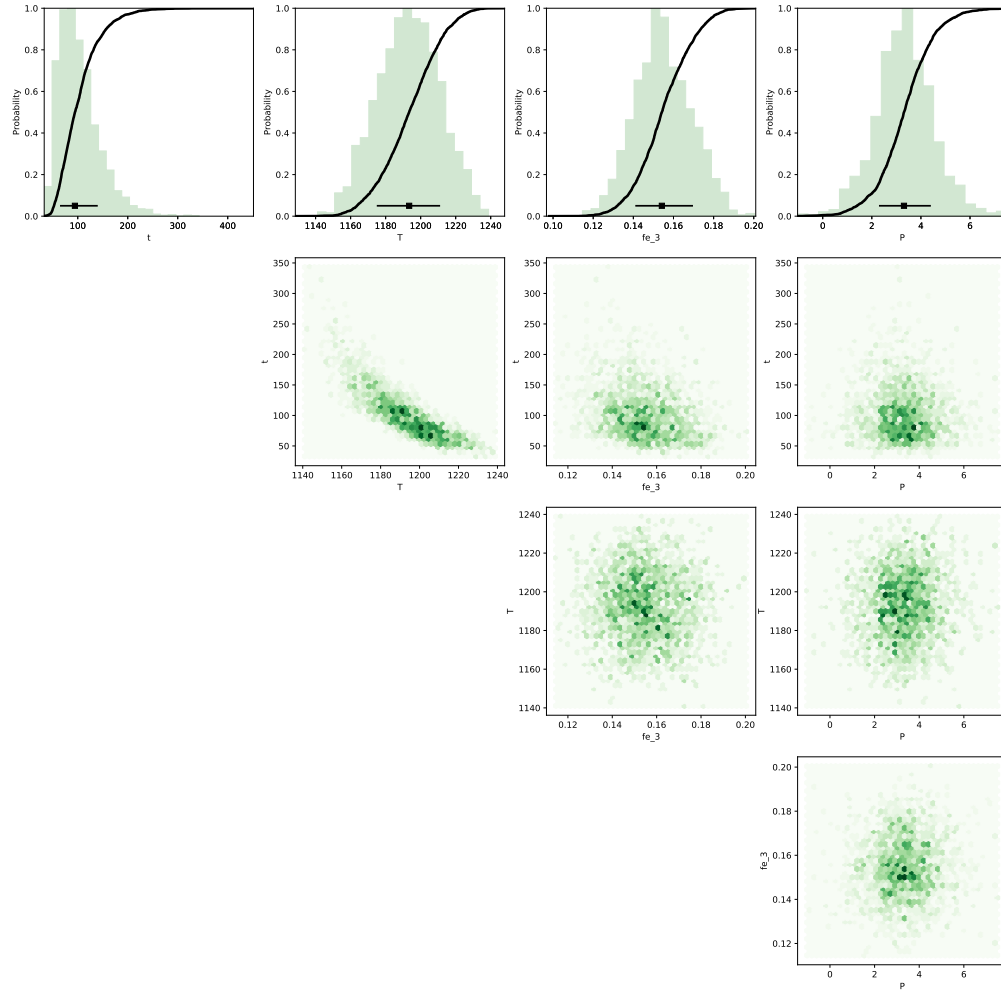


**Figure S16.** Bayesian inversion results for sample HOR\_1\_OL\_C3\_P3. Marginal plot showing the posterior distributions of the Nested Sampling Bayesian Inversion for the main intensive parameters:  $t$  is time (days),  $T$  is temperature ( $^{\circ}\text{C}$ ),  $fe\_3$  is ferric iron content of the melt and  $P$  is pressure (kbar). The top row shows histograms (green bars) and probability density functions (black curves) of the aforementioned intensive parameters. The black bar shows the median result and  $1\sigma$  standard deviation. The bottom three rows are density plots that show the trade offs between the different intensive parameters.

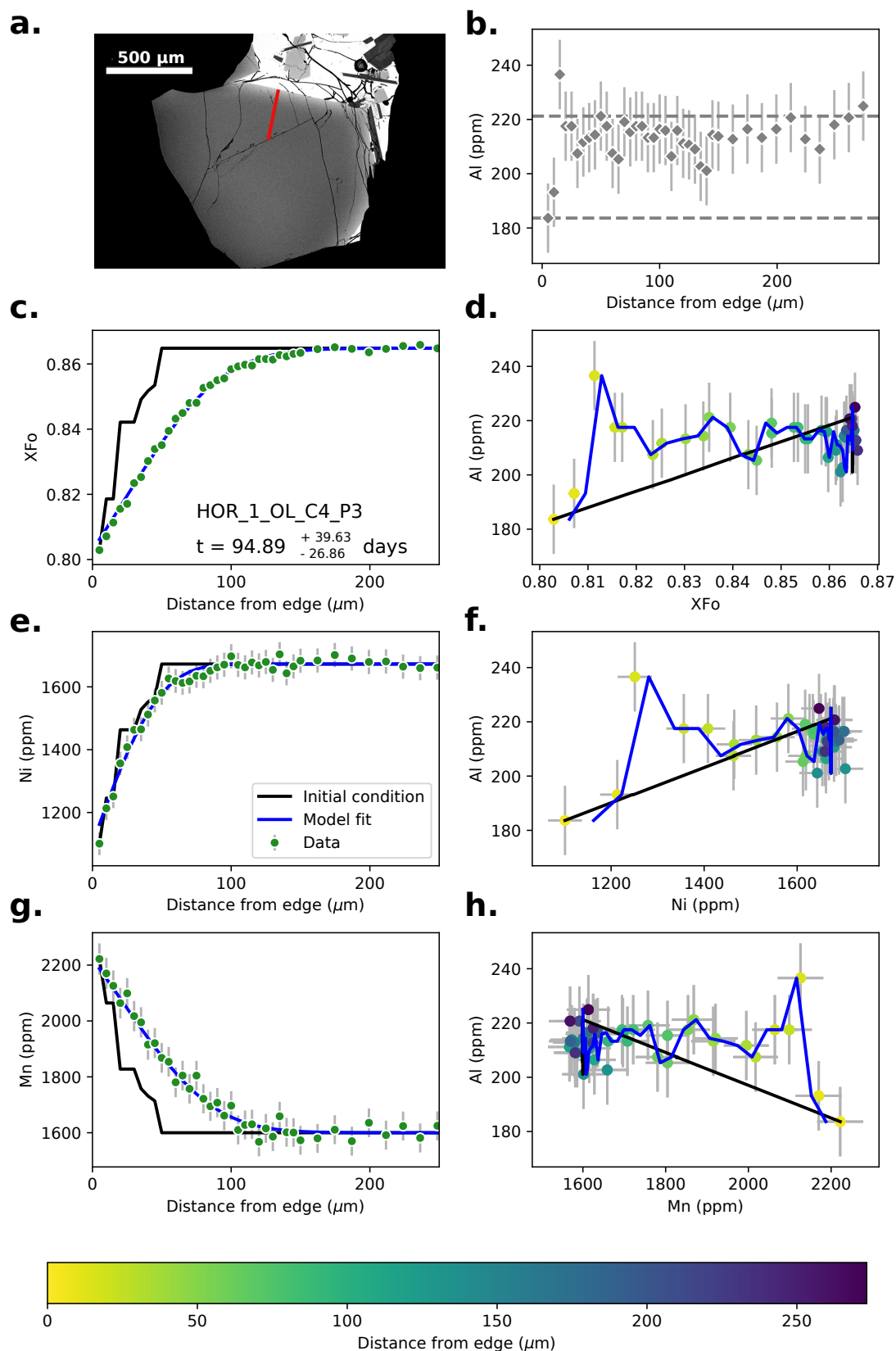


**Figure S17.** Data, initial conditions and model fits for sample HOR\_1\_OL\_C4\_P3. Caption the same as Supplementary Fig. S11.

July 16, 2020, 11:34pm



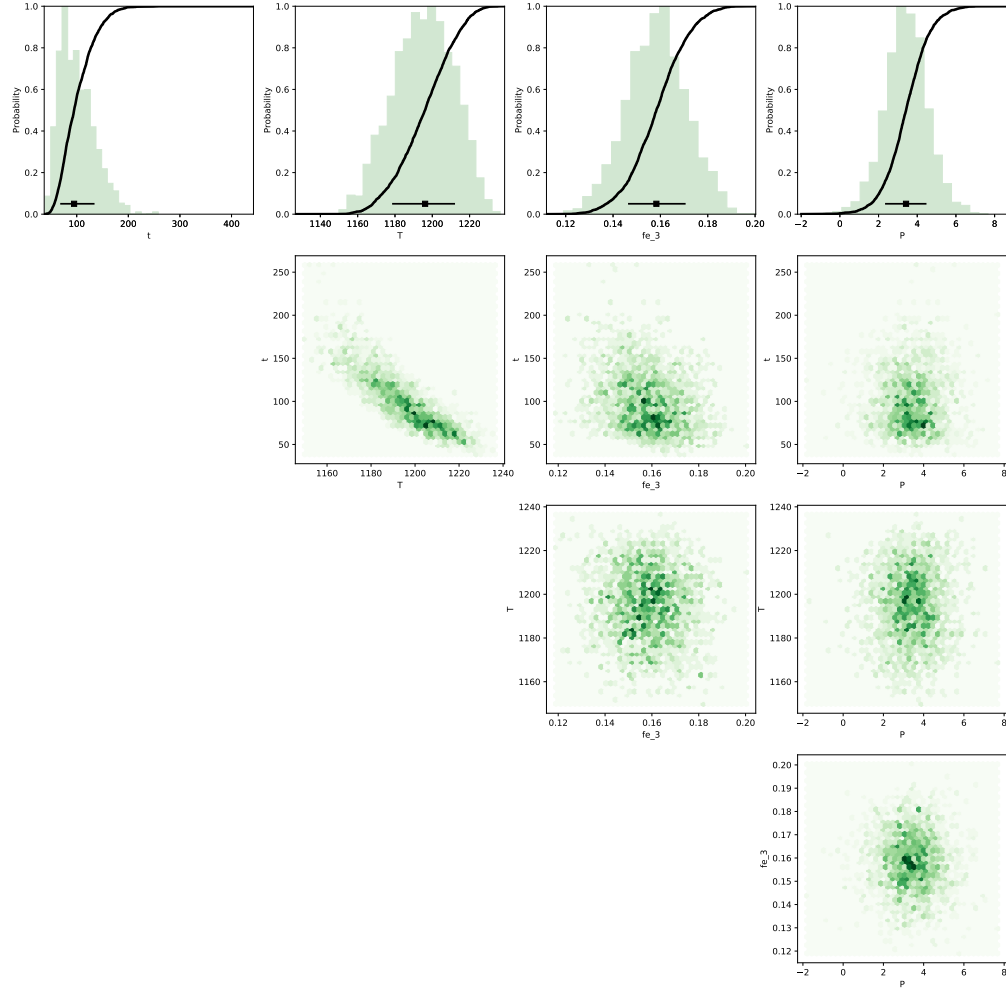


**Figure S18.** Bayesian inversion results for sample HOR\_1\_OL\_C4\_P3. Marginal plot showing the posterior distributions of the Nested Sampling Bayesian Inversion for the main intensive parameters:  $t$  is time (days),  $T$  is temperature ( $^{\circ}\text{C}$ ),  $fe\_3$  is ferric iron content of the melt and  $P$  is pressure (kbar). The top row shows histograms (green bars) and probability density functions (black curves) of the aforementioned intensive parameters. The black bar shows the median result and  $1\sigma$  standard deviation. The bottom three rows are density plots that show the trade offs between the different intensive parameters.

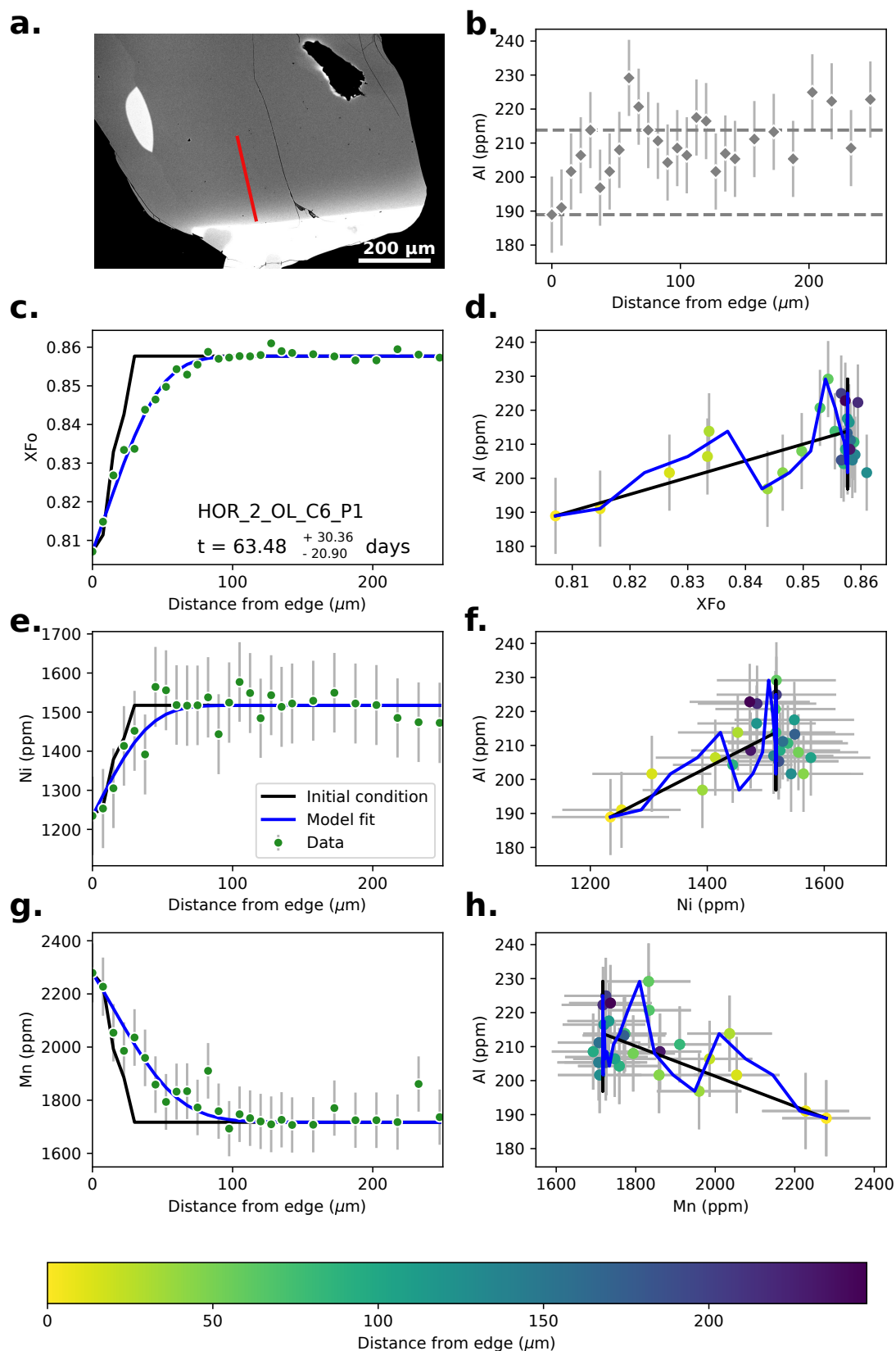


**Figure S19.** Data, initial conditions and model fits for sample HOR\_2\_OL\_C6\_P1. Caption the same as Supplementary Fig. S11.

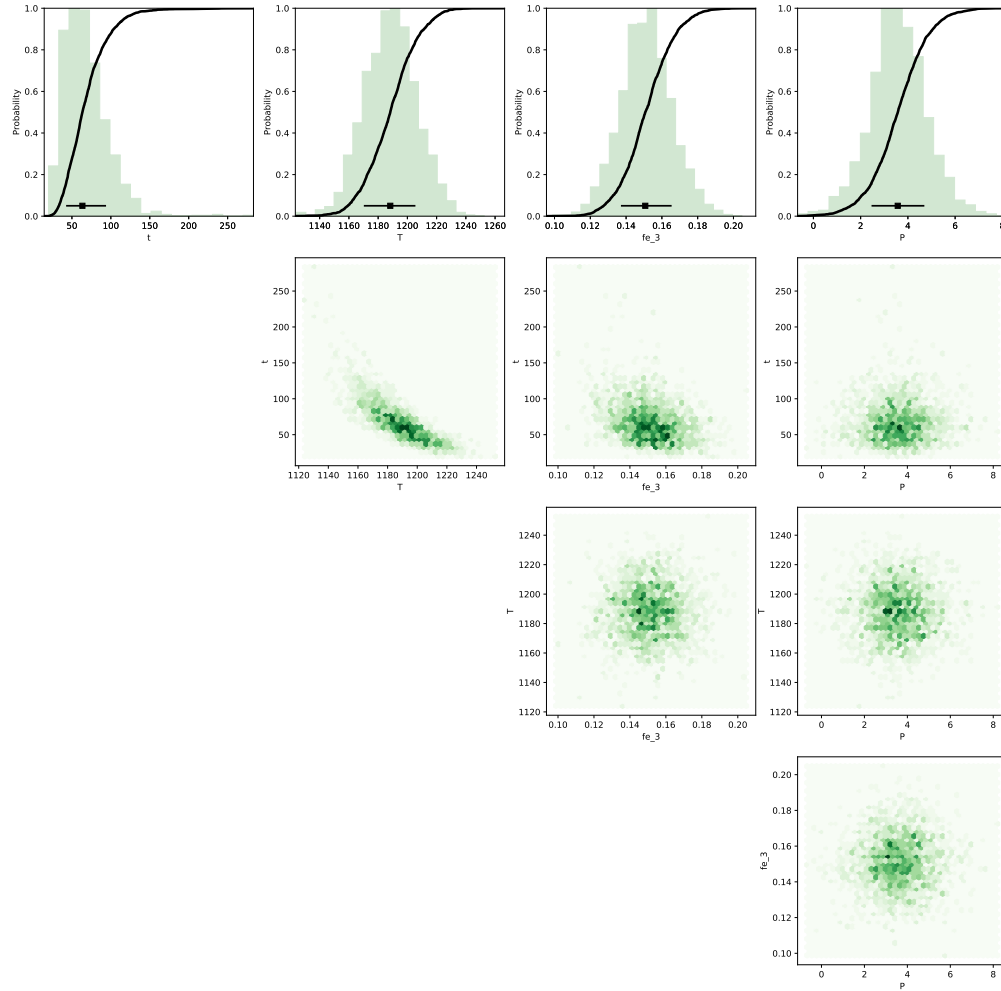


**Figure S20.** Bayesian inversion results for sample HOR\_1\_OL\_C6\_P1. Marginal plot showing the posterior distributions of the Nested Sampling Bayesian Inversion for the main intensive parameters:  $t$  is time (days),  $T$  is temperature ( $^{\circ}\text{C}$ ),  $fe\_3$  is ferric iron content of the melt and  $P$  is pressure (kbar). The top row shows histograms (green bars) and probability density functions (black curves) of the aforementioned intensive parameters. The black bar shows the median result and  $1\sigma$  standard deviation. The bottom three rows are density plots that show the trade offs between the different intensive parameters.

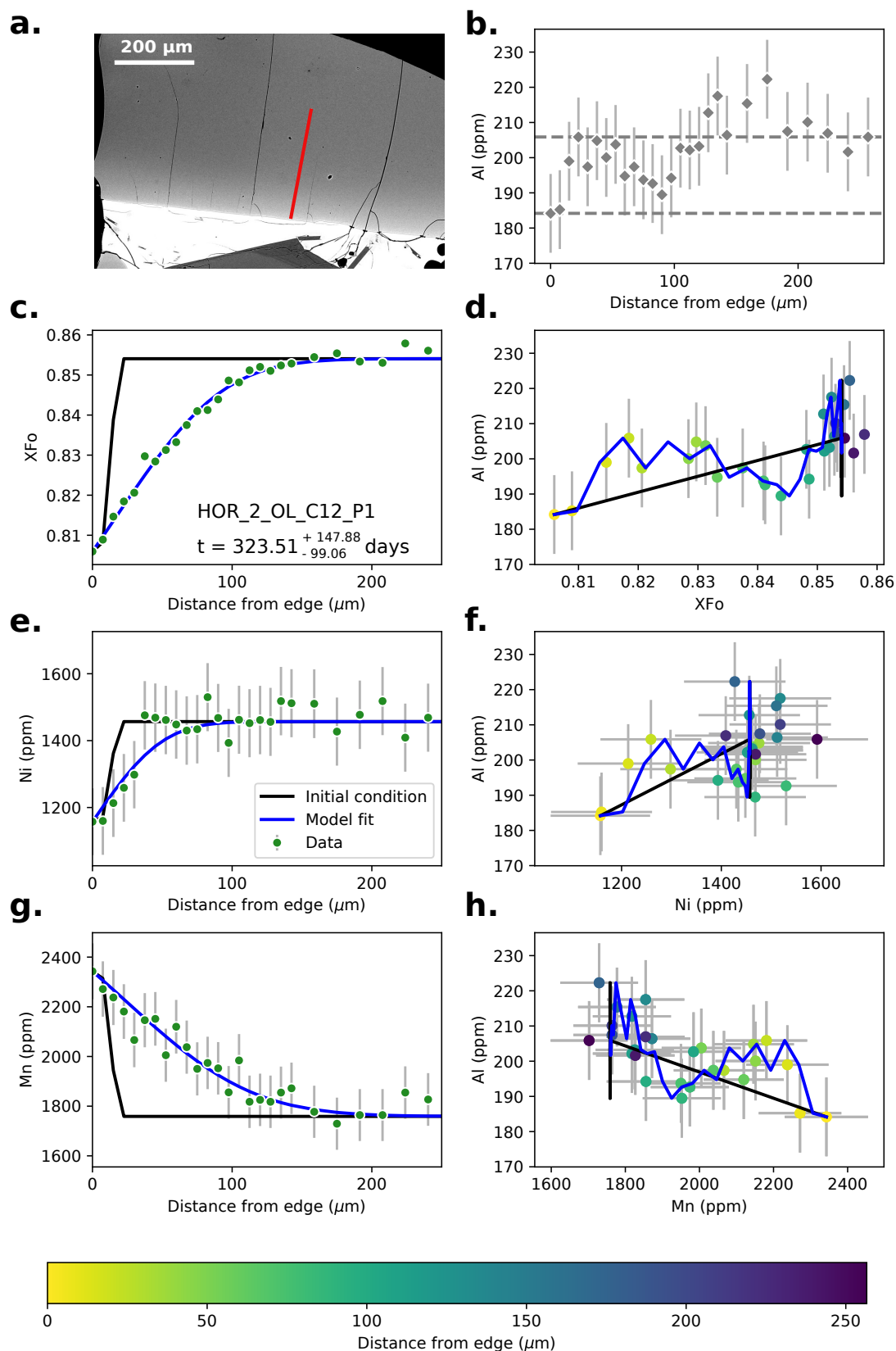


**Figure S21.** Data, initial conditions and model fits for sample HOR\_2\_OL\_C12\_P1. Caption the same as Supplementary Fig. S11.

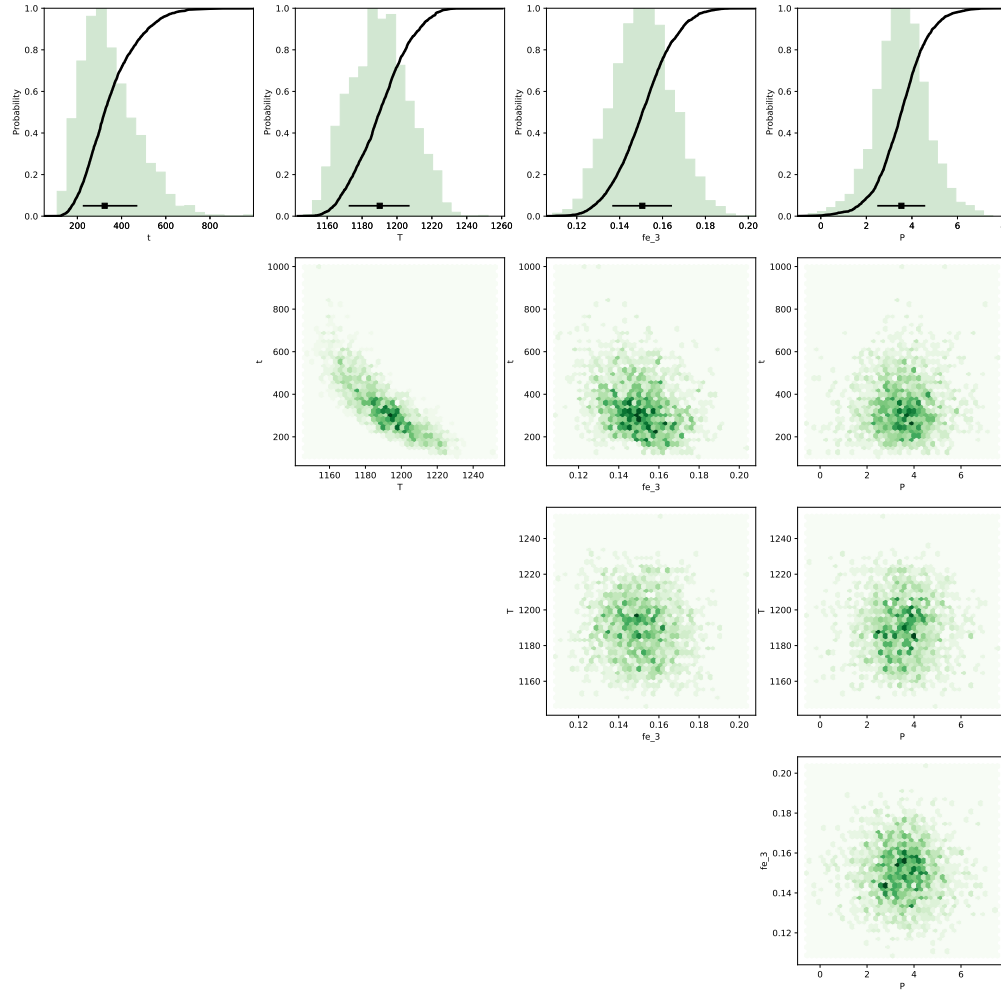


**Figure S22.** Bayesian inversion results for sample HOR\_1\_OL\_C12\_P1. Marginal plot showing the posterior distributions of the Nested Sampling Bayesian Inversion for the main intensive parameters:  $t$  is time (days),  $T$  is temperature ( $^{\circ}\text{C}$ ),  $fe\_3$  is ferric iron content of the melt and  $P$  is pressure (kbar). The top row shows histograms (green bars) and probability density functions (black curves) of the aforementioned intensive parameters. The black bar shows the median result and  $1\sigma$  standard deviation. The bottom three rows are density plots that show the trade offs between the different intensive parameters.

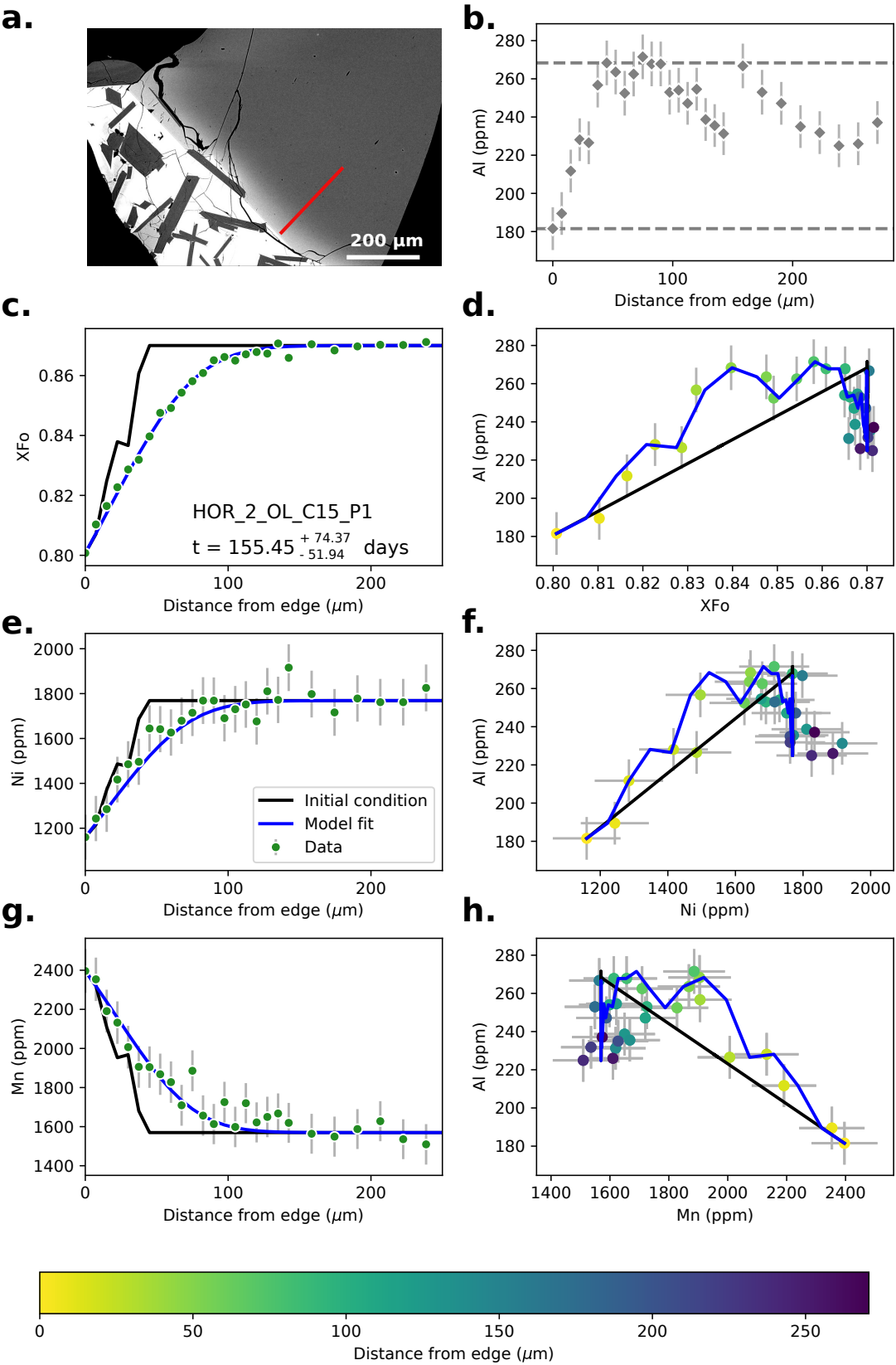


**Figure S23.** Data, initial conditions and model fits for sample HOR\_2\_OL\_C15\_P1. Caption the same as Supplementary Fig. S11.

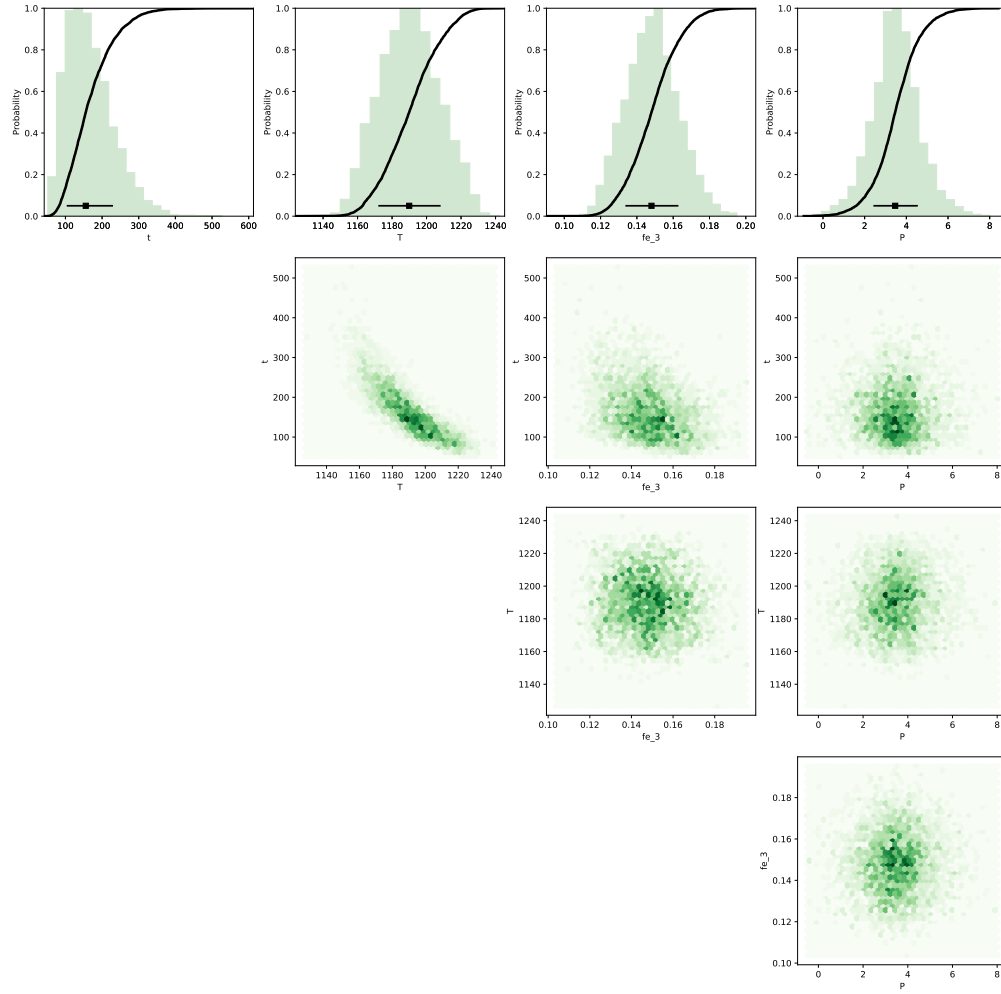


**Figure S24.** Bayesian inversion results for sample HOR\_1\_OL\_C15\_P1. Marginal plot showing the posterior distributions of the Nested Sampling Bayesian Inversion for the main intensive parameters:  $t$  is time (days),  $T$  is temperature ( $^{\circ}\text{C}$ ),  $fe\_3$  is ferric iron content of the melt and  $P$  is pressure (kbar). The top row shows histograms (green bars) and probability density functions (black curves) of the aforementioned intensive parameters. The black bar shows the median result and  $1\sigma$  standard deviation. The bottom three rows are density plots that show the trade offs between the different intensive parameters.



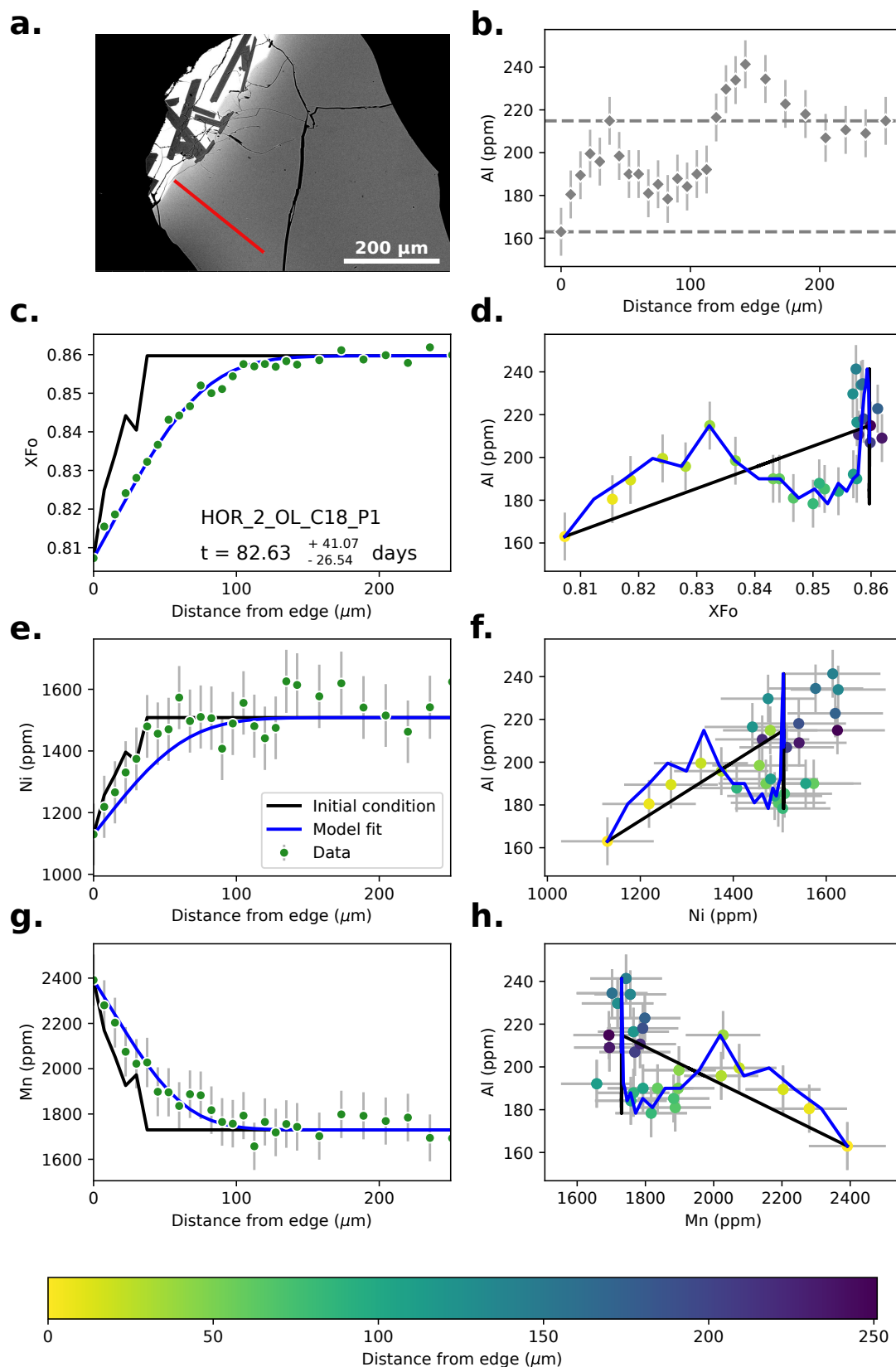


**Figure S25.** Data, initial conditions and model fits for sample HOR\_2\_OL\_C18\_P1. Caption the same as Supplementary Fig. S11.

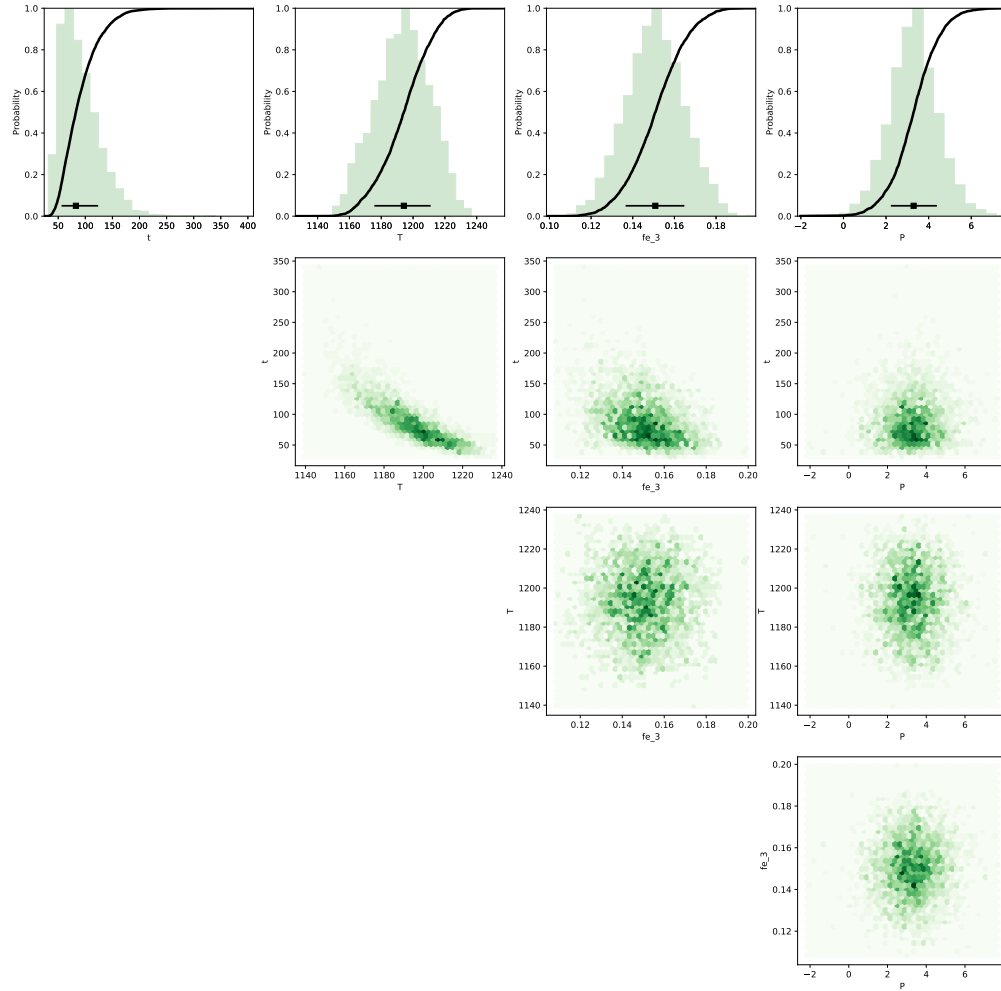


**Figure S26.** Bayesian inversion results for sample HOR\_1\_OL\_C18\_P1. Marginal plot showing the posterior distributions of the Nested Sampling Bayesian Inversion for the main intensive parameters:  $t$  is time (days),  $T$  is temperature ( $^{\circ}\text{C}$ ),  $fe\_3$  is ferric iron content of the melt and  $P$  is pressure (kbar). The top row shows histograms (green bars) and probability density functions (black curves) of the aforementioned intensive parameters. The black bar shows the median result and  $1\sigma$  standard deviation. The bottom three rows are density plots that show the trade offs between the different intensive parameters.

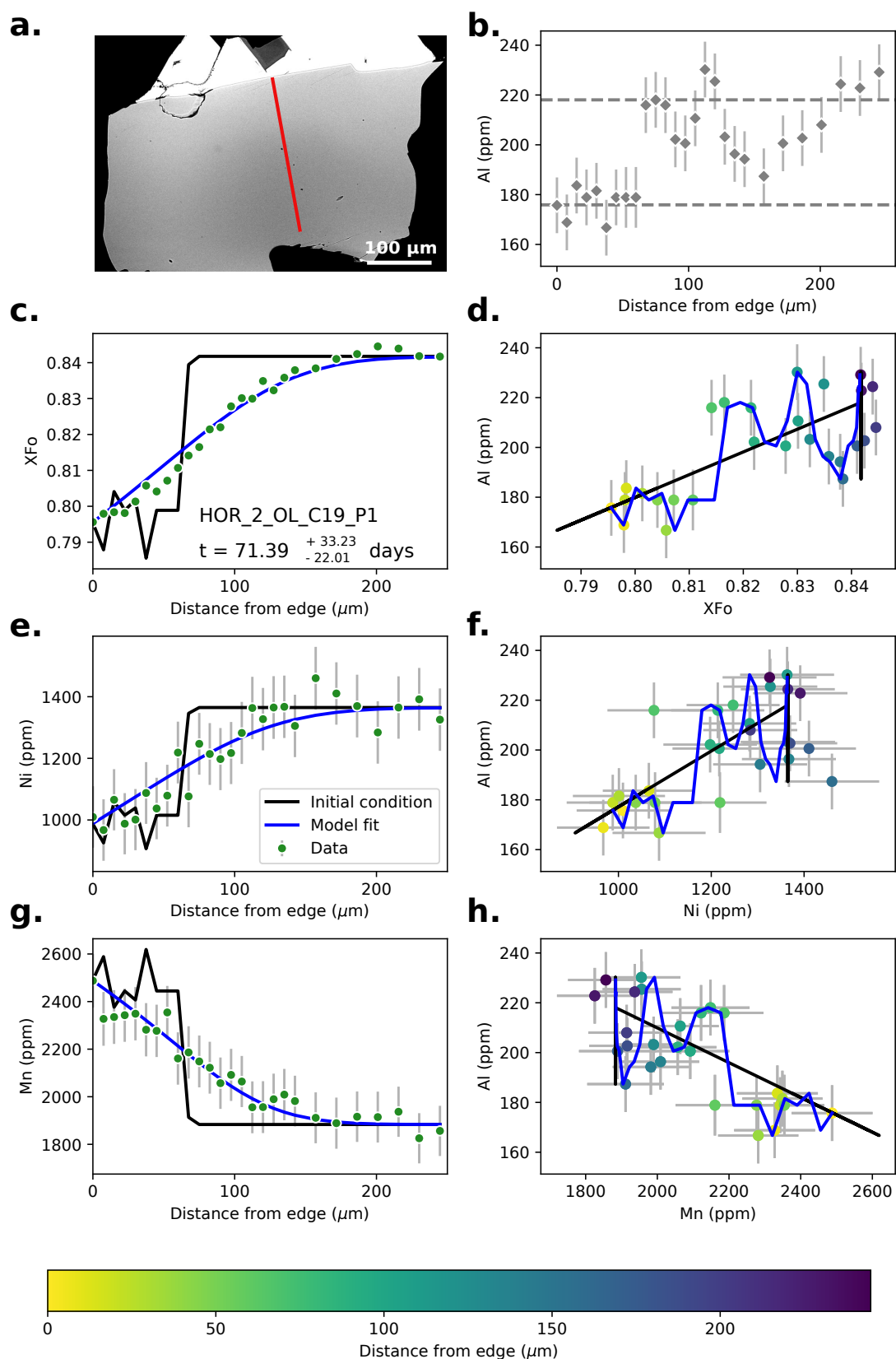


**Figure S27.** Data, initial conditions and model fits for sample HOR\_2\_OL\_C19\_P1. Caption the same as Supplementary Fig. S11.

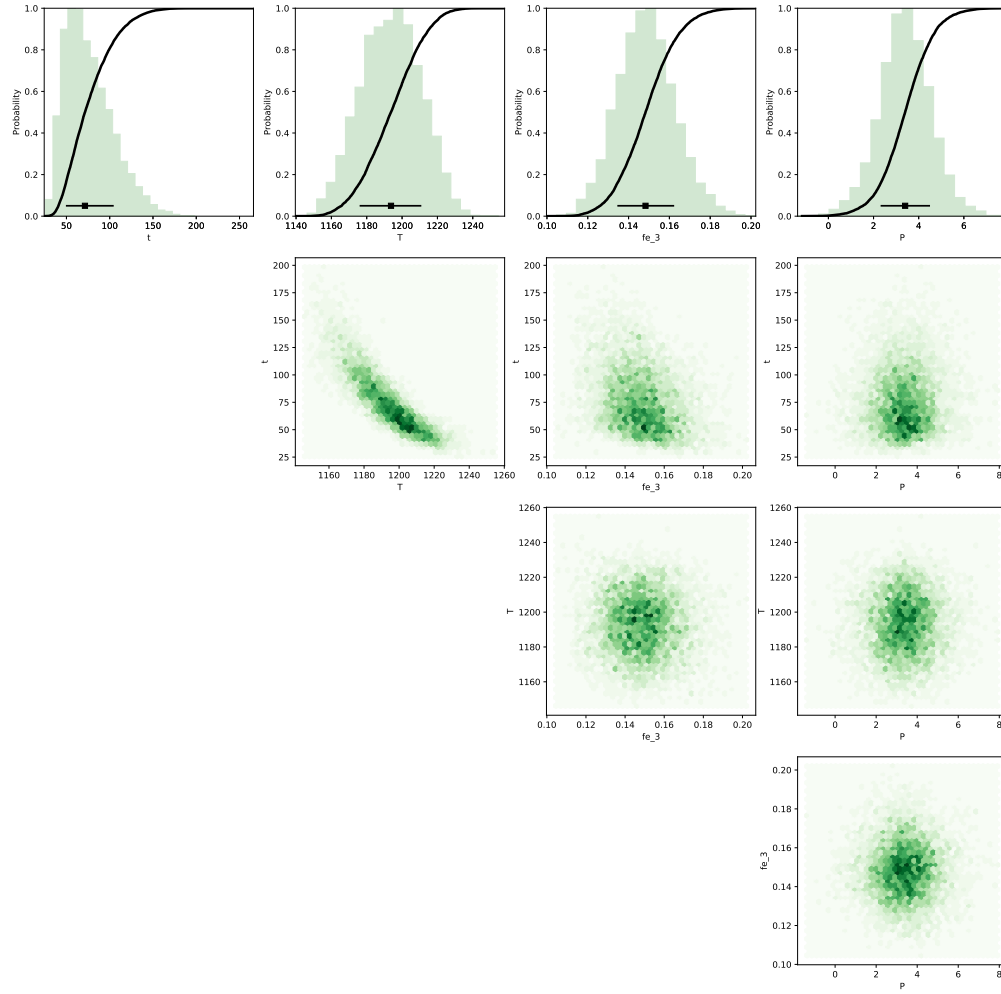


**Figure S28.** Bayesian inversion results for sample HOR\_1\_OL\_C19\_P1. Marginal plot showing the posterior distributions of the Nested Sampling Bayesian Inversion for the main intensive parameters:  $t$  is time (days),  $T$  is temperature ( $^{\circ}\text{C}$ ),  $fe\_3$  is ferric iron content of the melt and  $P$  is pressure (kbar). The top row shows histograms (green bars) and probability density functions (black curves) of the aforementioned intensive parameters. The black bar shows the median result and  $1\sigma$  standard deviation. The bottom three rows are density plots that show the trade offs between the different intensive parameters.

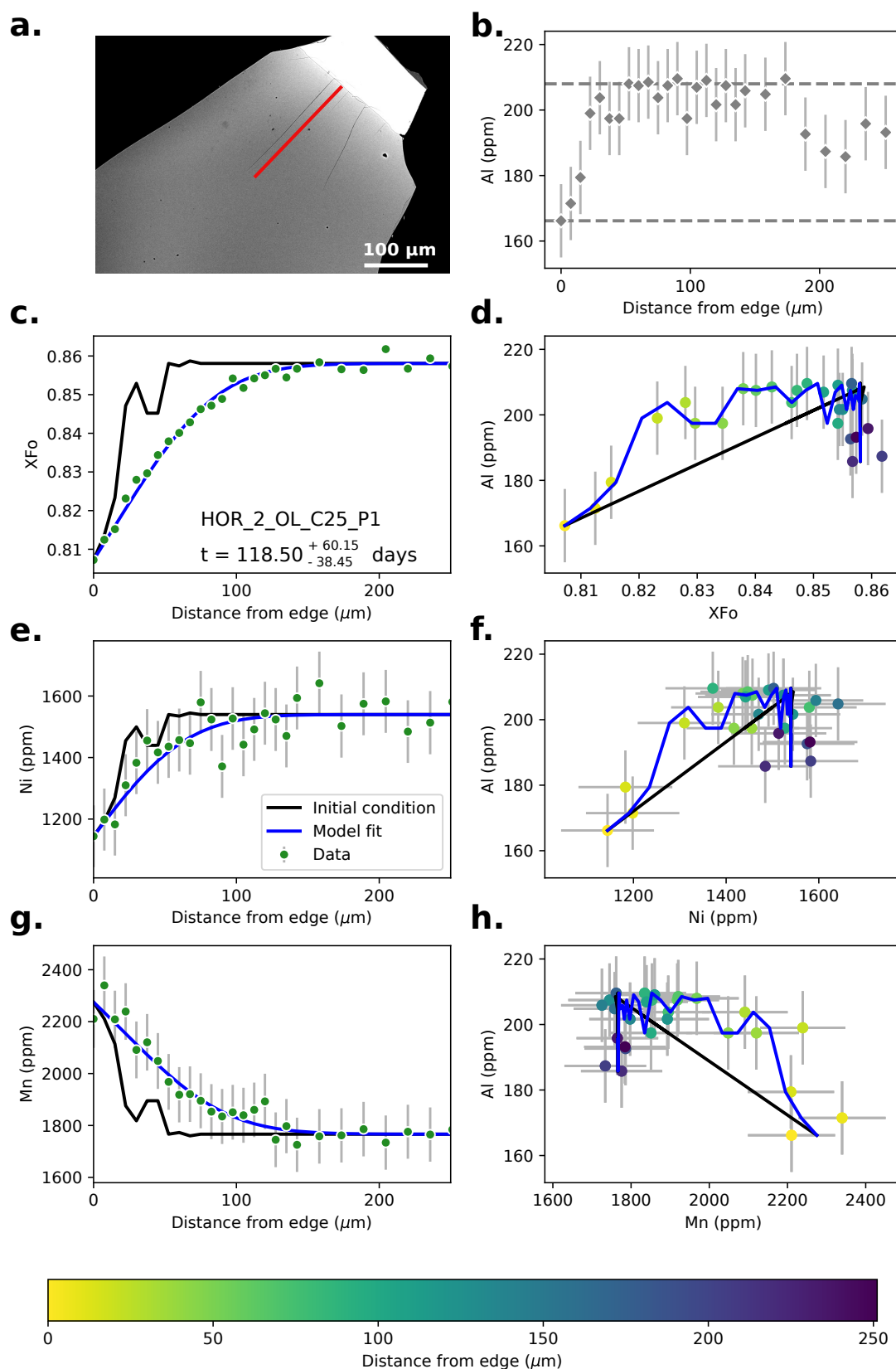


**Figure S29.** Data, initial conditions and model fits for sample HOR\_2\_OL\_C25\_P1. Caption the same as Supplementary Fig. S11.

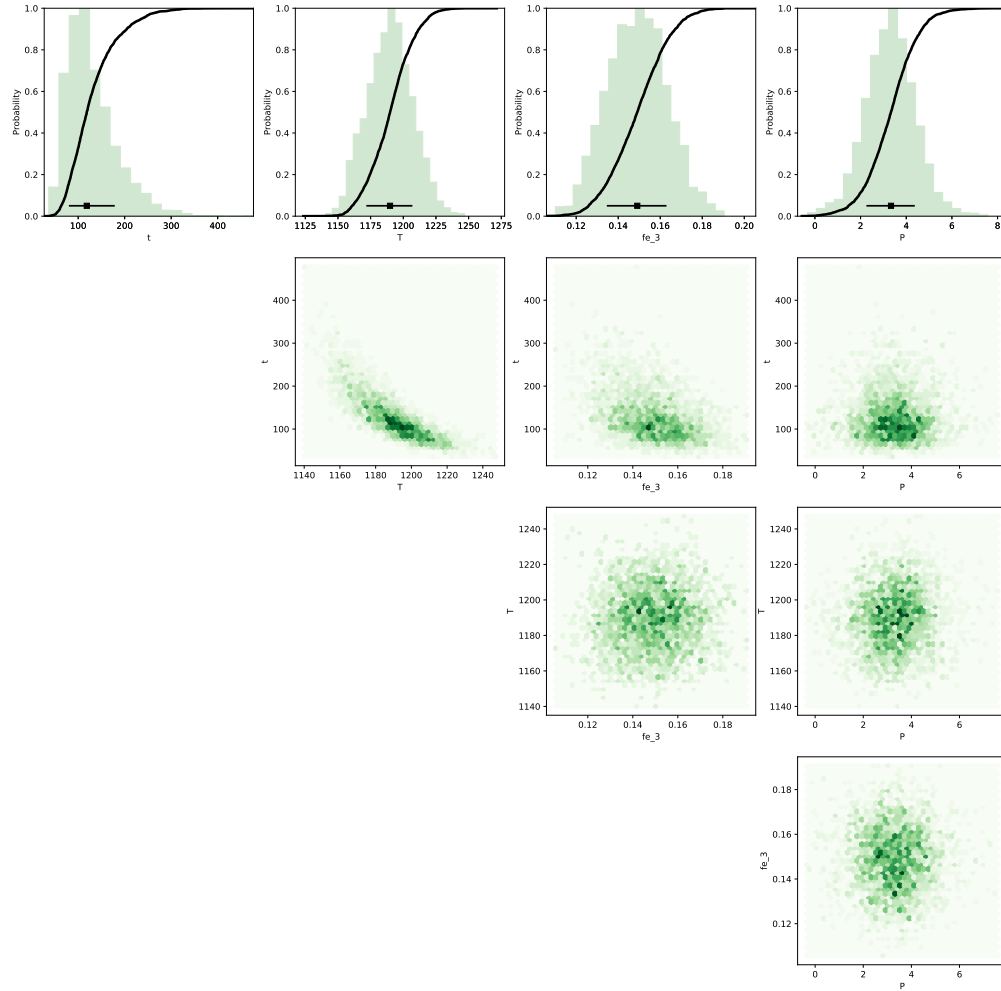


**Figure S30.** Bayesian inversion results for sample HOR\_1\_OL\_C25\_P1. Marginal plot showing the posterior distributions of the Nested Sampling Bayesian Inversion for the main intensive parameters:  $t$  is time (days),  $T$  is temperature ( $^{\circ}\text{C}$ ),  $fe\_3$  is ferric iron content of the melt and  $P$  is pressure (kbar). The top row shows histograms (green bars) and probability density functions (black curves) of the aforementioned intensive parameters. The black bar shows the median result and  $1\sigma$  standard deviation. The bottom three rows are density plots that show the trade offs between the different intensive parameters.

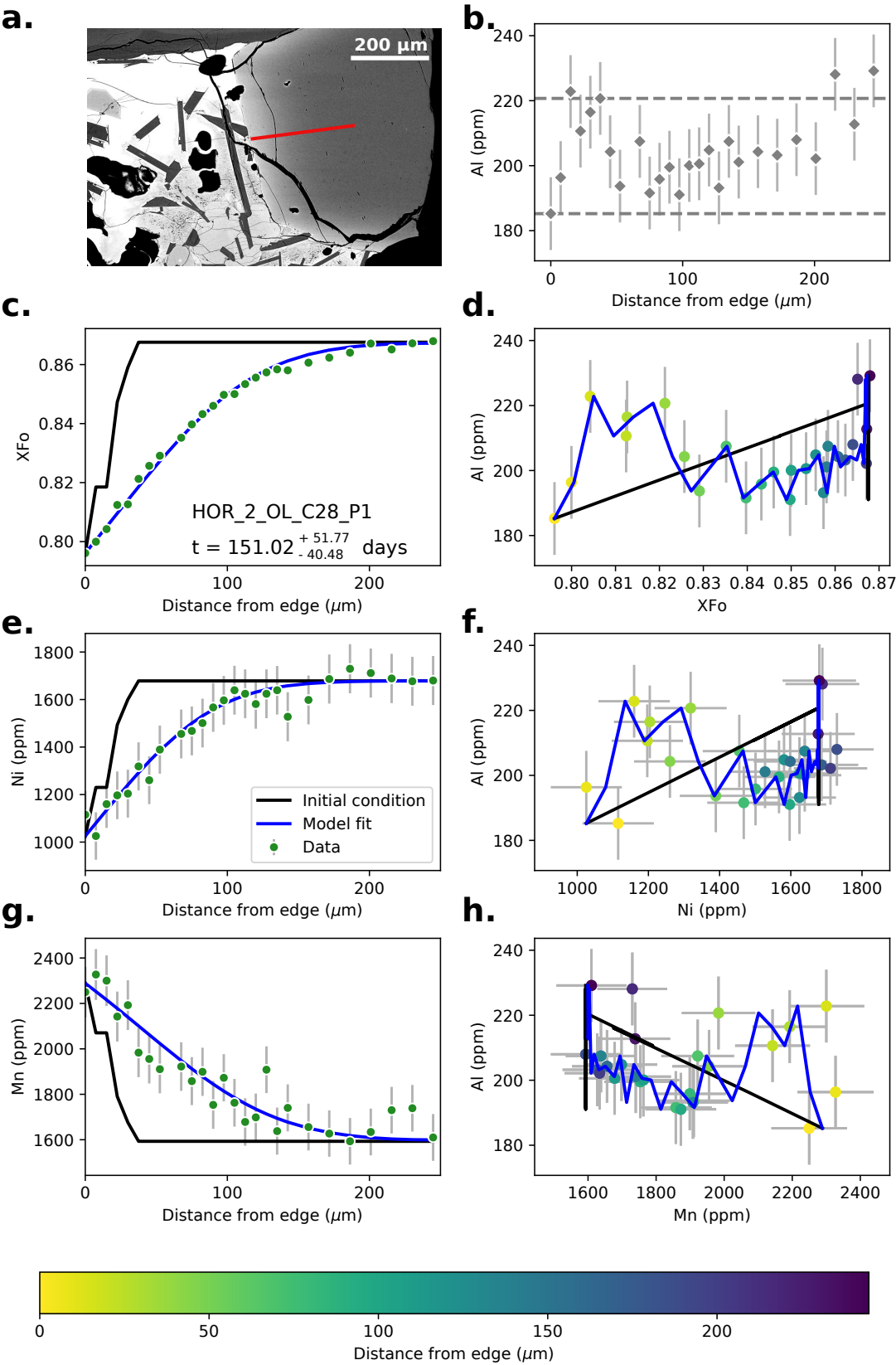


**Figure S31.** Data, initial conditions and model fits for sample HOR\_2\_OL\_C28\_P1. Caption the same as Supplementary Fig. S11.



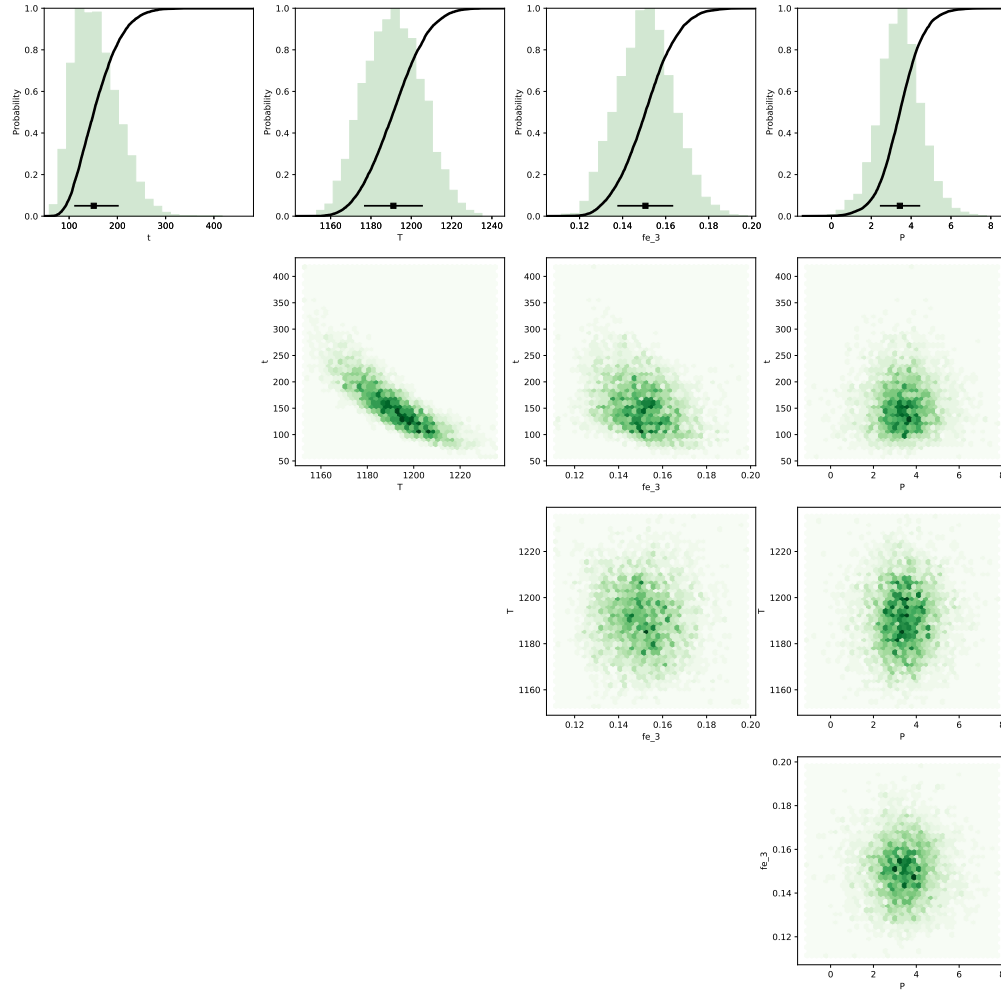


**Figure S32.** Bayesian inversion results for sample HOR\_1\_OL\_C28\_P1. Marginal plot showing the posterior distributions of the Nested Sampling Bayesian Inversion for the main intensive parameters:  $t$  is time (days),  $T$  is temperature ( $^{\circ}\text{C}$ ),  $fe\_3$  is ferric iron content of the melt and  $P$  is pressure (kbar). The top row shows histograms (green bars) and probability density functions (black curves) of the aforementioned intensive parameters. The black bar shows the median result and  $1\sigma$  standard deviation. The bottom three rows are density plots that show the trade offs between the different intensive parameters.

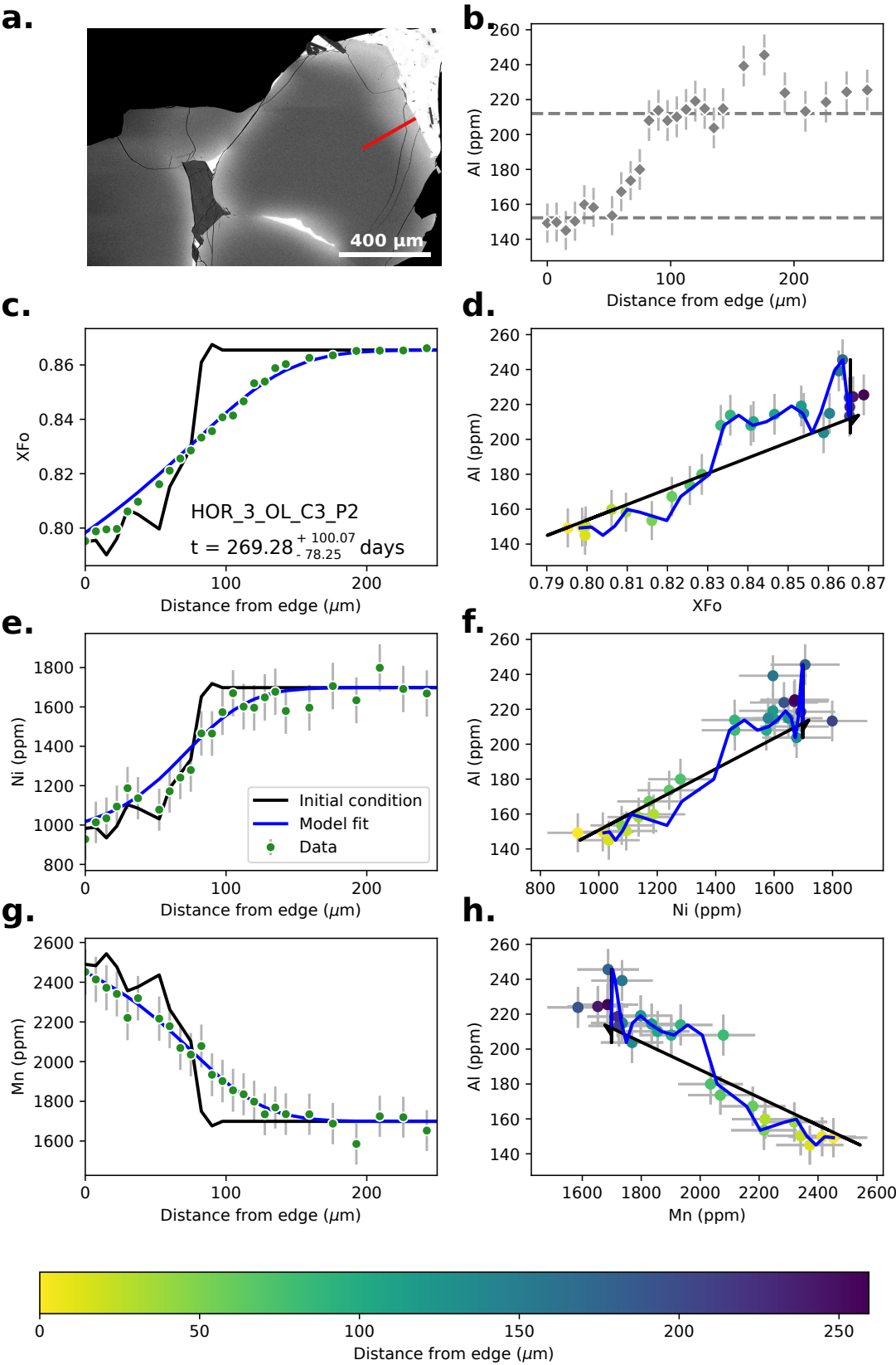


**Figure S33.** Data, initial conditions and model fits for sample HOR\_3\_OL\_C3\_P2. Caption the same as Supplementary Fig. S11.

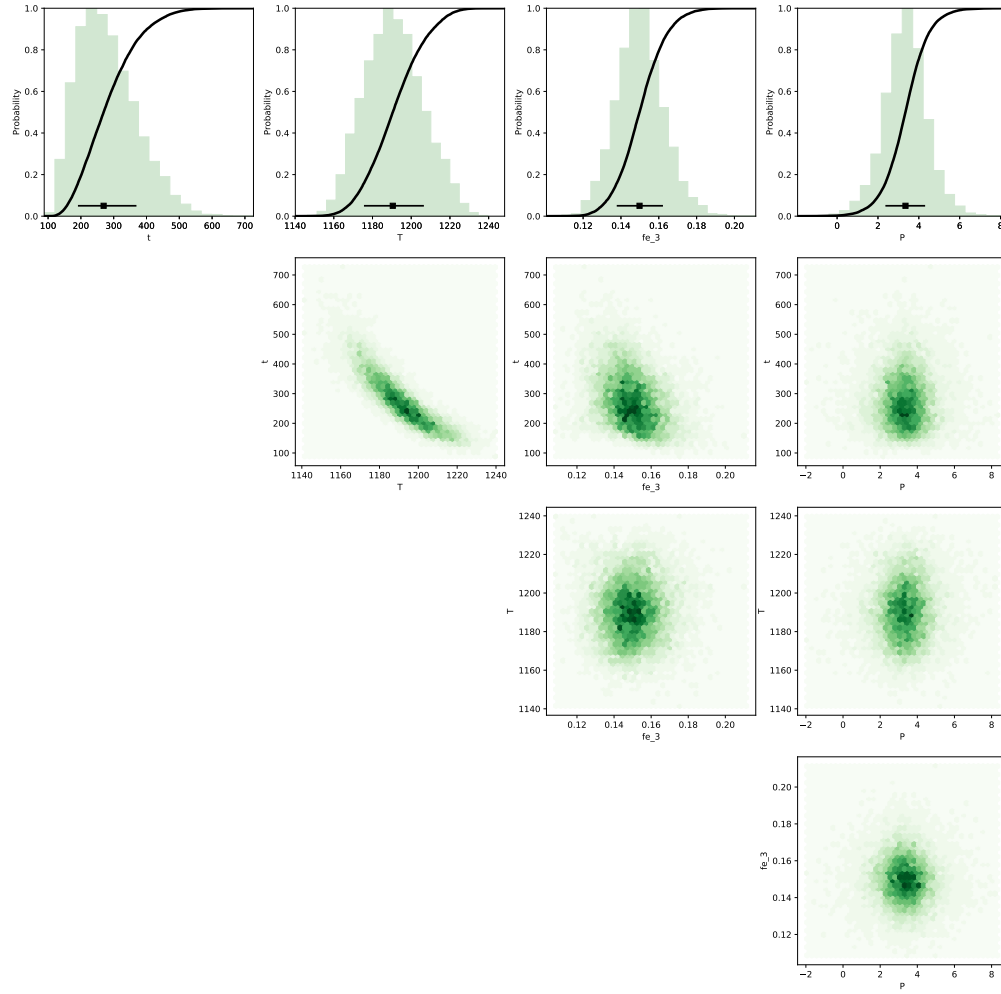


**Figure S34.** Bayesian inversion results for sample HOR\_3\_OL\_C3\_P2. Marginal plot showing the posterior distributions of the Nested Sampling Bayesian Inversion for the main intensive parameters:  $t$  is time (days),  $T$  is temperature ( $^{\circ}\text{C}$ ),  $fe\_3$  is ferric iron content of the melt and  $P$  is pressure (kbar). The top row shows histograms (green bars) and probability density functions (black curves) of the aforementioned intensive parameters. The black bar shows the median result and  $1\sigma$  standard deviation. The bottom three rows are density plots that show the trade offs between the different intensive parameters.

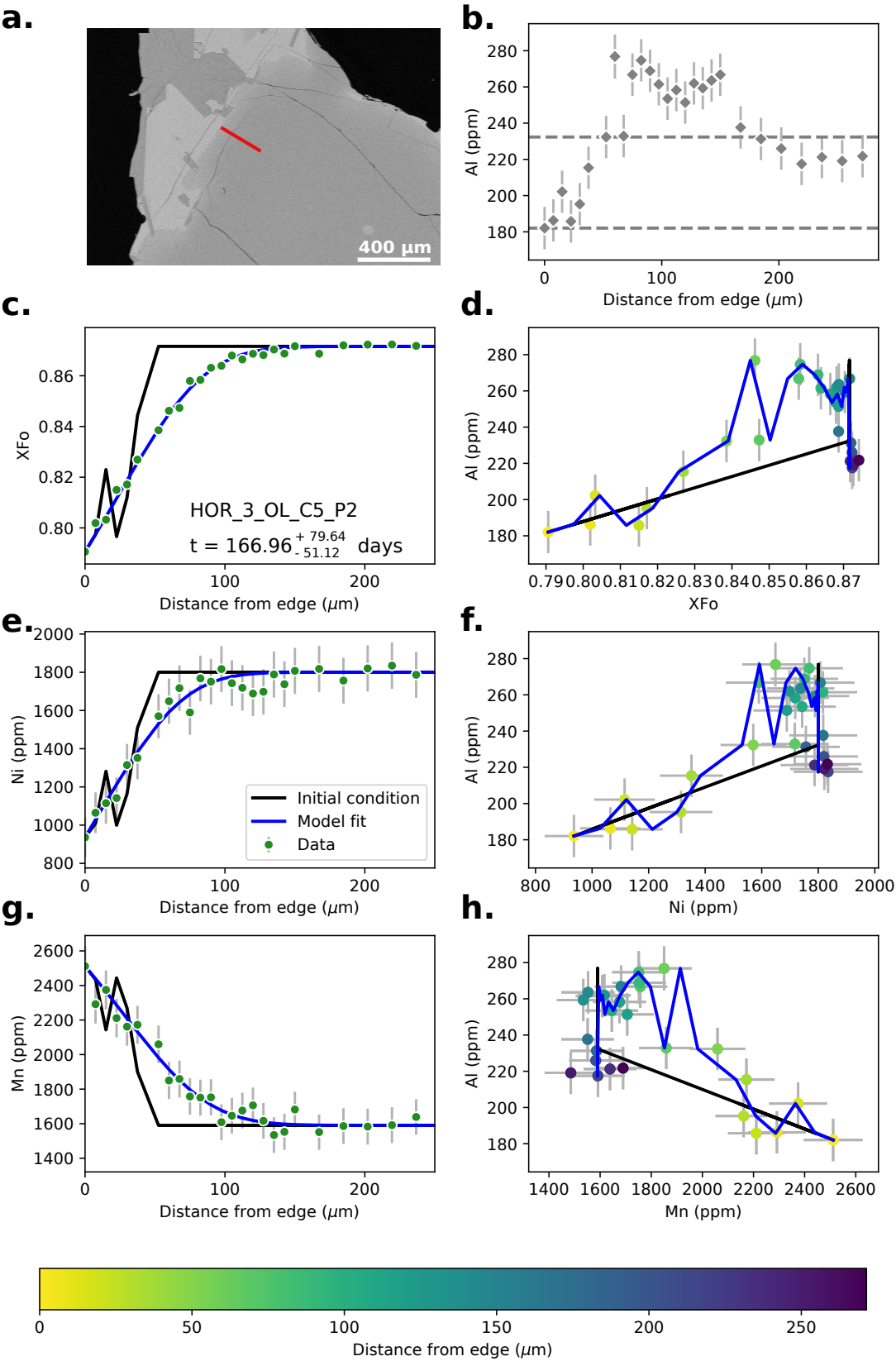


**Figure S35.** Data, initial conditions and model fits for sample HOR\_3\_OL\_C5\_P2. Caption the same as Supplementary Fig. S11.

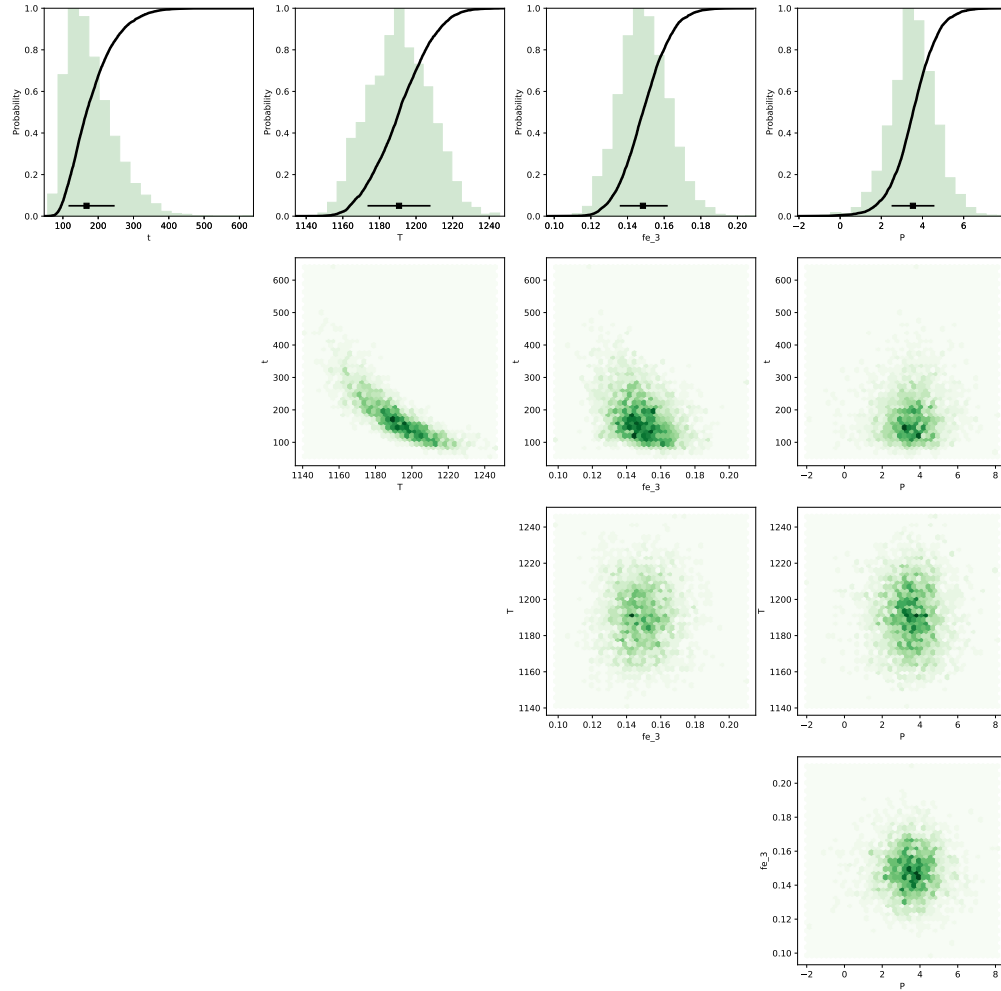


**Figure S36.** Bayesian inversion results for sample HOR\_3\_OL\_C5\_P2. Marginal plot showing the posterior distributions of the Nested Sampling Bayesian Inversion for the main intensive parameters:  $t$  is time (days),  $T$  is temperature ( $^{\circ}\text{C}$ ),  $fe\_3$  is ferric iron content of the melt and  $P$  is pressure (kbar). The top row shows histograms (green bars) and probability density functions (black curves) of the aforementioned intensive parameters. The black bar shows the median result and  $1\sigma$  standard deviation. The bottom three rows are density plots that show the trade offs between the different intensive parameters.

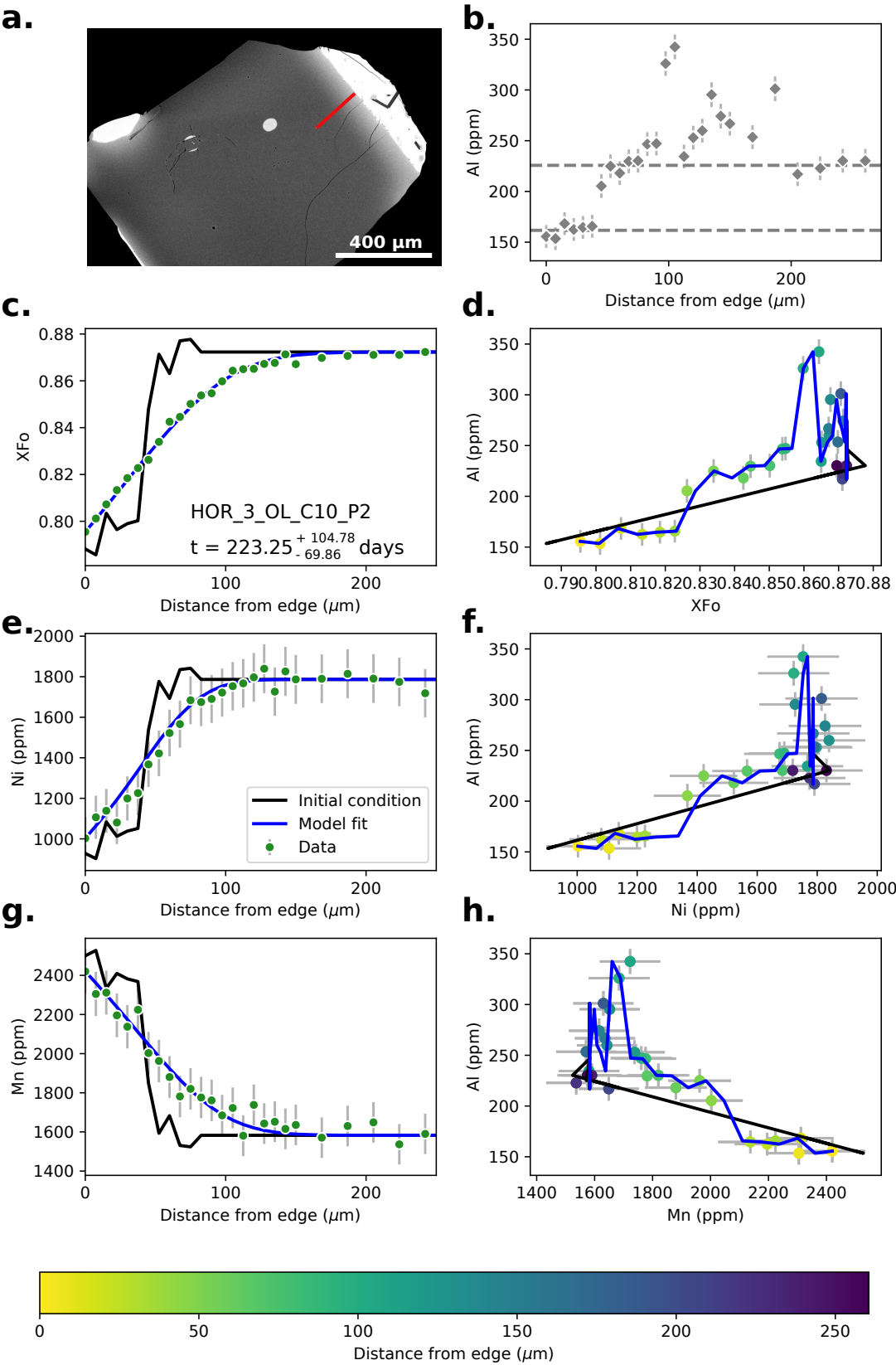


**Figure S37.** Data, initial conditions and model fits for sample HOR\_3\_OL\_C10\_P2. Caption the same as Supplementary Fig. S11.

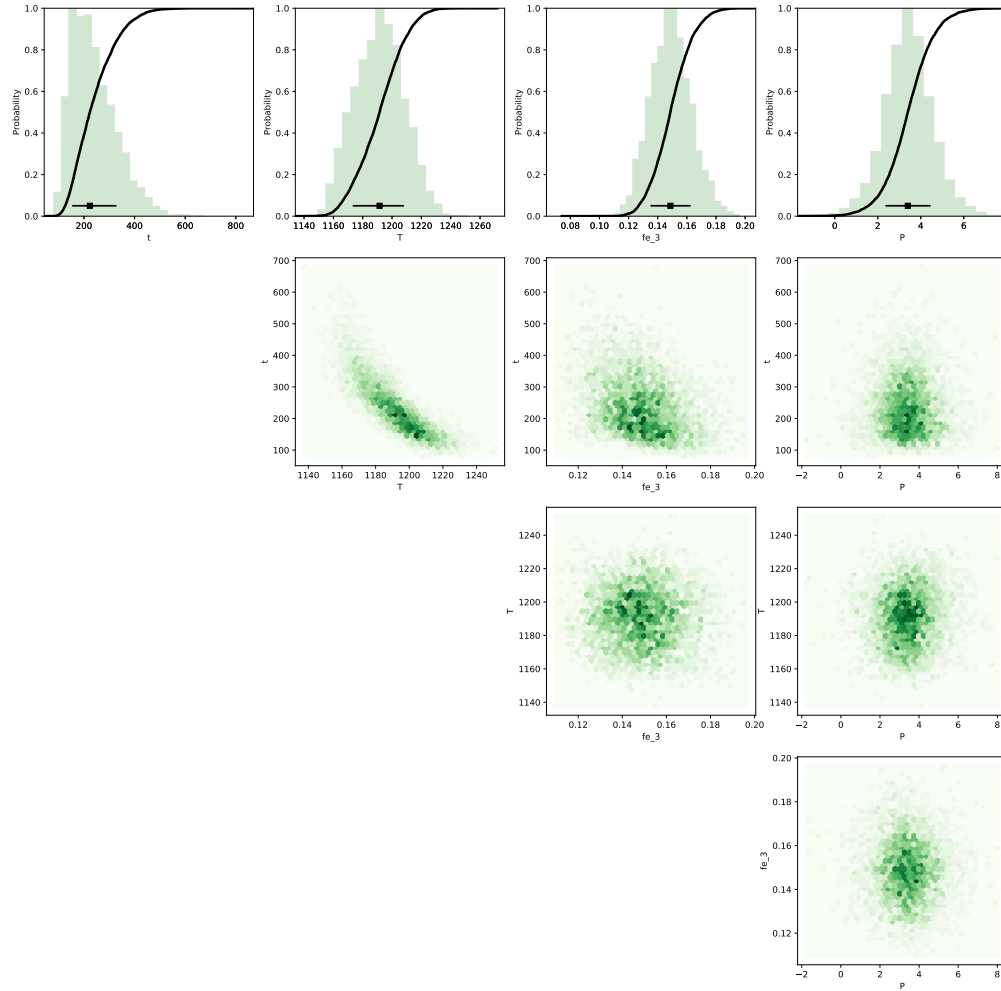


**Figure S38.** Bayesian inversion results for sample HOR\_3\_OL\_C10\_P2. Marginal plot showing the posterior distributions of the Nested Sampling Bayesian Inversion for the main intensive parameters:  $t$  is time (days),  $T$  is temperature ( $^{\circ}\text{C}$ ),  $fe\_3$  is ferric iron content of the melt and  $P$  is pressure (kbar). The top row shows histograms (green bars) and probability density functions (black curves) of the aforementioned intensive parameters. The black bar shows the median result and  $1\sigma$  standard deviation. The bottom three rows are density plots that show the trade offs between the different intensive parameters.



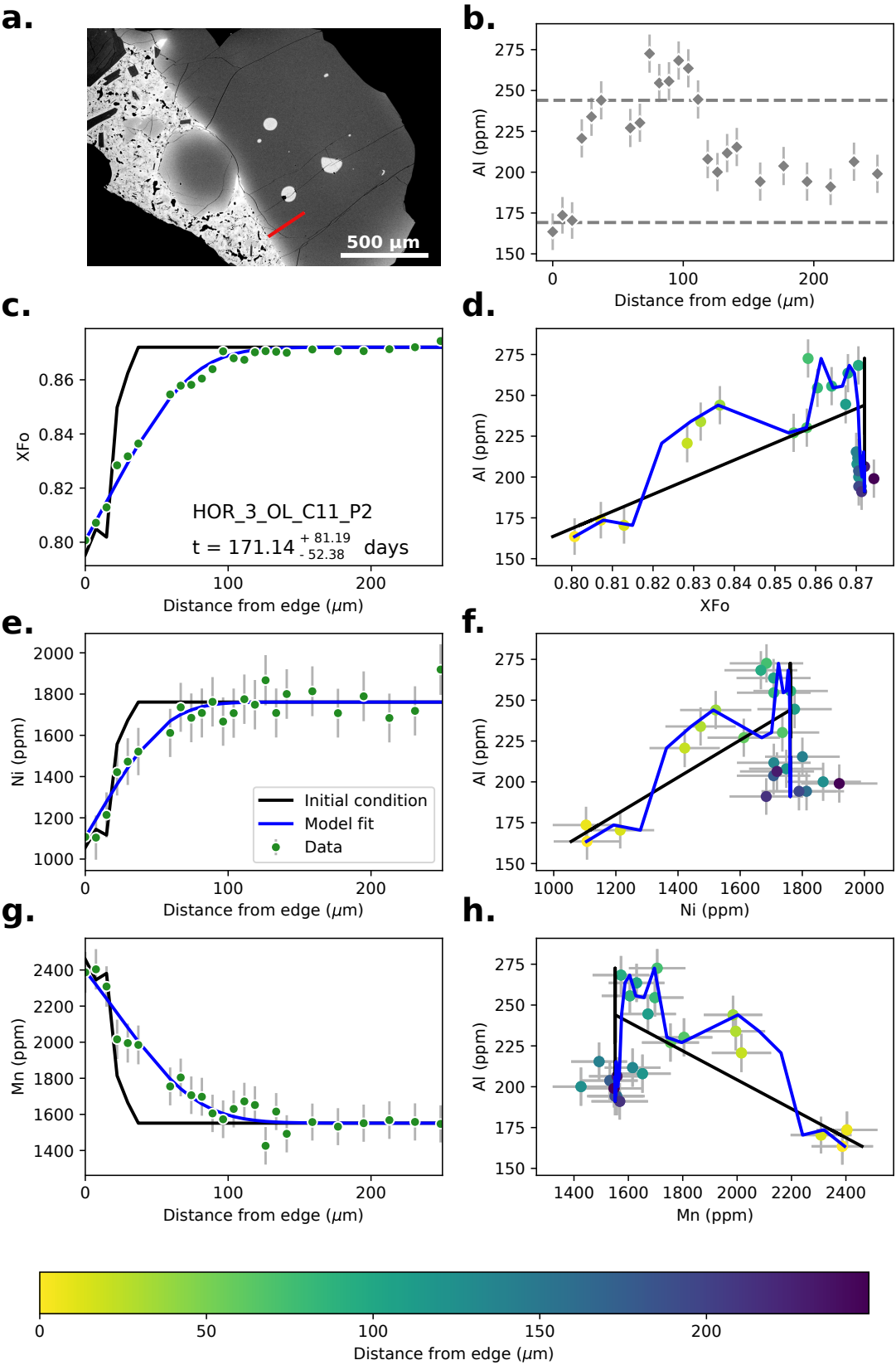


**Figure S39.** Data, initial conditions and model fits for sample HOR\_3\_OL\_C11\_P2. Caption the same as Supplementary Fig. S11.

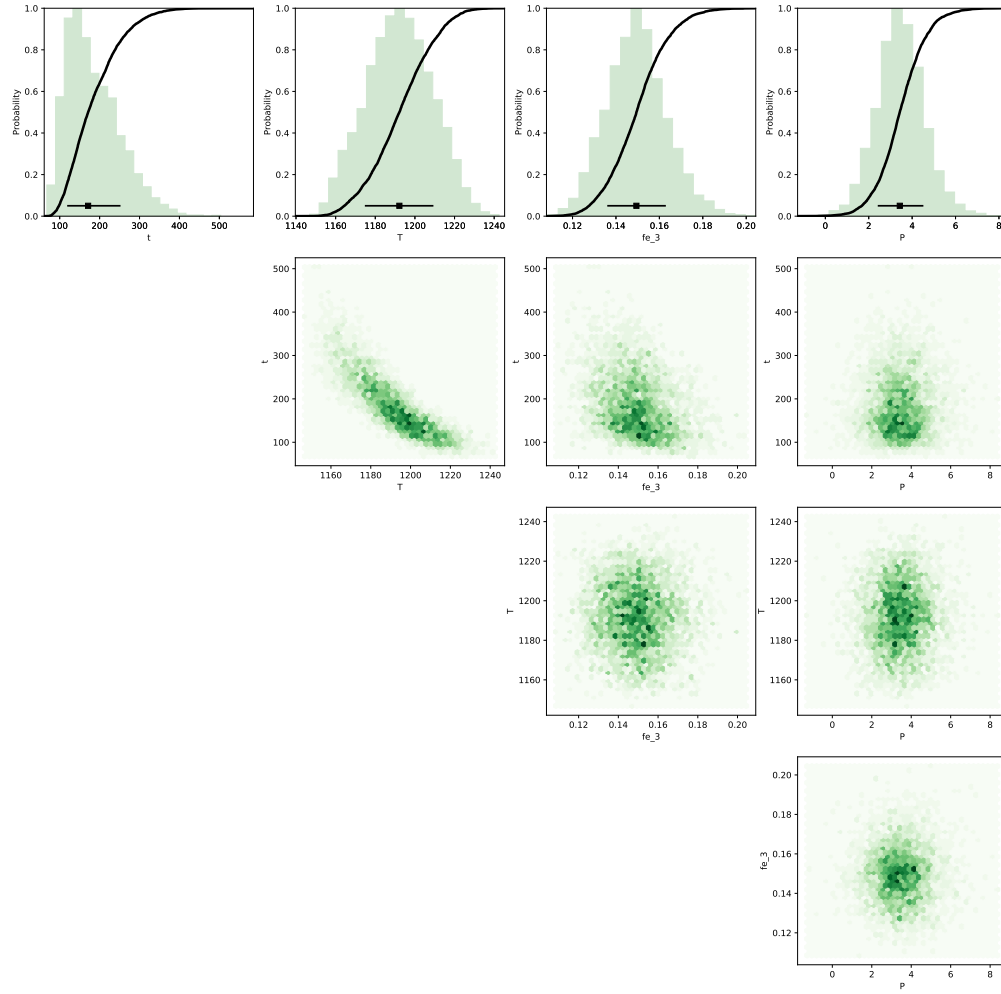


**Figure S40.** Bayesian inversion results for sample HOR\_3\_OL\_C11\_P2. Marginal plot showing the posterior distributions of the Nested Sampling Bayesian Inversion for the main intensive parameters:  $t$  is time (days),  $T$  is temperature ( $^{\circ}\text{C}$ ),  $fe\_3$  is ferric iron content of the melt and  $P$  is pressure (kbar). The top row shows histograms (green bars) and probability density functions (black curves) of the aforementioned intensive parameters. The black bar shows the median result and  $1\sigma$  standard deviation. The bottom three rows are density plots that show the trade offs between the different intensive parameters.

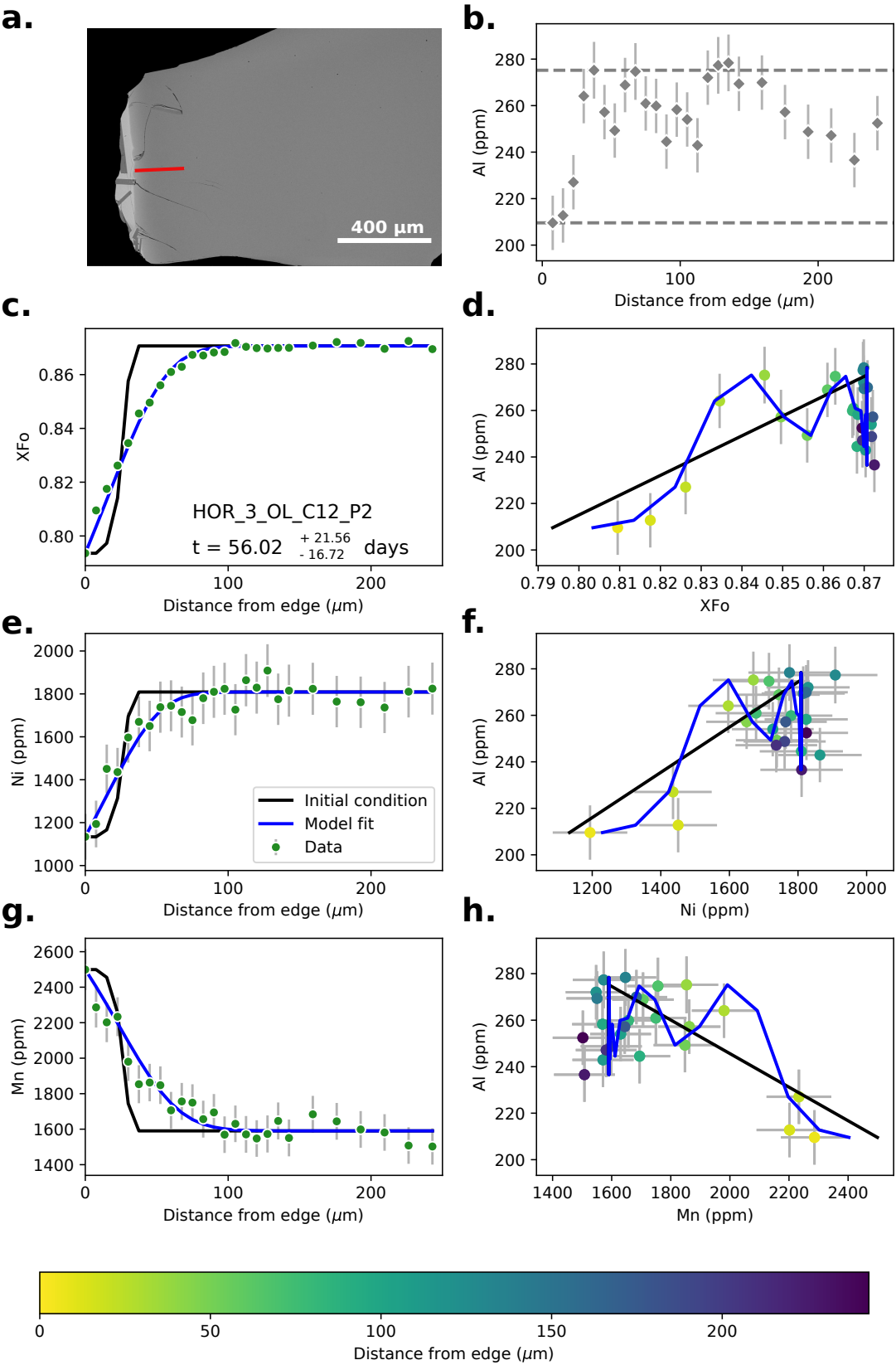


**Figure S41.** Data, initial conditions and model fits for sample HOR\_3\_OL\_C12\_P2. Caption the same as Supplementary Fig. S11.

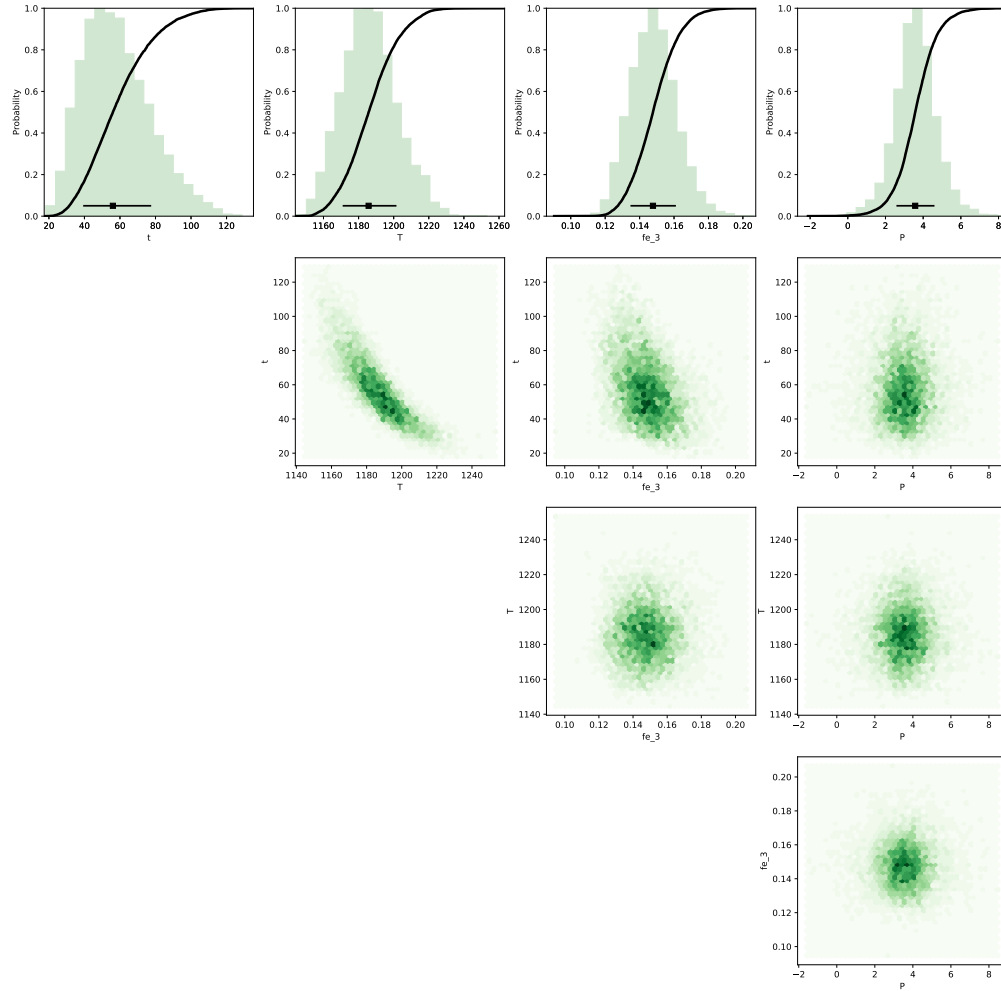


**Figure S42.** Bayesian inversion results for sample HOR\_3\_OL\_C12\_P2. Marginal plot showing the posterior distributions of the Nested Sampling Bayesian Inversion for the main intensive parameters:  $t$  is time (days),  $T$  is temperature ( $^{\circ}\text{C}$ ),  $fe\_3$  is ferric iron content of the melt and  $P$  is pressure (kbar). The top row shows histograms (green bars) and probability density functions (black curves) of the aforementioned intensive parameters. The black bar shows the median result and  $1\sigma$  standard deviation. The bottom three rows are density plots that show the trade offs between the different intensive parameters.

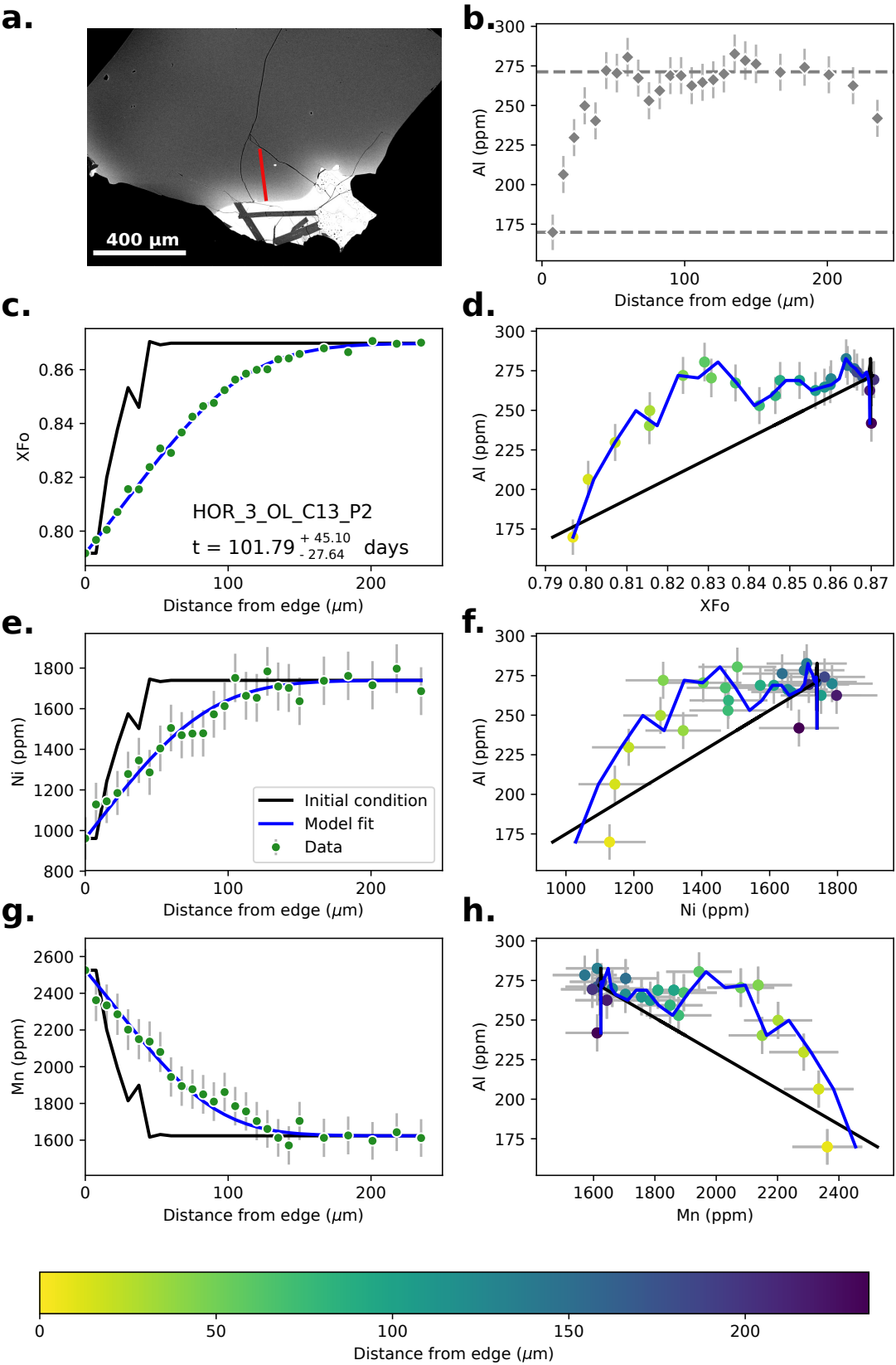


**Figure S43.** Data, initial conditions and model fits for sample HOR\_3\_OL\_C13\_P2. Caption the same as Supplementary Fig. S11.

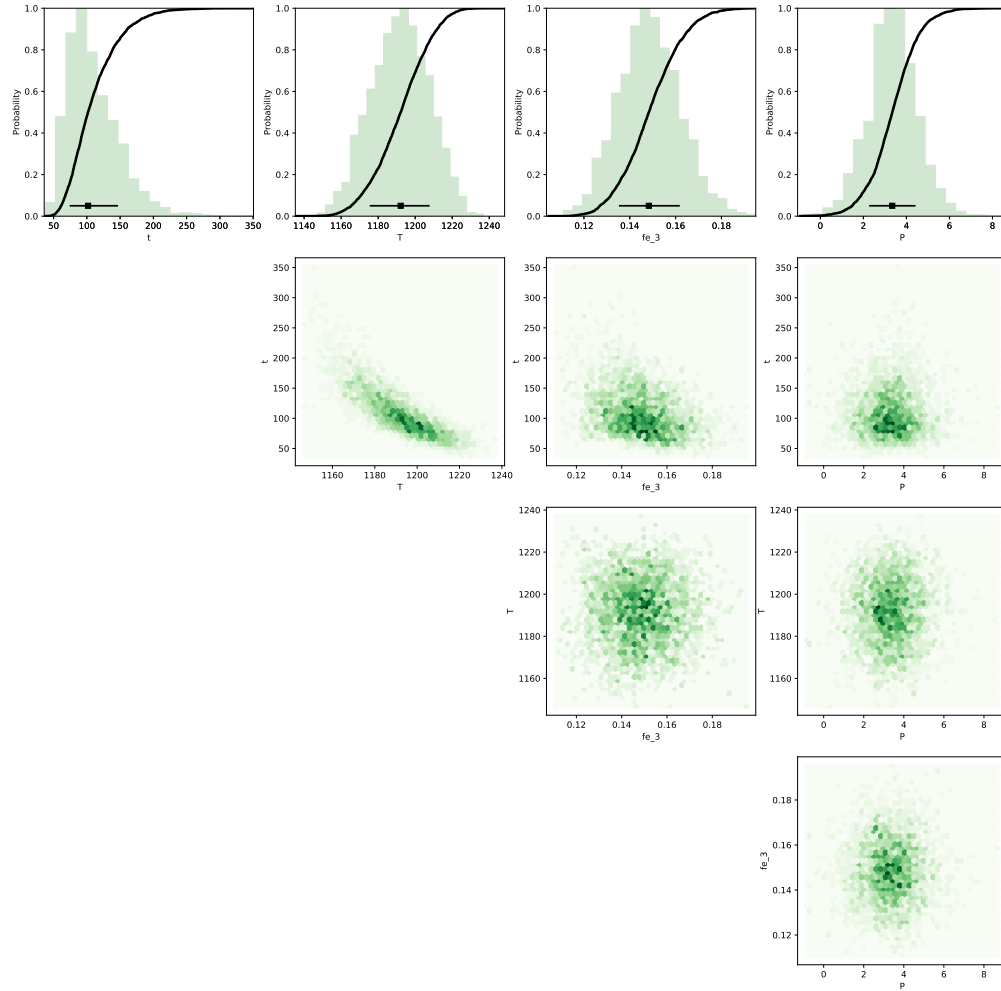


**Figure S44.** Bayesian inversion results for sample HOR\_3\_OL\_C13\_P2. Marginal plot showing the posterior distributions of the Nested Sampling Bayesian Inversion for the main intensive parameters:  $t$  is time (days),  $T$  is temperature ( $^{\circ}\text{C}$ ),  $fe\_3$  is ferric iron content of the melt and  $P$  is pressure (kbar). The top row shows histograms (green bars) and probability density functions (black curves) of the aforementioned intensive parameters. The black bar shows the median result and  $1\sigma$  standard deviation. The bottom three rows are density plots that show the trade offs between the different intensive parameters.

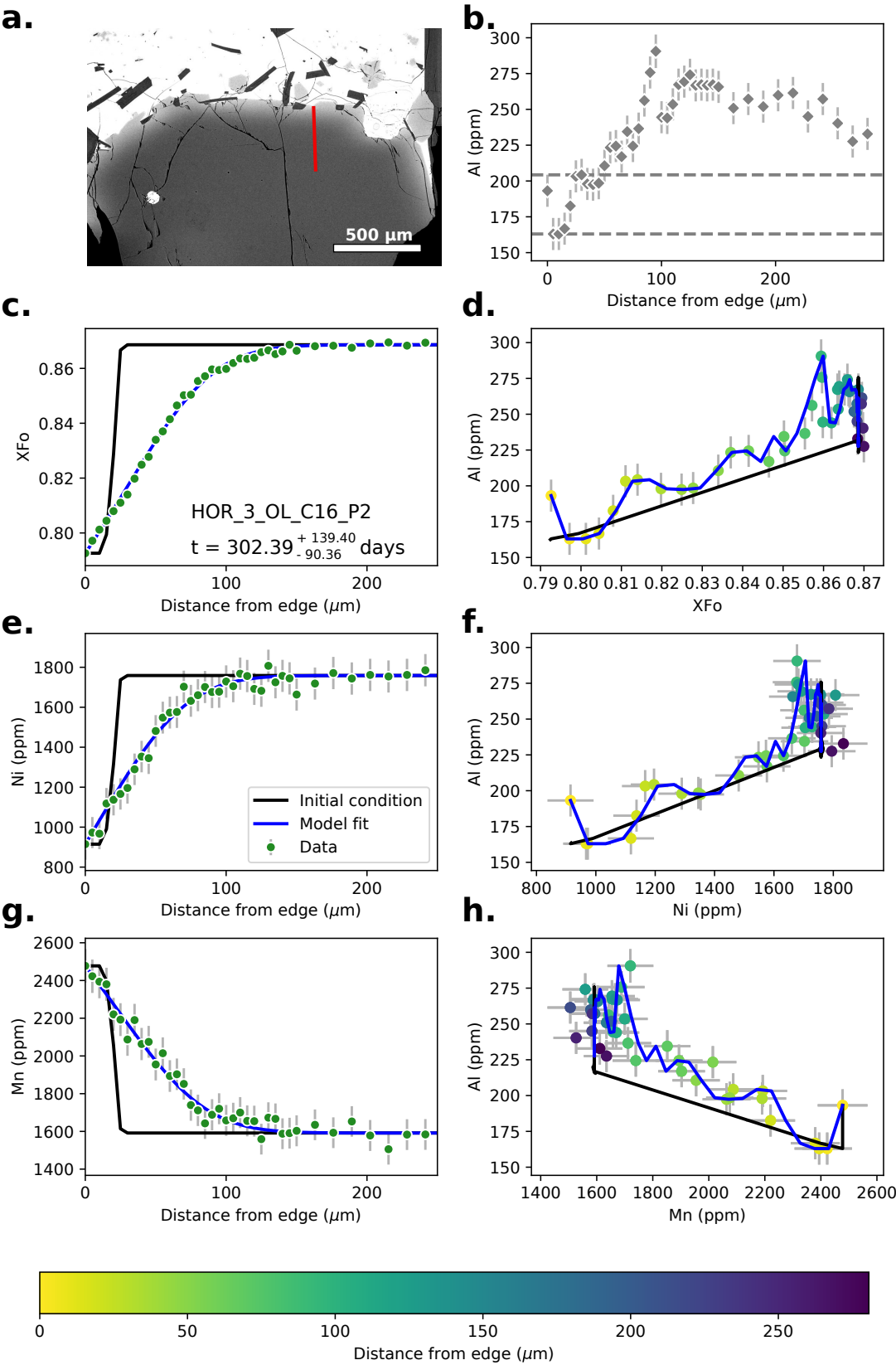


**Figure S45.** Data, initial conditions and model fits for sample HOR\_3\_OL\_C16\_P2. Caption the same as Supplementary Fig. S11.



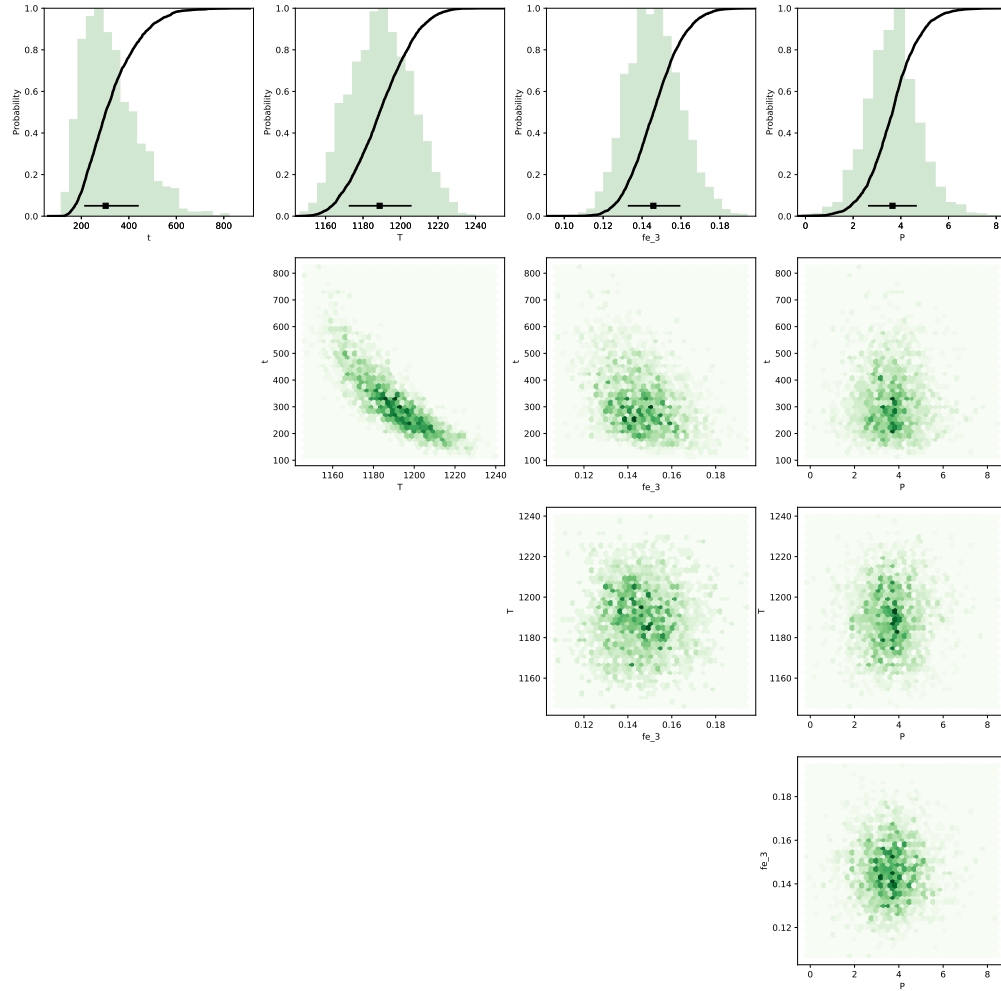


**Figure S46.** Bayesian inversion results for sample HOR\_3\_OL\_C16\_P2. Marginal plot showing the posterior distributions of the Nested Sampling Bayesian Inversion for the main intensive parameters:  $t$  is time (days),  $T$  is temperature ( $^{\circ}\text{C}$ ),  $fe\_3$  is ferric iron content of the melt and  $P$  is pressure (kbar). The top row shows histograms (green bars) and probability density functions (black curves) of the aforementioned intensive parameters. The black bar shows the median result and  $1\sigma$  standard deviation. The bottom three rows are density plots that show the trade offs between the different intensive parameters.

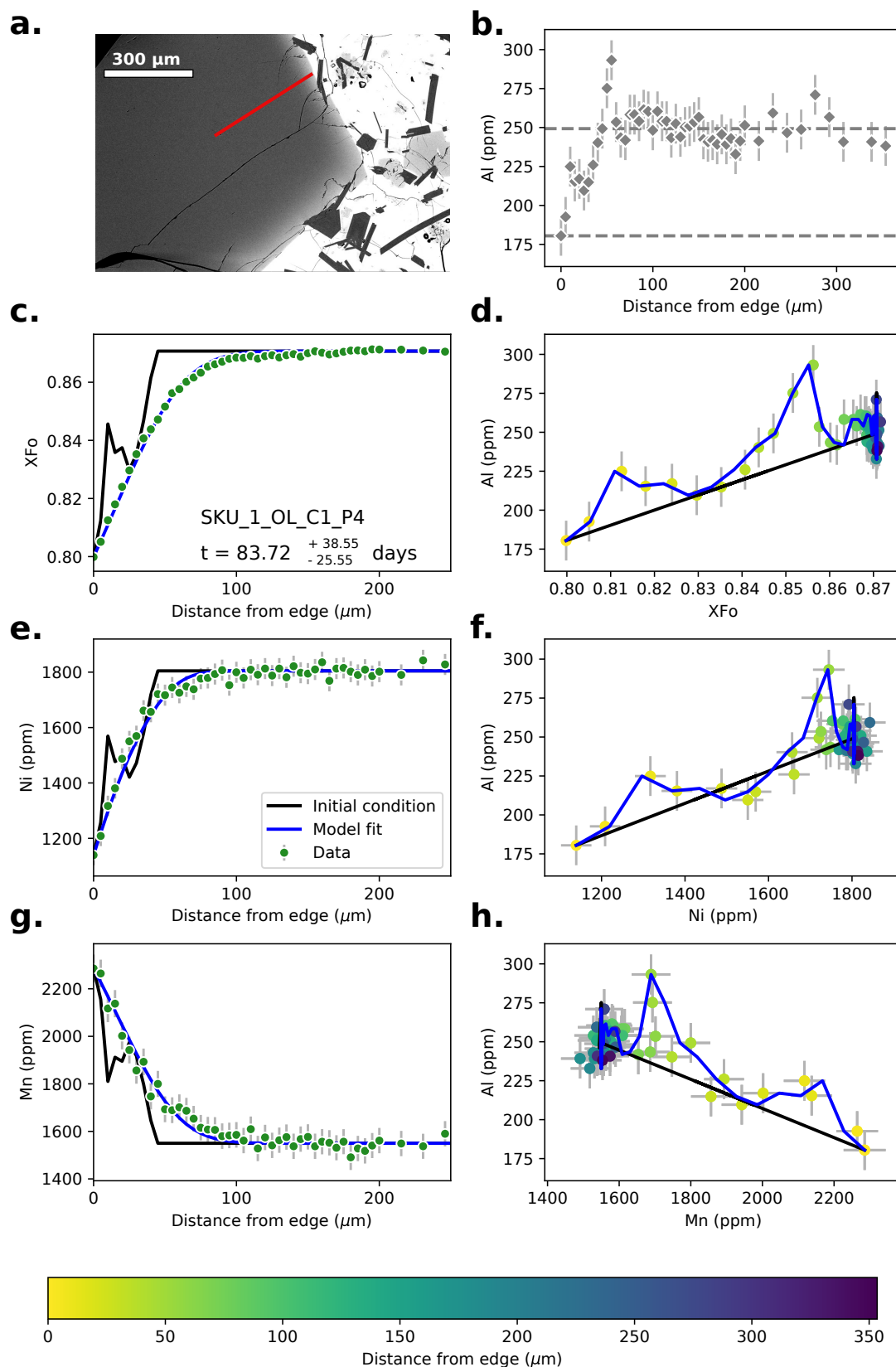


**Figure S47.** Data, initial conditions and model fits for sample SKU\_1\_OL\_C1\_P4. Caption the same as Supplementary Fig. S11.

July 16, 2020, 11:34pm

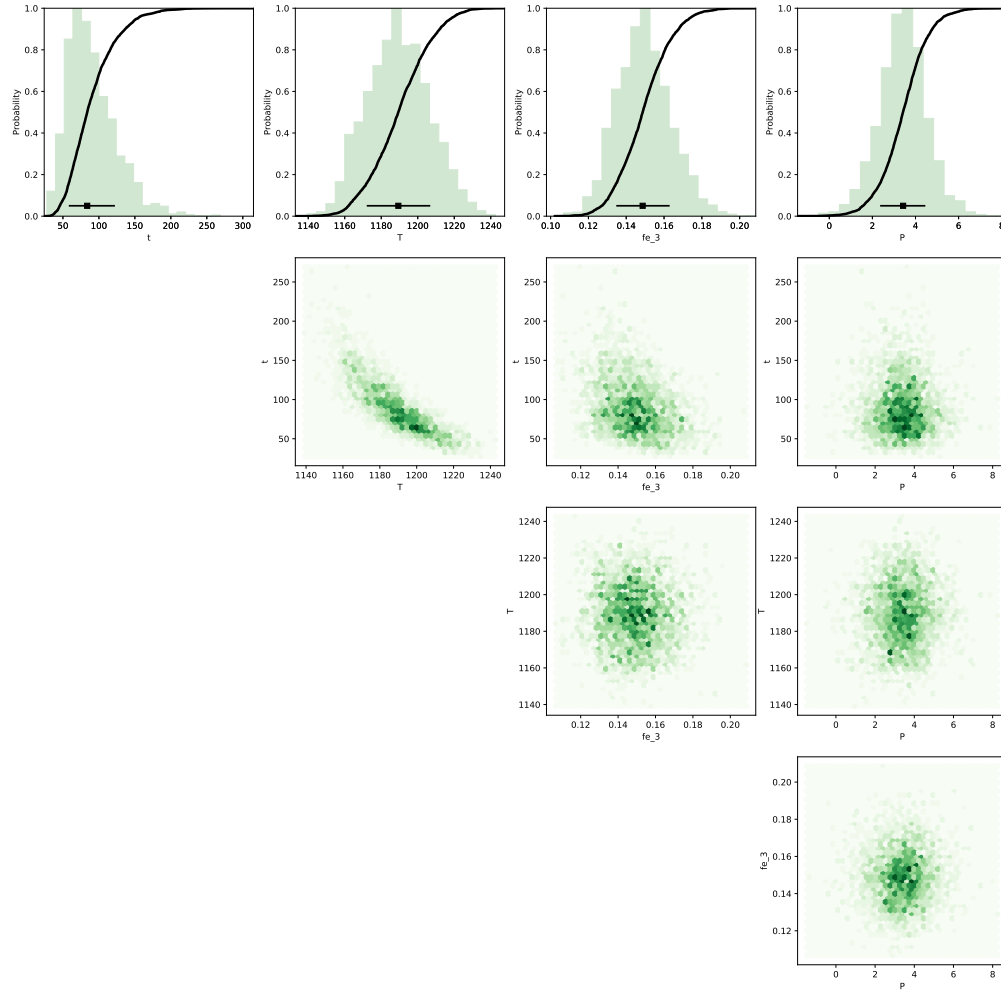


**Figure S48.** Bayesian inversion results for sample SKU\_1\_OL\_C1\_P4. Marginal plot showing the posterior distributions of the Nested Sampling Bayesian Inversion for the main intensive parameters:  $t$  is time (days),  $T$  is temperature ( $^{\circ}\text{C}$ ),  $fe\_3$  is ferric iron content of the melt and  $P$  is pressure (kbar). The top row shows histograms (green bars) and probability density functions (black curves) of the aforementioned intensive parameters. The black bar shows the median result and  $1\sigma$  standard deviation. The bottom three rows are density plots that show the trade offs between the different intensive parameters.

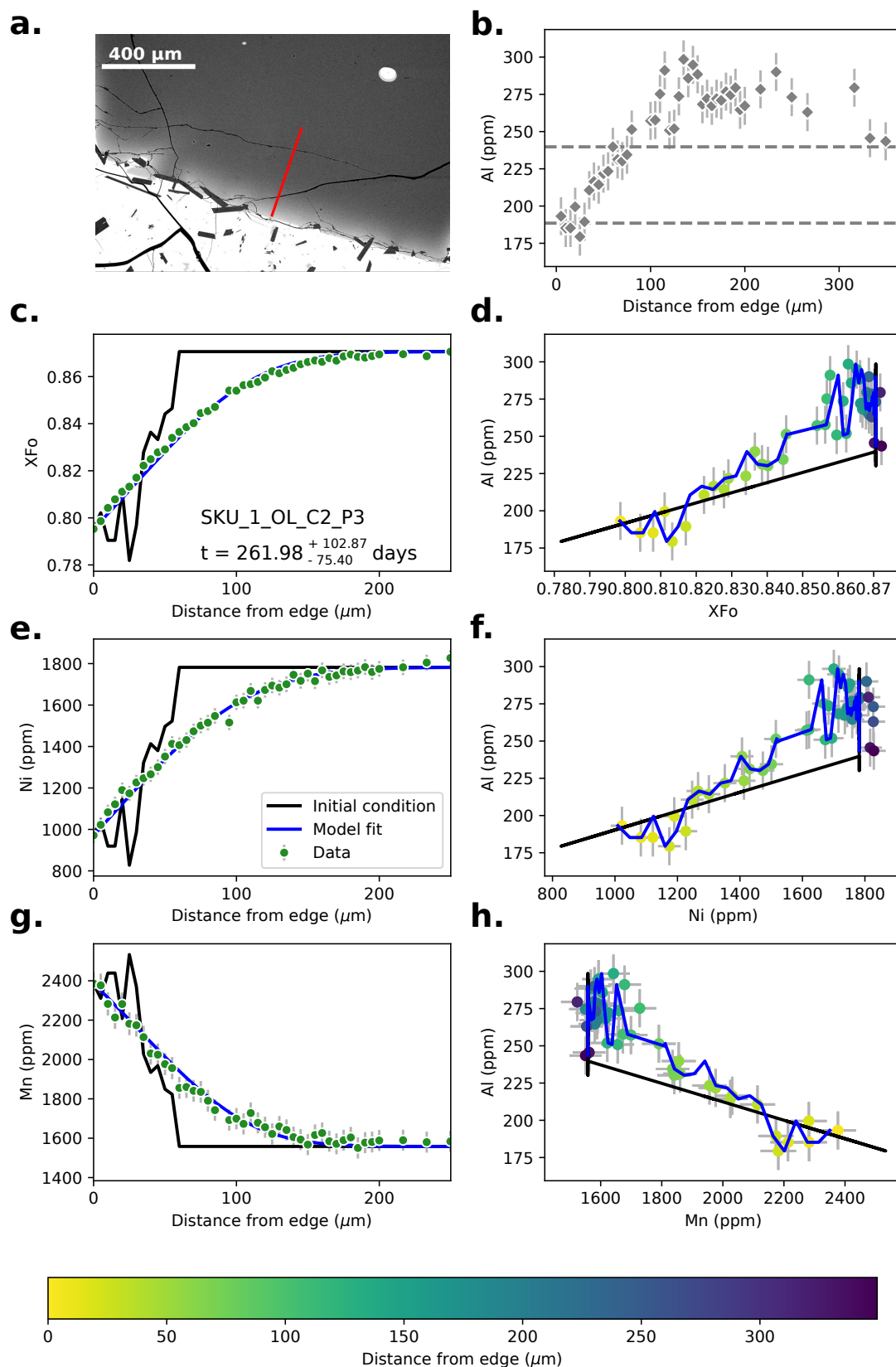


**Figure S49.** Data, initial conditions and model fits for sample SKU\_1\_OL\_C2\_P3. Caption the same as Supplementary Fig. S11.

July 16, 2020, 11:34pm

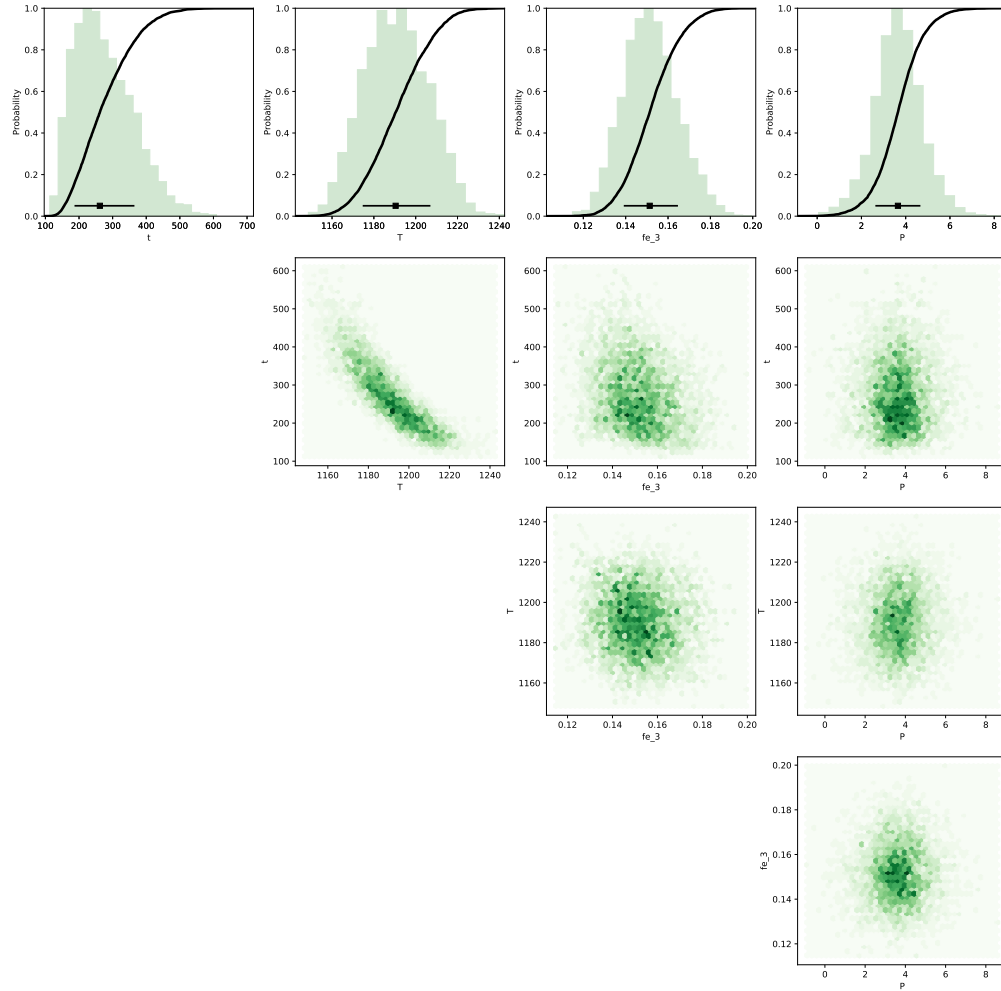


**Figure S50.** Bayesian inversion results for sample SKU\_1\_OL\_C2\_P3. Marginal plot showing the posterior distributions of the Nested Sampling Bayesian Inversion for the main intensive parameters:  $t$  is time (days),  $T$  is temperature ( $^{\circ}\text{C}$ ),  $fe\_3$  is ferric iron content of the melt and  $P$  is pressure (kbar). The top row shows histograms (green bars) and probability density functions (black curves) of the aforementioned intensive parameters. The black bar shows the median result and  $1\sigma$  standard deviation. The bottom three rows are density plots that show the trade offs between the different intensive parameters.

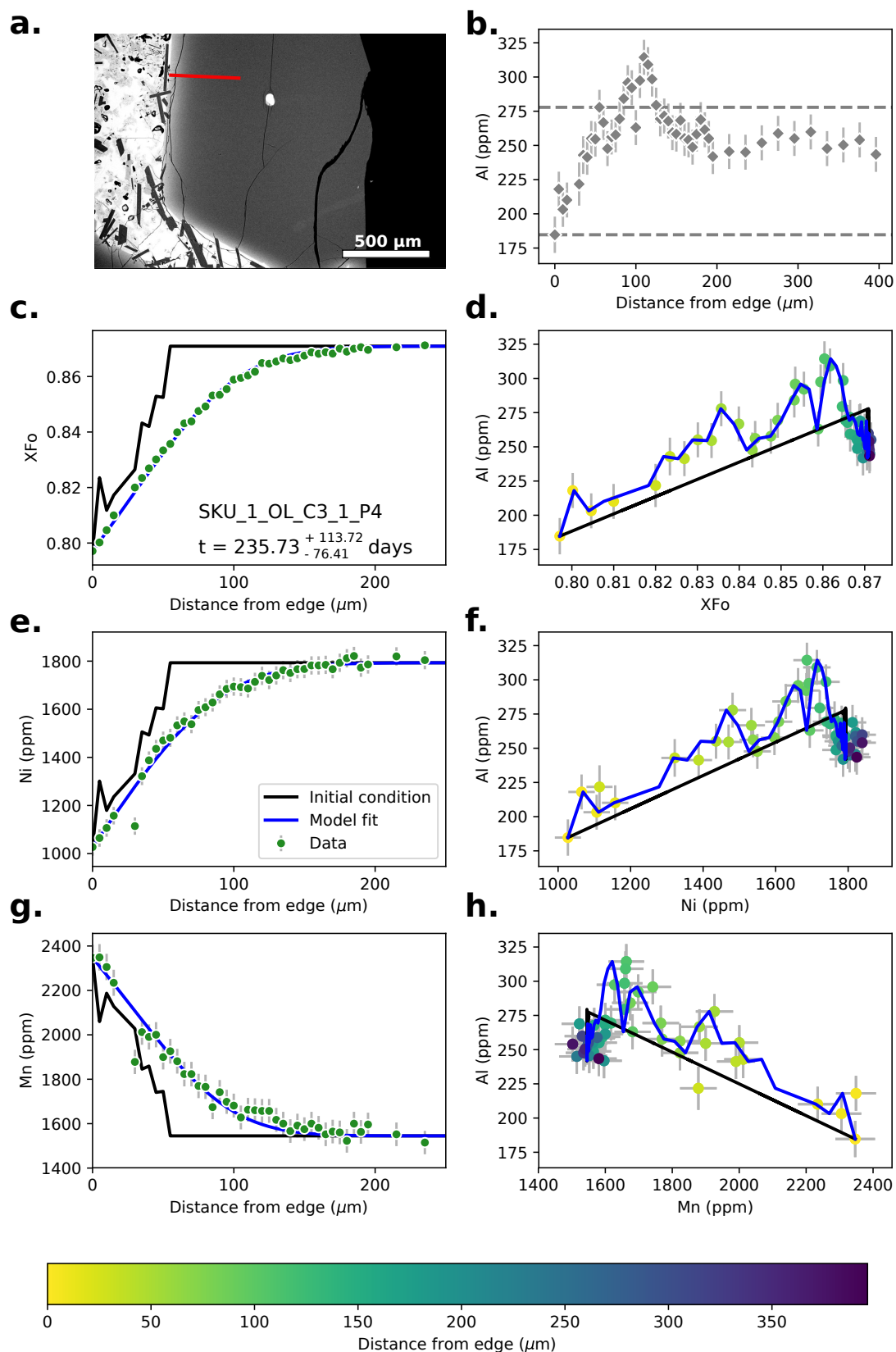


**Figure S51.** Data, initial conditions and model fits for sample SKU\_1\_OL\_C3\_1\_P4.

Caption the same as Supplementary Fig. S11.

July 16, 2020, 11:34pm

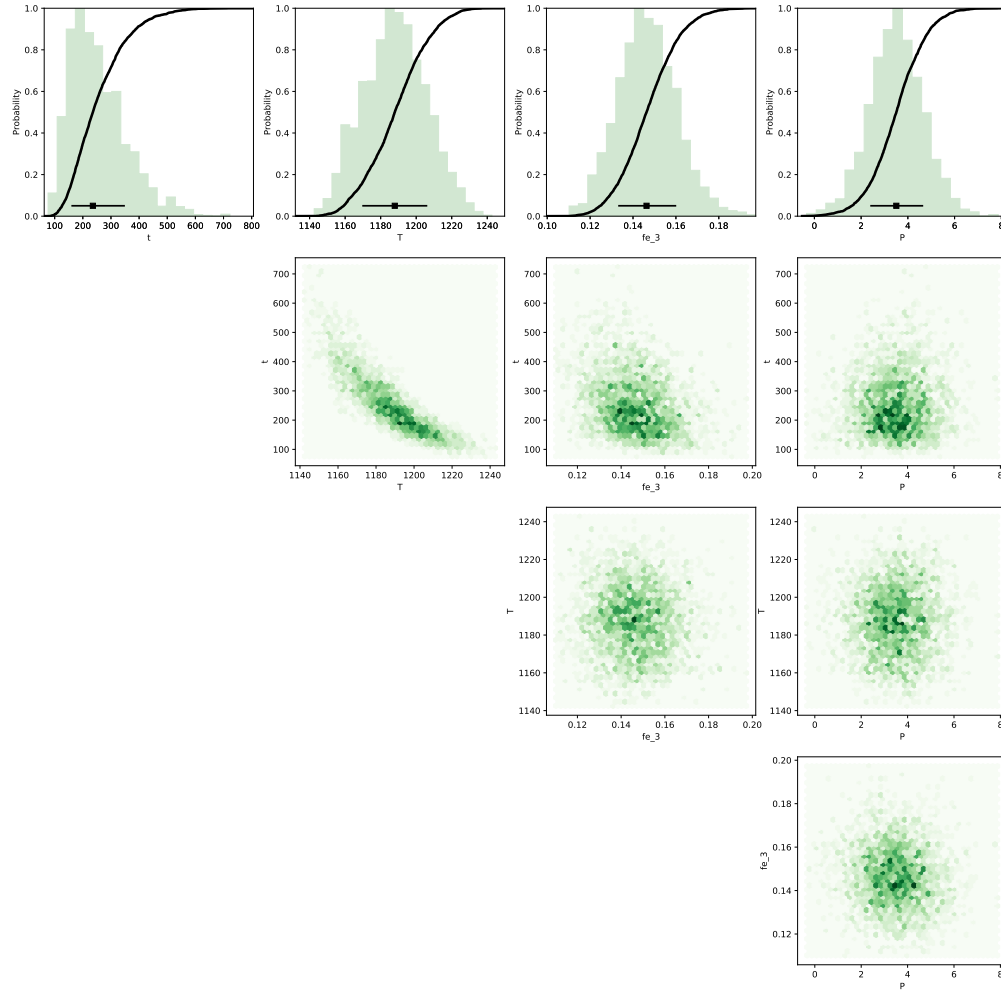


**Figure S52.** Bayesian inversion results for sample SKU\_1\_OL\_C3\_1\_P4. Marginal plot showing the posterior distributions of the Nested Sampling Bayesian Inversion for the main intensive parameters:  $t$  is time (days),  $T$  is temperature ( $^{\circ}\text{C}$ ),  $fe\_3$  is ferric iron content of the melt and  $P$  is pressure (kbar). The top row shows histograms (green bars) and probability density functions (black curves) of the aforementioned intensive parameters. The black bar shows the median result and  $1\sigma$  standard deviation. The bottom three rows are density plots that show the trade offs between the different intensive parameters.

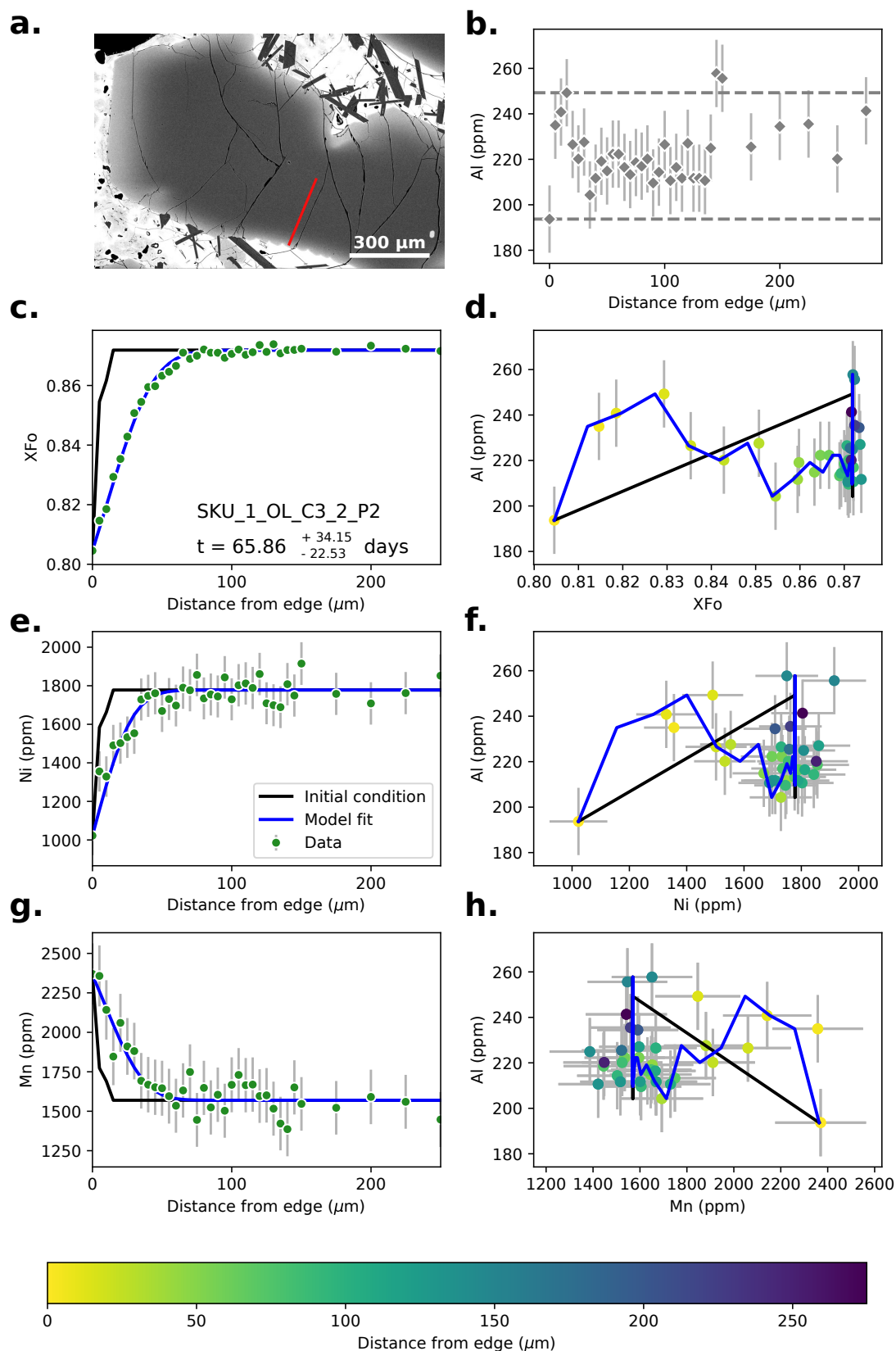


**Figure S53.** Data, initial conditions and model fits for sample SKU\_1\_OL\_C3\_2\_P2.

Caption the same as Supplementary Fig. S11.

July 16, 2020, 11:34pm



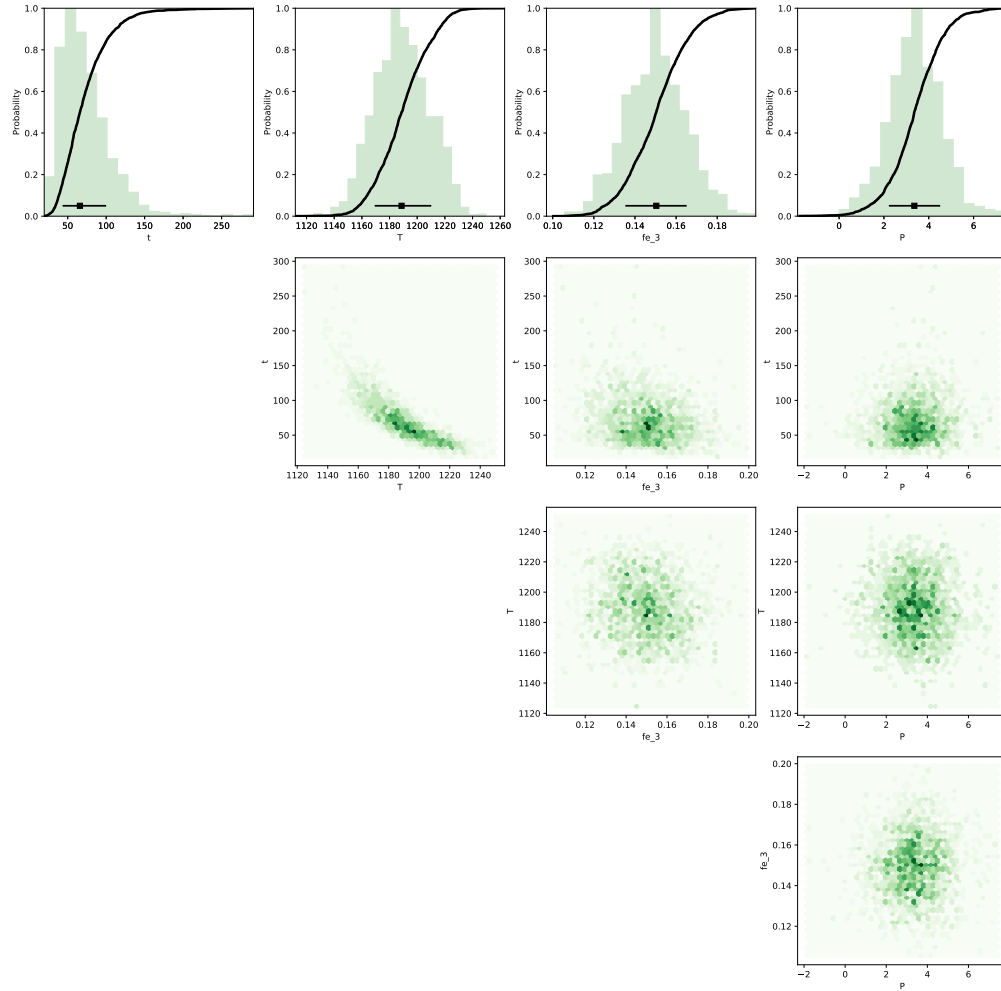


**Figure S54.** Bayesian inversion results for sample SKU\_1\_OL\_C3\_2\_P2. Marginal plot showing the posterior distributions of the Nested Sampling Bayesian Inversion for the main intensive parameters:  $t$  is time (days),  $T$  is temperature ( $^{\circ}\text{C}$ ),  $fe\_3$  is ferric iron content of the melt and  $P$  is pressure (kbar). The top row shows histograms (green bars) and probability density functions (black curves) of the aforementioned intensive parameters. The black bar shows the median result and  $1\sigma$  standard deviation. The bottom three rows are density plots that show the trade offs between the different intensive parameters.

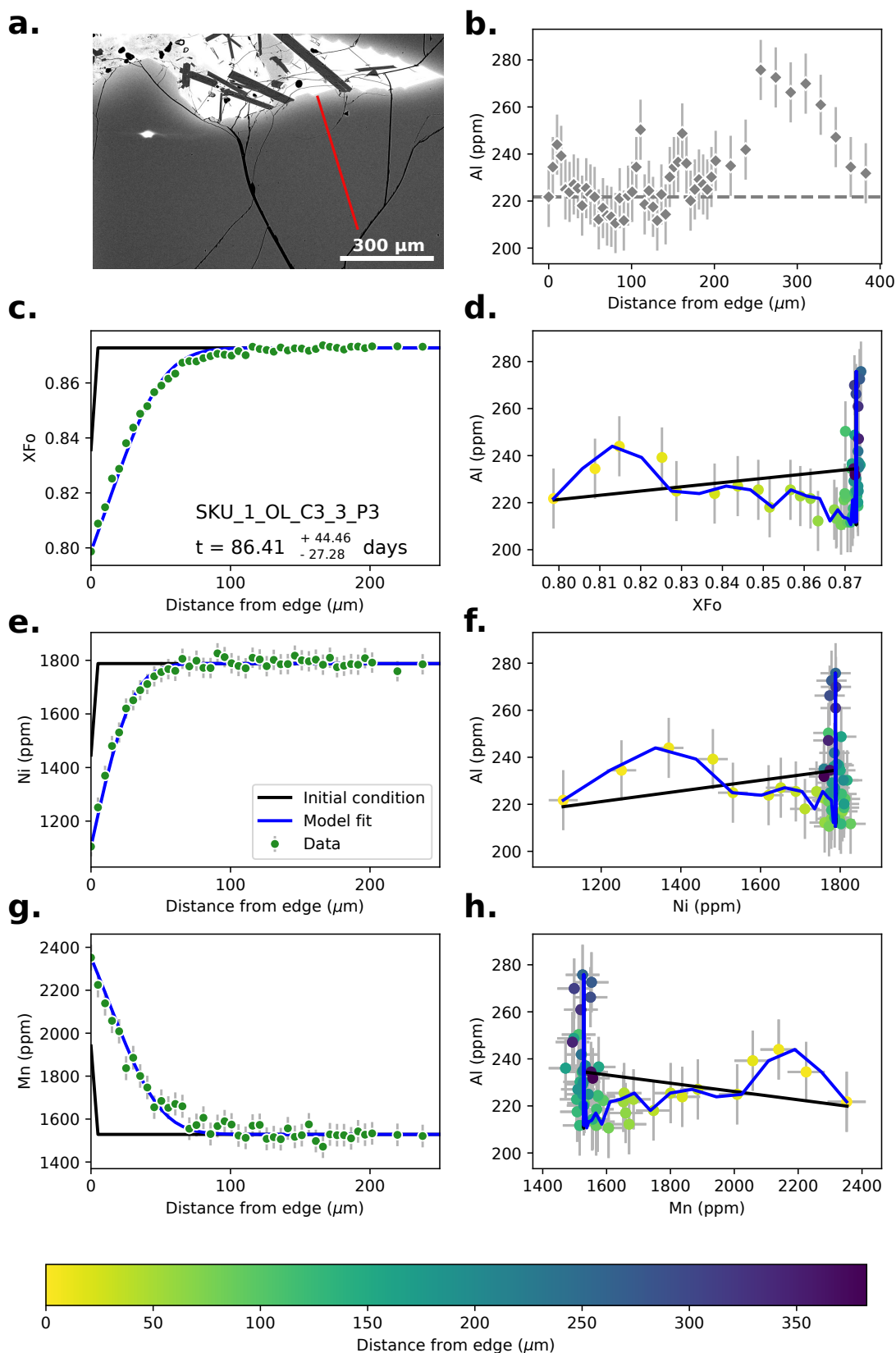


**Figure S55.** Data, initial conditions and model fits for sample SKU\_1\_OL\_C3\_3\_P3.

Caption the same as Supplementary Fig. S11.

July 16, 2020, 11:34pm

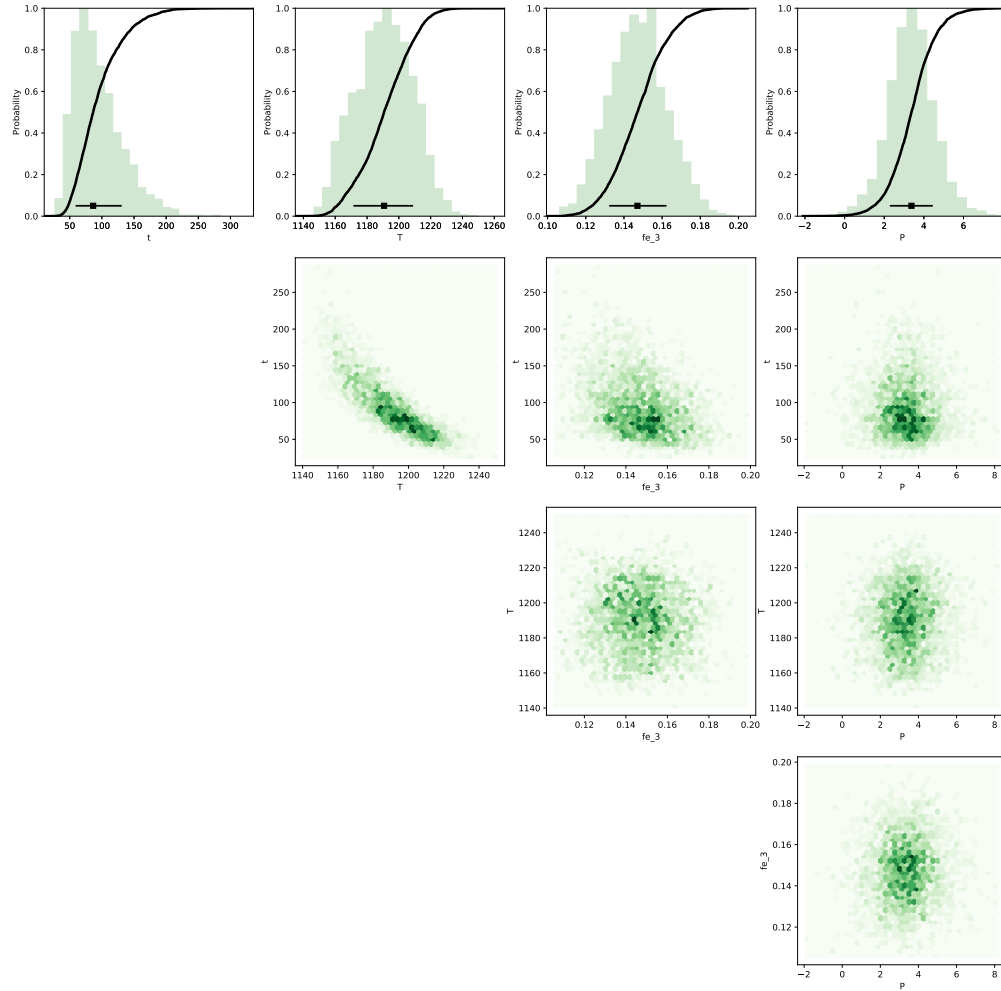


**Figure S56.** Bayesian inversion results for sample SKU\_1\_OL\_C3\_3\_P3. Marginal plot showing the posterior distributions of the Nested Sampling Bayesian Inversion for the main intensive parameters:  $t$  is time (days),  $T$  is temperature ( $^{\circ}\text{C}$ ),  $fe\_3$  is ferric iron content of the melt and  $P$  is pressure (kbar). The top row shows histograms (green bars) and probability density functions (black curves) of the aforementioned intensive parameters. The black bar shows the median result and  $1\sigma$  standard deviation. The bottom three rows are density plots that show the trade offs between the different intensive parameters.

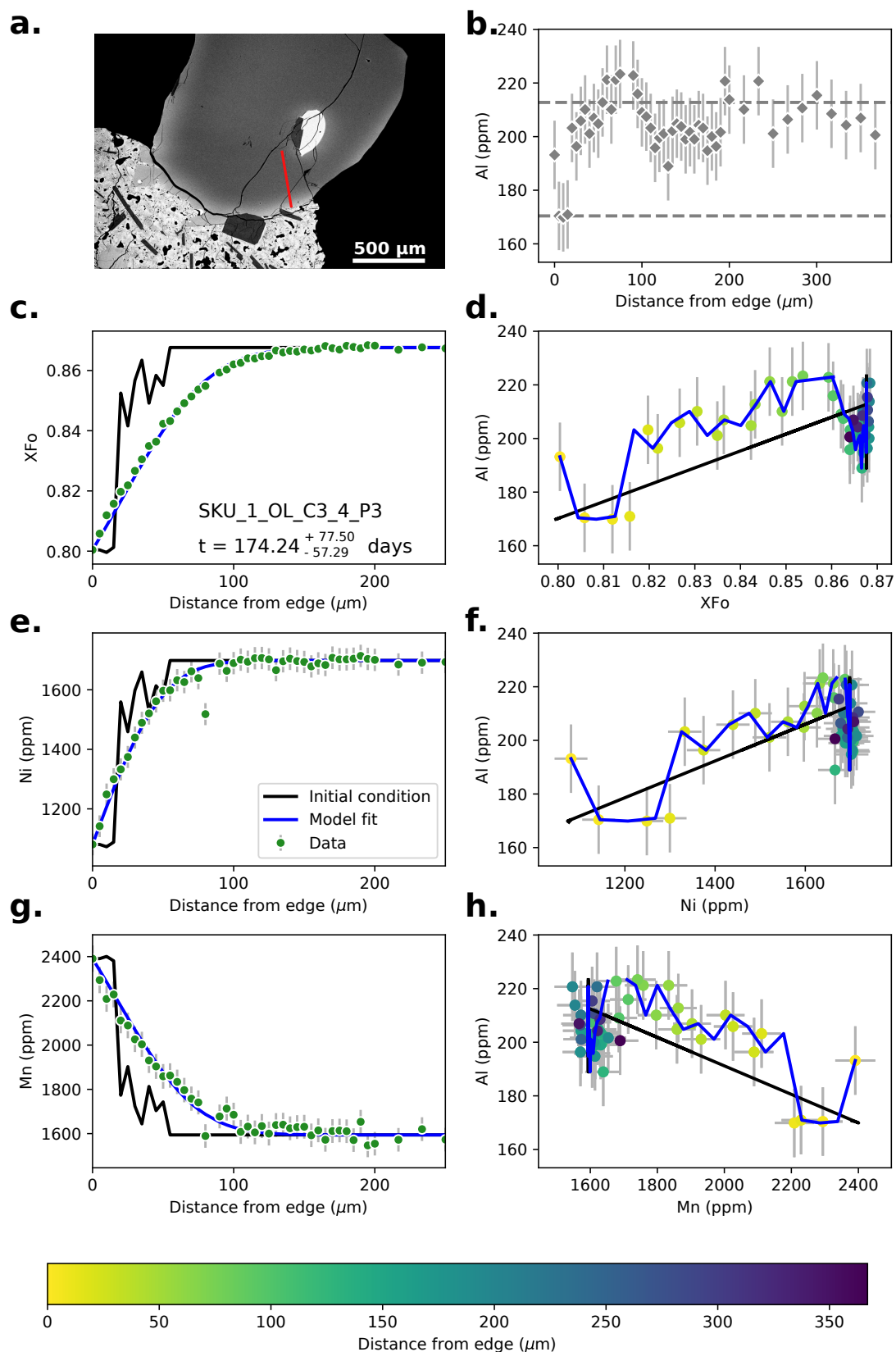


**Figure S57.** Data, initial conditions and model fits for sample SKU\_1\_OL\_C3\_4\_P3.

Caption the same as Supplementary Fig. S11.

July 16, 2020, 11:34pm

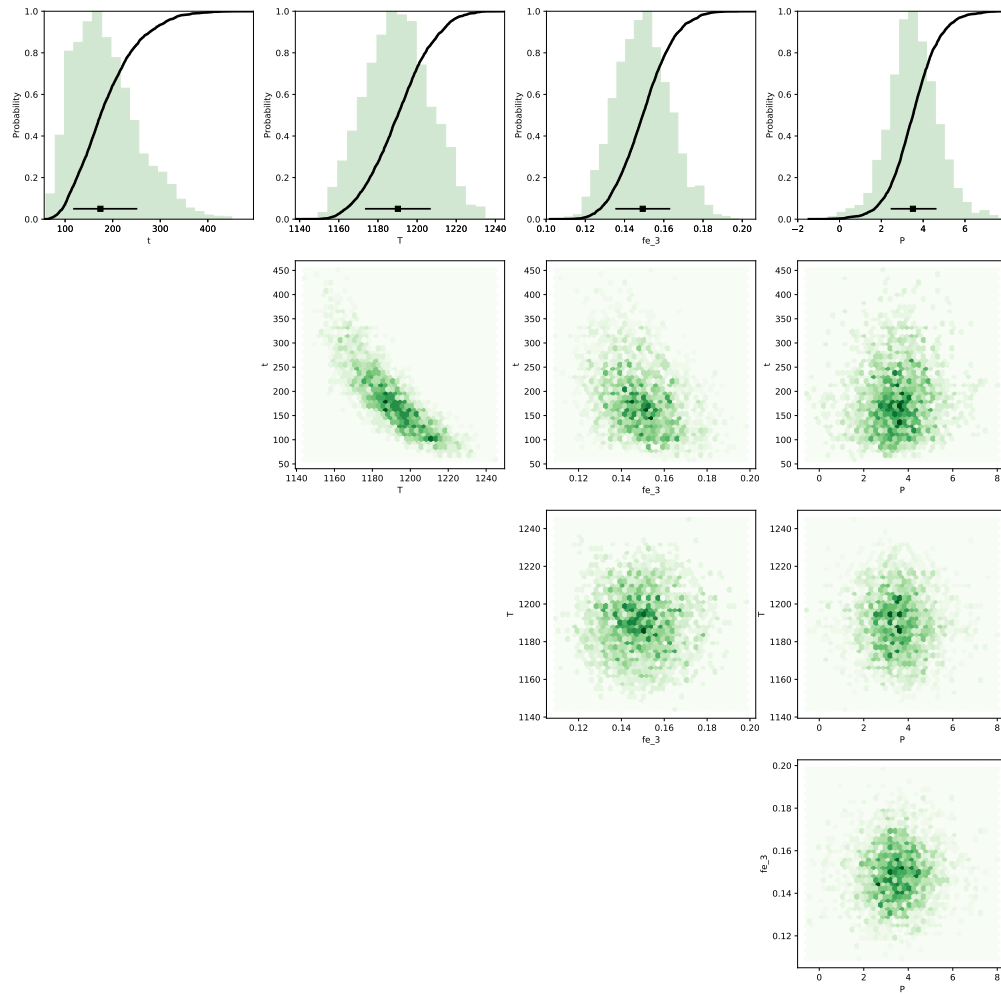


**Figure S58.** Bayesian inversion results for sample SKU\_1\_OL\_C3\_4\_P3. Marginal plot showing the posterior distributions of the Nested Sampling Bayesian Inversion for the main intensive parameters:  $t$  is time (days),  $T$  is temperature ( $^{\circ}\text{C}$ ),  $fe\_3$  is ferric iron content of the melt and  $P$  is pressure (kbar). The top row shows histograms (green bars) and probability density functions (black curves) of the aforementioned intensive parameters. The black bar shows the median result and  $1\sigma$  standard deviation. The bottom three rows are density plots that show the trade offs between the different intensive parameters.

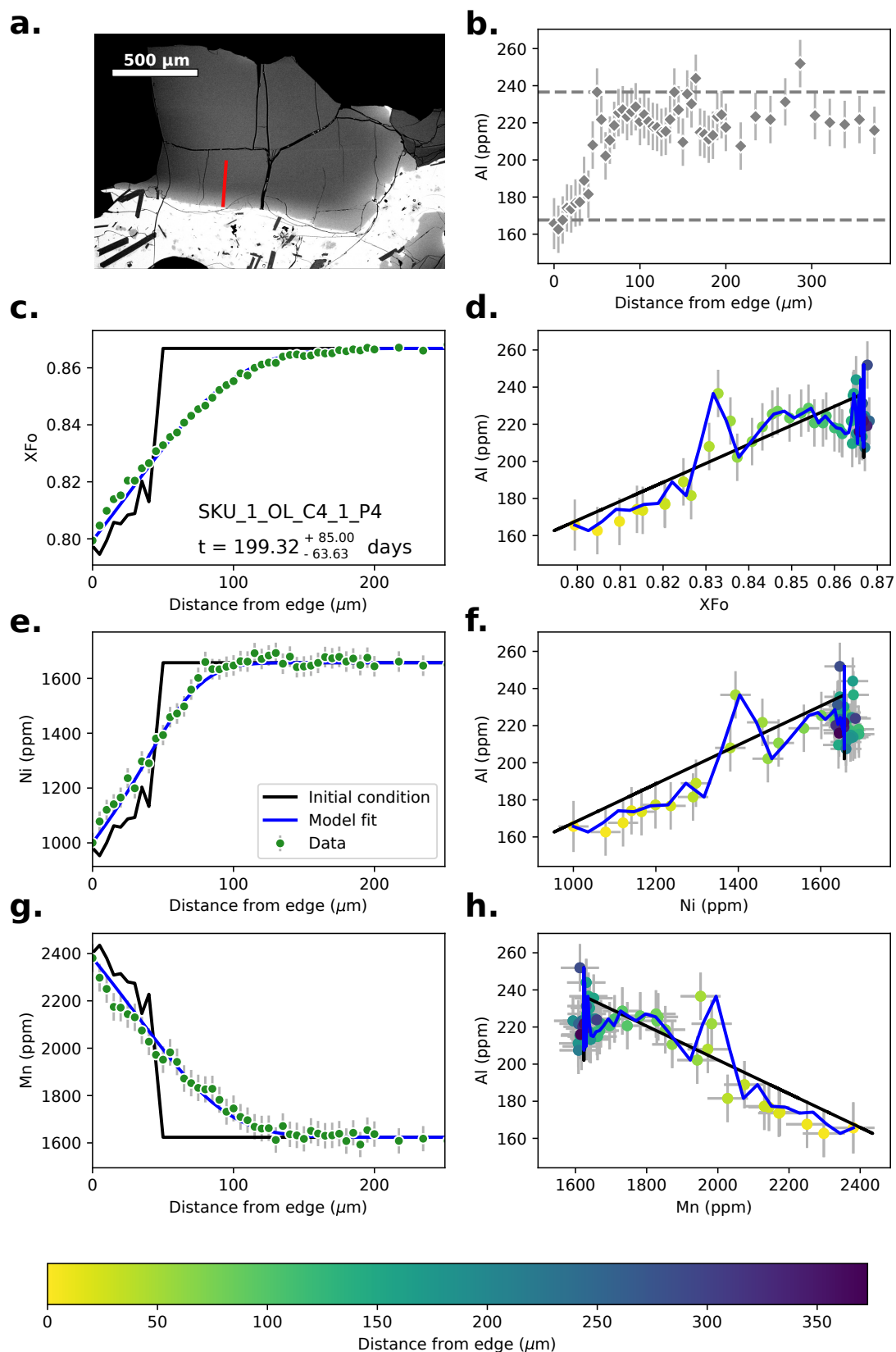


**Figure S59.** Data, initial conditions and model fits for sample SKU\_1\_OL\_C4\_1\_P4.

Caption the same as Supplementary Fig. S11.

July 16, 2020, 11:34pm

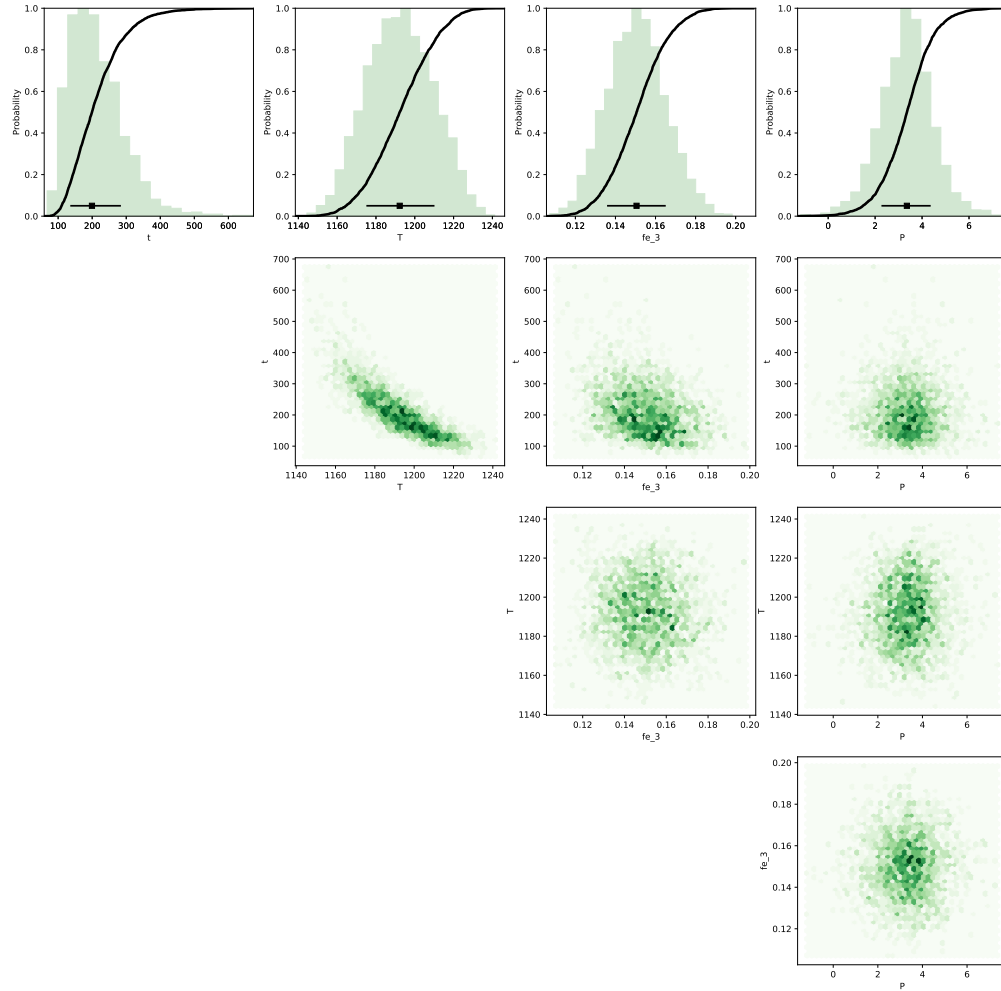


**Figure S60.** Bayesian inversion results for sample SKU\_1\_OL\_C4\_1\_P4. Marginal plot showing the posterior distributions of the Nested Sampling Bayesian Inversion for the main intensive parameters:  $t$  is time (days),  $T$  is temperature ( $^{\circ}\text{C}$ ),  $fe_3$  is ferric iron content of the melt and  $P$  is pressure (kbar). The top row shows histograms (green bars) and probability density functions (black curves) of the aforementioned intensive parameters. The black bar shows the median result and  $1\sigma$  standard deviation. The bottom three rows are density plots that show the trade offs between the different intensive parameters.

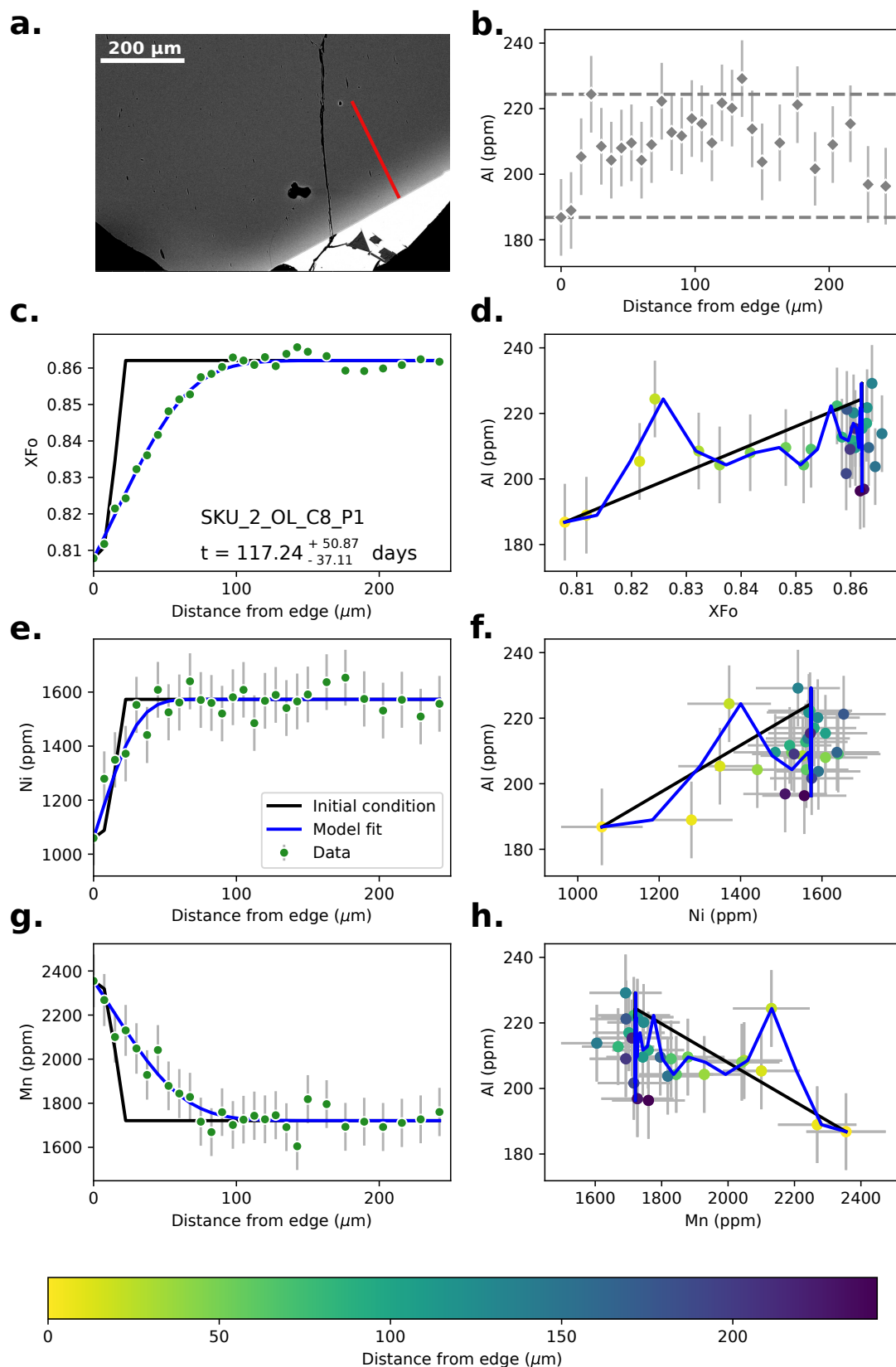


**Figure S61.** Data, initial conditions and model fits for sample SKU\_2\_OL\_C8\_P1. Caption the same as Supplementary Fig. S11.



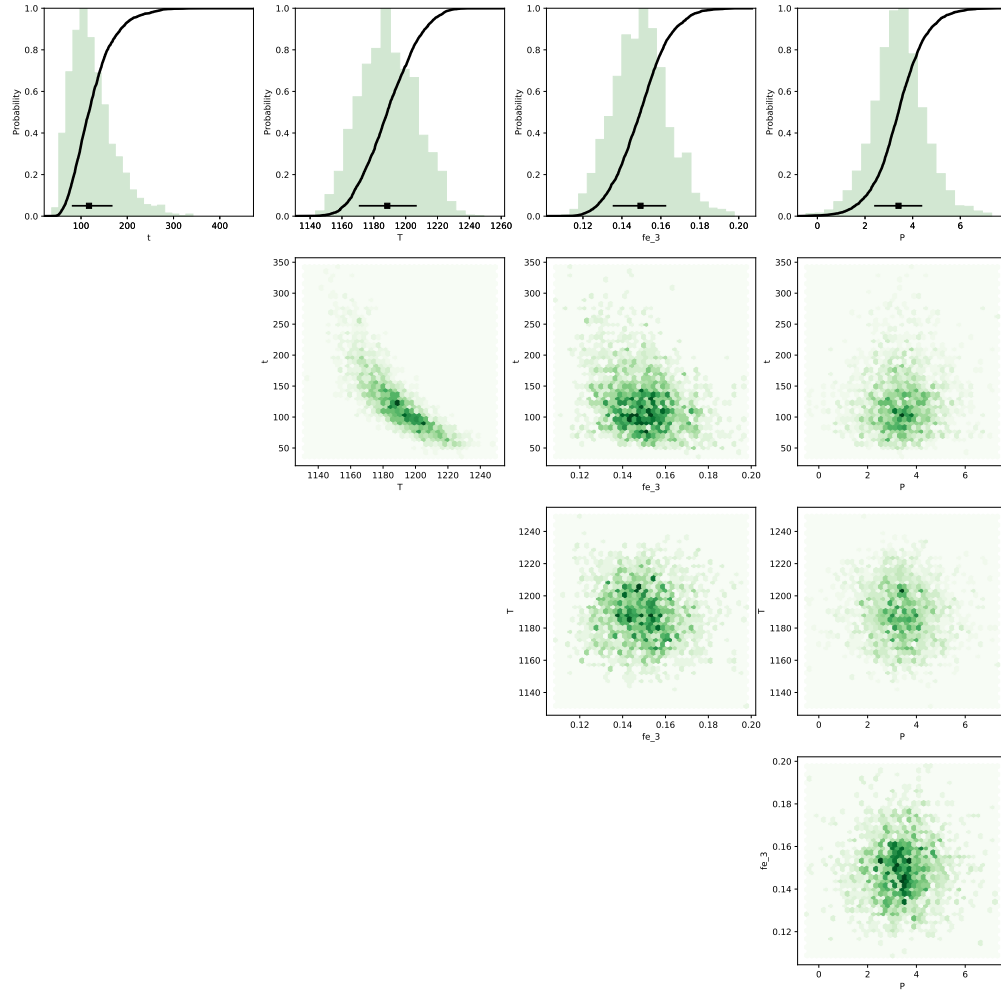


**Figure S62.** Bayesian inversion results for sample SKU\_2\_OL\_C8\_P1. Marginal plot showing the posterior distributions of the Nested Sampling Bayesian Inversion for the main intensive parameters:  $t$  is time (days),  $T$  is temperature ( $^{\circ}\text{C}$ ),  $fe\_3$  is ferric iron content of the melt and  $P$  is pressure (kbar). The top row shows histograms (green bars) and probability density functions (black curves) of the aforementioned intensive parameters. The black bar shows the median result and  $1\sigma$  standard deviation. The bottom three rows are density plots that show the trade offs between the different intensive parameters.

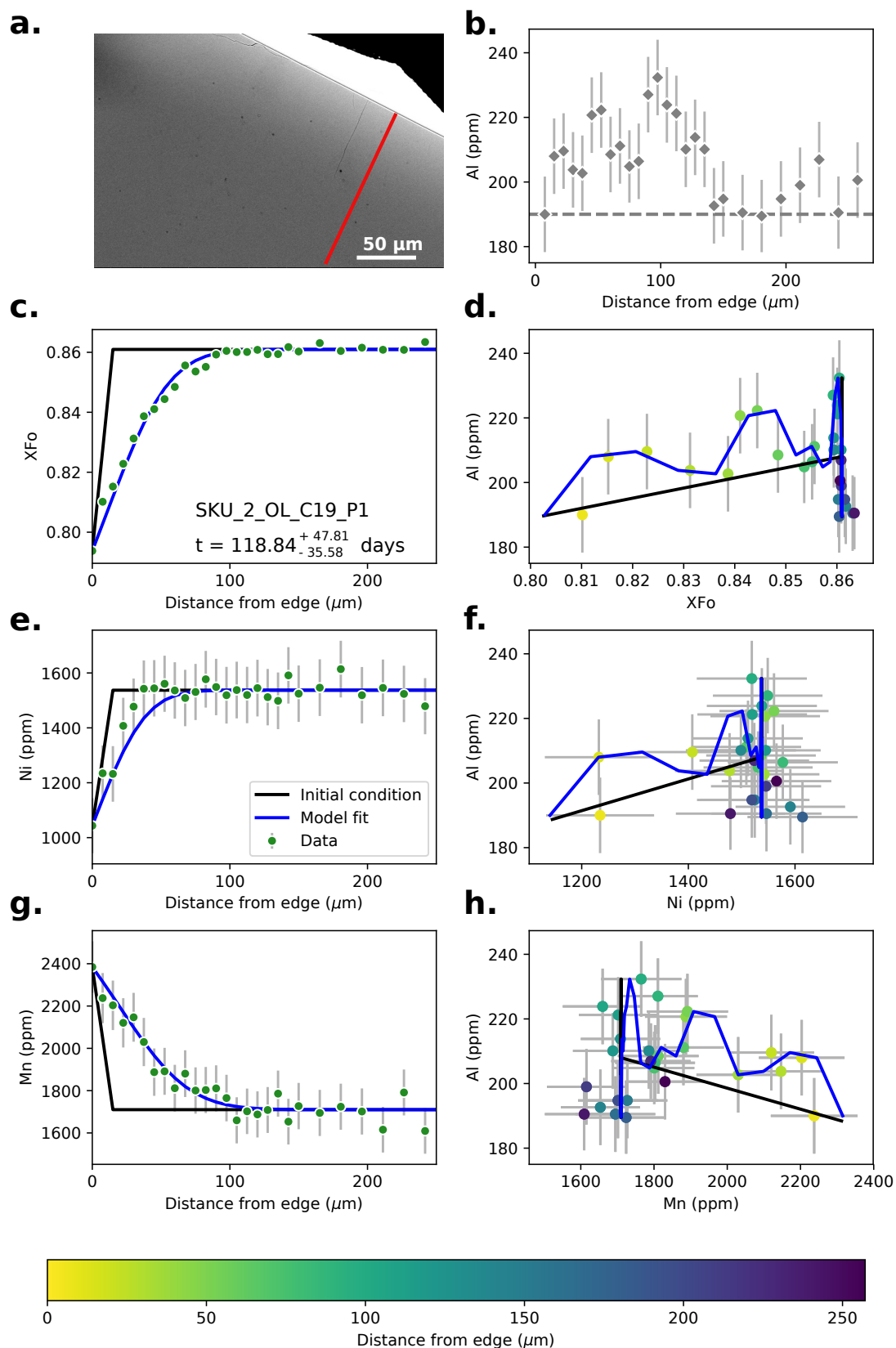


**Figure S63.** Data, initial conditions and model fits for sample SKU\_2\_OL\_C19\_P1. Caption the same as Supplementary Fig. S11.

July 16, 2020, 11:34pm

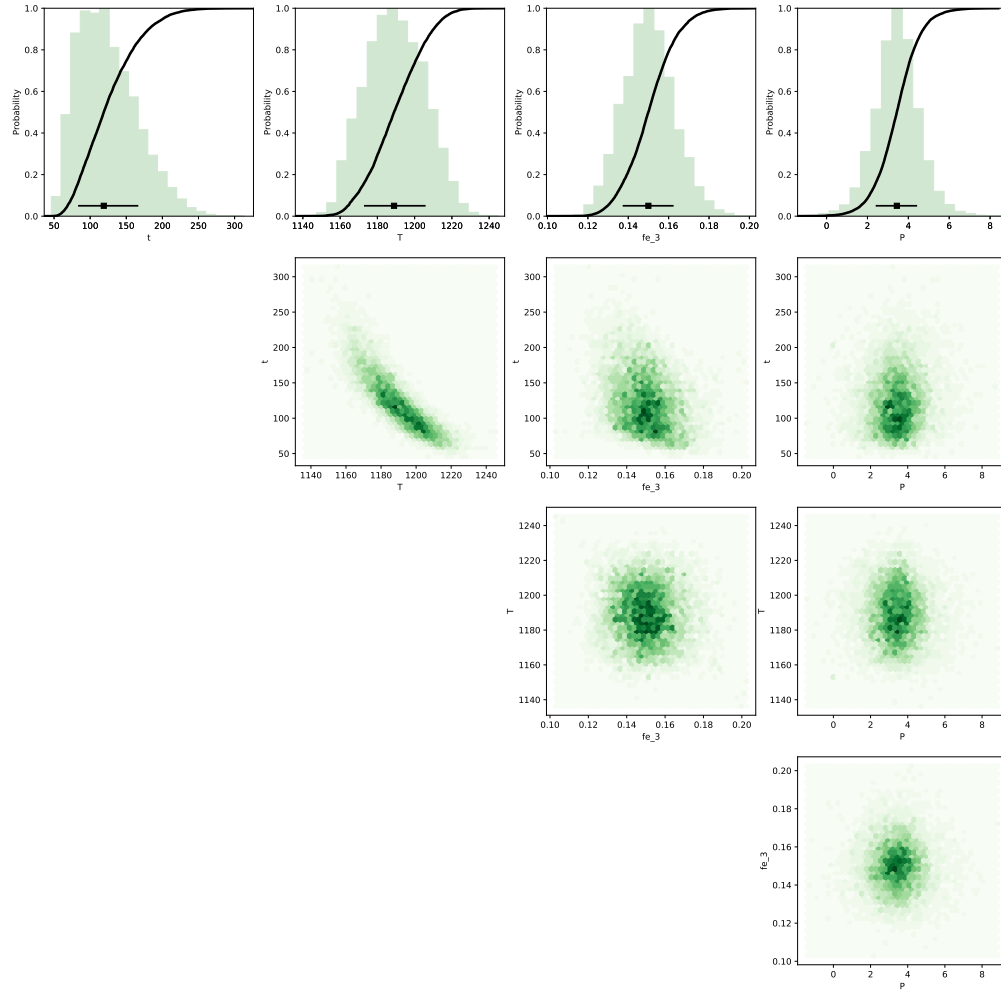


**Figure S64.** Bayesian inversion results for sample SKU\_2\_OL\_C19\_P1. Marginal plot showing the posterior distributions of the Nested Sampling Bayesian Inversion for the main intensive parameters:  $t$  is time (days),  $T$  is temperature ( $^{\circ}\text{C}$ ),  $fe\_3$  is ferric iron content of the melt and  $P$  is pressure (kbar). The top row shows histograms (green bars) and probability density functions (black curves) of the aforementioned intensive parameters. The black bar shows the median result and  $1\sigma$  standard deviation. The bottom three rows are density plots that show the trade offs between the different intensive parameters.

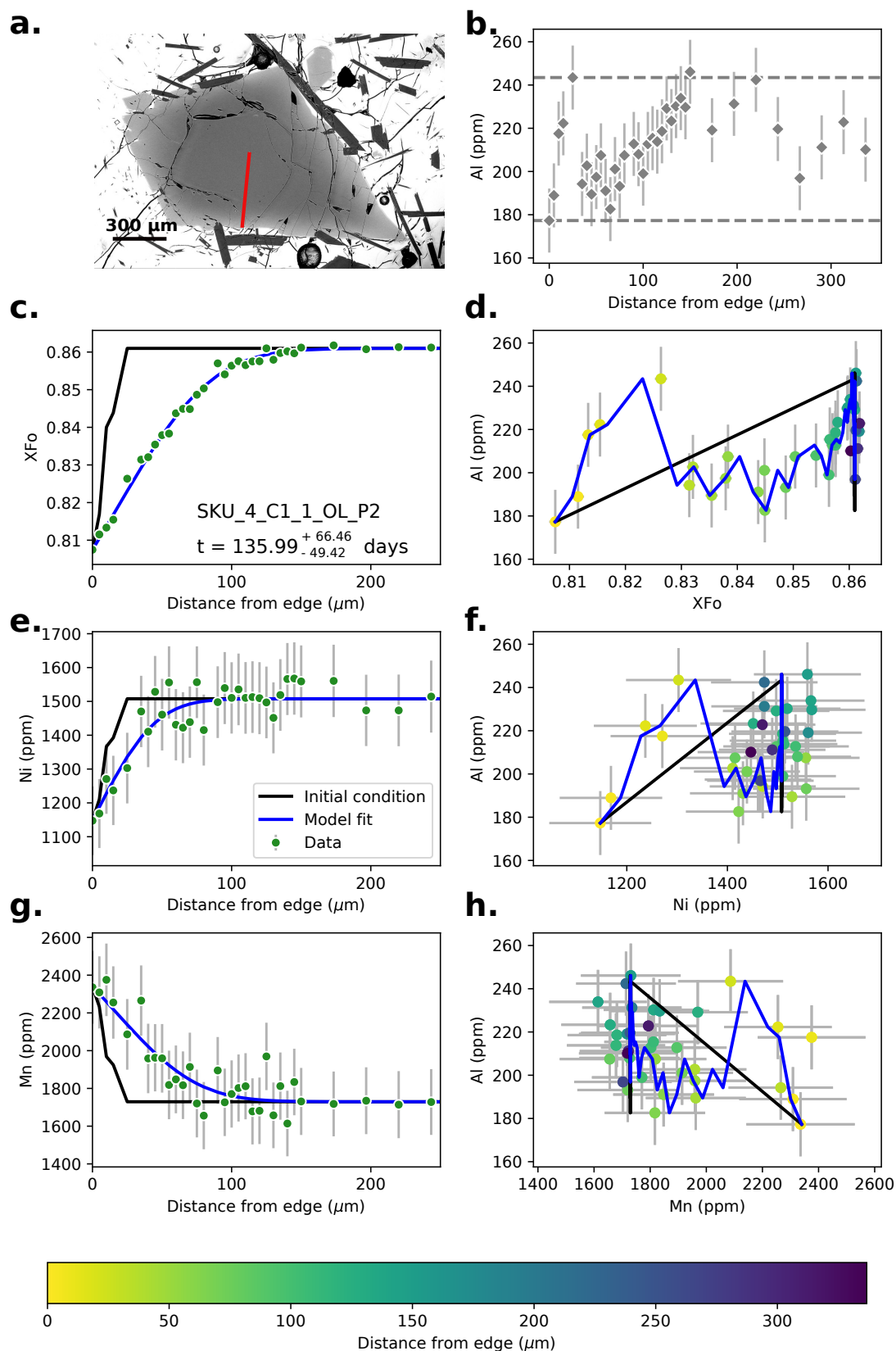


**Figure S65.** Data, initial conditions and model fits for sample SKU\_4\_C1\_1\_OL\_P2.

Caption the same as Supplementary Fig. S11.

July 16, 2020, 11:34pm

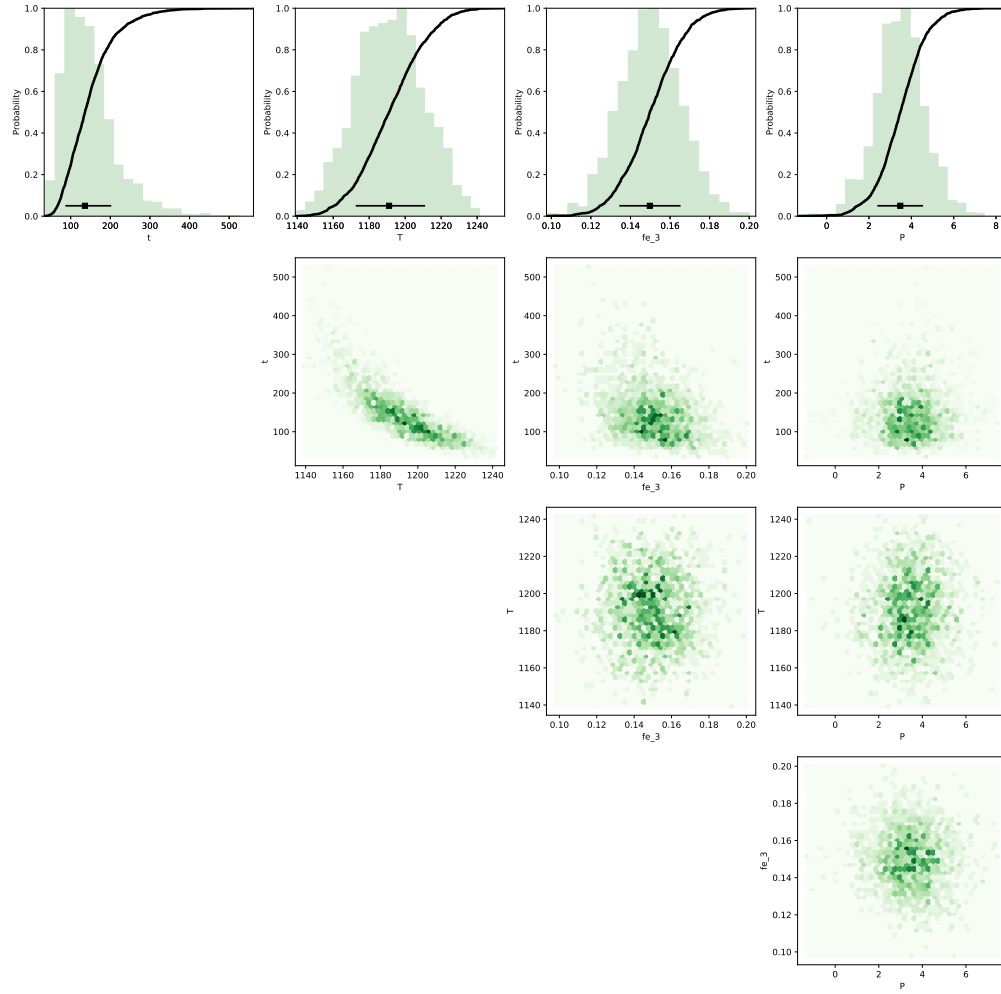


**Figure S66.** Bayesian inversion results for sample SKU\_4\_C1\_1\_OL\_P2. Marginal plot showing the posterior distributions of the Nested Sampling Bayesian Inversion for the main intensive parameters:  $t$  is time (days),  $T$  is temperature ( $^{\circ}\text{C}$ ),  $fe\_3$  is ferric iron content of the melt and  $P$  is pressure (kbar). The top row shows histograms (green bars) and probability density functions (black curves) of the aforementioned intensive parameters. The black bar shows the median result and  $1\sigma$  standard deviation. The bottom three rows are density plots that show the trade offs between the different intensive parameters.

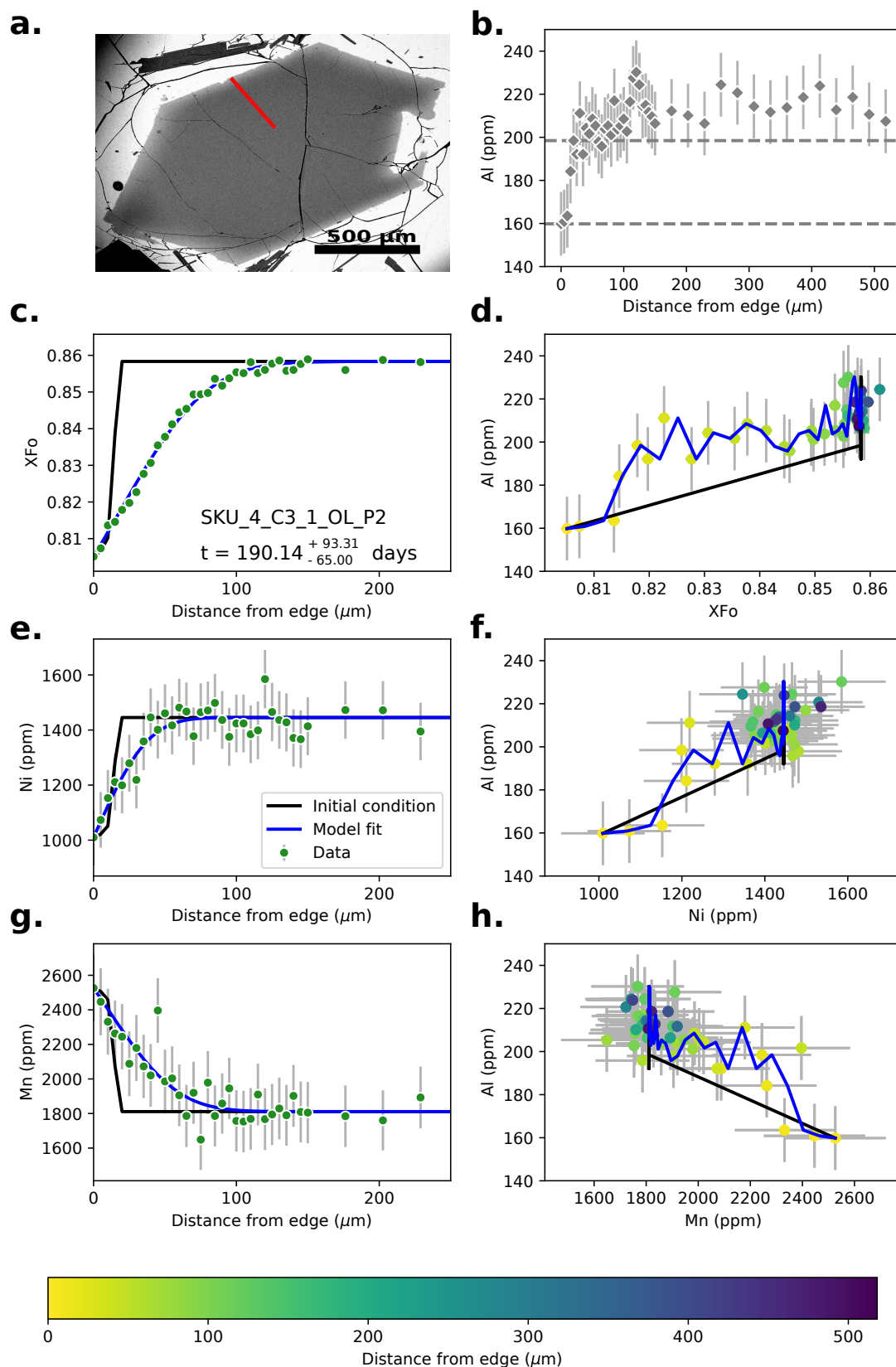


**Figure S67.** Data, initial conditions and model fits for sample SKU\_4\_C3\_1\_OL\_P2.

Caption the same as Supplementary Fig. S11.

July 16, 2020, 11:34pm

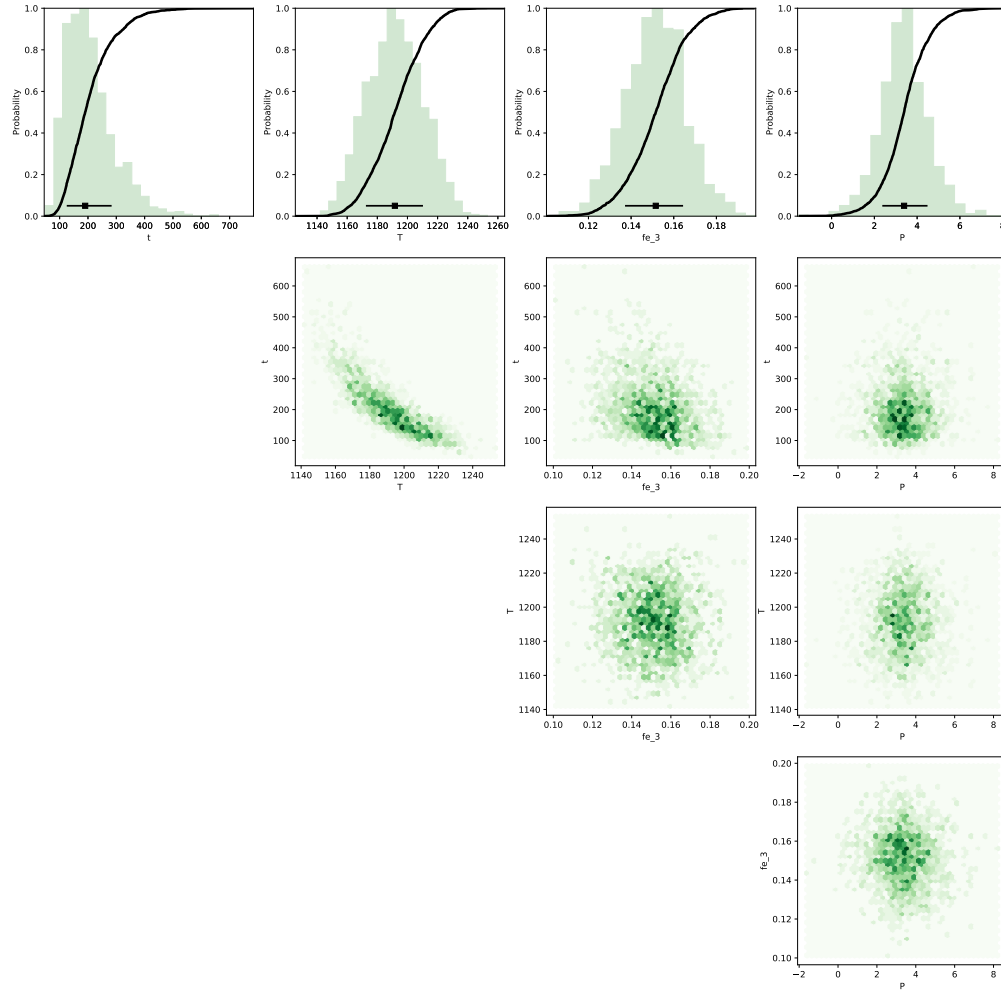


**Figure S68.** Bayesian inversion results for sample SKU\_4\_C3\_1\_OL\_P2. Marginal plot showing the posterior distributions of the Nested Sampling Bayesian Inversion for the main intensive parameters:  $t$  is time (days),  $T$  is temperature ( $^{\circ}\text{C}$ ),  $fe\_3$  is ferric iron content of the melt and  $P$  is pressure (kbar). The top row shows histograms (green bars) and probability density functions (black curves) of the aforementioned intensive parameters. The black bar shows the median result and  $1\sigma$  standard deviation. The bottom three rows are density plots that show the trade offs between the different intensive parameters.

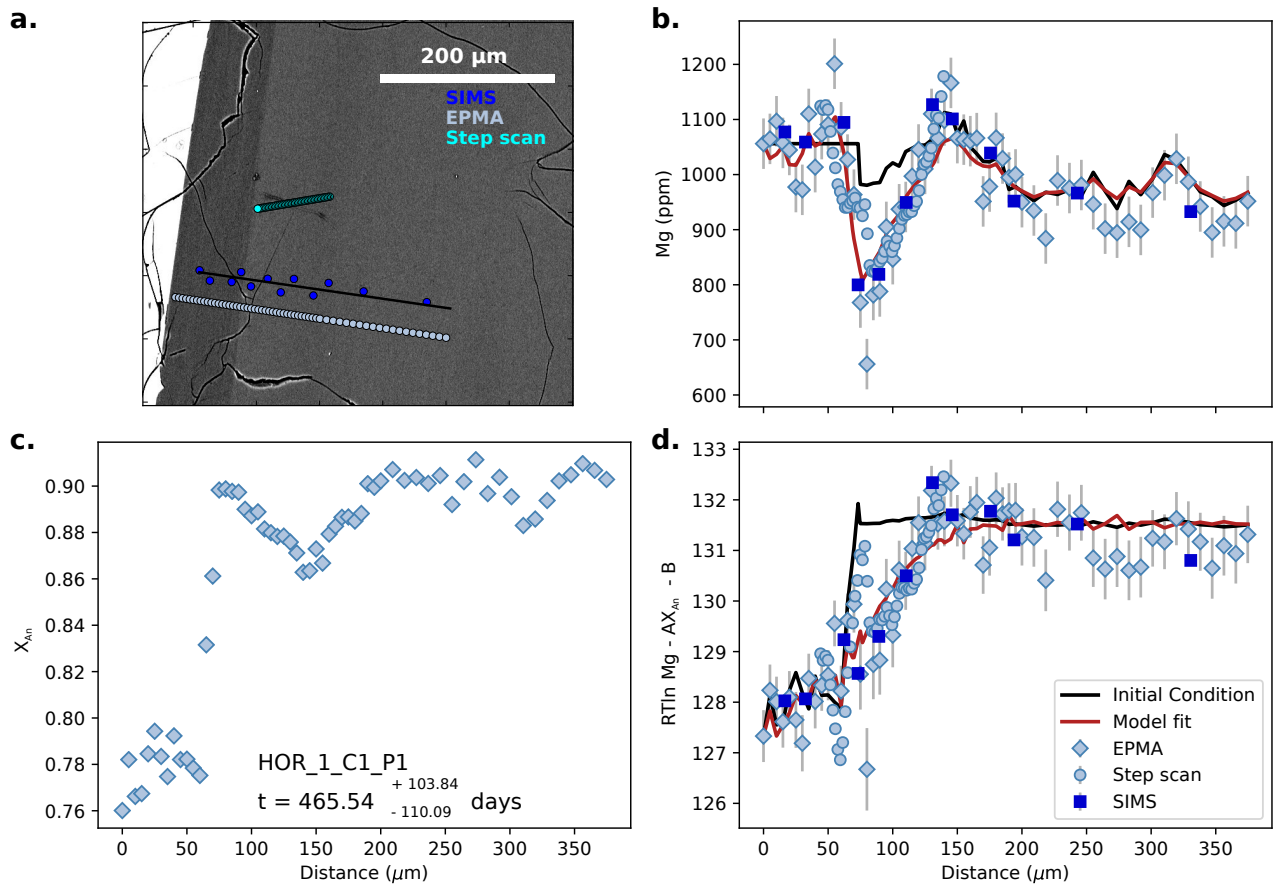


**Figure S69.** Data, initial conditions and model fits for plagioclase crystal HOR\_1\_C1\_P1. **a** is a BSE image of the plagioclase crystal showing the location of coarse SIMS spot analyses (blue spots), EPMA traverse (light blue spots) and SIMS step scan analyses (cyan points). Points from each profile were projected onto the black line. **b**, Mg compositional profile with point shapes and colours marked by analytical method. Dark blue squares are SIMS coarse spot analyses, light blue circles are SIMS step scan analyses and light blue diamonds are EPMA analyses. The black line is calculated initial conditions used in the modelling, and the red line is the model fit using the maximum likelihood of all of the parameters used in the Bayesian inversion. **c**, Anorthite profile of plagioclase as measured by EPMA. **d**, calculated melt equivalent Mg in plagioclase using the most likely partitioning parameters estimated from the Bayesian inversion. Symbols and colours are the same as in **b**.



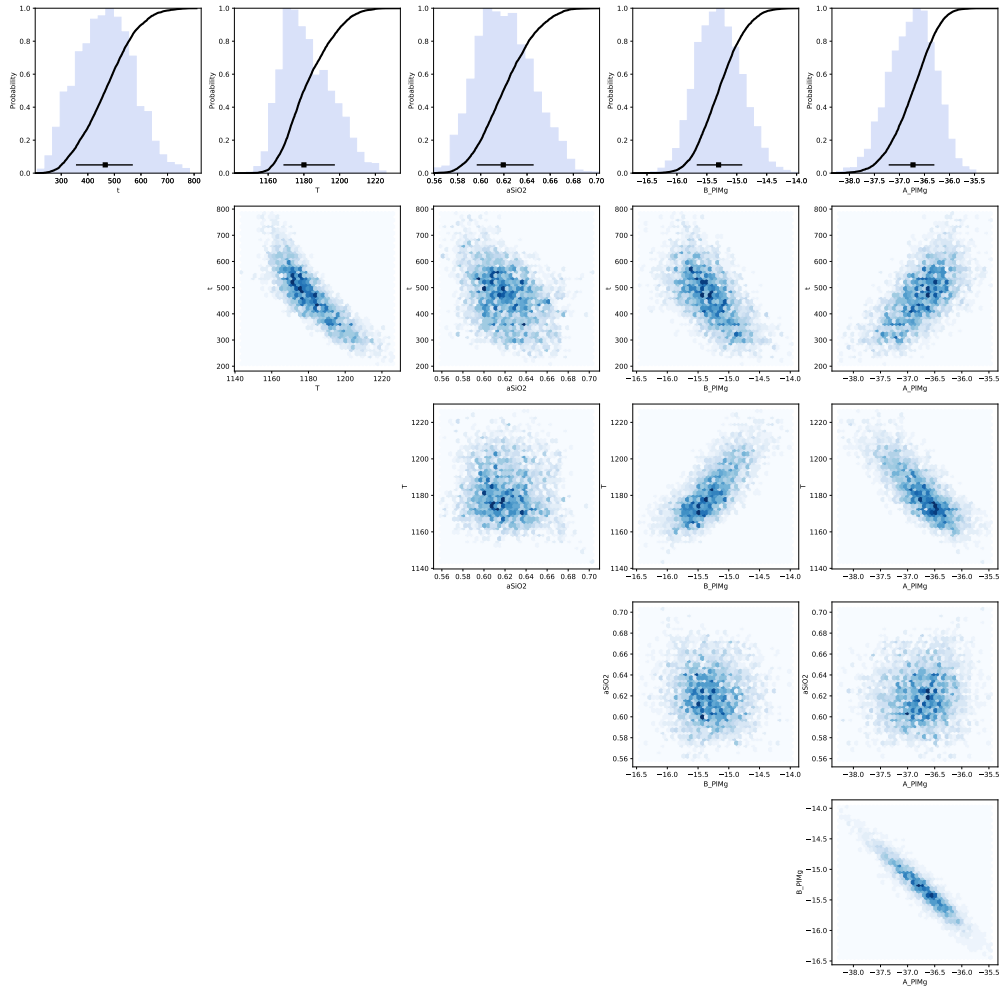


**Figure S70.** Bayesian inversion results for sample HOR\_1\_C1\_P1. Marginal plot showing the posterior distributions of the main intensive parameters modelled for the diffusion of Mg in Plagioclase:  $t$  is time (days),  $T$  is temperature ( $^{\circ}\text{C}$ ),  $a_{\text{SiO}_2}$  is  $a_{\text{SiO}_2}$ ,  $B_{\text{PlMg}}$  and  $A_{\text{PlMg}}$  are the intercept and slope of the Mg-in-plagioclase partitioning relationship. The top row shows histograms (blue bars) and probability density functions (black curves) of the aforementioned intensive parameters. The black bar shows the median result and  $1\sigma$  standard deviation. The bottom four rows are density plots that show the trade offs between the different parameters.

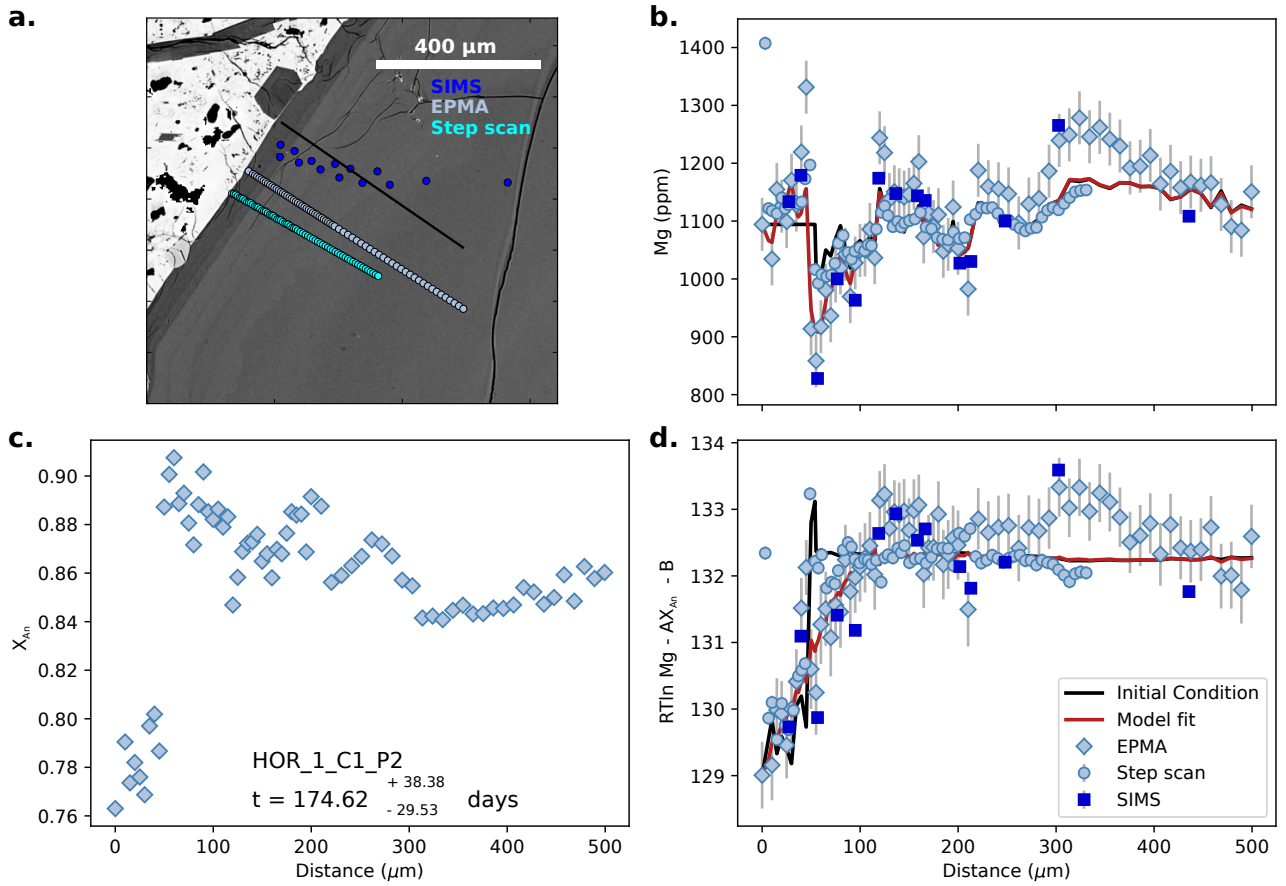


**Figure S71.** Data, initial conditions and model fits for plagioclase crystal HOR\_1\_C1\_P2. **a** is a BSE image of the plagioclase crystal showing the location of coarse SIMS spot analyses (blue spots), EPMA traverse (light blue spots) and SIMS step scan analyses (cyan points). Points from each profile were projected onto the black line. **b**, Mg compositional profile with point shapes and colours marked by analytical method. Dark blue squares are SIMS coarse spot analyses, light blue circles are SIMS step scan analyses and light blue diamonds are EPMA analyses. The black line is calculated initial conditions used in the modelling, and the red line is the model fit using the maximum likelihood of all of the parameters used in the Bayesian inversion. **c**, Anorthite profile of plagioclase as measured by EPMA. **d**, calculated melt equivalent Mg in plagioclase using the most likely partitioning parameters estimated from the Bayesian inversion. Symbols and colours are the same as in **b**.

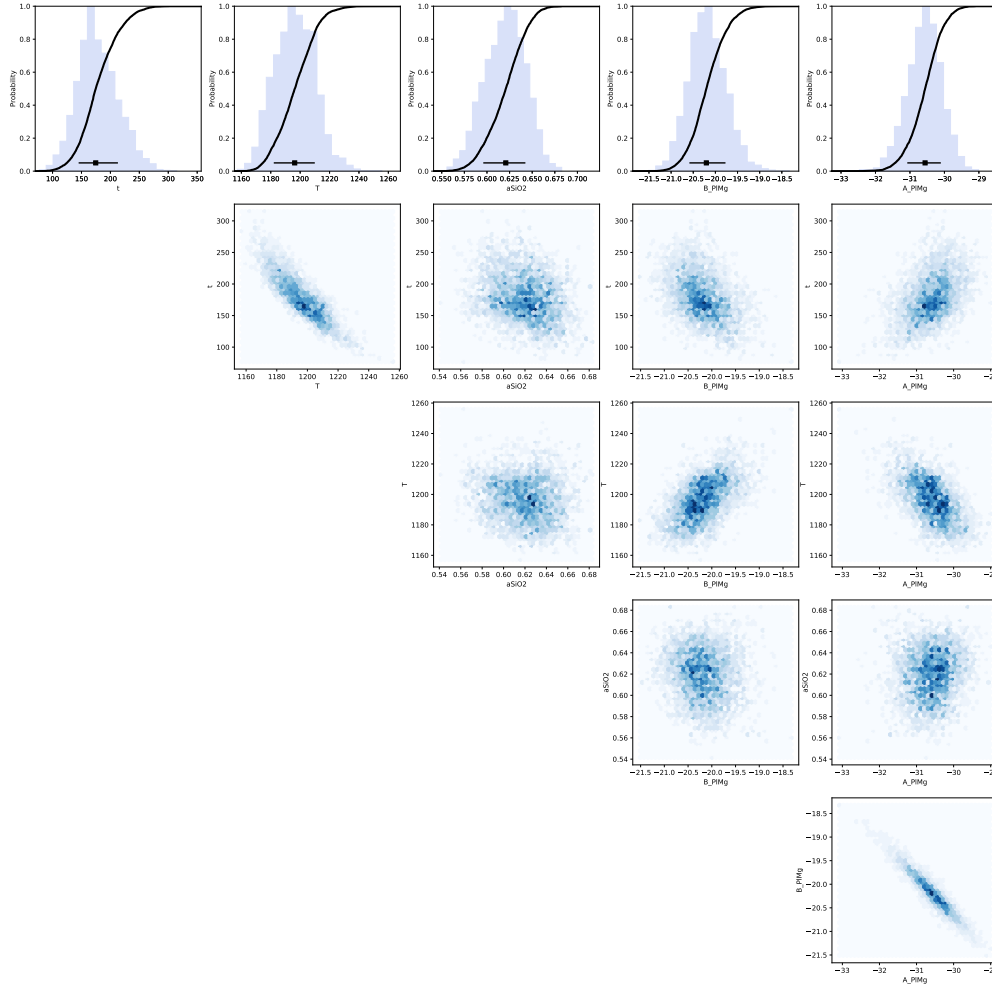


**Figure S72.** Bayesian inversion results for sample HOR\_1\_C1\_P2. Marginal plot showing the posterior distributions of the main intensive parameters modelled for the diffusion of Mg in Plagioclase:  $t$  is time (days),  $T$  is temperature ( $^{\circ}\text{C}$ ),  $a_{\text{SiO}_2}$  is  $a_{\text{SiO}_2}$ ,  $B_{\text{PlMg}}$  and  $A_{\text{PlMg}}$  are the intercept and slope of the Mg-in-plagioclase partitioning relationship. The top row shows histograms (blue bars) and probability density functions (black curves) of the aforementioned intensive parameters. The black bar shows the median result and  $1\sigma$  standard deviation. The bottom four rows are density plots that show the trade offs between the different parameters.

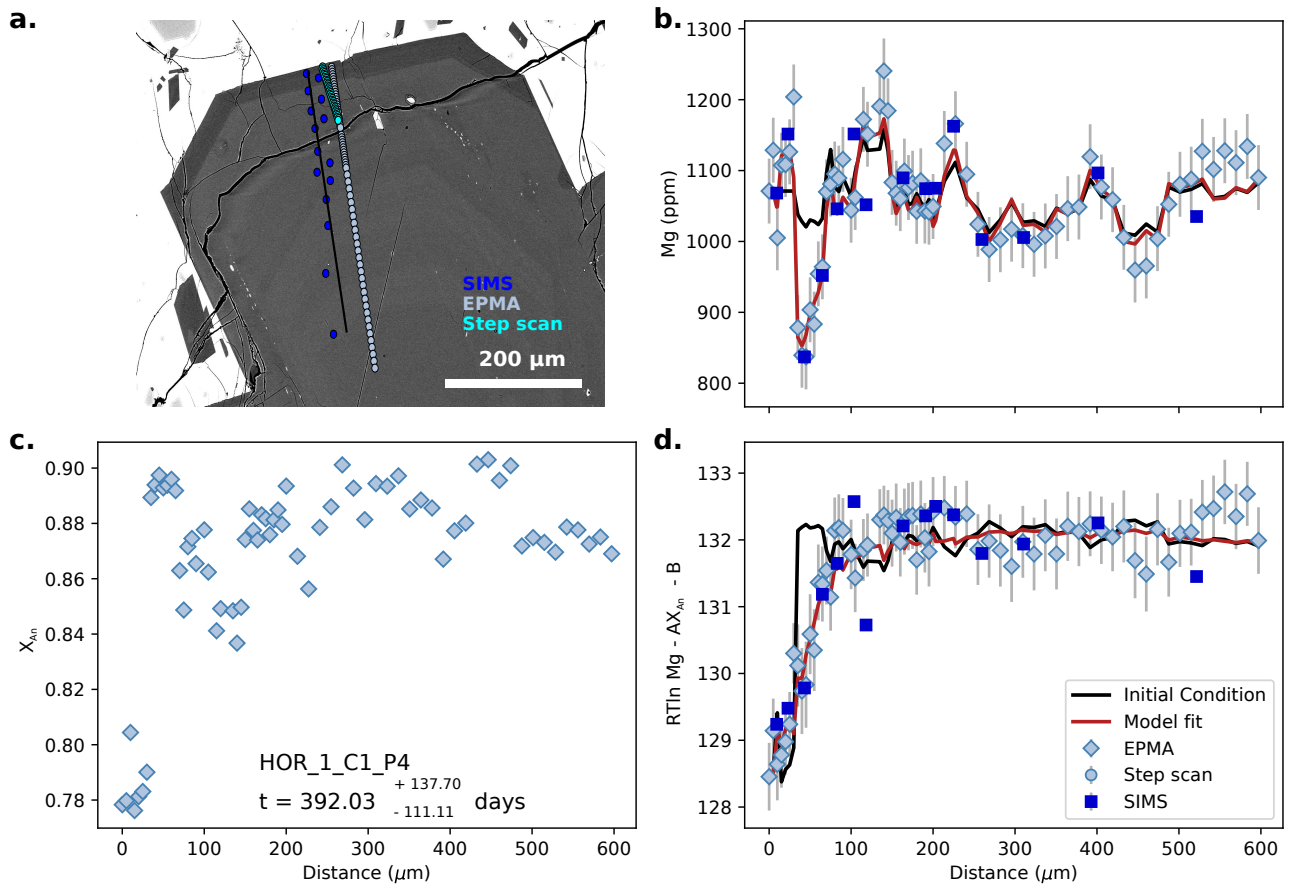


**Figure S73.** Data, initial conditions and model fits for plagioclase crystal HOR\_1\_C1\_P4. **a** is a BSE image of the plagioclase crystal showing the location of coarse SIMS spot analyses (blue spots), EPMA traverse (light blue spots) and SIMS step scan analyses (cyan points). Points from each profile were projected onto the black line. **b**, Mg compositional profile with point shapes and colours marked by analytical method. Dark blue squares are SIMS coarse spot analyses, light blue circles are SIMS step scan analyses and light blue diamonds are EPMA analyses. The black line is calculated initial conditions used in the modelling, and the red line is the model fit using the maximum likelihood of all of the parameters used in the Bayesian inversion. **c**, Anorthite profile of plagioclase as measured by EPMA. **d**, calculated melt equivalent Mg in plagioclase using the most likely partitioning parameters estimated from the Bayesian inversion. Symbols and colours are the same as in **b**.

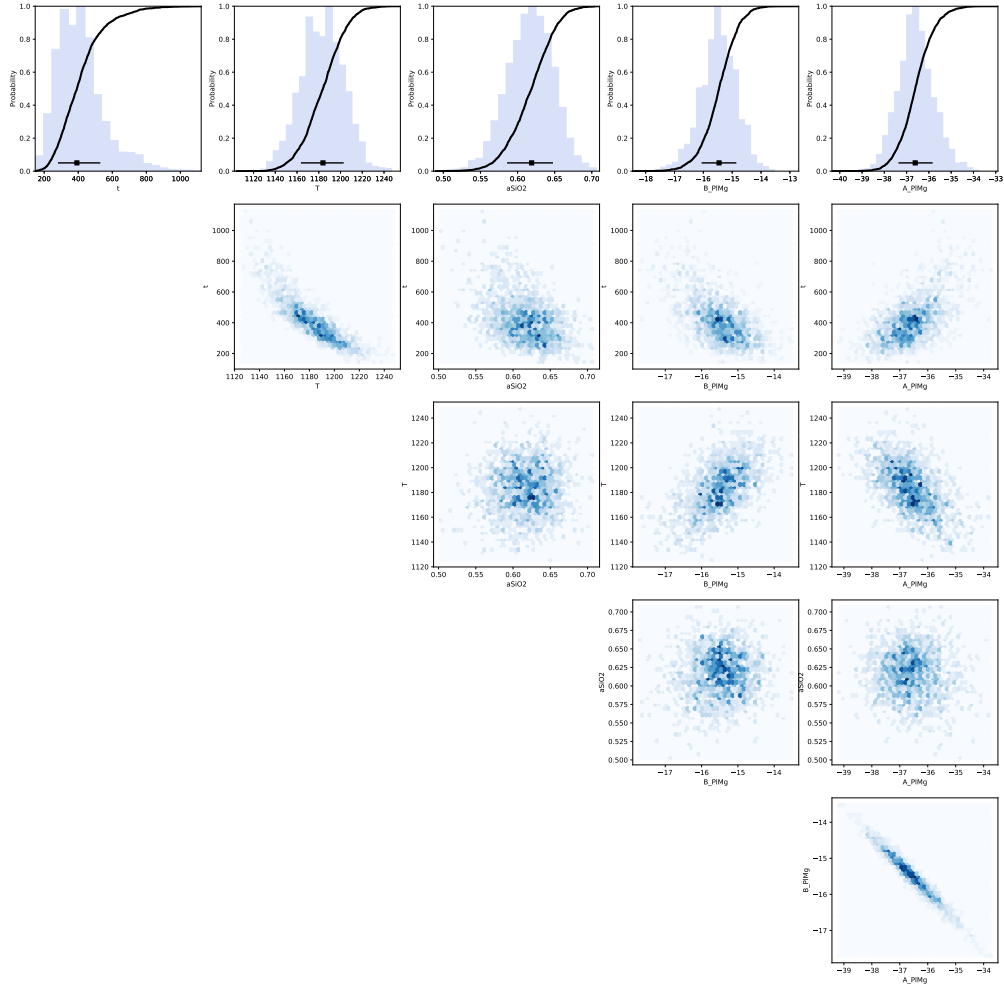


**Figure S74.** Bayesian inversion results for sample HOR\_1\_C1\_P4. Marginal plot showing the posterior distributions of the main intensive parameters modelled for the diffusion of Mg in Plagioclase:  $t$  is time (days),  $T$  is temperature ( $^{\circ}\text{C}$ ),  $a_{\text{SiO}_2}$  is  $a_{\text{SiO}_2}$ ,  $B_{\text{PlMg}}$  and  $A_{\text{PlMg}}$  are the intercept and slope of the Mg-in-plagioclase partitioning relationship. The top row shows histograms (blue bars) and probability density functions (black curves) of the aforementioned intensive parameters. The black bar shows the median result and  $1\sigma$  standard deviation. The bottom four rows are density plots that show the trade offs between the different parameters.

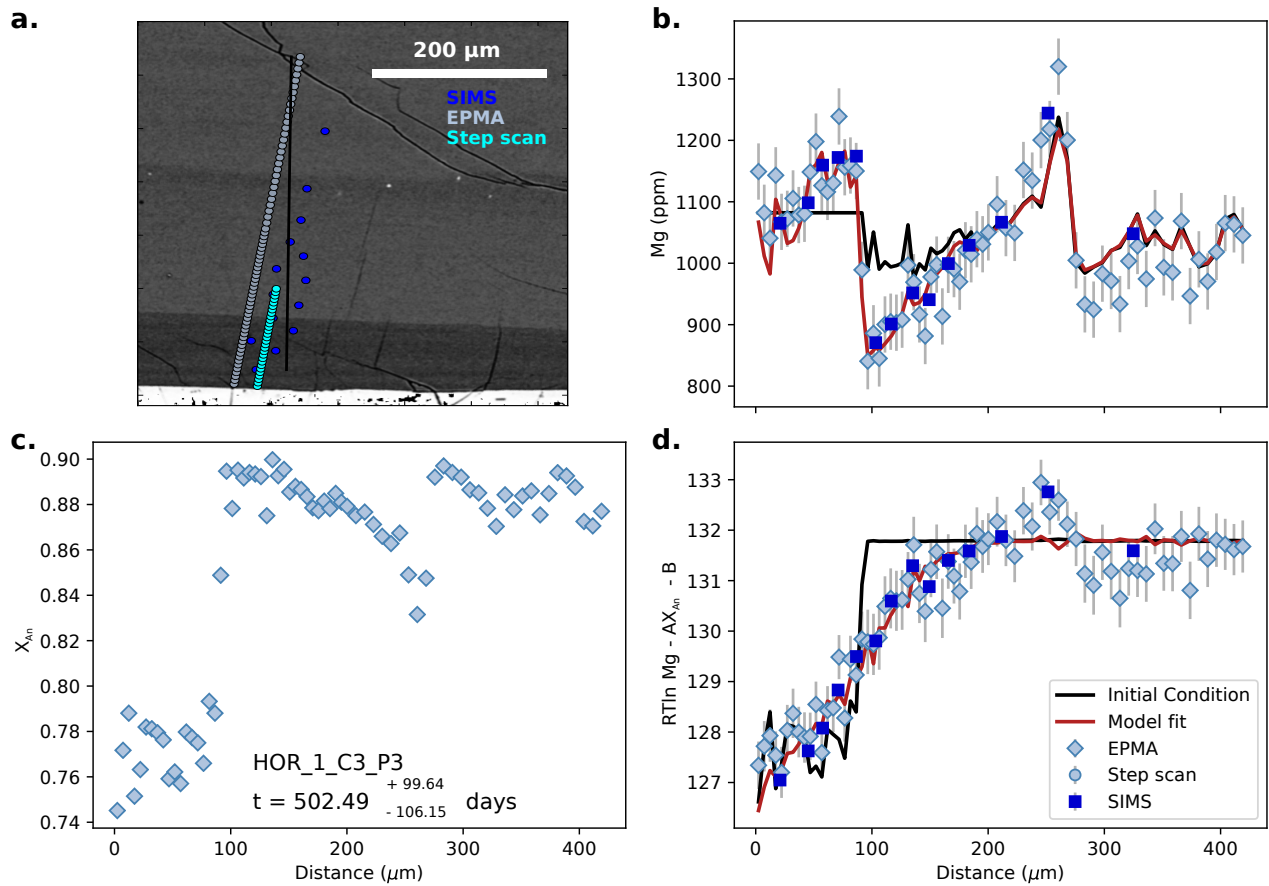


**Figure S75.** Data, initial conditions and model fits for plagioclase crystal HOR\_1\_C3\_P3. **a** is a BSE image of the plagioclase crystal showing the location of coarse SIMS spot analyses (blue spots), EPMA traverse (light blue spots) and SIMS step scan analyses (cyan points). Points from each profile were projected onto the black line. **b**, Mg compositional profile with point shapes and colours marked by analytical method. Dark blue squares are SIMS coarse spot analyses, light blue circles are SIMS step scan analyses and light blue diamonds are EPMA analyses. The black line is calculated initial conditions used in the modelling, and the red line is the model fit using the maximum likelihood of all of the parameters used in the Bayesian inversion. **c**, Anorthite profile of plagioclase as measured by EPMA. **d**, calculated melt equivalent Mg in plagioclase using the most likely partitioning parameters estimated from the Bayesian inversion. Symbols and colours are the same as in **b**.

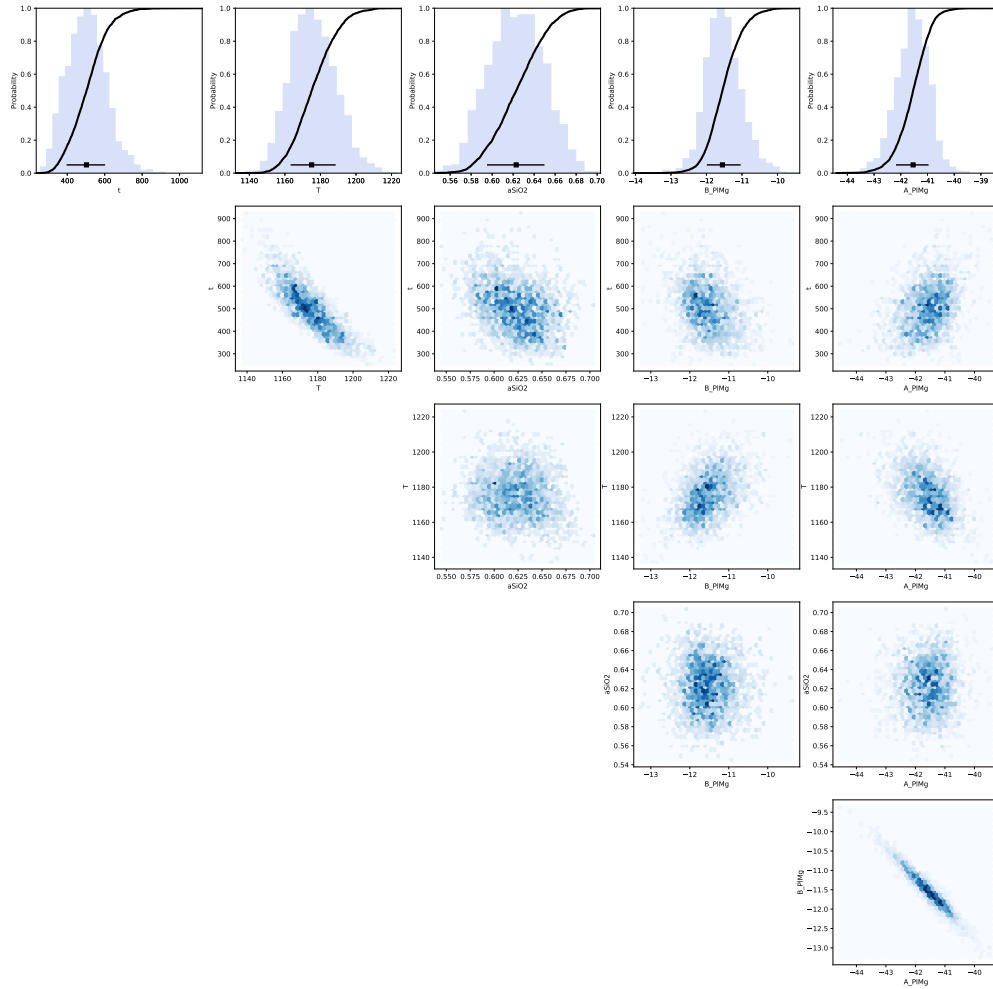


**Figure S76.** Bayesian inversion results for sample HOR\_1\_C3\_P3. Marginal plot showing the posterior distributions of the main intensive parameters modelled for the diffusion of Mg in Plagioclase:  $t$  is time (days),  $T$  is temperature ( $^{\circ}\text{C}$ ),  $a_{\text{SiO}_2}$  is  $a_{\text{SiO}_2}$ ,  $B_{\text{PlMg}}$  and  $A_{\text{PlMg}}$  are the intercept and slope of the Mg-in-plagioclase partitioning relationship. The top row shows histograms (blue bars) and probability density functions (black curves) of the aforementioned intensive parameters. The black bar shows the median result and  $1\sigma$  standard deviation. The bottom four rows are density plots that show the trade offs between the different parameters.

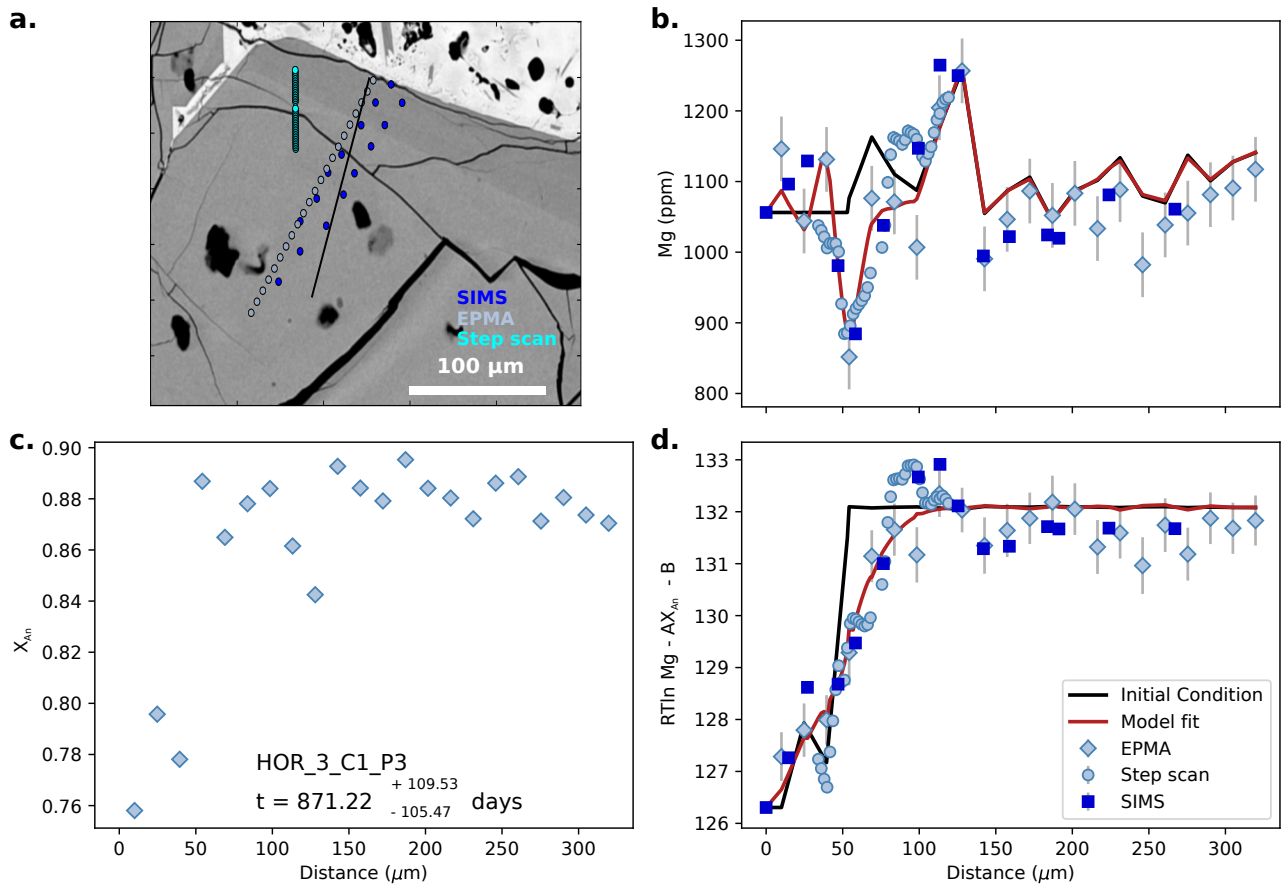


**Figure S77.** Data, initial conditions and model fits for plagioclase crystal HOR\_3\_C1\_P3. **a** is a BSE image of the plagioclase crystal showing the location of coarse SIMS spot analyses (blue spots), EPMA traverse (light blue spots) and SIMS step scan analyses (cyan points). Points from each profile were projected onto the black line. **b**, Mg compositional profile with point shapes and colours marked by analytical method. Dark blue squares are SIMS coarse spot analyses, light blue circles are SIMS step scan analyses and light blue diamonds are EPMA analyses. The black line is calculated initial conditions used in the modelling, and the red line is the model fit using the maximum likelihood of all of the parameters used in the Bayesian inversion. **c**, Anorthite profile of plagioclase as measured by EPMA. **d**, calculated melt equivalent Mg in plagioclase using the most likely partitioning parameters estimated from the Bayesian inversion. Symbols and colours are the same as in **b**.



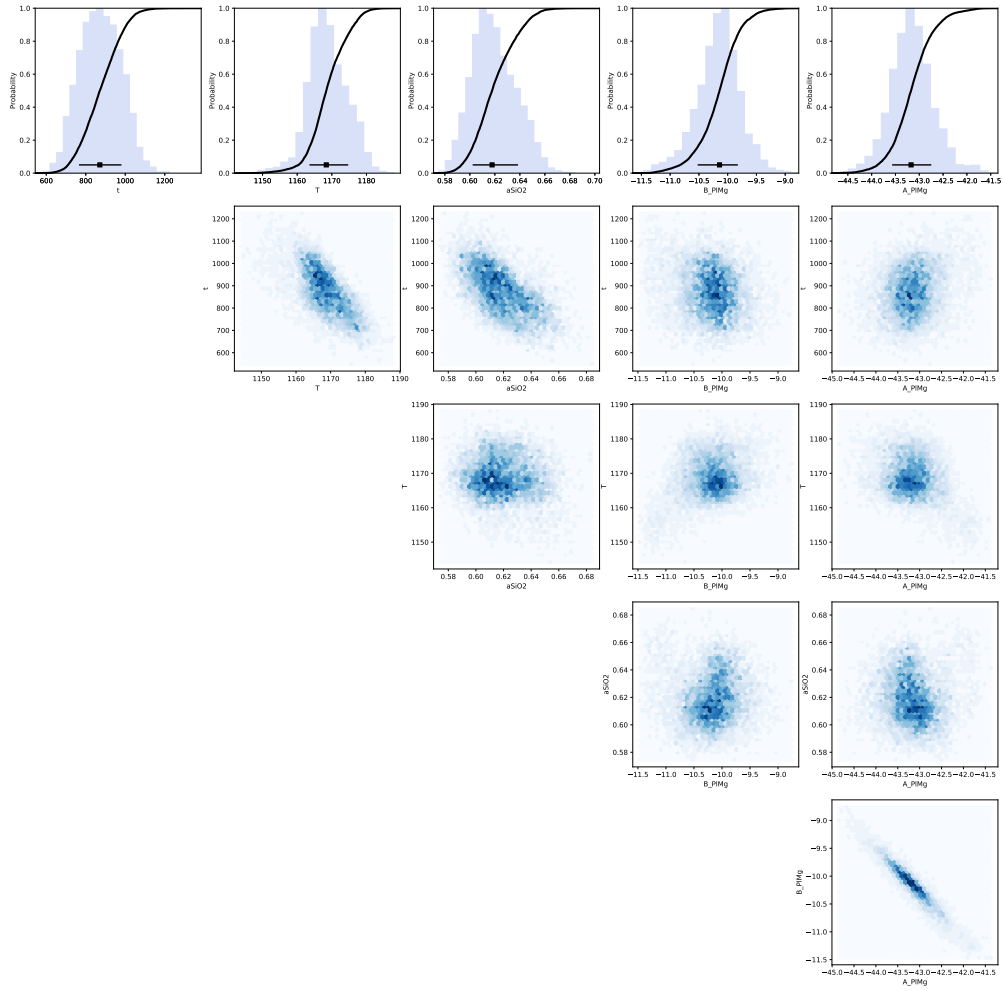


**Figure S78.** Bayesian inversion results for sample HOR\_3\_C1\_P3. Marginal plot showing the posterior distributions of the main intensive parameters modelled for the diffusion of Mg in Plagioclase:  $t$  is time (days),  $T$  is temperature ( $^{\circ}\text{C}$ ),  $a\text{SiO}_2$  is  $a_{\text{SiO}_2}$ ,  $B_{\text{PlMg}}$  and  $A_{\text{PlMg}}$  are the intercept and slope of the Mg-in-plagioclase partitioning relationship. The top row shows histograms (blue bars) and probability density functions (black curves) of the aforementioned intensive parameters. The black bar shows the median result and  $1\sigma$  standard deviation. The bottom four rows are density plots that show the trade offs between the different parameters.

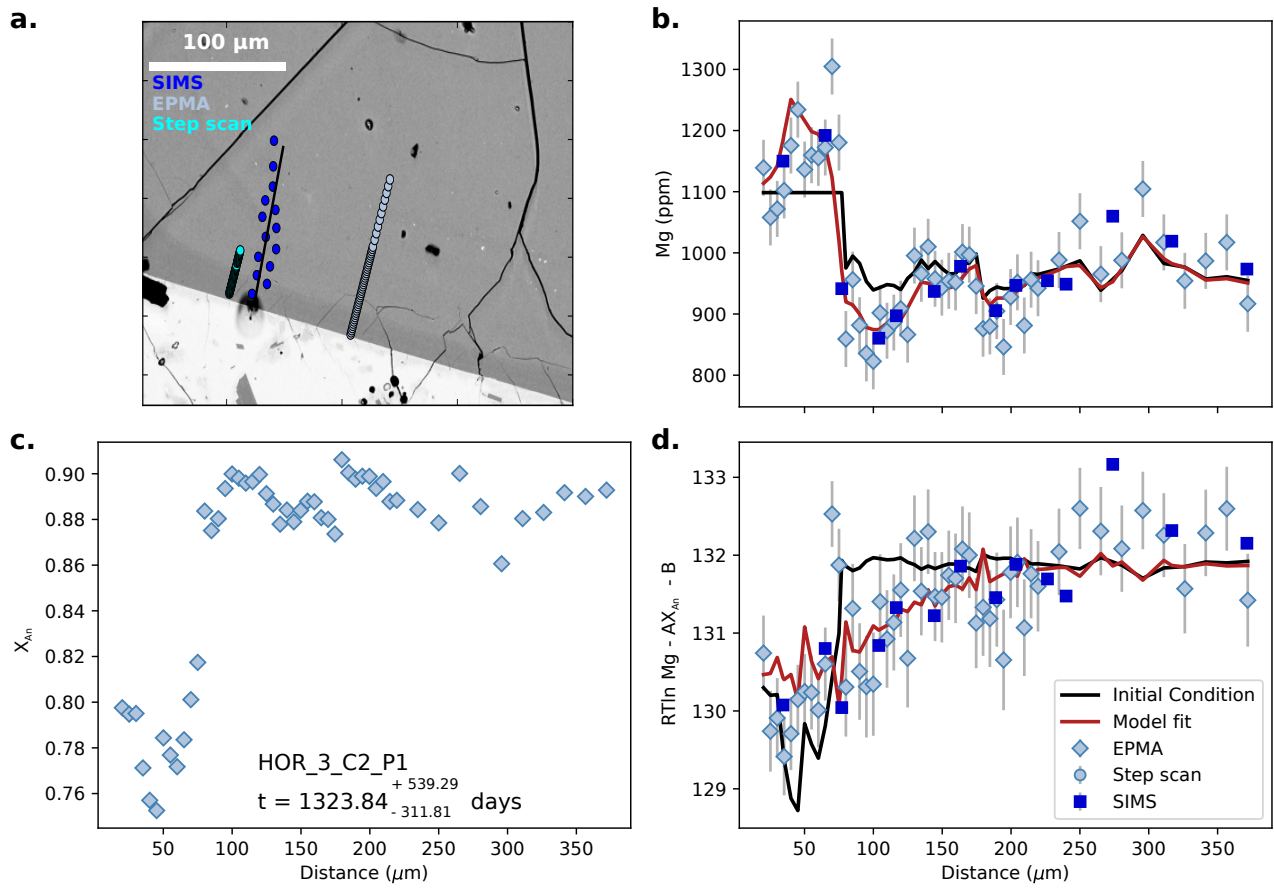


**Figure S79.** Data, initial conditions and model fits for plagioclase crystal HOR\_3\_C2\_P1. **a** is a BSE image of the plagioclase crystal showing the location of coarse SIMS spot analyses (blue spots), EPMA traverse (light blue spots) and SIMS step scan analyses (cyan points). Points from each profile were projected onto the black line. **b**, Mg compositional profile with point shapes and colours marked by analytical method. Dark blue squares are SIMS coarse spot analyses, light blue circles are SIMS step scan analyses and light blue diamonds are EPMA analyses. The black line is calculated initial conditions used in the modelling, and the red line is the model fit using the maximum likelihood of all of the parameters used in the Bayesian inversion. **c**, Anorthite profile of plagioclase as measured by EPMA. **d**, calculated melt equivalent Mg in plagioclase using the most likely partitioning parameters estimated from the Bayesian inversion. Symbols and colours are the same as in **b**.

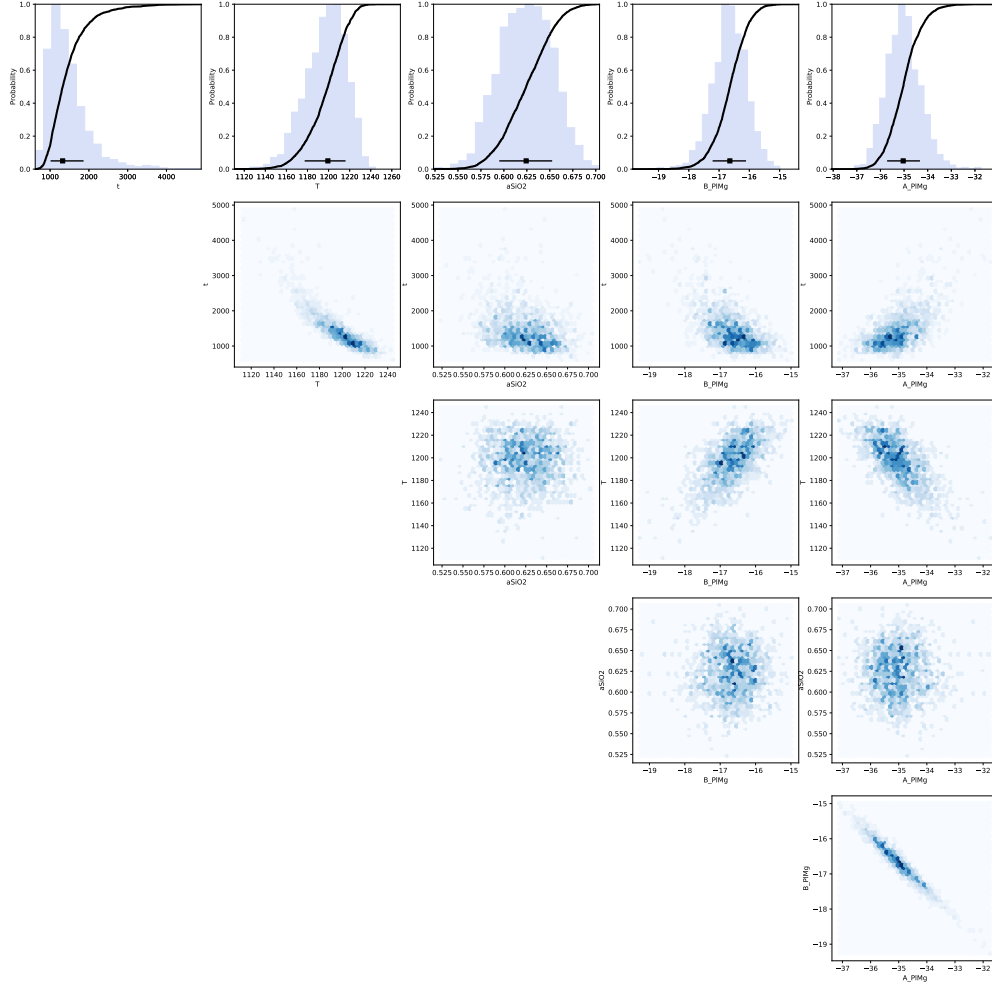


**Figure S80.** Bayesian inversion results for sample HOR\_3\_C2\_P1. Marginal plot showing the posterior distributions of the main intensive parameters modelled for the diffusion of Mg in Plagioclase:  $t$  is time (days),  $T$  is temperature ( $^{\circ}\text{C}$ ),  $a\text{SiO}_2$  is  $a_{\text{SiO}_2}$ ,  $B_{\text{PlMg}}$  and  $A_{\text{PlMg}}$  are the intercept and slope of the Mg-in-plagioclase partitioning relationship. The top row shows histograms (blue bars) and probability density functions (black curves) of the aforementioned intensive parameters. The black bar shows the median result and  $1\sigma$  standard deviation. The bottom four rows are density plots that show the trade offs between the different parameters.

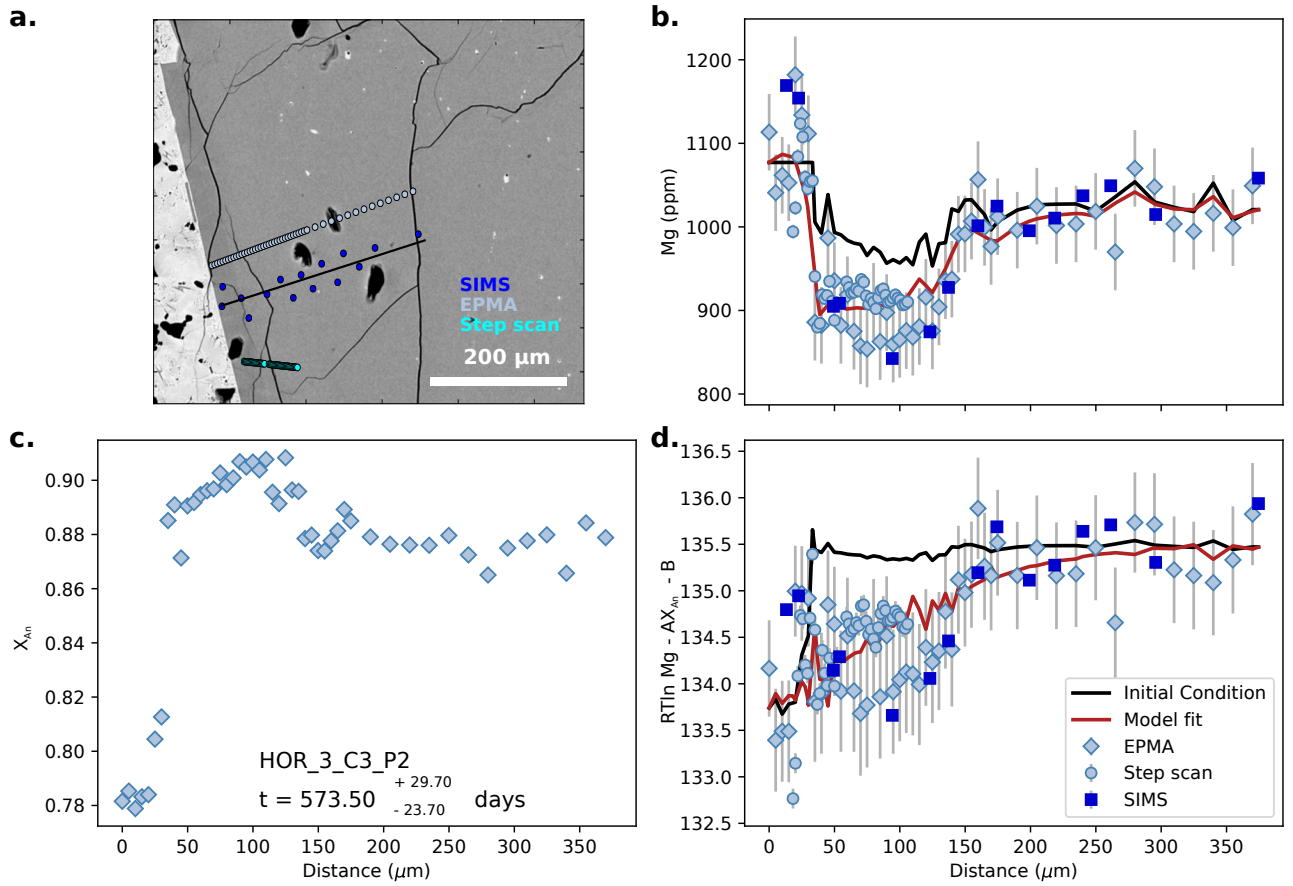


**Figure S81.** Data, initial conditions and model fits for plagioclase crystal HOR\_3\_C3\_P2. **a** is a BSE image of the plagioclase crystal showing the location of coarse SIMS spot analyses (blue spots), EPMA traverse (light blue spots) and SIMS step scan analyses (cyan points). Points from each profile were projected onto the black line. **b**, Mg compositional profile with point shapes and colours marked by analytical method. Dark blue squares are SIMS coarse spot analyses, light blue circles are SIMS step scan analyses and light blue diamonds are EPMA analyses. The black line is calculated initial conditions used in the modelling, and the red line is the model fit using the maximum likelihood of all of the parameters used in the Bayesian inversion. **c**, Anorthite profile of plagioclase as measured by EPMA. **d**, calculated melt equivalent Mg in plagioclase using the most likely partitioning parameters estimated from the Bayesian inversion. Symbols and colours are the same as in **b**.

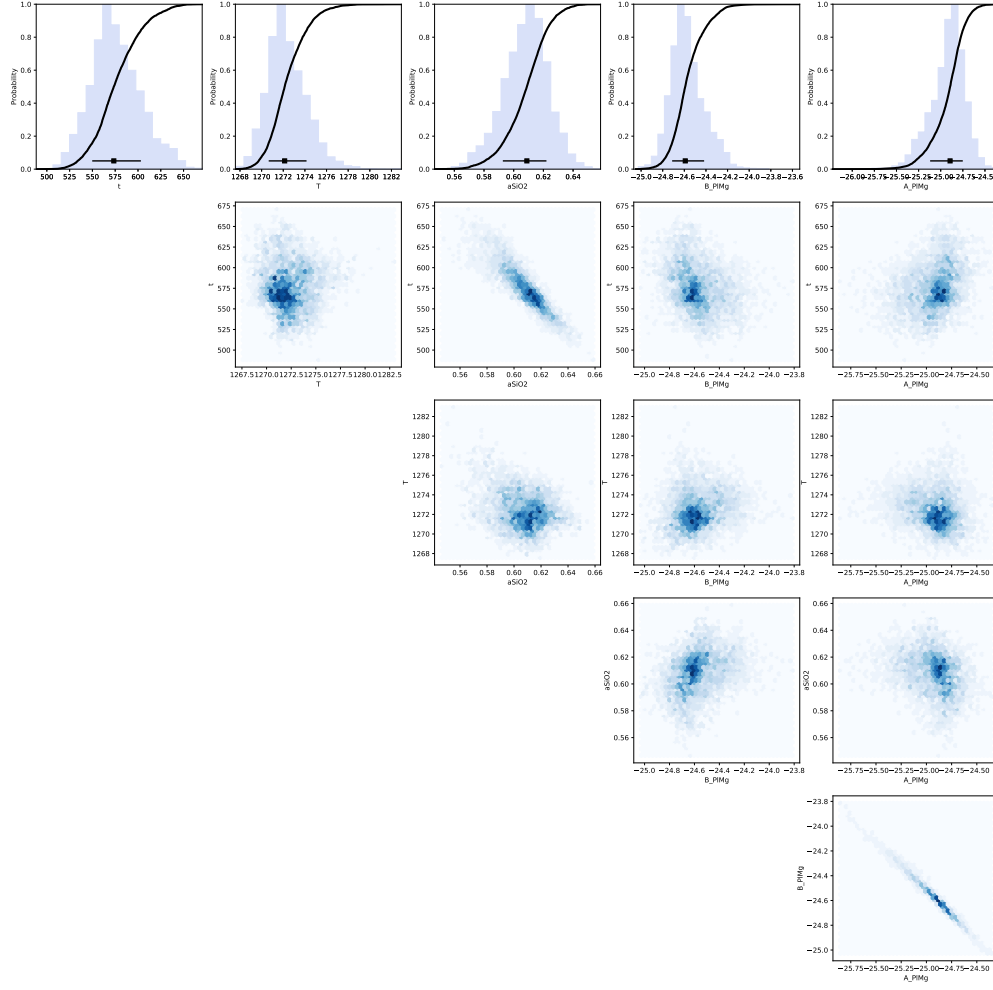


**Figure S82.** Bayesian inversion results for sample HOR\_3\_C3\_P2. Marginal plot showing the posterior distributions of the main intensive parameters modelled for the diffusion of Mg in Plagioclase:  $t$  is time (days),  $T$  is temperature ( $^{\circ}\text{C}$ ),  $a_{\text{SiO}_2}$  is  $a_{\text{SiO}_2}$ ,  $B_{\text{PlMg}}$  and  $A_{\text{PlMg}}$  are the intercept and slope of the Mg-in-plagioclase partitioning relationship. The top row shows histograms (blue bars) and probability density functions (black curves) of the aforementioned intensive parameters. The black bar shows the median result and  $1\sigma$  standard deviation. The bottom four rows are density plots that show the trade offs between the different parameters.

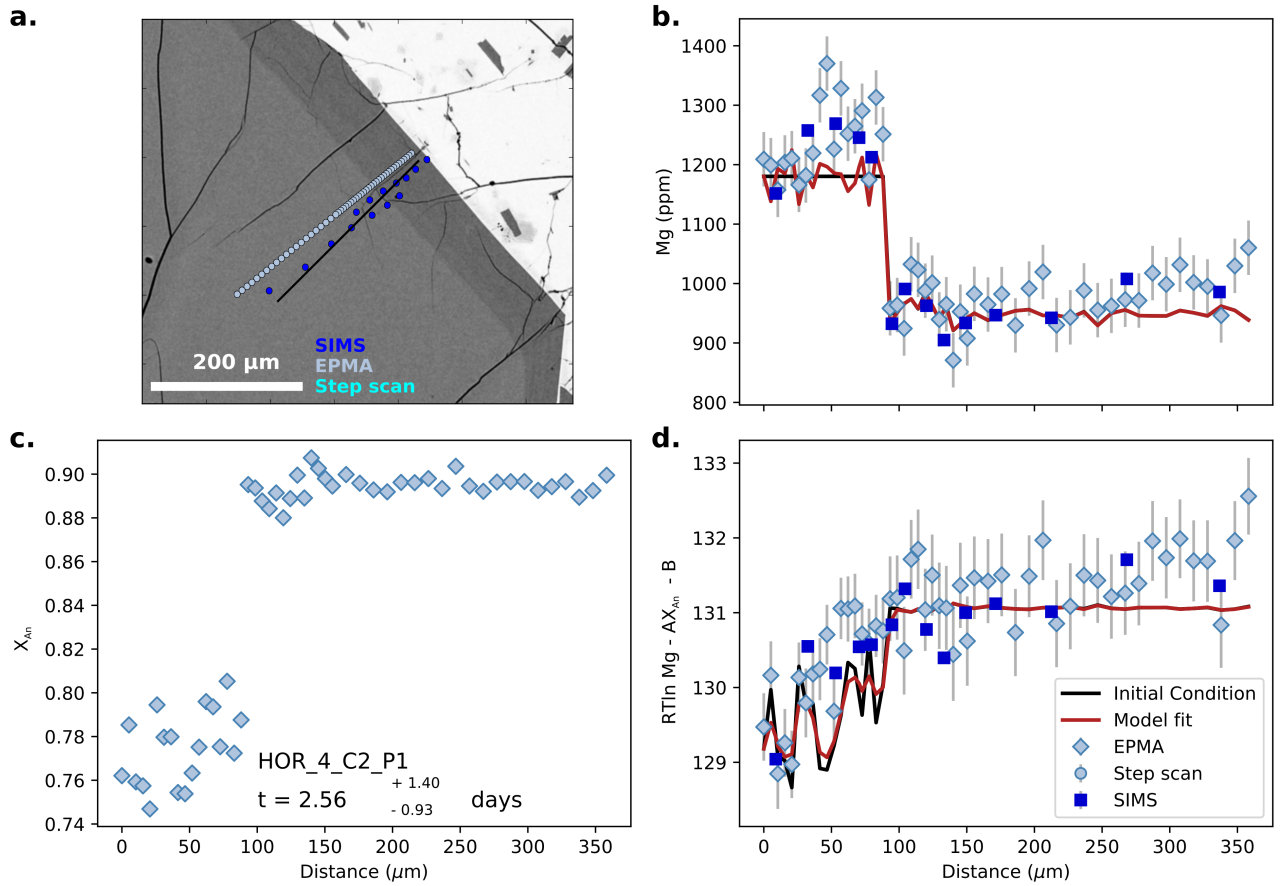


**Figure S83.** Data, initial conditions and model fits for plagioclase crystal HOR\_4\_C2\_P1. **a** is a BSE image of the plagioclase crystal showing the location of coarse SIMS spot analyses (blue spots), EPMA traverse (light blue spots) and SIMS step scan analyses (cyan points). Points from each profile were projected onto the black line. **b**, Mg compositional profile with point shapes and colours marked by analytical method. Dark blue squares are SIMS coarse spot analyses, light blue circles are SIMS step scan analyses and light blue diamonds are EPMA analyses. The black line is calculated initial conditions used in the modelling, and the red line is the model fit using the maximum likelihood of all of the parameters used in the Bayesian inversion. **c**, Anorthite profile of plagioclase as measured by EPMA. **d**, calculated melt equivalent Mg in plagioclase using the most likely partitioning parameters estimated from the Bayesian inversion. Symbols and colours are the same as in **b**.

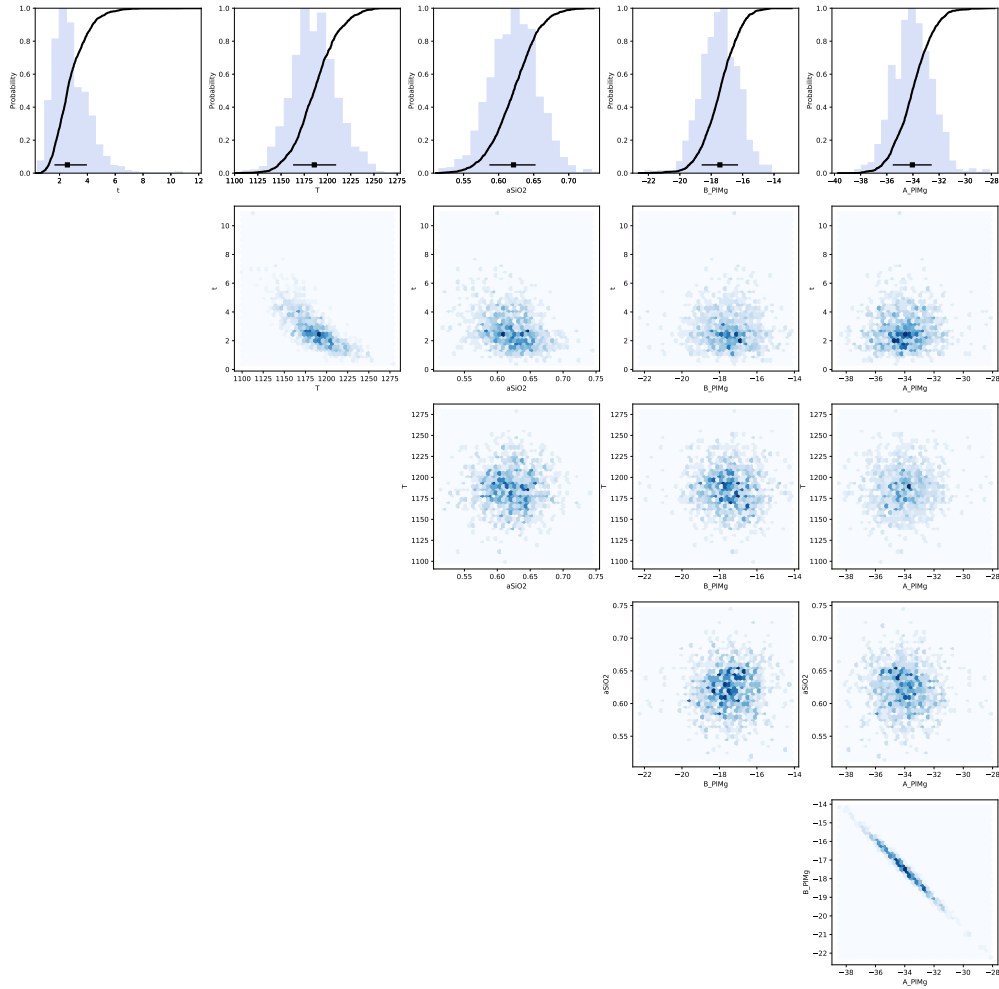


**Figure S84.** Bayesian inversion results for sample HOR\_4\_C2\_P1. Marginal plot showing the posterior distributions of the main intensive parameters modelled for the diffusion of Mg in Plagioclase:  $t$  is time (days),  $T$  is temperature ( $^{\circ}\text{C}$ ),  $a_{\text{SiO}_2}$  is  $a_{\text{SiO}_2}$ ,  $B_{\text{PlMg}}$  and  $A_{\text{PlMg}}$  are the intercept and slope of the Mg-in-plagioclase partitioning relationship. The top row shows histograms (blue bars) and probability density functions (black curves) of the aforementioned intensive parameters. The black bar shows the median result and  $1\sigma$  standard deviation. The bottom four rows are density plots that show the trade offs between the different parameters.

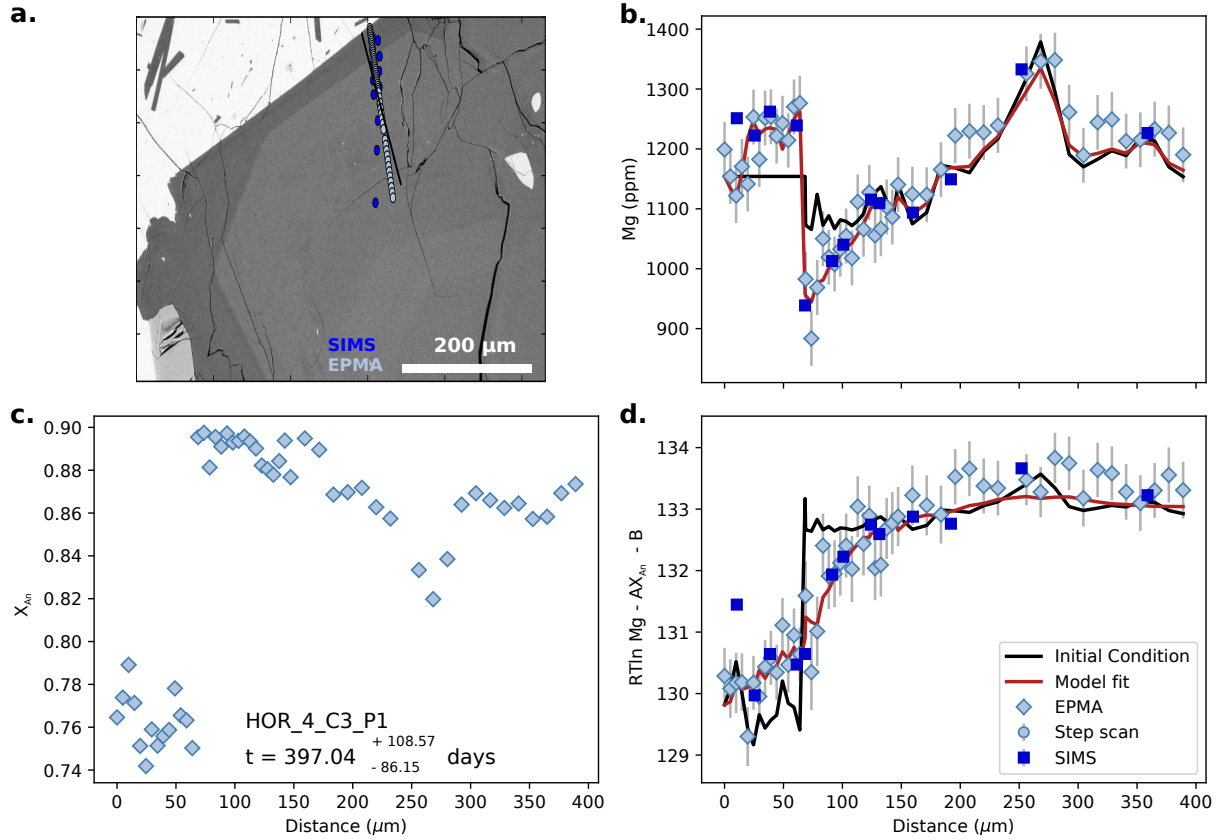


**Figure S85.** Data, initial conditions and model fits for plagioclase crystal HOR\_4\_C3\_P1. **a** is a BSE image of the plagioclase crystal showing the location of coarse SIMS spot analyses (blue spots), EPMA traverse (light blue spots) and SIMS step scan analyses (cyan points). Points from each profile were projected onto the black line. **b**, Mg compositional profile with point shapes and colours marked by analytical method. Dark blue squares are SIMS coarse spot analyses, light blue circles are SIMS step scan analyses and light blue diamonds are EPMA analyses. The black line is calculated initial conditions used in the modelling, and the red line is the model fit using the maximum likelihood of all of the parameters used in the Bayesian inversion. **c**, Anorthite profile of plagioclase as measured by EPMA. **d**, calculated melt equivalent Mg in plagioclase using the most likely partitioning parameters estimated from the Bayesian inversion. Symbols and colours are the same as in **b**.



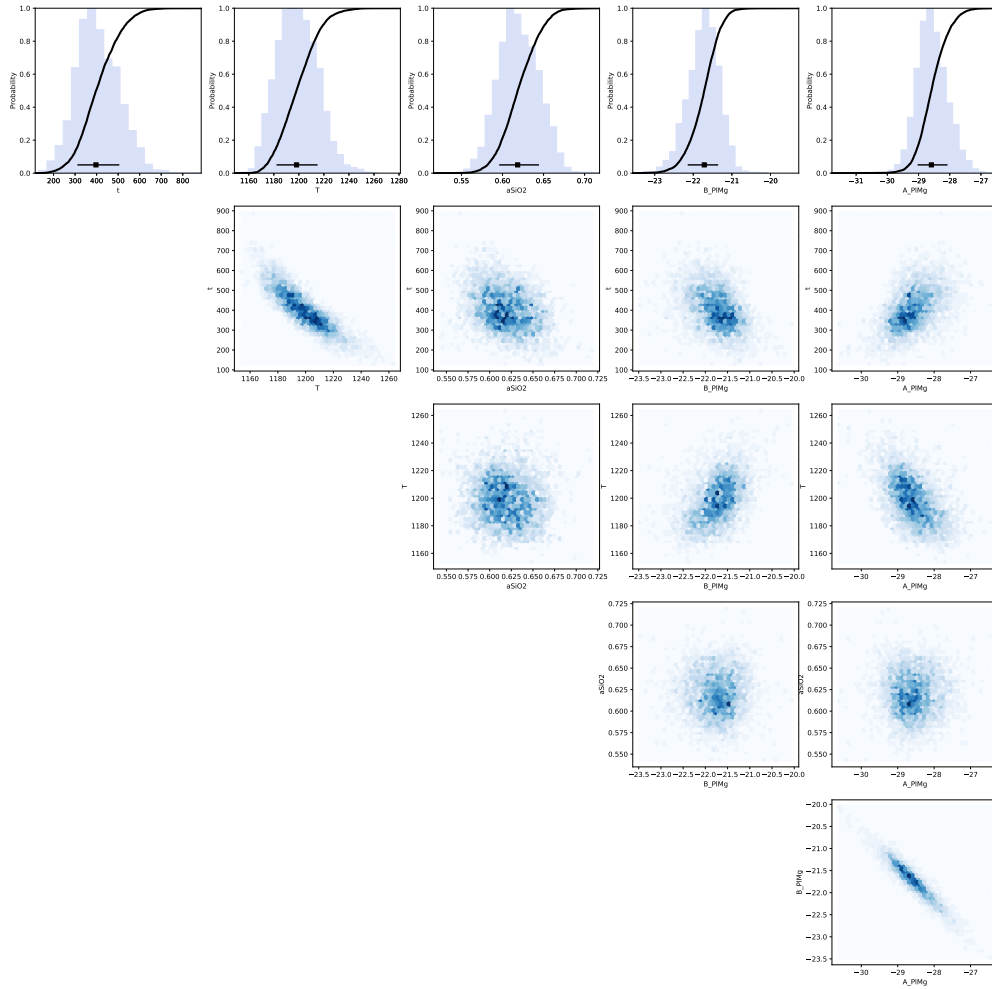


**Figure S86.** Bayesian inversion results for sample HOR\_4\_C3\_P1. Marginal plot showing the posterior distributions of the main intensive parameters modelled for the diffusion of Mg in Plagioclase:  $t$  is time (days),  $T$  is temperature ( $^{\circ}\text{C}$ ),  $a_{\text{SiO}_2}$  is  $a_{\text{SiO}_2}$ ,  $B_{\text{PlMg}}$  and  $A_{\text{PlMg}}$  are the intercept and slope of the Mg-in-plagioclase partitioning relationship. The top row shows histograms (blue bars) and probability density functions (black curves) of the aforementioned intensive parameters. The black bar shows the median result and  $1\sigma$  standard deviation. The bottom four rows are density plots that show the trade offs between the different parameters.

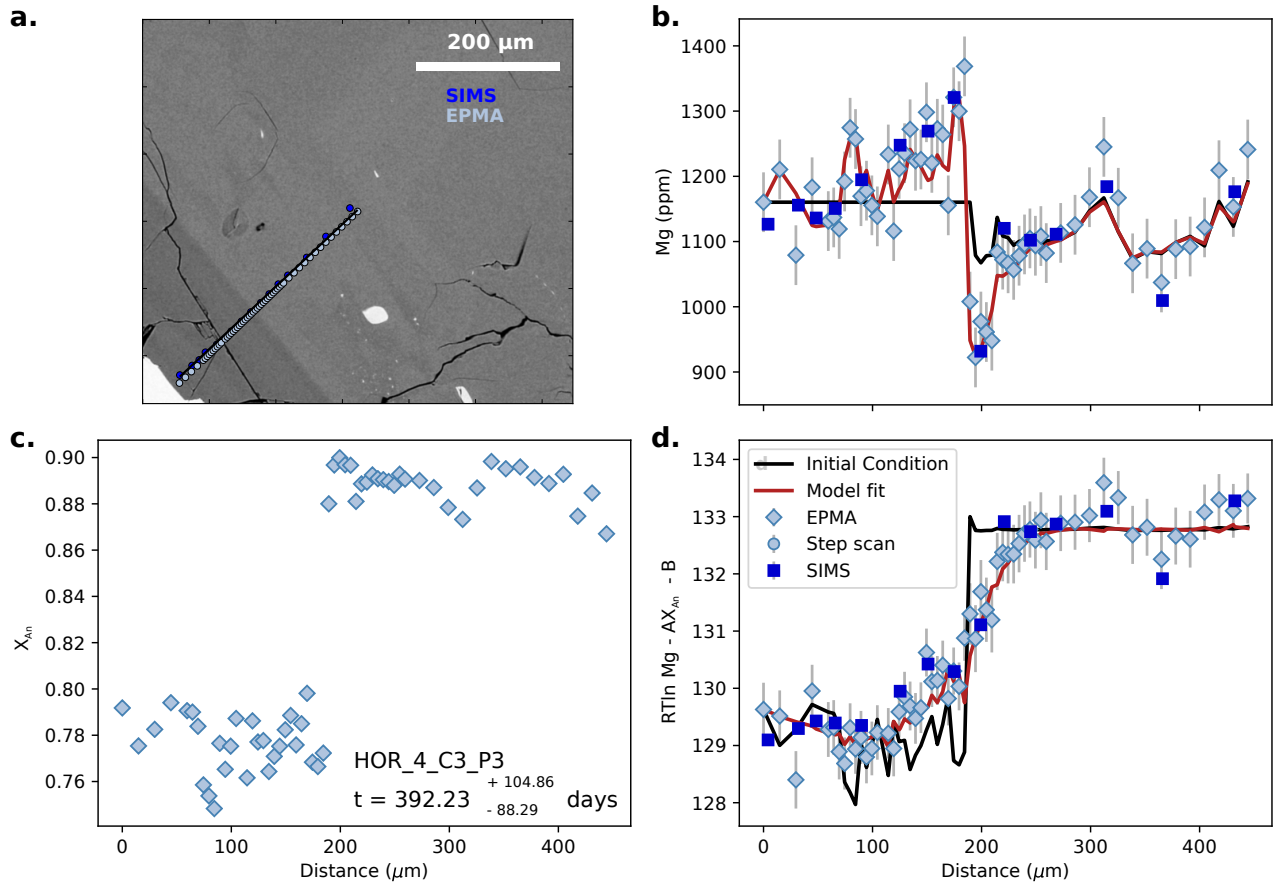


**Figure S87.** Data, initial conditions and model fits for plagioclase crystal HOR\_4\_C3\_P3. **a** is a BSE image of the plagioclase crystal showing the location of coarse SIMS spot analyses (blue spots), EPMA traverse (light blue spots) and SIMS step scan analyses (cyan points). Points from each profile were projected onto the black line. **b**, Mg compositional profile with point shapes and colours marked by analytical method. Dark blue squares are SIMS coarse spot analyses, light blue circles are SIMS step scan analyses and light blue diamonds are EPMA analyses. The black line is calculated initial conditions used in the modelling, and the red line is the model fit using the maximum likelihood of all of the parameters used in the Bayesian inversion. **c**, Anorthite profile of plagioclase as measured by EPMA. **d**, calculated melt equivalent Mg in plagioclase using the most likely partitioning parameters estimated from the Bayesian inversion. Symbols and colours are the same as in **b**.

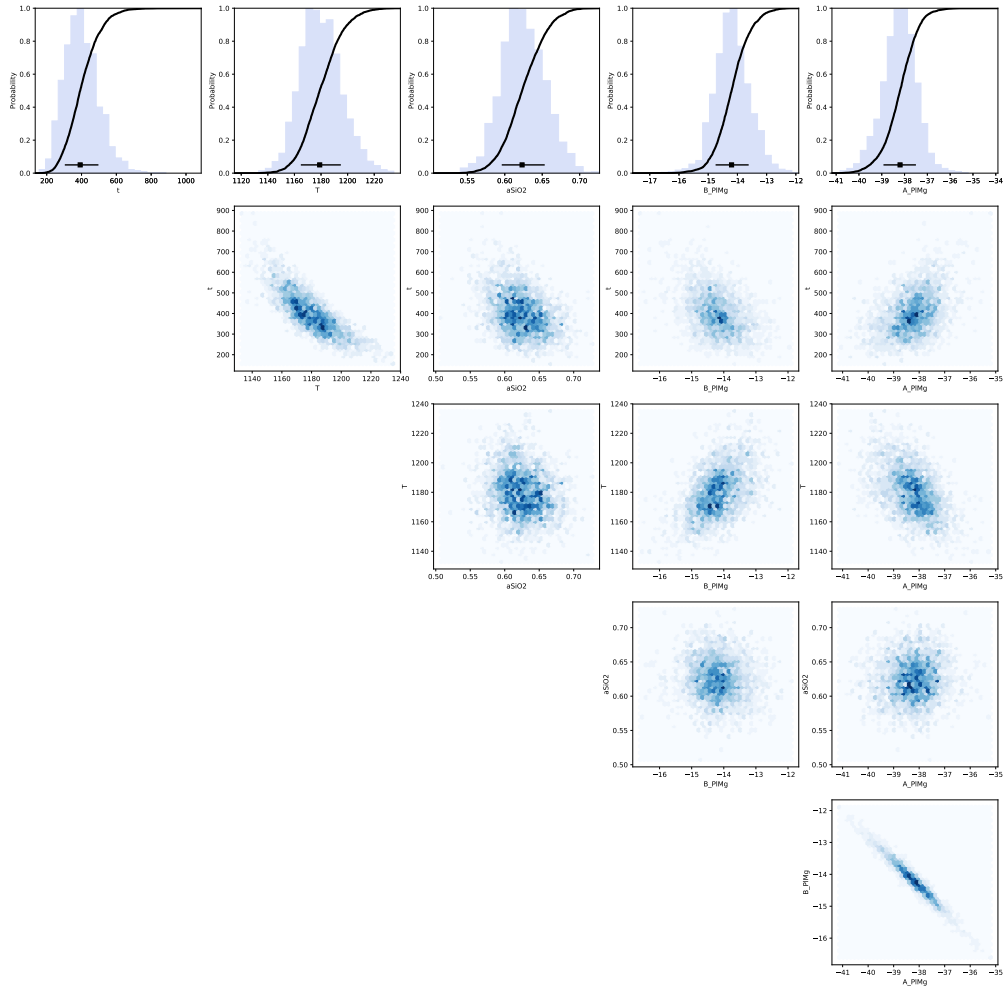


**Figure S88.** Bayesian inversion results for sample HOR\_4\_C3\_P3. Marginal plot showing the posterior distributions of the main intensive parameters modelled for the diffusion of Mg in Plagioclase:  $t$  is time (days),  $T$  is temperature ( $^{\circ}\text{C}$ ),  $a_{\text{SiO}_2}$  is  $a_{\text{SiO}_2}$ ,  $B_{\text{PlMg}}$  and  $A_{\text{PlMg}}$  are the intercept and slope of the Mg-in-plagioclase partitioning relationship. The top row shows histograms (blue bars) and probability density functions (black curves) of the aforementioned intensive parameters. The black bar shows the median result and  $1\sigma$  standard deviation. The bottom four rows are density plots that show the trade offs between the different parameters.

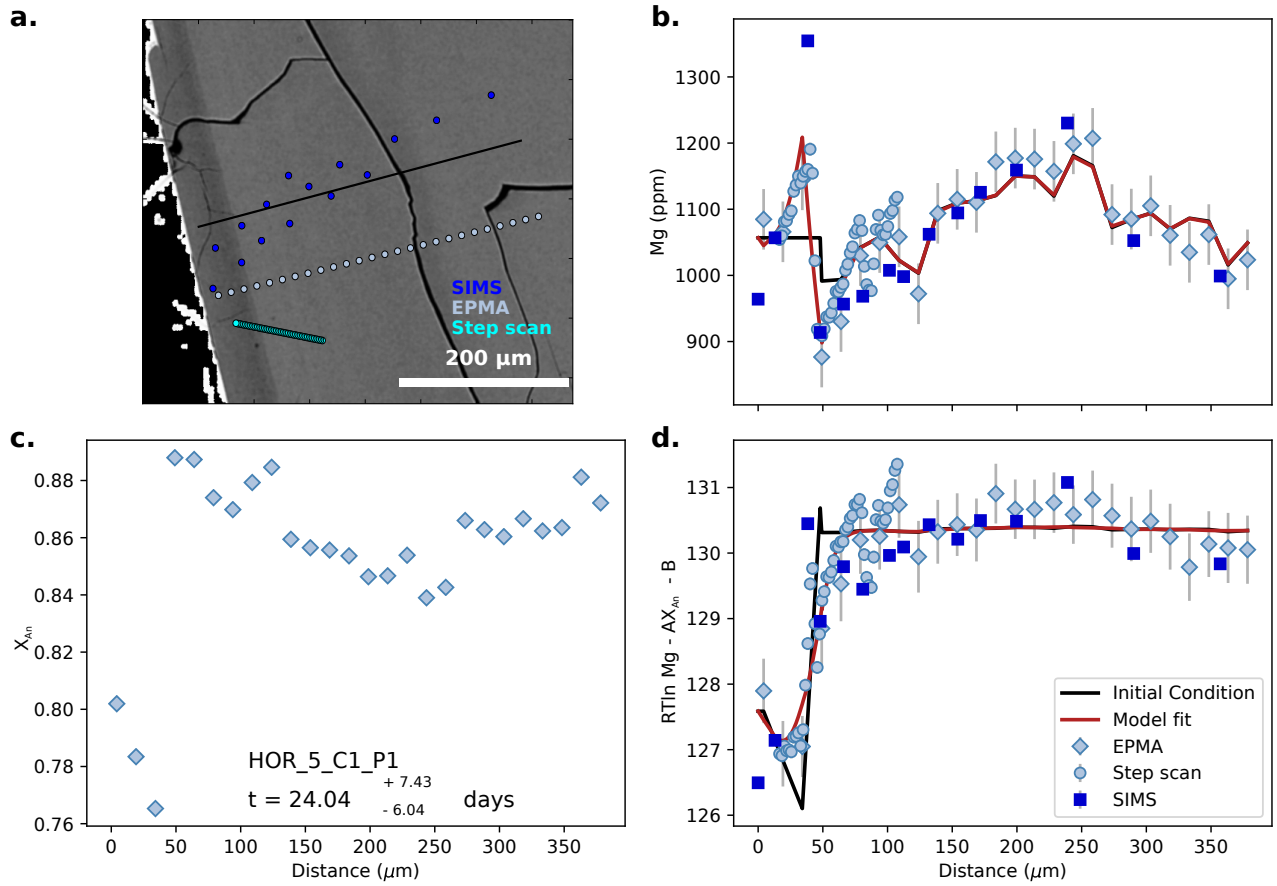


**Figure S89.** Data, initial conditions and model fits for plagioclase crystal HOR\_5\_C1\_P1. **a** is a BSE image of the plagioclase crystal showing the location of coarse SIMS spot analyses (blue spots), EPMA traverse (light blue spots) and SIMS step scan analyses (cyan points). Points from each profile were projected onto the black line. **b**, Mg compositional profile with point shapes and colours marked by analytical method. Dark blue squares are SIMS coarse spot analyses, light blue circles are SIMS step scan analyses and light blue diamonds are EPMA analyses. The black line is calculated initial conditions used in the modelling, and the red line is the model fit using the maximum likelihood of all of the parameters used in the Bayesian inversion. **c**, Anorthite profile of plagioclase as measured by EPMA. **d**, calculated melt equivalent Mg in plagioclase using the most likely partitioning parameters estimated from the Bayesian inversion. Symbols and colours are the same as in **b**.

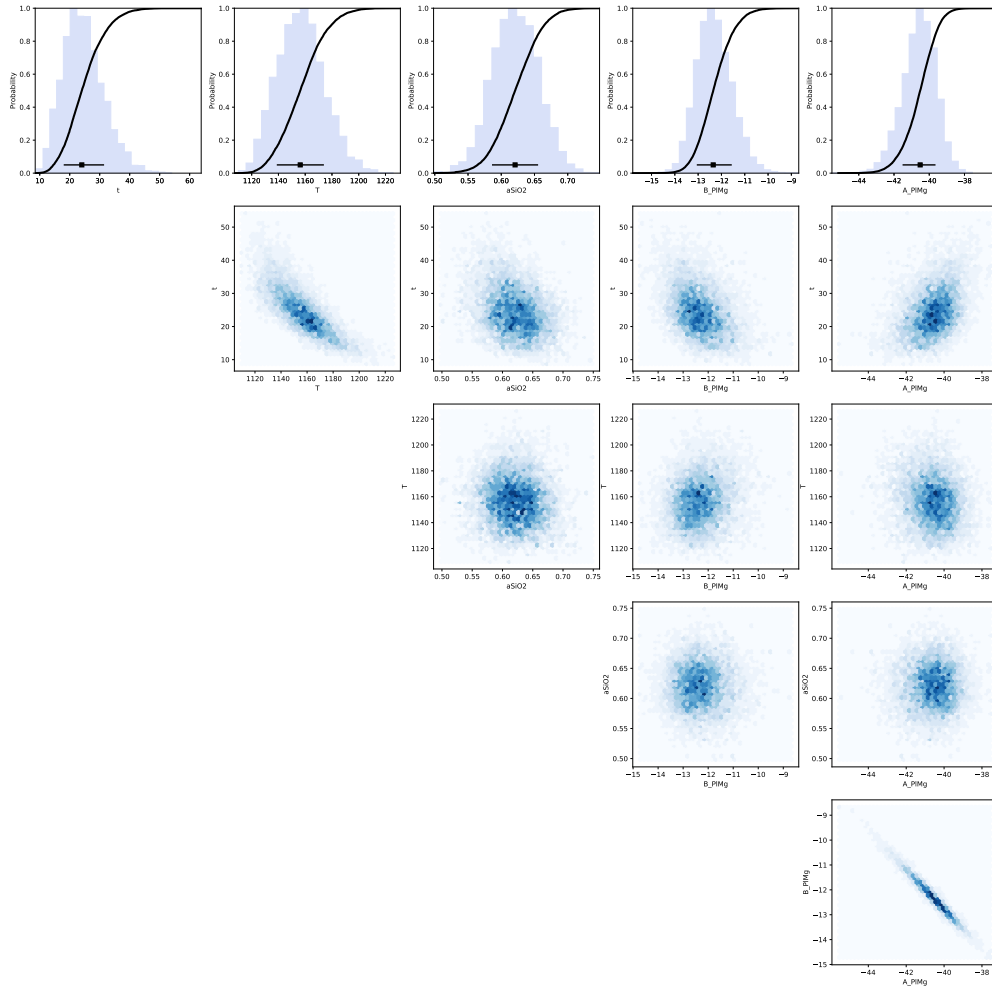


**Figure S90.** Bayesian inversion results for sample HOR\_5\_C1\_P1. Marginal plot showing the posterior distributions of the main intensive parameters modelled for the diffusion of Mg in Plagioclase:  $t$  is time (days),  $T$  is temperature ( $^{\circ}\text{C}$ ),  $a_{\text{SiO}_2}$  is  $a_{\text{SiO}_2}$ ,  $B_{\text{PlMg}}$  and  $A_{\text{PlMg}}$  are the intercept and slope of the Mg-in-plagioclase partitioning relationship. The top row shows histograms (blue bars) and probability density functions (black curves) of the aforementioned intensive parameters. The black bar shows the median result and  $1\sigma$  standard deviation. The bottom four rows are density plots that show the trade offs between the different parameters.

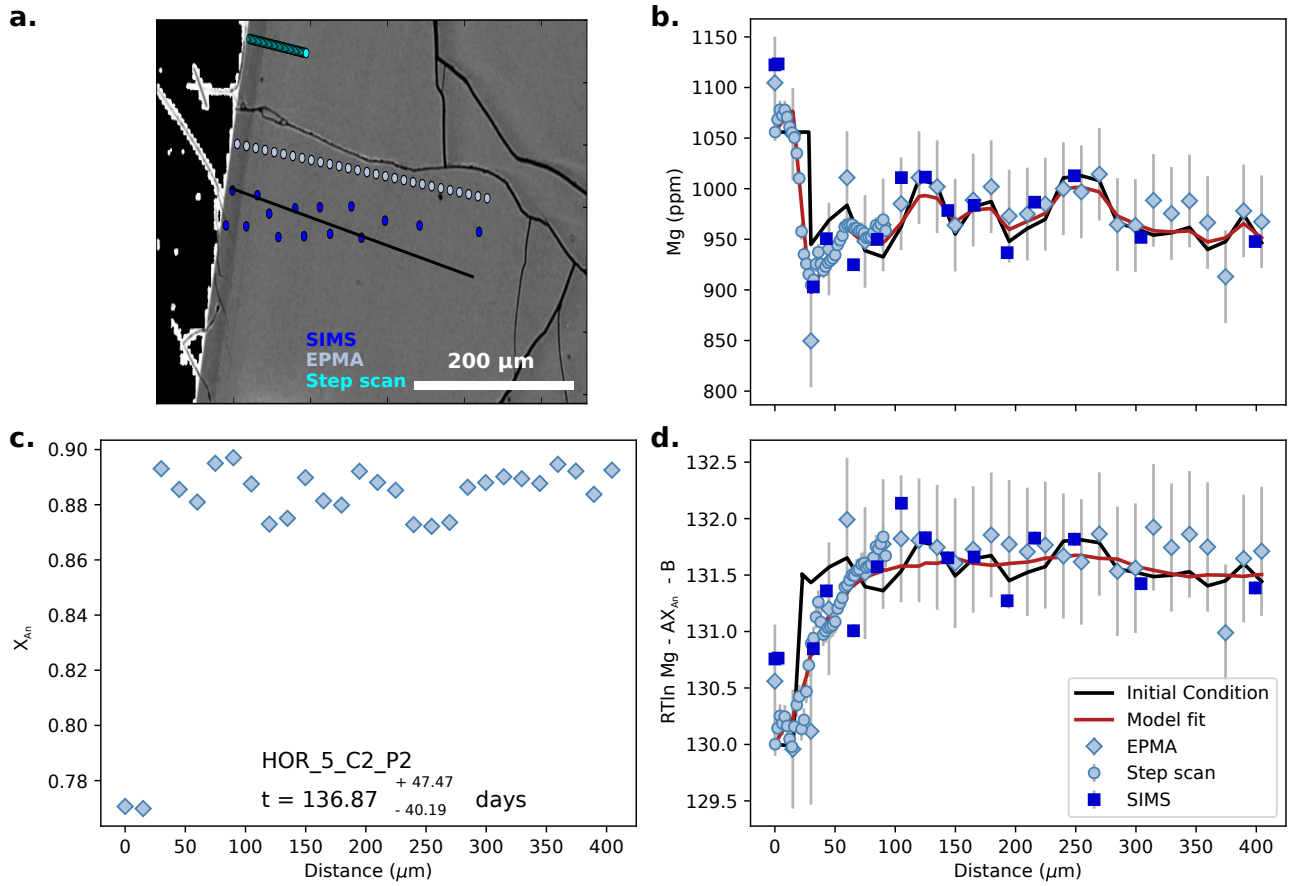


**Figure S91.** Data, initial conditions and model fits for plagioclase crystal HOR\_5\_C2\_P2. **a** is a BSE image of the plagioclase crystal showing the location of coarse SIMS spot analyses (blue spots), EPMA traverse (light blue spots) and SIMS step scan analyses (cyan points). Points from each profile were projected onto the black line. **b**, Mg compositional profile with point shapes and colours marked by analytical method. Dark blue squares are SIMS coarse spot analyses, light blue circles are SIMS step scan analyses and light blue diamonds are EPMA analyses. The black line is calculated initial conditions used in the modelling, and the red line is the model fit using the maximum likelihood of all of the parameters used in the Bayesian inversion. **c**, Anorthite profile of plagioclase as measured by EPMA. **d**, calculated melt equivalent Mg in plagioclase using the most likely partitioning parameters estimated from the Bayesian inversion. Symbols and colours are the same as in **b**.

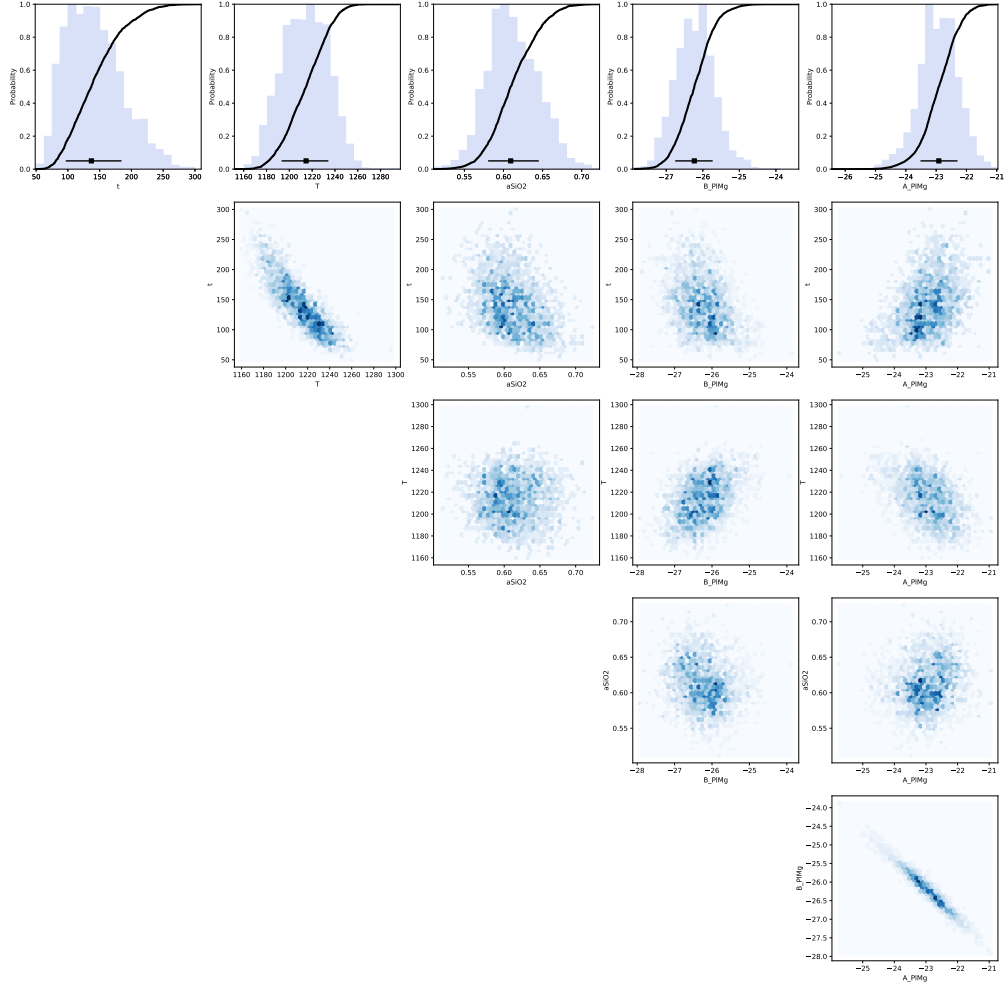


**Figure S92.** Bayesian inversion results for sample HOR\_5\_C2\_P2. Marginal plot showing the posterior distributions of main intensive parameters modelled for the diffusion of Mg in Plagioclase:  $t$  is time (days),  $T$  is temperature ( $^{\circ}\text{C}$ ),  $a_{\text{SiO}_2}$  is  $a_{\text{SiO}_2}$ ,  $B_{\text{PlMg}}$  and  $A_{\text{PlMg}}$  are the intercept and slope of the Mg-in-plagioclase partitioning relationship. The top row shows histograms (blue bars) and probability density functions (black curves) of the aforementioned intensive parameters. The black bar shows the median result and  $1\sigma$  standard deviation. The bottom four rows are density plots that show the trade offs between the different parameters.

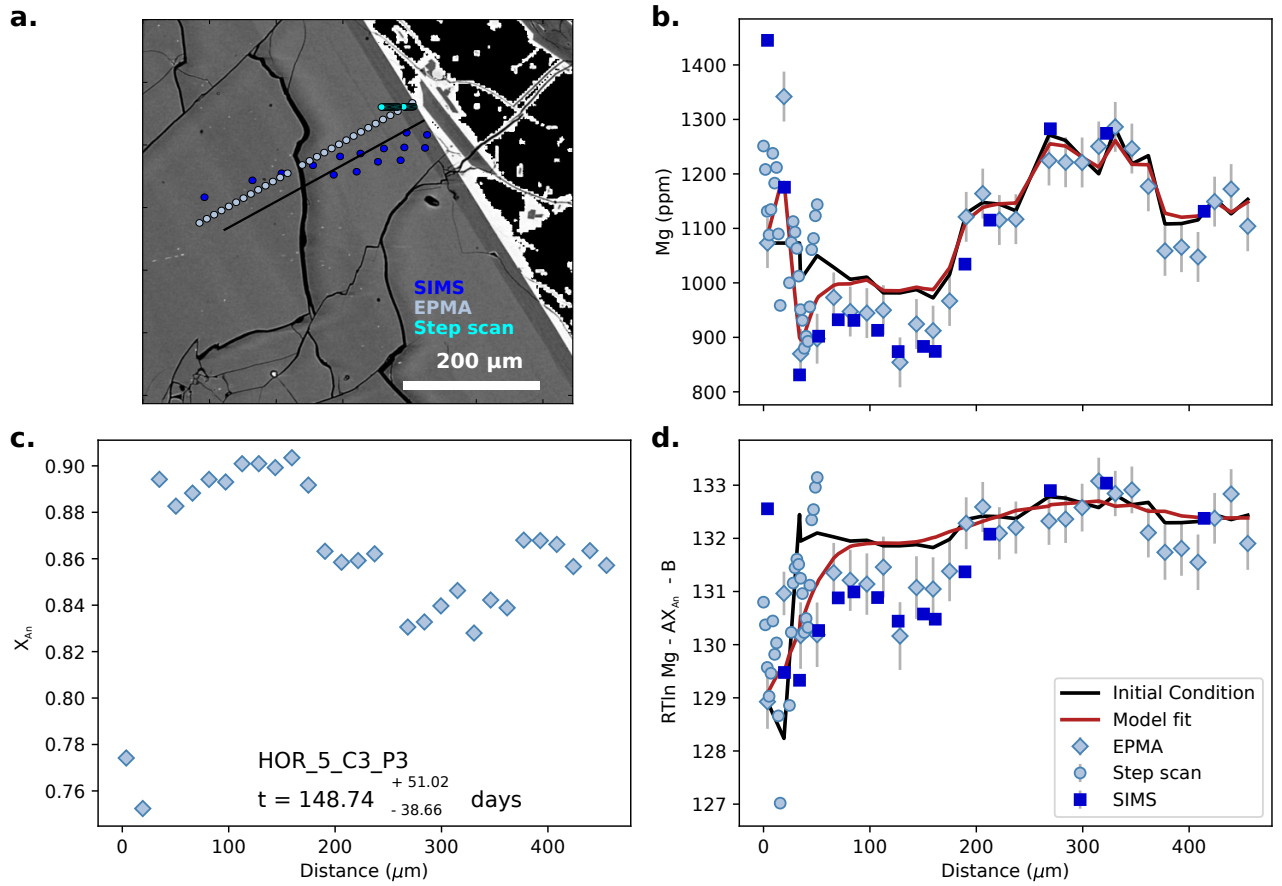


**Figure S93.** Data, initial conditions and model fits for plagioclase crystal HOR\_5\_C3\_P3. **a** is a BSE image of the plagioclase crystal showing the location of coarse SIMS spot analyses (blue spots), EPMA traverse (light blue spots) and SIMS step scan analyses (cyan points). Points from each profile were projected onto the black line. **b**, Mg compositional profile with point shapes and colours marked by analytical method. Dark blue squares are SIMS coarse spot analyses, light blue circles are SIMS step scan analyses and light blue diamonds are EPMA analyses. The black line is calculated initial conditions used in the modelling, and the red line is the model fit using the maximum likelihood of all of the parameters used in the Bayesian inversion. **c**, Anorthite profile of plagioclase as measured by EPMA. **d**, calculated melt equivalent Mg in plagioclase using the most likely partitioning parameters estimated from the Bayesian inversion. Symbols and colours are the same as in **b**.



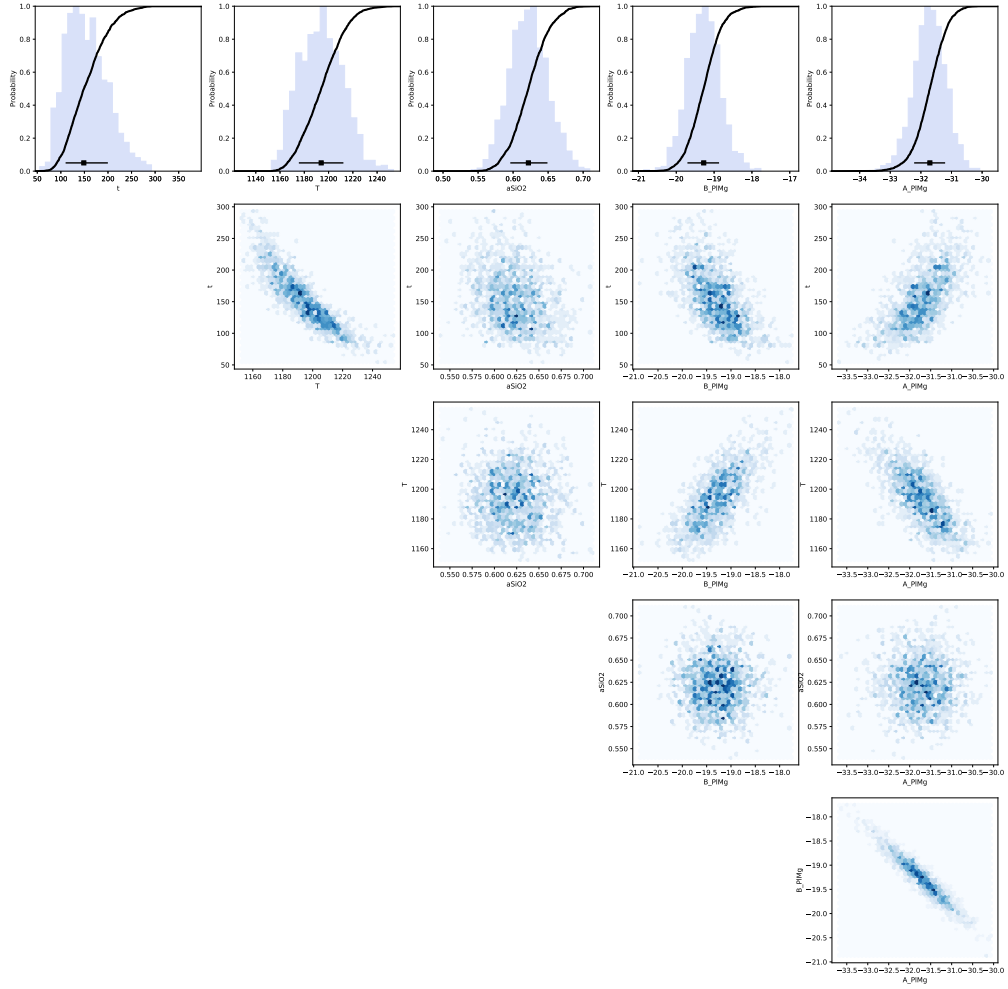


**Figure S94.** Bayesian inversion results for sample HOR\_5\_C3\_P3. Marginal plot showing the posterior distributions of main intensive parameters modelled for the diffusion of Mg in Plagioclase:  $t$  is time (days),  $T$  is temperature ( $^{\circ}\text{C}$ ),  $a\text{SiO}_2$  is  $a_{\text{SiO}_2}$ ,  $B_{\text{PlMg}}$  and  $A_{\text{PlMg}}$  are the intercept and slope of the Mg-in-plagioclase partitioning relationship. The top row shows histograms (blue bars) and probability density functions (black curves) of the aforementioned intensive parameters. The black bar shows the median result and  $1\sigma$  standard deviation. The bottom four rows are density plots that show the trade offs between the different parameters.

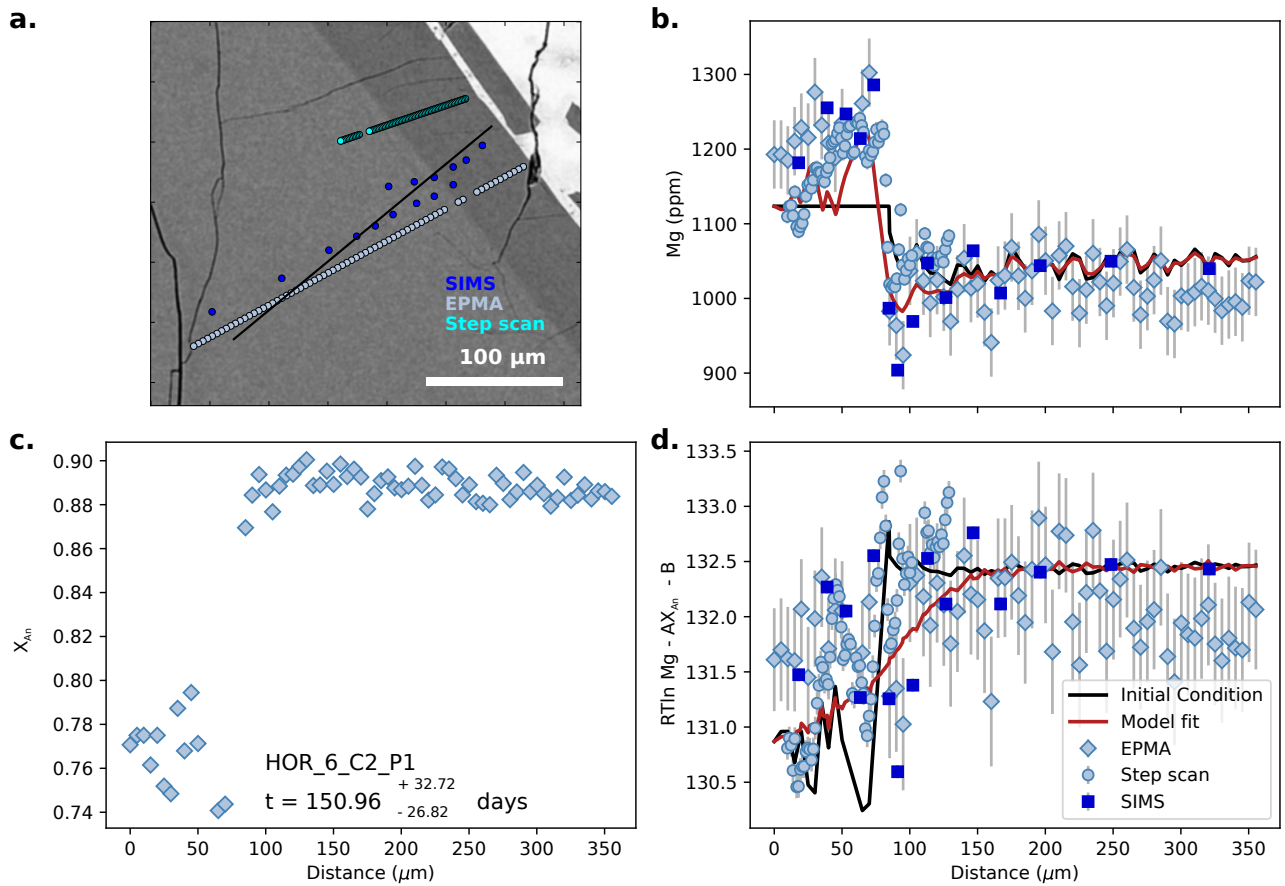


**Figure S95.** Data, initial conditions and model fits for plagioclase crystal HOR\_6\_C2\_P1. **a** is a BSE image of the plagioclase crystal showing the location of coarse SIMS spot analyses (blue spots), EPMA traverse (light blue spots) and SIMS step scan analyses (cyan points). Points from each profile were projected onto the black line. **b**, Mg compositional profile with point shapes and colours marked by analytical method. Dark blue squares are SIMS coarse spot analyses, light blue circles are SIMS step scan analyses and light blue diamonds are EPMA analyses. The black line is calculated initial conditions used in the modelling, and the red line is the model fit using the maximum likelihood of all of the parameters used in the Bayesian inversion. **c**, Anorthite profile of plagioclase as measured by EPMA. **d**, calculated melt equivalent Mg in plagioclase using the most likely partitioning parameters estimated from the Bayesian inversion. Symbols and colours are the same as in **b**.

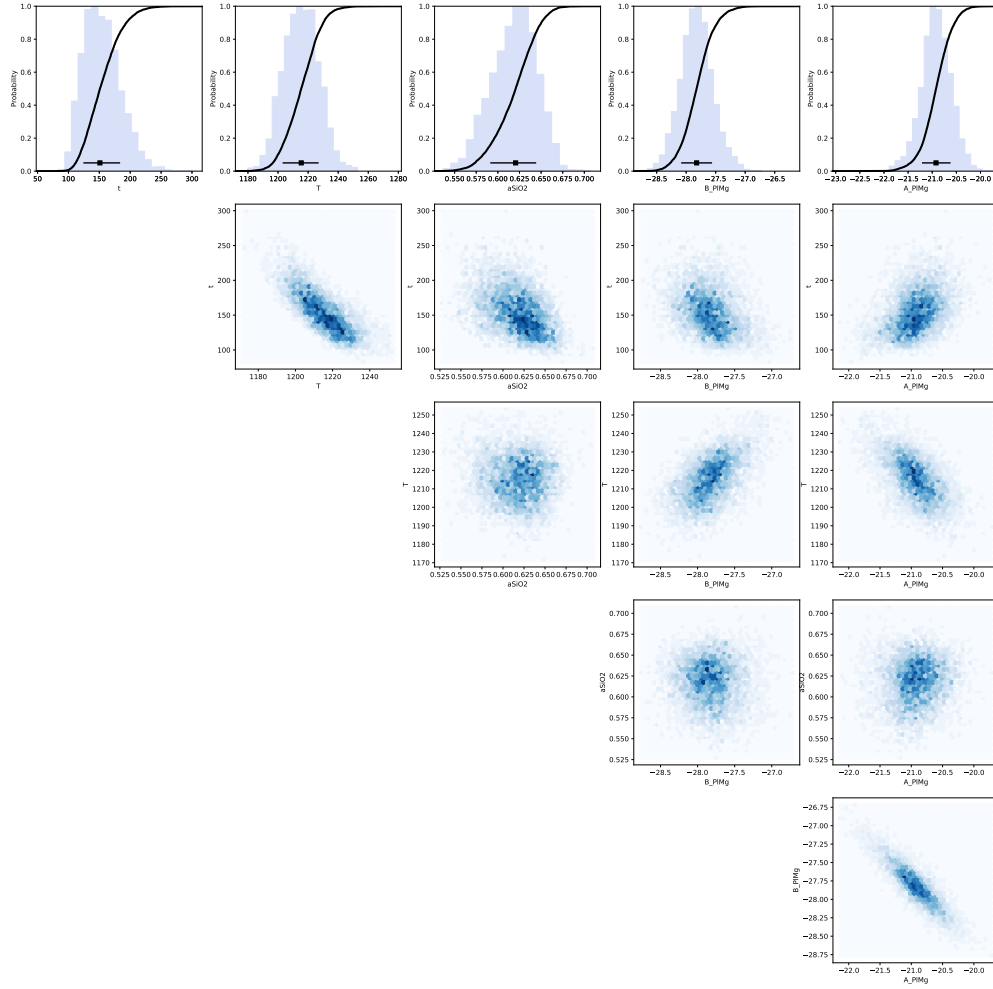


**Figure S96.** Bayesian inversion results for sample HOR\_6\_C2\_P1. Marginal plot showing the posterior distributions of the main intensive parameters modelled for the diffusion of Mg in Plagioclase:  $t$  is time (days),  $T$  is temperature ( $^{\circ}\text{C}$ ),  $a_{\text{SiO}_2}$  is  $a_{\text{SiO}_2}$ ,  $B_{\text{PlMg}}$  and  $A_{\text{PlMg}}$  are the intercept and slope of the Mg-in-plagioclase partitioning relationship. The top row shows histograms (blue bars) and probability density functions (black curves) of the aforementioned intensive parameters. The black bar shows the median result and  $1\sigma$  standard deviation. The bottom four rows are density plots that show the trade offs between the different parameters.

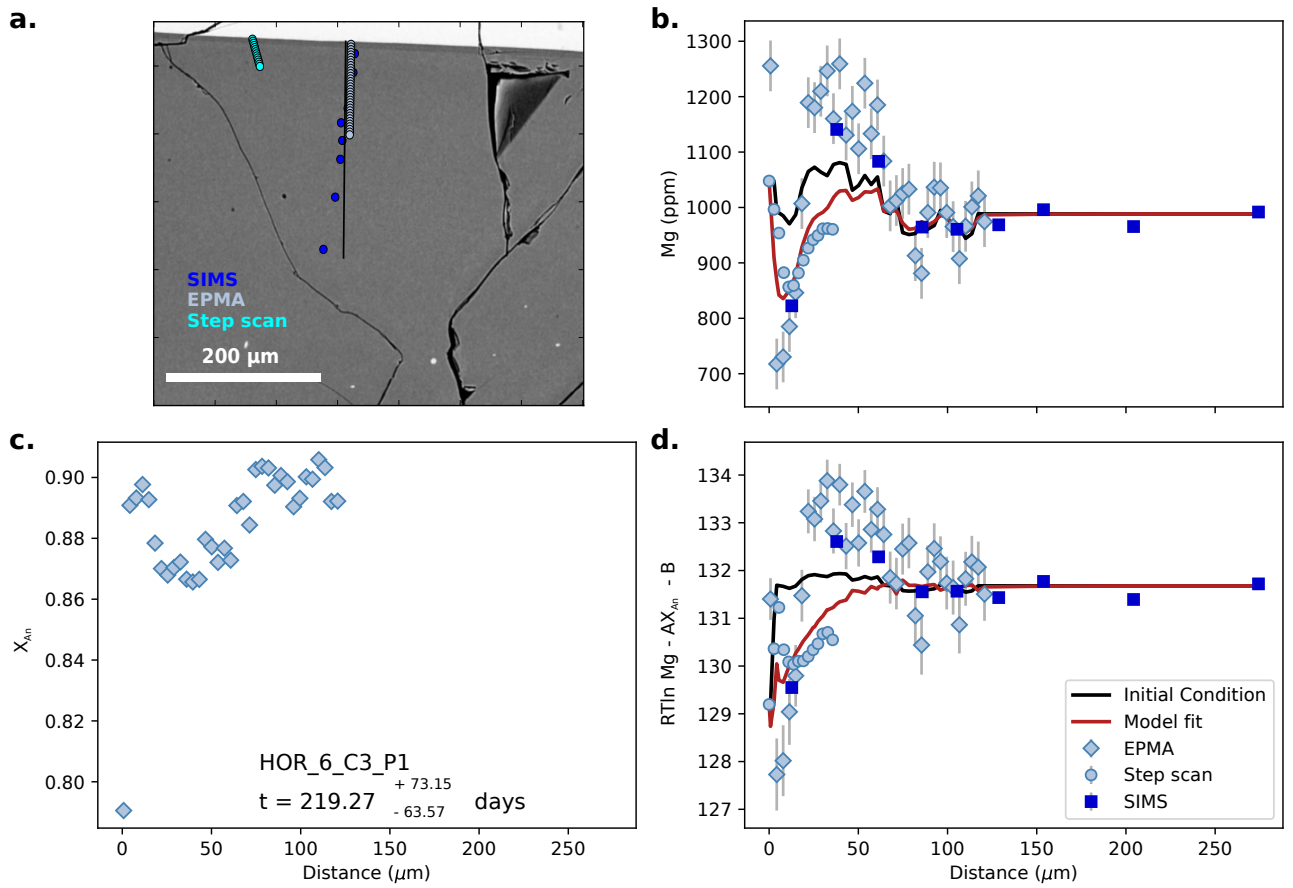


**Figure S97.** Data, initial conditions and model fits for plagioclase crystal HOR\_6\_C3\_P1. **a** is a BSE image of the plagioclase crystal showing the location of coarse SIMS spot analyses (blue spots), EPMA traverse (light blue spots) and SIMS step scan analyses (cyan points). Points from each profile were projected onto the black line. **b**, Mg compositional profile with point shapes and colours marked by analytical method. Dark blue squares are SIMS coarse spot analyses, light blue circles are SIMS step scan analyses and light blue diamonds are EPMA analyses. The black line is calculated initial conditions used in the modelling, and the red line is the model fit using the maximum likelihood of all of the parameters used in the Bayesian inversion. **c**, Anorthite profile of plagioclase as measured by EPMA. **d**, calculated melt equivalent Mg in plagioclase using the most likely partitioning parameters estimated from the Bayesian inversion. Symbols and colours are the same as in **b**.

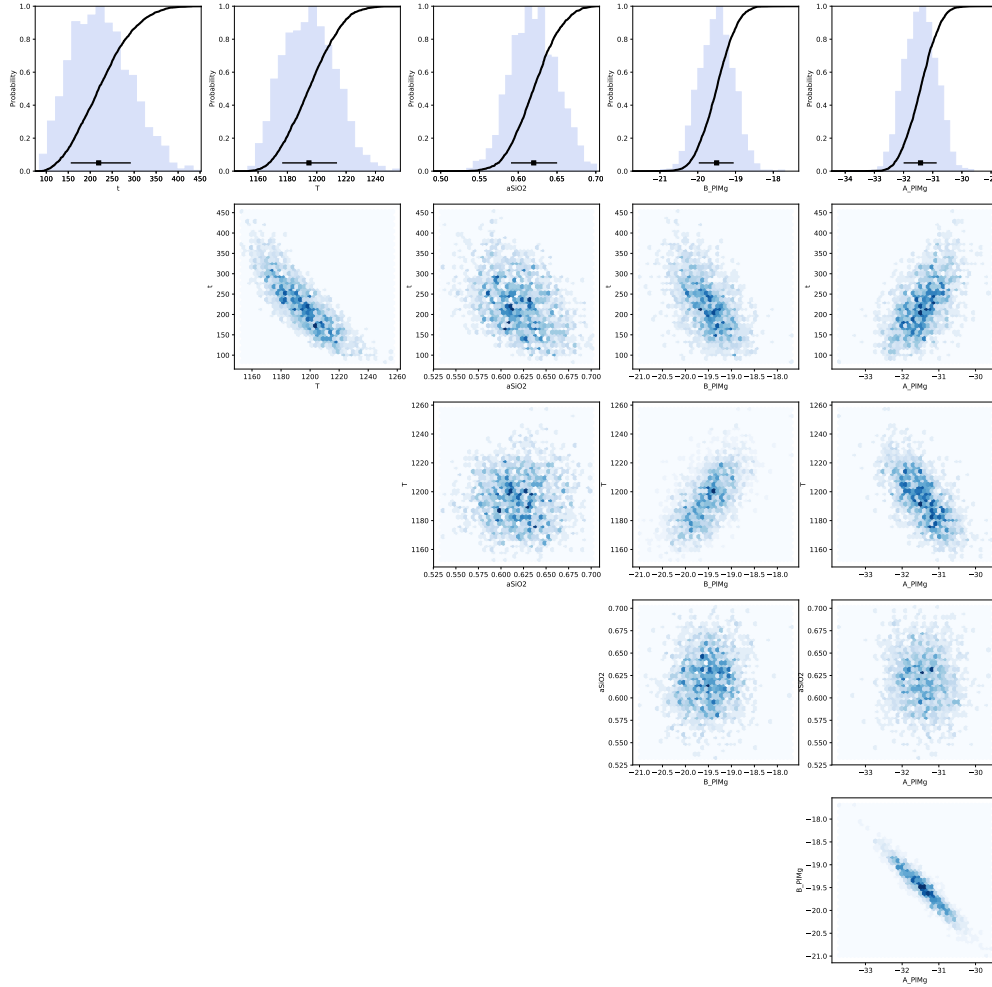


**Figure S98.** Bayesian inversion results for sample HOR\_6\_C3\_P1. Marginal plot showing the posterior distributions of the main intensive parameters modelled for the diffusion of Mg in Plagioclase:  $t$  is time (days),  $T$  is temperature ( $^{\circ}\text{C}$ ),  $a\text{SiO}_2$  is  $a_{\text{SiO}_2}$ ,  $B_{\text{PlMg}}$  and  $A_{\text{PlMg}}$  are the intercept and slope of the Mg-in-plagioclase partitioning relationship. The top row shows histograms (blue bars) and probability density functions (black curves) of the aforementioned intensive parameters. The black bar shows the median result and  $1\sigma$  standard deviation. The bottom four rows are density plots that show the trade offs between the different parameters.

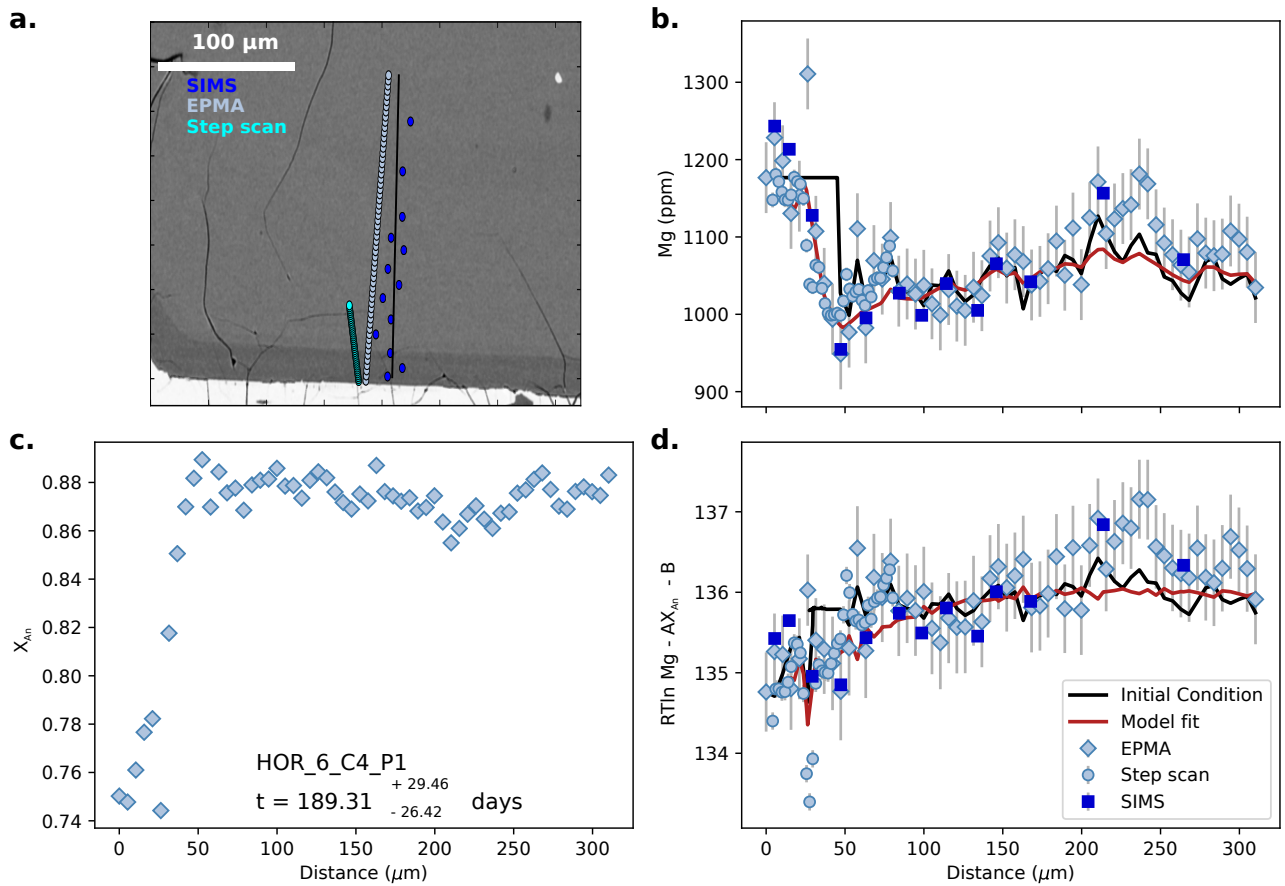


**Figure S99.** Data, initial conditions and model fits for plagioclase crystal HOR\_6\_C4\_P1. **a** is a BSE image of the plagioclase crystal showing the location of coarse SIMS spot analyses (blue spots), EPMA traverse (light blue spots) and SIMS step scan analyses (cyan points). Points from each profile were projected onto the black line. **b**, Mg compositional profile with point shapes and colours marked by analytical method. Dark blue squares are SIMS coarse spot analyses, light blue circles are SIMS step scan analyses and light blue diamonds are EPMA analyses. The black line is calculated initial conditions used in the modelling, and the red line is the model fit using the maximum likelihood of all of the parameters used in the Bayesian inversion. **c**, Anorthite profile of plagioclase as measured by EPMA. **d**, calculated melt equivalent Mg in plagioclase using the most likely partitioning parameters estimated from the Bayesian inversion. Symbols and colours are the same as in **b**.

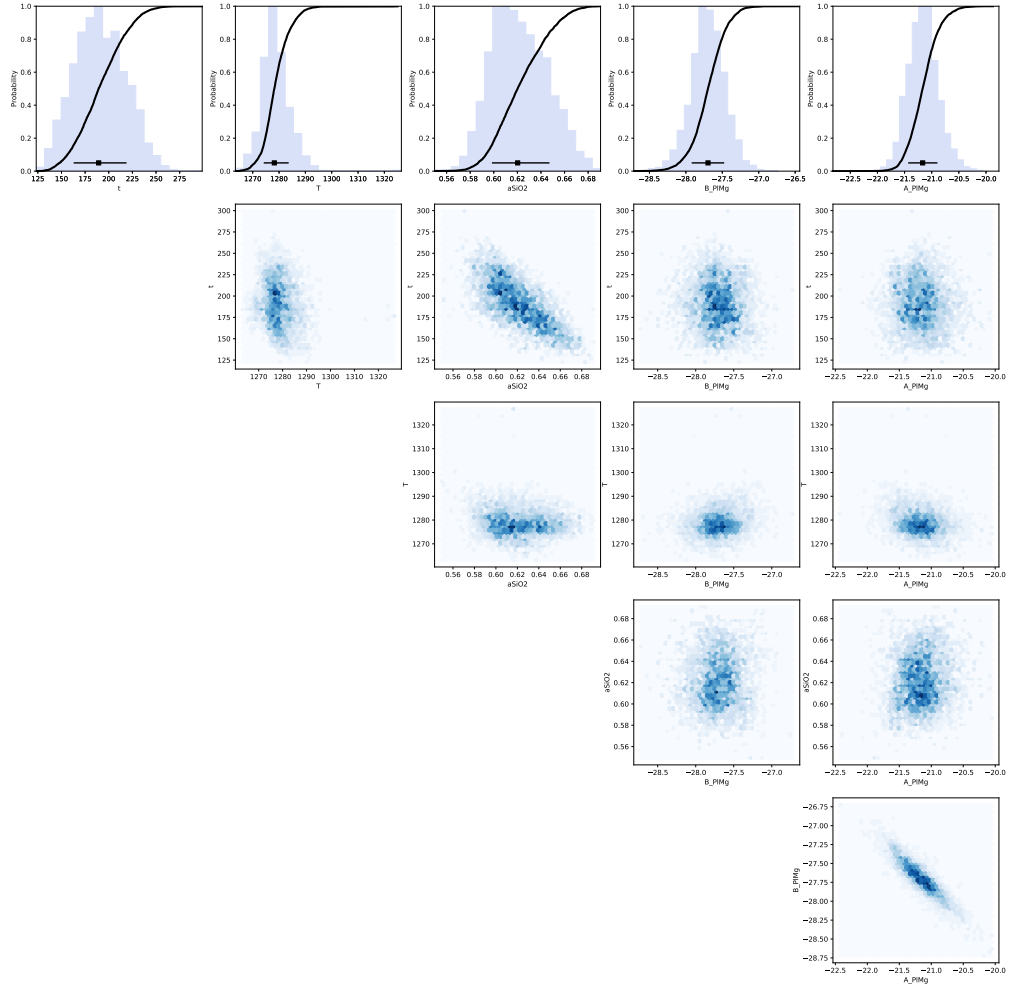


**Figure S100.** Bayesian inversion results for sample HOR\_6\_C4\_P1. Marginal plot showing the posterior distributions of the main intensive parameters modelled for the diffusion of Mg in Plagioclase:  $t$  is time (days),  $T$  is temperature ( $^{\circ}\text{C}$ ),  $a_{\text{SiO}_2}$  is  $a_{\text{SiO}_2}$ ,  $B_{\text{PlMg}}$  and  $A_{\text{PlMg}}$  are the intercept and slope of the Mg-in-plagioclase partitioning relationship. The top row shows histograms (blue bars) and probability density functions (black curves) of the aforementioned intensive parameters. The black bar shows the median result and  $1\sigma$  standard deviation. The bottom four rows are density plots that show the trade offs between the different parameters.

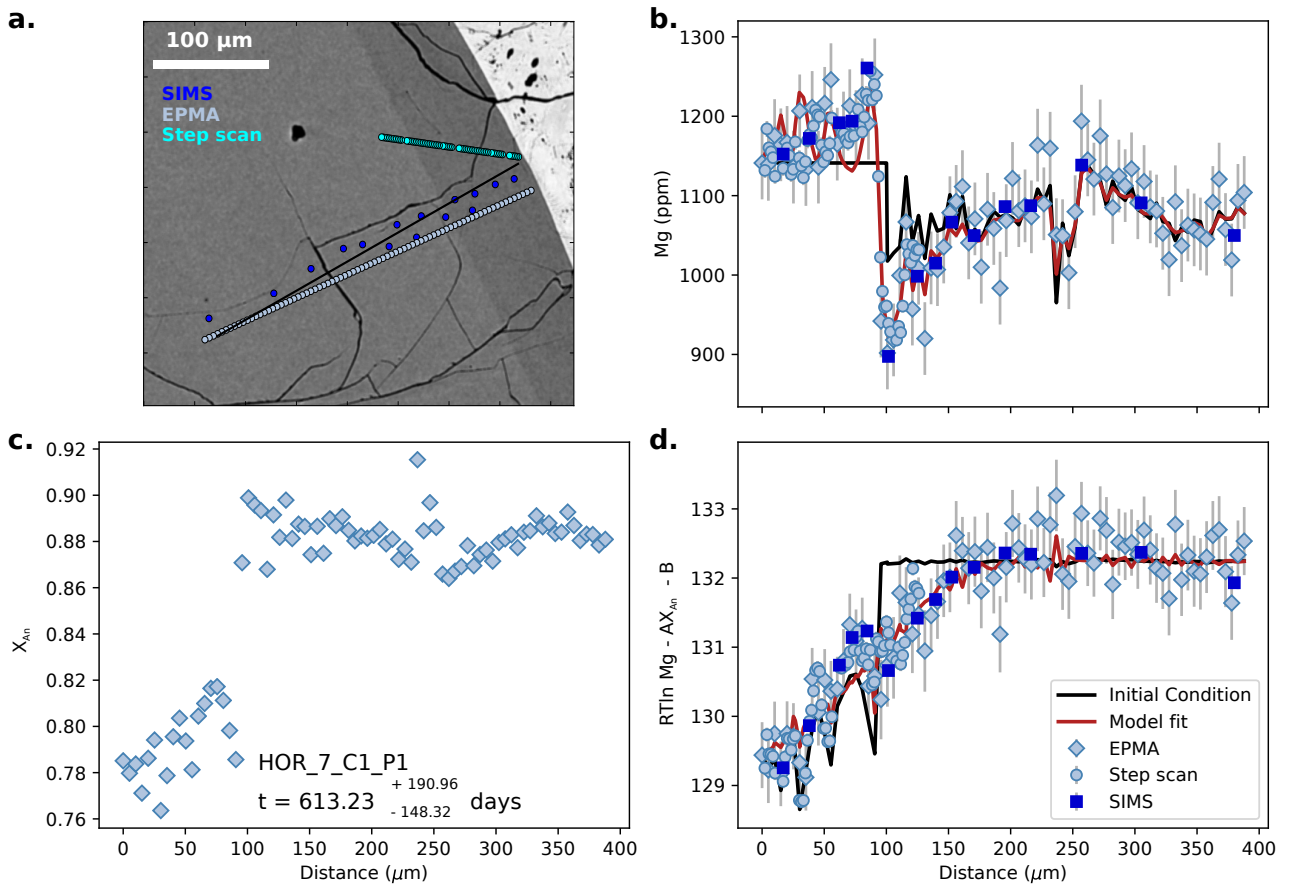


**Figure S101.** Data, initial conditions and model fits for plagioclase crystal HOR\_7\_C1\_P1. **a** is a BSE image of the plagioclase crystal showing the location of coarse SIMS spot analyses (blue spots), EPMA traverse (light blue spots) and SIMS step scan analyses (cyan points). Points from each profile were projected onto the black line. **b**, Mg compositional profile with point shapes and colours marked by analytical method. Dark blue squares are SIMS coarse spot analyses, light blue circles are SIMS step scan analyses and light blue diamonds are EPMA analyses. The black line is calculated initial conditions used in the modelling, and the red line is the model fit using the maximum likelihood of all of the parameters used in the Bayesian inversion. **c**, Anorthite profile of plagioclase as measured by EPMA. **d**, calculated melt equivalent Mg in plagioclase using the most likely partitioning parameters estimated from the Bayesian inversion. Symbols and colours are the same as in **b**.



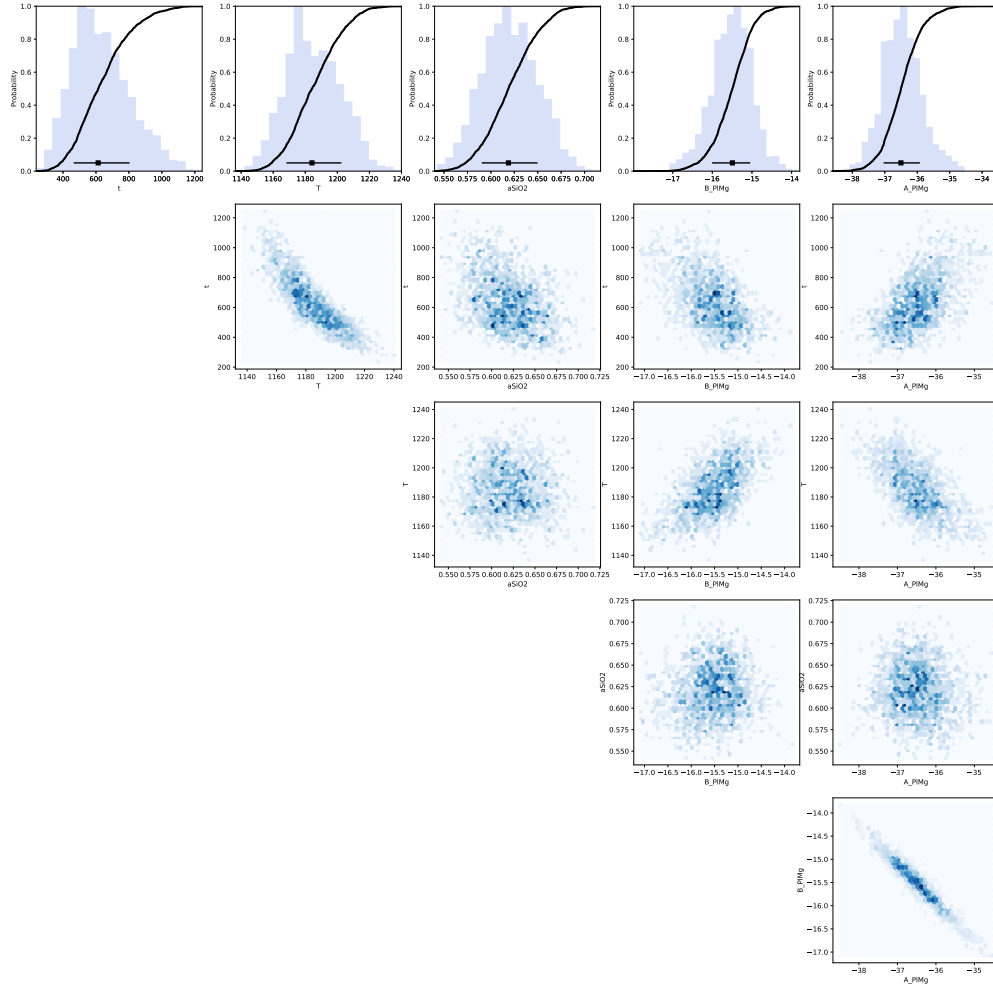


**Figure S102.** Bayesian inversion results for sample HOR\_7\_C1\_P1. Marginal plot showing the posterior distributions of the main intensive parameters modelled for the diffusion of Mg in Plagioclase:  $t$  is time (days),  $T$  is temperature ( $^{\circ}\text{C}$ ),  $a_{\text{SiO}_2}$  is  $a_{\text{SiO}_2}$ ,  $B_{\text{PlMg}}$  and  $A_{\text{PlMg}}$  are the intercept and slope of the Mg-in-plagioclase partitioning relationship. The top row shows histograms (blue bars) and probability density functions (black curves) of the aforementioned intensive parameters. The black bar shows the median result and  $1\sigma$  standard deviation. The bottom four rows are density plots that show the trade offs between the different parameters.

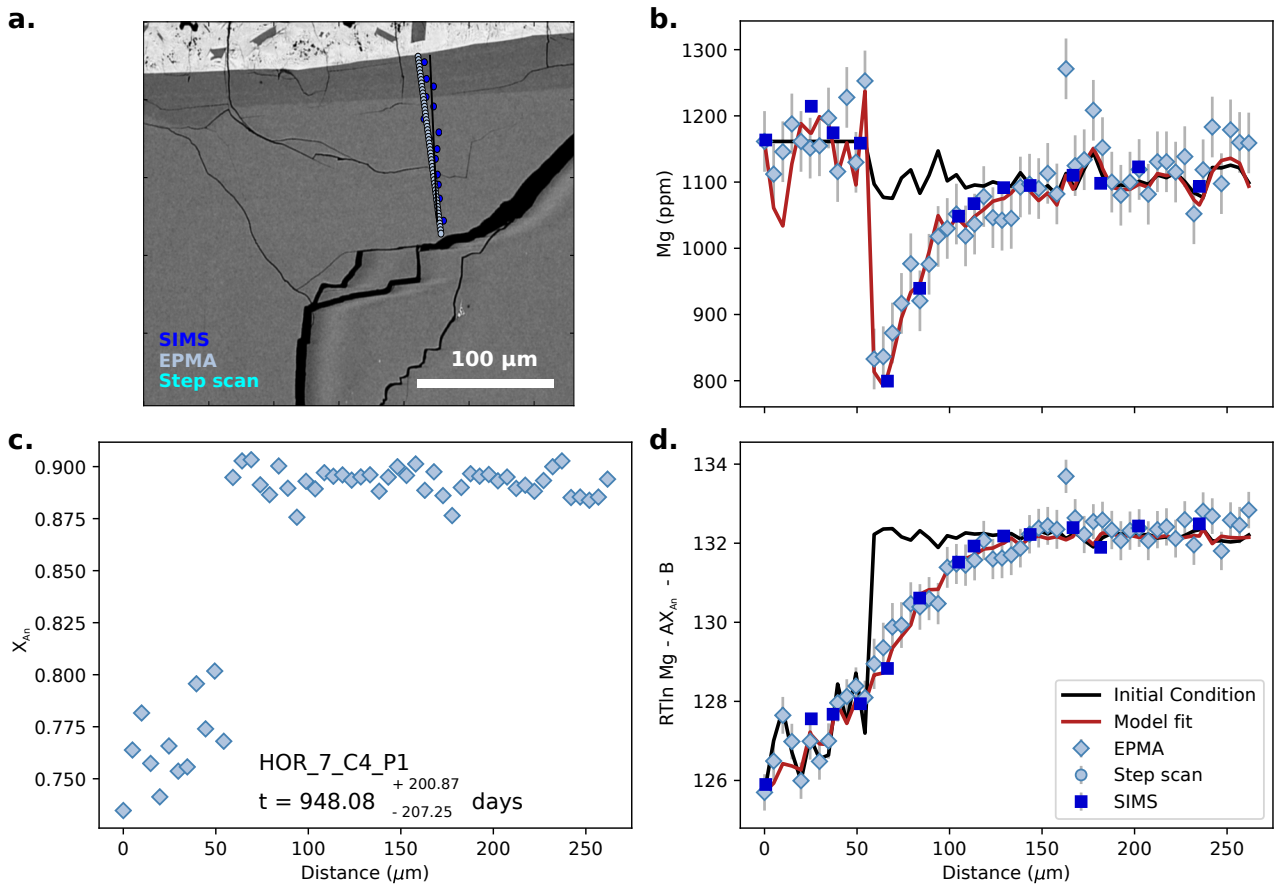


**Figure S103.** Data, initial conditions and model fits for plagioclase crystal HOR\_7\_C4\_P1. **a** is a BSE image of the plagioclase crystal showing the location of coarse SIMS spot analyses (blue spots), EPMA traverse (light blue spots) and SIMS step scan analyses (cyan points). Points from each profile were projected onto the black line. **b**, Mg compositional profile with point shapes and colours marked by analytical method. Dark blue squares are SIMS coarse spot analyses, light blue circles are SIMS step scan analyses and light blue diamonds are EPMA analyses. The black line is calculated initial conditions used in the modelling, and the red line is the model fit using the maximum likelihood of all of the parameters used in the Bayesian inversion. **c**, Anorthite profile of plagioclase as measured by EPMA. **d**, calculated melt equivalent Mg in plagioclase using the most likely partitioning parameters estimated from the Bayesian inversion. Symbols and colours are the same as in **b**.

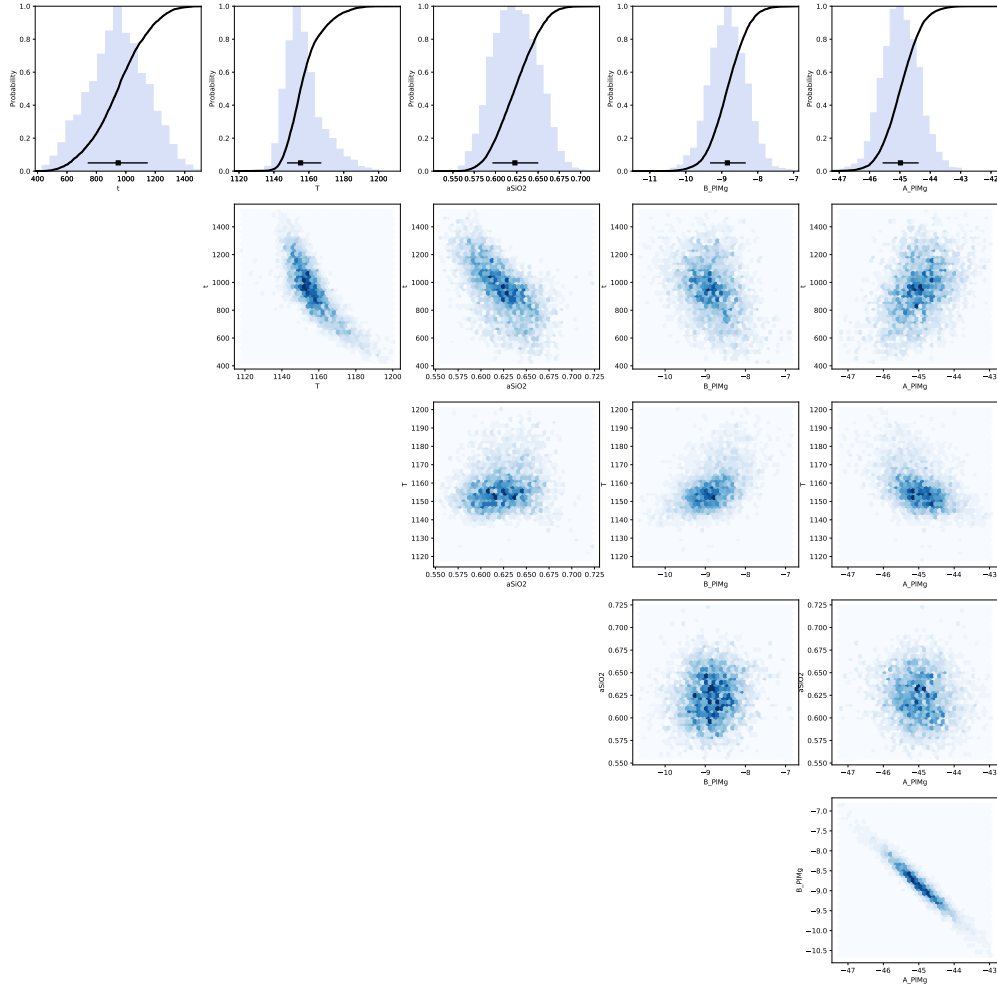


**Figure S104.** Bayesian inversion results for sample HOR\_7\_C4\_P1. Marginal plot showing the posterior distributions of the main intensive parameters modelled for the diffusion of Mg in Plagioclase:  $t$  is time (days),  $T$  is temperature ( $^{\circ}\text{C}$ ),  $a_{\text{SiO}_2}$  is  $a_{\text{SiO}_2}$ ,  $B_{\text{PlMg}}$  and  $A_{\text{PlMg}}$  are the intercept and slope of the Mg-in-plagioclase partitioning relationship. The top row shows histograms (blue bars) and probability density functions (black curves) of the aforementioned intensive parameters. The black bar shows the median result and  $1\sigma$  standard deviation. The bottom four rows are density plots that show the trade offs between the different parameters.

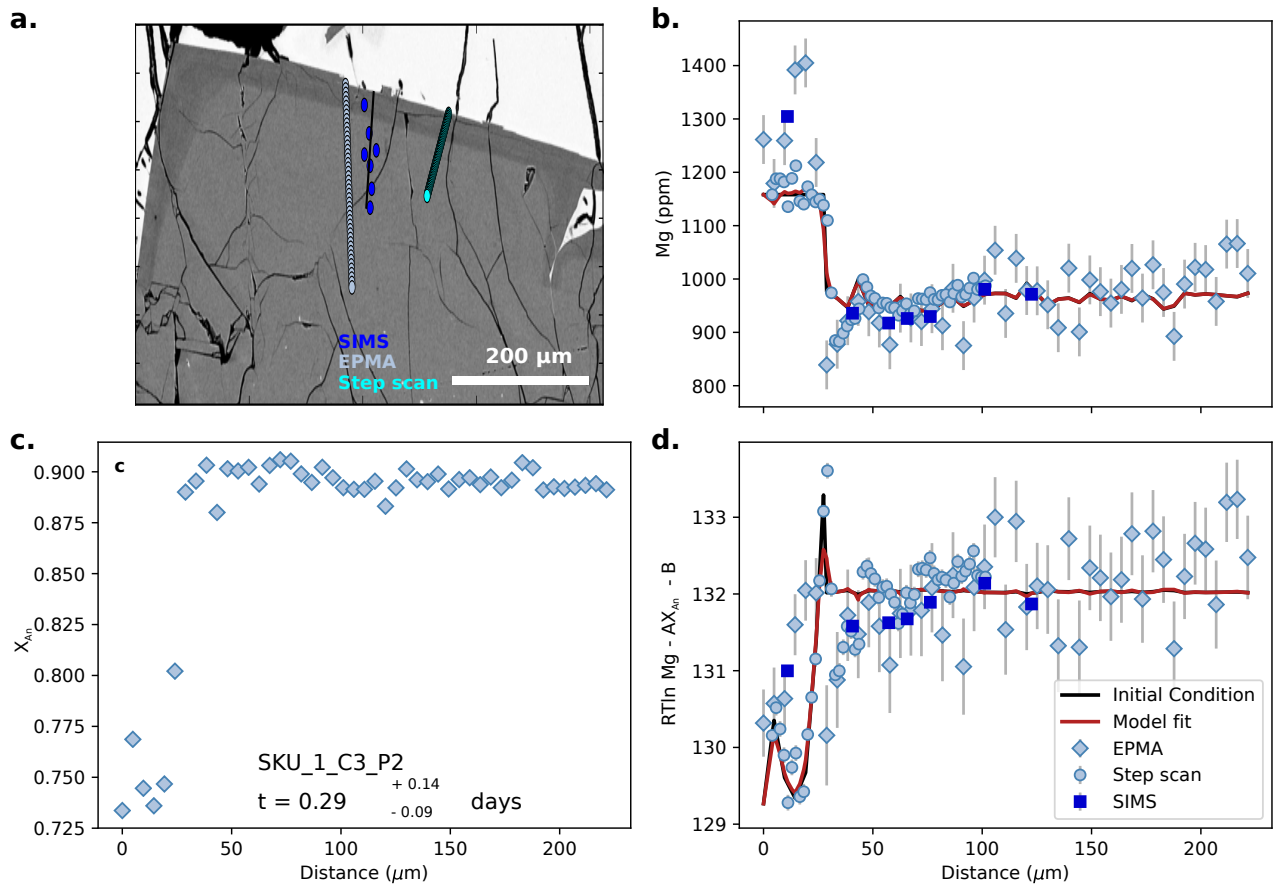


**Figure S105.** Data, initial conditions and model fits for plagioclase crystal SKU\_1\_C3\_P2. **a** is a BSE image of the plagioclase crystal showing the location of coarse SIMS spot analyses (blue spots), EPMA traverse (light blue spots) and SIMS step scan analyses (cyan points). Points from each profile were projected onto the black line. **b**, Mg compositional profile with point shapes and colours marked by analytical method. Dark blue squares are SIMS coarse spot analyses, light blue circles are SIMS step scan analyses and light blue diamonds are EPMA analyses. The black line is calculated initial conditions used in the modelling, and the red line is the model fit using the maximum likelihood of all of the parameters used in the Bayesian inversion. **c**, Anorthite profile of plagioclase as measured by EPMA. **d**, calculated melt equivalent Mg in plagioclase using the most likely partitioning parameters estimated from the Bayesian inversion. Symbols and colours are the same as in **b**.

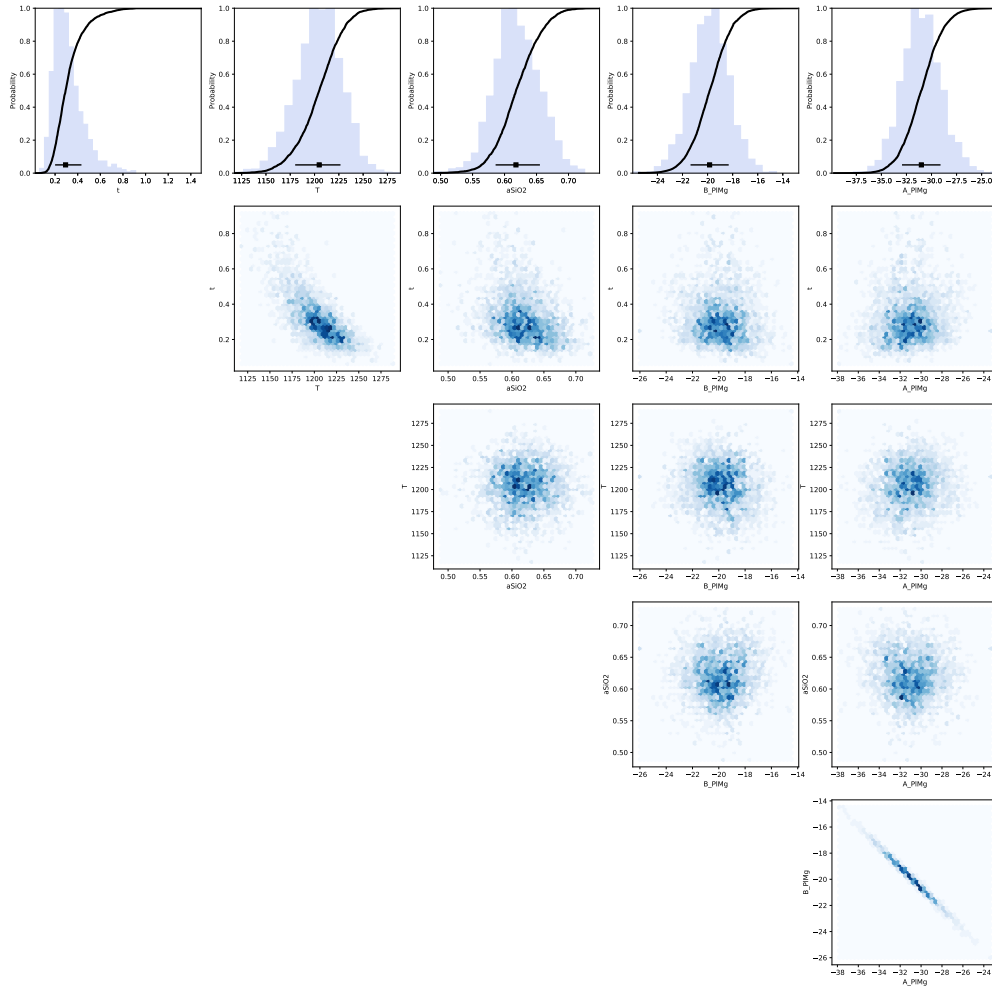


**Figure S106.** Bayesian inversion results for sample SKU\_1\_C3\_P2. Marginal plot showing the posterior distributions of the main intensive parameters modelled for the diffusion of Mg in Plagioclase:  $t$  is time (days),  $T$  is temperature ( $^{\circ}\text{C}$ ),  $a_{\text{SiO}_2}$  is  $a_{\text{SiO}_2}$ ,  $B_{\text{PlMg}}$  and  $A_{\text{PlMg}}$  are the intercept and slope of the Mg-in-plagioclase partitioning relationship. The top row shows histograms (blue bars) and probability density functions (black curves) of the aforementioned intensive parameters. The black bar shows the median result and  $1\sigma$  standard deviation. The bottom four rows are density plots that show the trade offs between the different parameters.

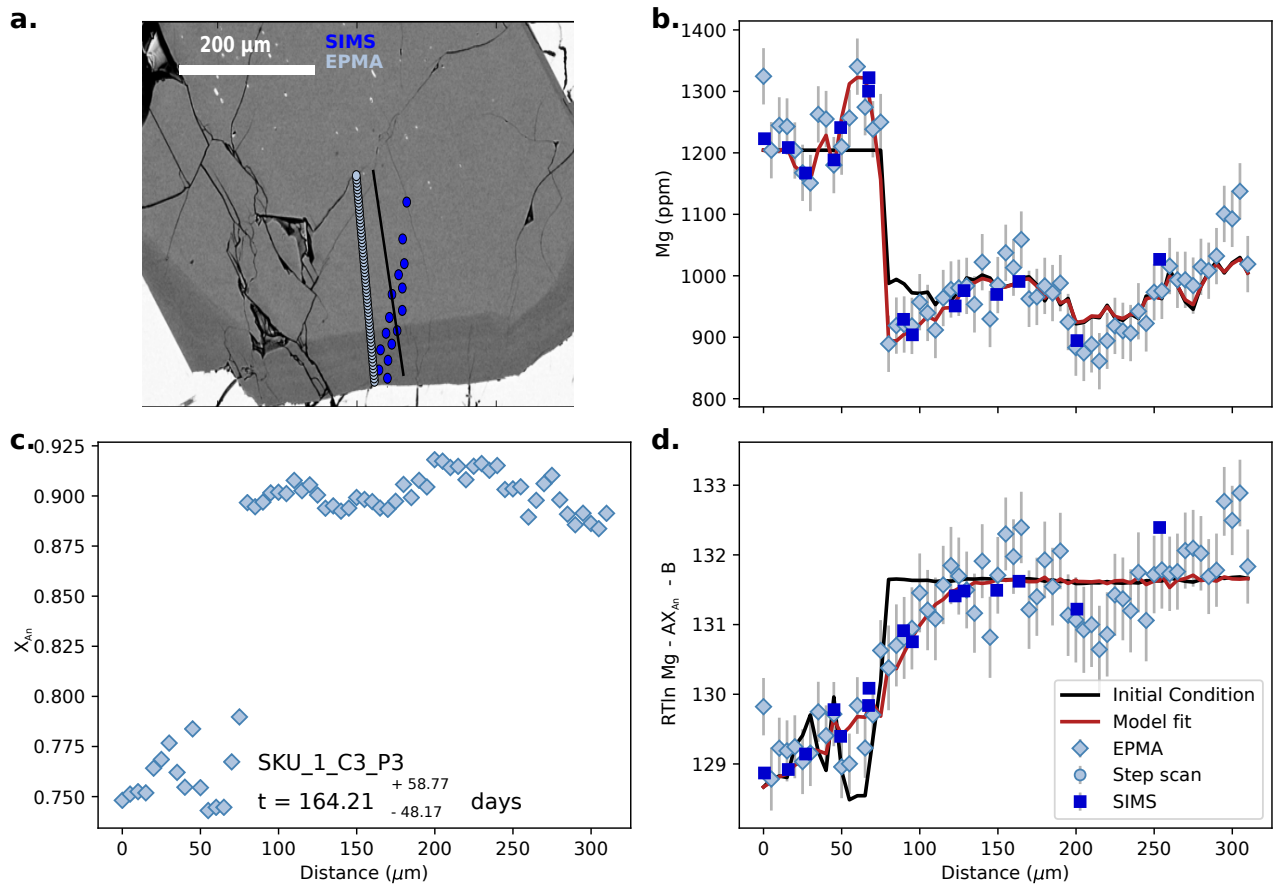


**Figure S107.** Data, initial conditions and model fits for plagioclase crystal SKU\_1\_C3\_P3. **a** is a BSE image of the plagioclase crystal showing the location of coarse SIMS spot analyses (blue spots), EPMA traverse (light blue spots) and SIMS step scan analyses (cyan points). Points from each profile were projected onto the black line. **b**, Mg compositional profile with point shapes and colours marked by analytical method. Dark blue squares are SIMS coarse spot analyses, light blue circles are SIMS step scan analyses and light blue diamonds are EPMA analyses. The black line is calculated initial conditions used in the modelling, and the red line is the model fit using the maximum likelihood of all of the parameters used in the Bayesian inversion. **c**, Anorthite profile of plagioclase as measured by EPMA. **d**, calculated melt equivalent Mg in plagioclase using the most likely partitioning parameters estimated from the Bayesian inversion. Symbols and colours are the same as in **b**.

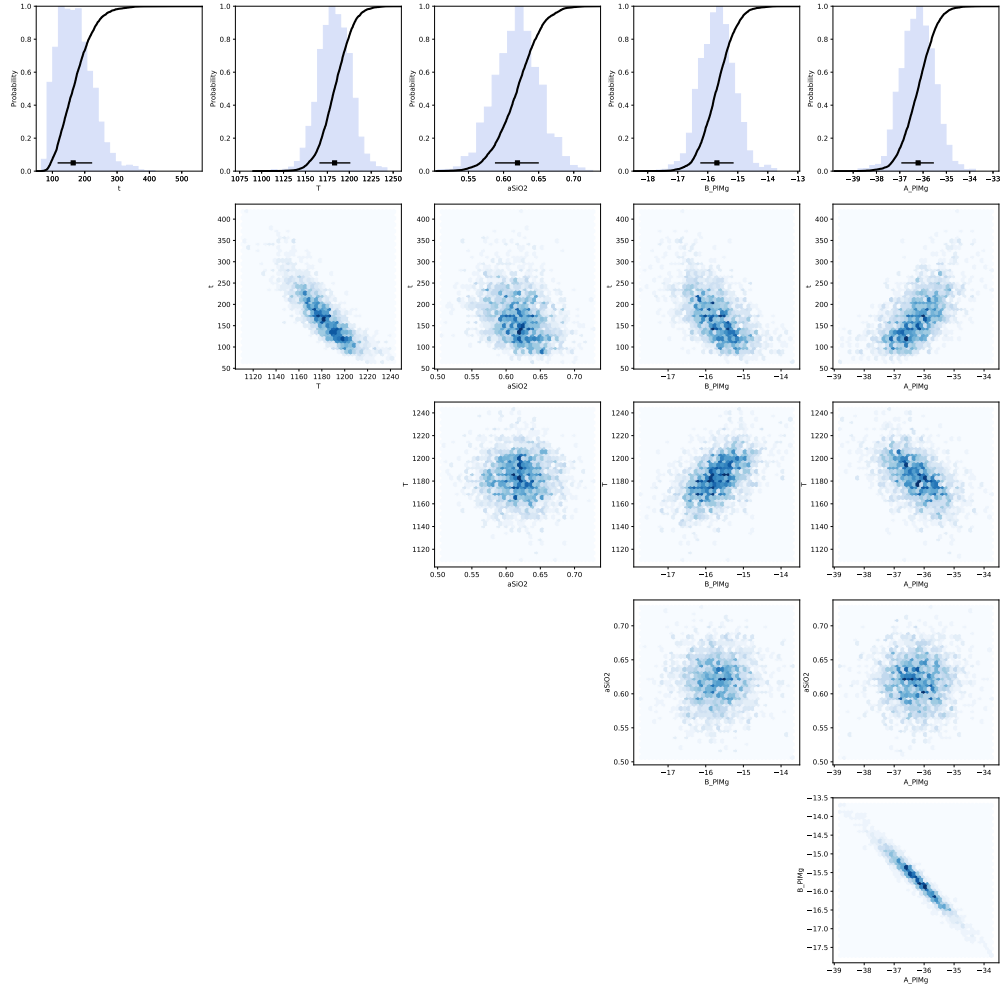


**Figure S108.** Bayesian inversion results for sample SKU\_1\_C3\_P3. Marginal plot showing the posterior distributions of the main intensive parameters modelled for the diffusion of Mg in Plagioclase:  $t$  is time (days),  $T$  is temperature ( $^{\circ}\text{C}$ ),  $a_{\text{SiO}_2}$  is  $a_{\text{SiO}_2}$ ,  $B_{\text{PlMg}}$  and  $A_{\text{PlMg}}$  are the intercept and slope of the Mg-in-plagioclase partitioning relationship. The top row shows histograms (blue bars) and probability density functions (black curves) of the aforementioned intensive parameters. The black bar shows the median result and  $1\sigma$  standard deviation. The bottom four rows are density plots that show the trade offs between the different parameters.

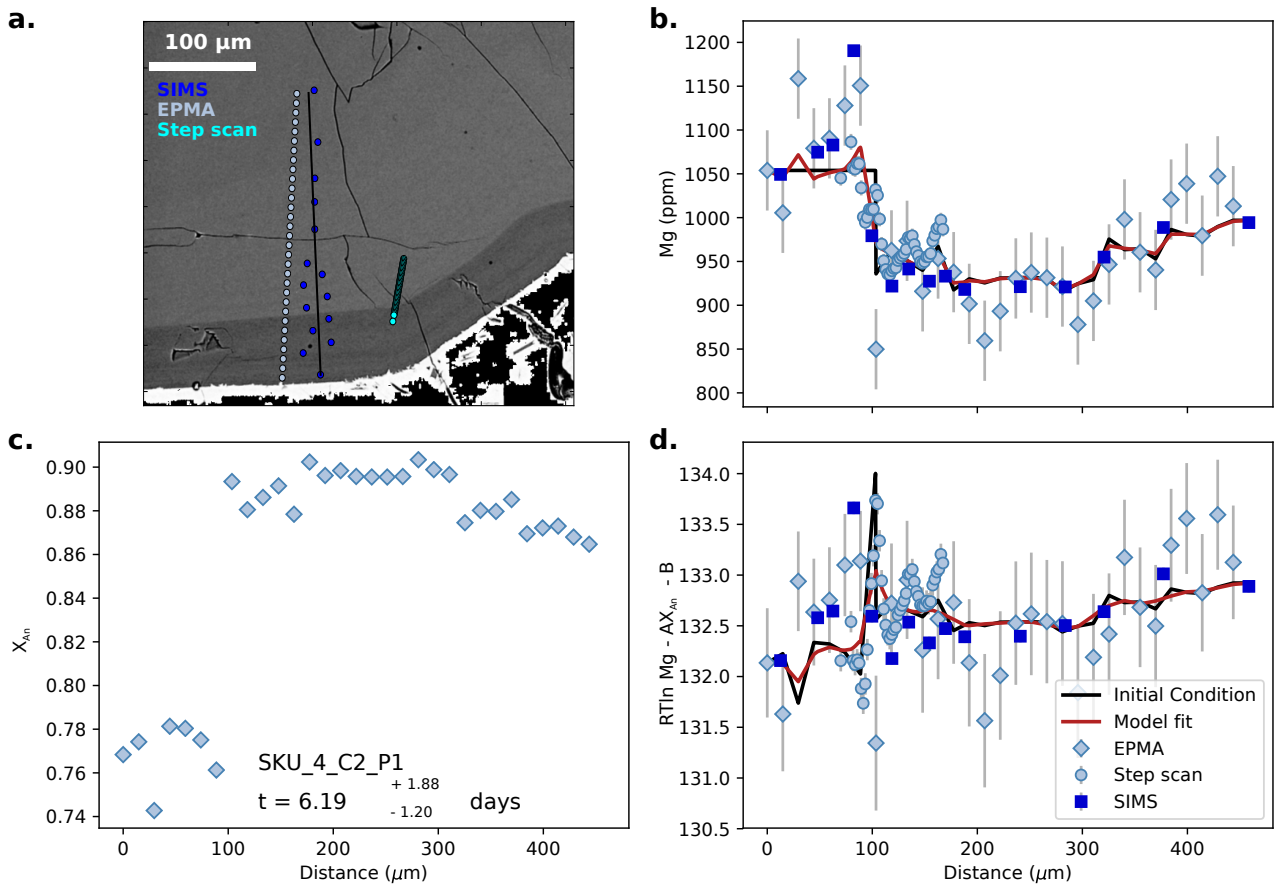


**Figure S109.** Data, initial conditions and model fits for plagioclase crystal SKU\_4\_C2\_P1. **a** is a BSE image of the plagioclase crystal showing the location of coarse SIMS spot analyses (blue spots), EPMA traverse (light blue spots) and SIMS step scan analyses (cyan points). Points from each profile were projected onto the black line. **b**, Mg compositional profile with point shapes and colours marked by analytical method. Dark blue squares are SIMS coarse spot analyses, light blue circles are SIMS step scan analyses and light blue diamonds are EPMA analyses. The black line is calculated initial conditions used in the modelling, and the red line is the model fit using the maximum likelihood of all of the parameters used in the Bayesian inversion. **c**, Anorthite profile of plagioclase as measured by EPMA. **d**, calculated melt equivalent Mg in plagioclase using the most likely partitioning parameters estimated from the Bayesian inversion. Symbols and colours are the same as in **b**.



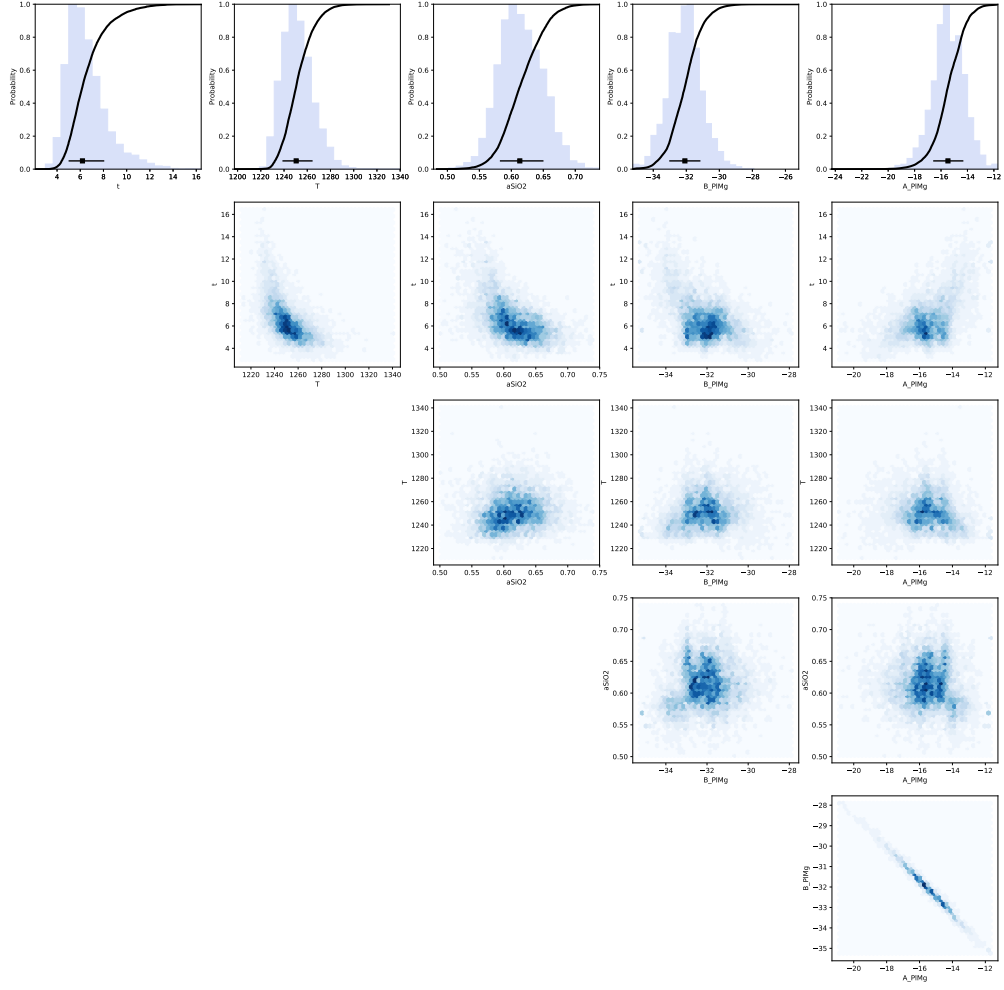


**Figure S110.** Bayesian inversion results for sample SKU\_4\_C2\_P1. Marginal plot showing the posterior distributions of the main intensive parameters modelled for the diffusion of Mg in Plagioclase:  $t$  is time (days),  $T$  is temperature ( $^{\circ}\text{C}$ ),  $a_{\text{SiO}_2}$  is  $a_{\text{SiO}_2}$ ,  $B_{\text{PlMg}}$  and  $A_{\text{PlMg}}$  are the intercept and slope of the Mg-in-plagioclase partitioning relationship. The top row shows histograms (blue bars) and probability density functions (black curves) of the aforementioned intensive parameters. The black bar shows the median result and  $1\sigma$  standard deviation. The bottom four rows are density plots that show the trade offs between the different parameters.

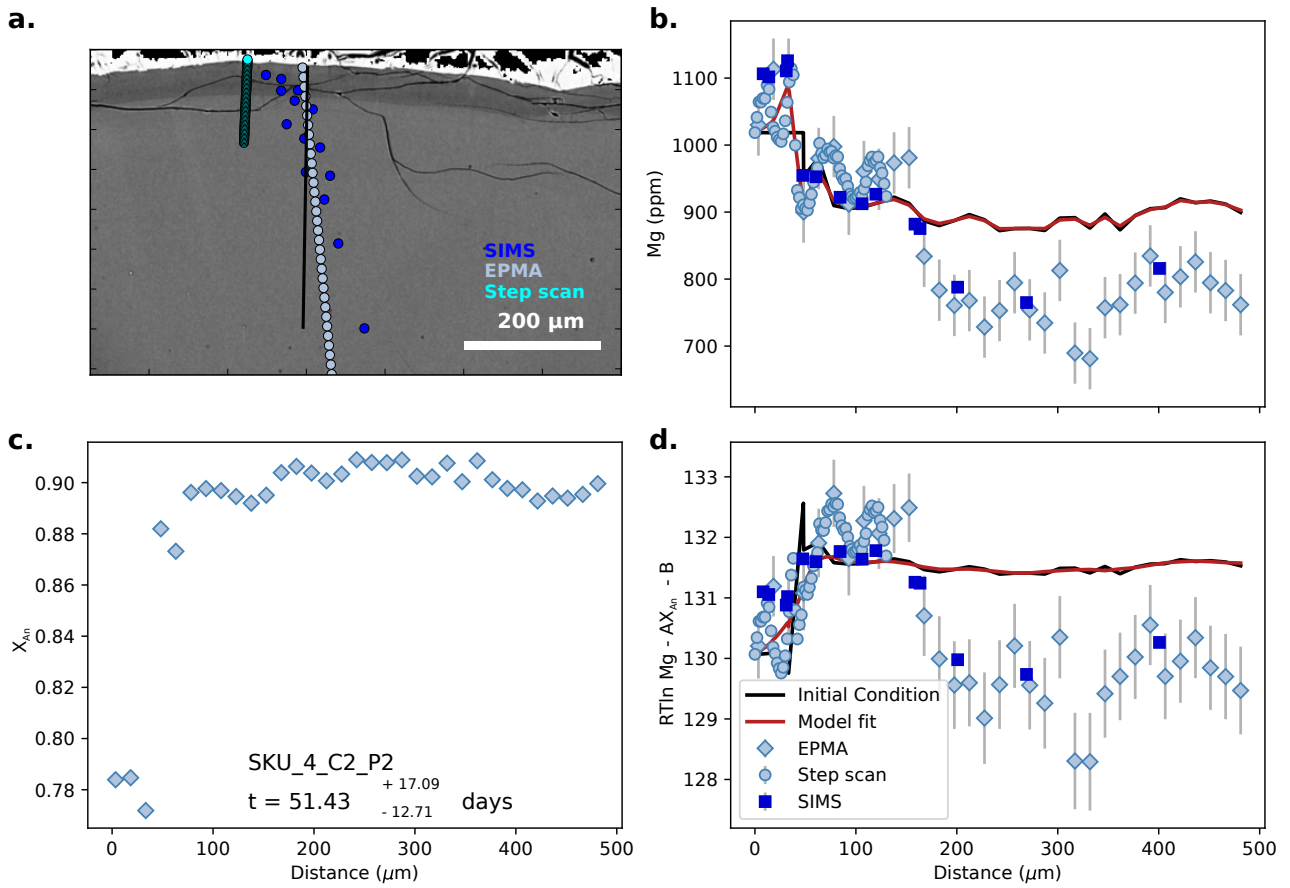


**Figure S111.** Data, initial conditions and model fits for plagioclase crystal SKU\_4\_C2\_P2. **a** is a BSE image of the plagioclase crystal showing the location of coarse SIMS spot analyses (blue spots), EPMA traverse (light blue spots) and SIMS step scan analyses (cyan points). Points from each profile were projected onto the black line. **b**, Mg compositional profile with point shapes and colours marked by analytical method. Dark blue squares are SIMS coarse spot analyses, light blue circles are SIMS step scan analyses and light blue diamonds are EPMA analyses. The black line is calculated initial conditions used in the modelling, and the red line is the model fit using the maximum likelihood of all of the parameters used in the Bayesian inversion. **c**, Anorthite profile of plagioclase as measured by EPMA. **d**, calculated melt equivalent Mg in plagioclase using the most likely partitioning parameters estimated from the Bayesian inversion. Symbols and colours are the same as in **b**.

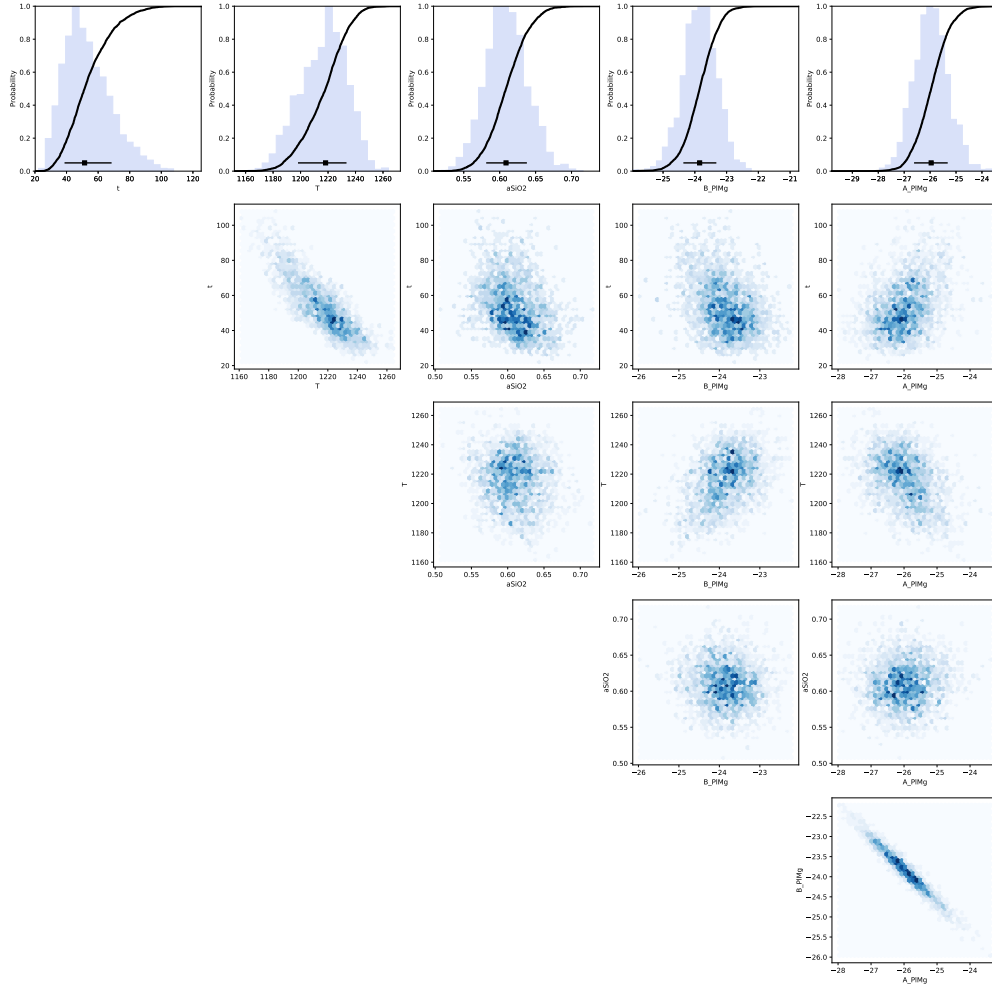


**Figure S112.** Bayesian inversion results for sample SKU\_4\_C2\_P2. Marginal plot showing the posterior distributions of the main intensive parameters modelled for the diffusion of Mg in Plagioclase:  $t$  is time (days),  $T$  is temperature ( $^{\circ}\text{C}$ ),  $a_{\text{SiO}_2}$  is  $a_{\text{SiO}_2}$ ,  $B_{\text{PlMg}}$  and  $A_{\text{PlMg}}$  are the intercept and slope of the Mg-in-plagioclase partitioning relationship. The top row shows histograms (blue bars) and probability density functions (black curves) of the aforementioned intensive parameters. The black bar shows the median result and  $1\sigma$  standard deviation. The bottom four rows are density plots that show the trade offs between the different parameters.

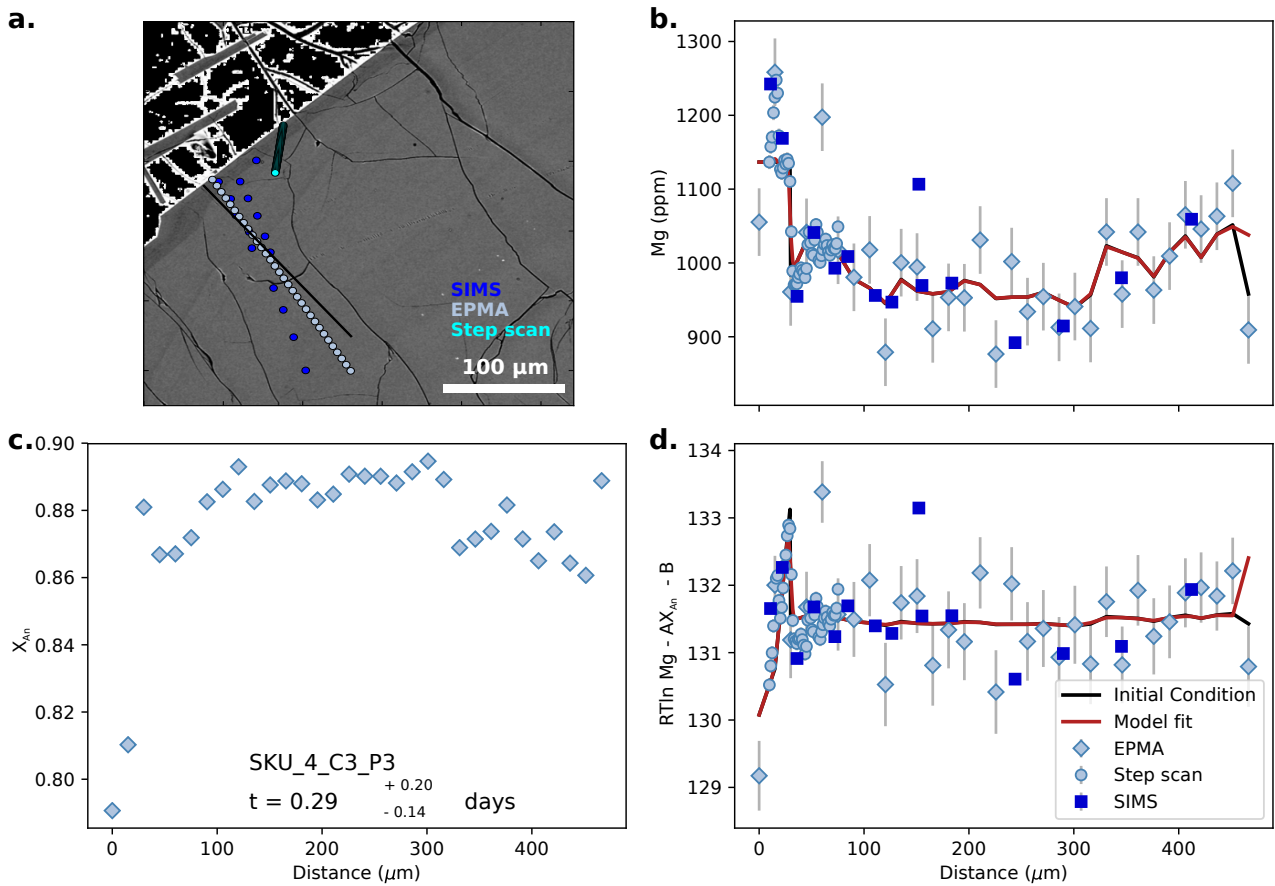


**Figure S113.** Data, initial conditions and model fits for plagioclase crystal SKU\_4\_C3\_P3. **a** is a BSE image of the plagioclase crystal showing the location of coarse SIMS spot analyses (blue spots), EPMA traverse (light blue spots) and SIMS step scan analyses (cyan points). Points from each profile were projected onto the black line. **b**, Mg compositional profile with point shapes and colours marked by analytical method. Dark blue squares are SIMS coarse spot analyses, light blue circles are SIMS step scan analyses and light blue diamonds are EPMA analyses. The black line is calculated initial conditions used in the modelling, and the red line is the model fit using the maximum likelihood of all of the parameters used in the Bayesian inversion. **c**, Anorthite profile of plagioclase as measured by EPMA. **d**, calculated melt equivalent Mg in plagioclase using the most likely partitioning parameters estimated from the Bayesian inversion. Symbols and colours are the same as in **b**.

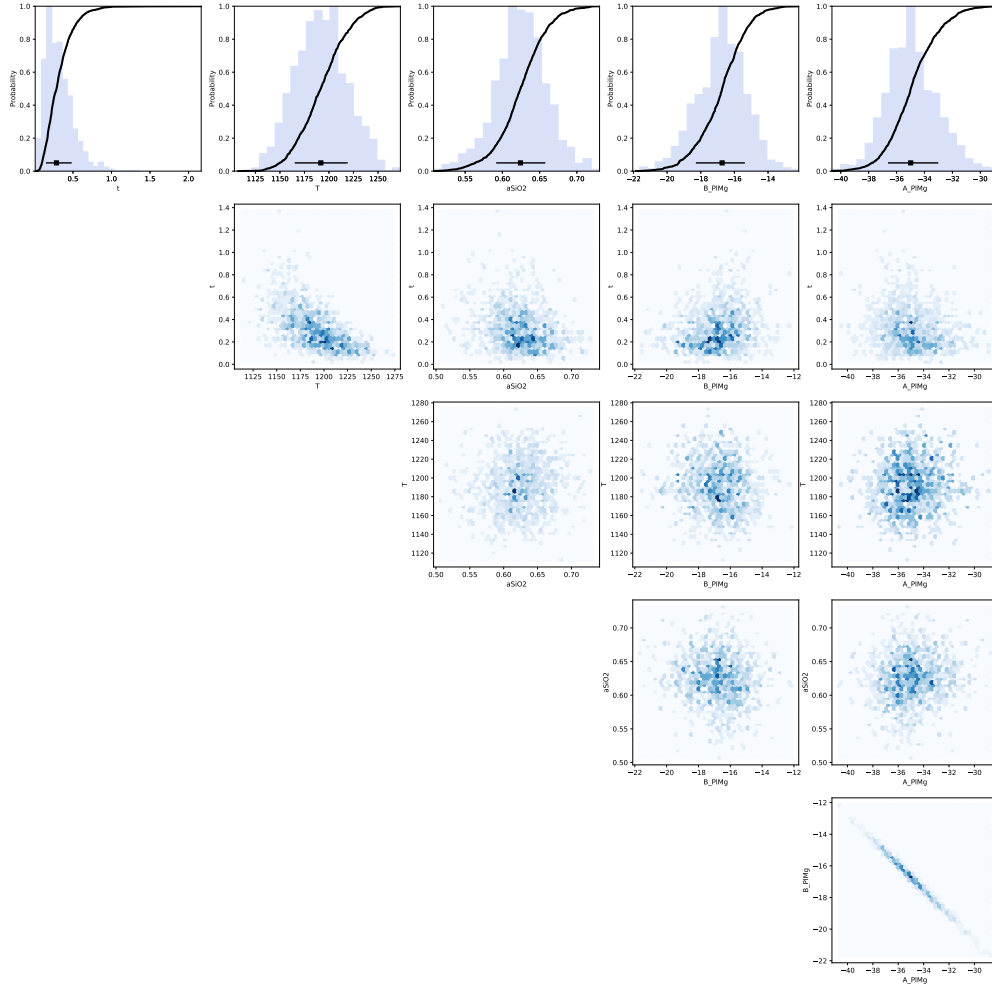


**Figure S114.** Bayesian inversion results for sample SKU\_4\_C3\_P3. Marginal plot showing the posterior distributions of the main intensive parameters modelled for the diffusion of Mg in Plagioclase:  $t$  is time (days),  $T$  is temperature ( $^{\circ}\text{C}$ ),  $a_{\text{SiO}_2}$  is  $a_{\text{SiO}_2}$ ,  $B_{\text{PlMg}}$  and  $A_{\text{PlMg}}$  are the intercept and slope of the Mg-in-plagioclase partitioning relationship. The top row shows histograms (blue bars) and probability density functions (black curves) of the aforementioned intensive parameters. The black bar shows the median result and  $1\sigma$  standard deviation. The bottom four rows are density plots that show the trade offs between the different parameters.

**Table S1.** Olivine diffusion coefficient regression parameters derived and used as part of the DFENS method and in (Mutch et al., 2019).  $a_i$  is the intercept,  $b_i$  is the coefficient in front of the  $\ln fO_2$  term (units in bars),  $c_i$  is the coefficient in front of the  $X_{Fe}$  (mole fraction),  $q_i$  is the coefficient in front of the  $1/T$  term (K),  $h_i$  is the coefficient in front of the  $P/T$  term (Pa/K),  $j_i$  is the coefficient in front of the  $P$  term (Pa), and  $k_i$  is the coefficient in front of the  $\ln a_{SiO_2}$  term. Data from Chakraborty (1997); Petry et al. (2004); Dohmen et al. (2007); Dohmen and Chakraborty (2007); Holzapfel et al. (2007); Spandler and O'Neill (2010); Zhukova et al. (2014); Jollands et al. (2016). FeMg (Global) uses all of the FeMg diffusion data (both TaMED and PED olivine diffusion mechanisms). FeMg (TaMED) is the TaMED olivine diffusion mechanism. Ni ( $a_{SiO_2}$ ) and Mn ( $a_{SiO_2}$ ) are both regressions through experimental data that have been buffered for  $a_{SiO_2}$  (Zhukova et al., 2014; Jollands et al., 2016)

Element	$a_i$	$b_i$	$c_i$	$q_i$	$j_i$	$h_i$	$k_i$
FeMg (Global)	-7.86	0.187	-7.21	-26600	-4.15E-10	-1.54E-07	-
FeMg (TaMED)	-6.76	0.224	-7.18	-26700	-5.21E-10	-1.03E-07	-
Ni	-11.1	0.277	-2.19	-25100	-1.25E-09	9.97E-07	-
Mn	-7.55	0.196	-7.15	-26700	-9.5E-10	7.20E-07	-
Ni ( $a_{SiO_2}$ )	-14.4	-0.107	-	-32980	-	-	0.714
Mn ( $a_{SiO_2}$ )	-7.46	-0.097	-	-44310	-	-	0.761

**Table S2.** Olivine diffusion coefficient regression parameters derived and used as part of the DFENS method in which the  $\ln fO_2$  term ( $b_i$ ) is expressed in Pa. Parameters are the same as in Table S1.

Element	$a_i$	$b_i$	$c_i$	$q_i$	$j_i$	$h_i$	$k_i$
FeMg (Global)	-10.01	0.187	-7.21	-26600	-4.15E-10	-1.54E-07	-
FeMg (TaMED)	-9.339	0.224	-7.18	-26700	-5.21E-10	-1.03E-07	-
Ni	-14.28	0.277	-2.19	-25100	-1.25E-09	0.000000997	-
Mn	-9.809	0.196	-7.15	-26700	-9.5E-10	0.00000072	-
Ni ( $a_{SiO_2}$ )	-13.2	-0.107	-	-32980	-	-	0.714
Mn ( $a_{SiO_2}$ )	-6.351	-0.097	-	-44310	-	-	0.761

**Table S3.** Covariance matrices for olivine diffusion equations from (Mutch et al., 2019).

Parameters are the same as those presented in Table S1.  $a_i$  is the intercept,  $b_i$  is the coefficient in front of the  $\ln fO_2$  term (units in bars),  $c_i$  is the coefficient in front of the  $X_{Fo}$  (mole fraction),  $q_i$  is the coefficient in front of the  $1/T$  term (K),  $h_i$  is the coefficient in front of the  $P/T$  term (Pa/K),  $j_i$  is the coefficient in front of the  $P$  term (Pa), and  $k_i$  is the coefficient in front of the  $\ln a_{SiO_2}$  term.

	$a_i$	$b_i$	$c_i$	$q_i$	$j_i$	$h_i$
<b>FeMg (Global)</b>						
$a_i$	4.97E-01	3.63E-03	-1.32E-01	-3.78E+02	-2.77E-11	2.69E-08
$b_i$	3.63E-03	4.31E-04	1.08E-03	1.02E+01	-6.41E-13	-1.99E-10
$c_i$	-1.32E-01	1.08E-03	1.49E-01	5.10E+01	-1.46E-13	-4.71E-09
$q_i$	-3.78E+02	1.02E+01	5.10E+01	8.40E+05	1.33E-08	-3.94E-05
$j_i$	-2.77E-11	-6.41E-13	-1.46E-13	1.33E-08	2.33E-19	-3.91E-16
$h_i$	2.69E-08	-1.99E-10	-4.71E-09	-3.94E-05	-3.91E-16	6.61E-13
<b>FeMg (TaMED)</b>						
$a_i$	7.20E-01	1.36E-02	-1.37E-01	-3.17E+02	-5.11E-11	3.57E-08
$b_i$	1.36E-02	8.25E-04	2.25E-04	1.18E+01	-1.61E-12	2.07E-10
$c_i$	-1.37E-01	2.25E-04	1.34E-01	4.45E+01	1.76E-12	-5.05E-09
$q_i$	-3.17E+02	1.18E+01	4.45E+01	8.20E+05	8.12E-09	-3.61E-05
$j_i$	-5.11E-11	-1.61E-12	1.76E-12	8.12E-09	2.08E-19	-3.46E-16
$h_i$	3.57E-08	2.07E-10	-5.05E-09	-3.61E-05	-3.46E-16	5.83E-13
<b>Ni</b>						
$a_i$	3.33E+00	1.09E-02	-1.77E+00	-2.19E+03	-1.40E-10	1.90E-07
$b_i$	1.09E-02	2.17E-03	-1.53E-02	8.50E+01	-1.98E-12	-1.98E-09
$c_i$	-1.77E+00	-1.53E-02	1.88E+00	-3.40E+02	2.68E-11	-2.61E-08
$q_i$	-2.19E+03	8.50E+01	-3.40E+02	6.79E+06	9.50E-08	-3.21E-04
$j_i$	-1.40E-10	-1.98E-12	2.68E-11	9.50E-08	2.23E-19	-3.69E-16
$h_i$	1.90E-07	-1.98E-09	-2.61E-08	-3.21E-04	-3.69E-16	6.25E-13
<b>Mn</b>						
$a_i$	3.24E+00	3.94E-03	-6.79E-01	-3.68E+03	-1.95E-10	2.69E-07
$b_i$	3.94E-03	3.48E-03	2.78E-03	1.19E+02	-4.03E-12	-2.04E-09
$c_i$	-6.79E-01	2.78E-03	3.23E-01	7.26E+02	2.82E-11	-5.37E-08
$q_i$	-3.68E+03	1.19E+02	7.26E+02	8.79E+06	9.61E-08	-3.99E-04
$j_i$	-1.95E-10	-4.03E-12	2.82E-11	9.61E-08	2.83E-19	-4.65E-16
$h_i$	2.69E-07	-2.04E-09	-5.37E-08	-3.99E-04	-4.65E-16	7.87E-13

**Table S4.** Covariance matrices for olivine diffusion equations derived for the DFENS method.

Parameters are the same as those presented in Table S1 but the  $\ln f\text{O}_2$  ( $b_i$ ) term is expressed in Pa.

	$a_i$	$b_i$	$c_i$	$q_i$	$j_i$	$h_i$
<b>FeMg (Global)</b>						
$a_i$	0.4705178	-0.0013301	-0.1447082	-496.07323	-2.03E-11	2.923E-08
$b_i$	-0.0013301	0.0004312	0.0010761	10.216281	-6.406E-13	-1.988E-10
$c_i$	-0.1447082	0.0010761	0.1491241	51.003423	-1.463E-13	-4.71E-09
$q_i$	-496.07323	10.216281	51.003423	839580.7	1.33E-08	-3.943E-05
$j_i$	-2.03E-11	-6.406E-13	-1.463E-13	1.33E-08	2.332E-19	-3.913E-16
$h_i$	2.923E-08	-1.988E-10	-4.71E-09	-3.943E-05	-3.913E-16	6.613E-13
<b>FeMg (TaMED)</b>						
$a_i$	0.5160337	0.0041103	-0.1397954	-452.5769	-3.259E-11	3.328E-08
$b_i$	0.0041103	0.0008247	0.0002248	11.815782	-1.605E-12	2.067E-10
$c_i$	-0.1397954	0.0002248	0.1335066	44.476205	1.763E-12	-5.048E-09
$q_i$	-452.5769	11.815782	44.476205	819871.01	8.116E-09	-3.61E-05
$j_i$	-3.259E-11	-1.605E-12	1.763E-12	8.116E-09	2.079E-19	-3.455E-16
$h_i$	3.328E-08	2.067E-10	-5.048E-09	-3.61E-05	-3.455E-16	5.826E-13
<b>Ni</b>						
$a_i$	3.3650223	-0.0140922	-1.5978161	-3165.2897	-1.174E-10	2.131E-07
$b_i$	-0.0140922	0.0021678	-0.0152819	85.006526	-1.982E-12	-1.975E-09
$c_i$	-1.5978161	-0.0152819	1.8780604	-339.86177	2.678E-11	-2.608E-08
$q_i$	-3165.2897	85.006526	-339.86177	6793292.3	9.495E-08	-0.0003205
$j_i$	-1.174E-10	-1.982E-12	2.678E-11	9.495E-08	2.225E-19	-3.685E-16
$h_i$	2.131E-07	-1.975E-09	-2.608E-08	-0.0003205	-3.685E-16	6.249E-13
<b>Mn</b>						
$a_i$	3.6093148	-0.0360999	-0.7108676	-5053.8668	-1.485E-10	2.92E-07
$b_i$	-0.0360999	0.0034781	0.0027846	119.28822	-4.033E-12	-2.04E-09
$c_i$	-0.7108676	0.0027846	0.3230116	726.30629	2.82E-11	-5.369E-08
$q_i$	-5053.8668	119.28822	726.30629	8787975	9.607E-08	-0.0003988
$j_i$	-1.485E-10	-4.033E-12	2.82E-11	9.607E-08	2.833E-19	-4.65E-16
$h_i$	2.92E-07	-2.04E-09	-5.369E-08	-0.0003988	-4.65E-16	7.87E-13



**Table S5.** Covariance matrices for  $a_{\text{SiO}_2}$  dependent olivine diffusion equations from (Mutch et al., 2019). Parameters are the same as those presented in Table S1.  $a_i$  is the intercept,  $b_i$  is the coefficient in front of the  $\ln f\text{O}_2$  term (units in bars),  $q_i$  is the coefficient in front of the  $1/T$  term (K), and  $k_i$  is the coefficient in front of the  $\ln a_{\text{SiO}_2}$  term.

	$a_i$	$b_i$	$k_i$	$q_i$
<b>Ni</b>				
$a_i$	2.15E+01	4.52E-02	2.02E-01	-3.42E+04
$b_i$	4.52E-02	1.04E-03	1.09E-03	-5.81E+01
$k_i$	2.02E-01	1.09E-03	2.26E-02	-2.23E+02
$q_i$	-3.42E+04	-5.81E+01	-2.23E+02	5.52E+07
<b>Mn</b>				
$a_i$	6.09E+00	4.68E-03	5.01E-02	-9.81E+03
$b_i$	4.68E-03	1.33E-04	6.50E-05	-4.73E+00
$k_i$	5.01E-02	6.50E-05	7.76E-03	-4.65E+01
$q_i$	-9.81E+03	-4.73E+00	-4.65E+01	1.61E+07

**Table S6.** Covariance matrices for  $a_{\text{SiO}_2}$  dependent olivine diffusion equations for the DFENS method. Parameters are the same as those presented in Table S1 but the  $\ln f\text{O}_2$  ( $b_i$ ) term is expressed in Pa.

	$a_i$	$b_i$	$k_i$	$q_i$
<b>Ni</b>				
$a_i$	21.501697	0.0452483	0.2018372	-34216.659
$b_i$	0.0452483	0.0010377	0.0010927	-58.079972
$k_i$	0.2018372	0.0010927	0.0225959	-223.22981
$q_i$	-34216.659	-58.079972	-223.22981	55159024
<b>Mn</b>				
$a_i$	6.0914756	0.0046841	0.0500947	-9812.5755
$b_i$	0.0046841	0.0001332	6.497E-05	-4.7258323
$k_i$	0.0500947	6.497E-05	0.007763	-46.457418
$q_i$	-9812.5755	-4.7258323	-46.457418	16061862

**Table S7.** Plagioclase diffusion coefficient regression parameters derived and used as part of the DFENS method in this study.  $a_i$  is the intercept,  $b_i$  is the coefficient in front of the  $X_{An}$  term (mole fraction),  $c$  is the coefficient in front of the  $\ln a_{SiO_2}$  term and  $q$  is the coefficient in front of the  $1/T$  term. Mg data from Van Orman et al. (2014) and Faak et al. (2013); Sr data from D. J. Cherniak and Watson (1994) and B. Giletti and Casserly (1994); Ba data from D. Cherniak (2002); K data from B. J. Giletti and Shanahan (1997).

Element	$a_i$	$b_i$	$c_i$	$q_i$
Mg	-1.06E+01	-5.35E+00	2.93E+00	-3.13E+04
Sr	-1.28E+01	-5.71E+00	-	-3.24E+04
Ba	-1.23E+01	-3.29E+00	-	-4.00E+04
K	-9.08E+00	-3.86E+00	-	-3.40E+04

**Table S8.** Covariance matrices for plagioclase diffusion equations derived in this study.  $a_i$  is the intercept,  $b_i$  is the coefficient in front of the  $X_{An}$  term (mole fraction),  $c$  is the coefficient in front of the  $\ln a_{SiO_2}$  term and  $q$  is the coefficient in front of the  $1/T$  term.

	$a_i$	$b_i$	$c_i$	$q_i$
<b>Mg</b>				
$a_i$	2.22E+00	-7.63E-02	2.41E-01	-2.91E+03
$b_i$	-7.63E-02	1.24E-01	-1.91E-02	-4.30E+00
$c_i$	2.41E-01	-1.91E-02	7.51E-02	-2.79E+02
$q_i$	-2.91E+03	-4.30E+00	-2.79E+02	3.92E+06
<b>Sr</b>				
$a_i$	9.48E-01	-1.65E-01	-	-1.03E+03
$b_i$	-1.65E-01	1.17E-01	-	1.24E+02
$c_i$	-	-	-	-
$q_i$	-1.03E+03	1.24E+02	-	1.16E+06
<b>Ba</b>				
$a_i$	2.54E+00	-1.51E-01	-	-2.96E+03
$b_i$	-1.51E-01	3.05E-01	-	-5.12E-02
$c_i$	-	-	-	-
$q_i$	-2.96E+03	-5.12E-02	-	3.56E+06
<b>K</b>				
$a_i$	6.21E-01	-9.53E-02	-	-6.35E+02
$b_i$	-9.53E-02	1.51E-01	-	6.62E+01
$c_i$	-	-	-	-
$q_i$	-6.35E+02	6.62E+01	-	6.68E+05

**Table S9.** Angles between the EPMA profile and the main crystallographic axes in olivine as measured by EBSD. These angles are incorporated into the anisotropy calculation used to determine the apparent diffusivity parallel to the measured profile. angle100P, angle010P and angle001P are the angles between the profile and [100], [010] and [001] respectively.

<b>Profile</b>	<b>angle100P (°)</b>	<b>angle010P (°)</b>	<b>angle001P (°)</b>
HOR_1_OL_C1_P3	38.90	51.84	83.55
HOR_1_OL_C2_P3	25.60	111.70	102.92
HOR_1_OL_C3_P3	34.65	55.77	85.26
HOR_1_OL_C4_P3	123.31	136.85	65.95
HOR_2_OL_C12_P1	158.14	69.61	97.54
HOR_2_OL_C15_P1	166.42	98.03	79.12
HOR_2_OL_C18_P1	119.73	42.93	117.83
HOR_2_OL_C19_P1	67.46	71.58	150.21
HOR_2_OL_C25_P1	149.83	80.62	61.62
HOR_2_OL_C28_P1	96.45	45.63	45.09
HOR_2_OL_C6_P1	146.36	58.74	78.80
HOR_3_OL_C10_P2	167.81	101.99	92.20
HOR_3_OL_C11_P2	12.98	77.39	93.06
HOR_3_OL_C12_P2	30.20	63.88	104.09
HOR_3_OL_C13_P2	109.16	54.69	41.65
HOR_3_OL_C15_P2	76.16	165.78	93.18
HOR_3_OL_C16_P2	3.88	93.13	92.28
HOR_3_OL_C3_P2	157.76	68.36	85.10
HOR_3_OL_C5_P2	5.59	94.66	93.09
SKU_1_OL_C1_P4	12.40	101.97	86.79
SKU_1_OL_C2_P3	80.75	17.73	75.01
SKU_1_OL_C3_1_P4	101.16	22.28	70.97
SKU_1_OL_C3_2_P2	160.90	73.04	81.48
SKU_1_OL_C3_3_P3	11.79	83.41	80.27
SKU_1_OL_C3_4_P3	135.13	134.76	87.58
SKU_1_OL_C4_1_P4	121.33	148.08	84.49
SKU_1_OL_C4_2_P2	88.60	144.61	125.35
SKU_2_OL_C19_P1	127.93	37.95	91.16
SKU_2_OL_C8_P1	20.64	74.84	103.67
SKU_4_C1_1_OL_P2	77.56	151.82	114.84
SKU_4_C3_1_OL_P2	128.65	141.12	86.43

**Table S10.** Olivine timescale results and uncertainties. Median timescales and  $1\sigma$  errors obtained from the posterior distributions of the Nested Sampling Bayesian inversion conducted on each olivine profile.

<b>Profile</b>	<b>Phase</b>	<b>Median (days)</b>	<b>+1<math>\sigma</math> (days)</b>	<b>-1<math>\sigma</math> (days)</b>
HOR_1_OL_C1_P3	Olivine	149.93	69.13	46.09
HOR_1_OL_C2_P3	Olivine	156.73	70.08	49.56
HOR_1_OL_C3_P3	Olivine	94.34	45.68	29.80
HOR_1_OL_C4_P3	Olivine	94.89	39.63	26.86
HOR_2_OL_C12_P1	Olivine	323.51	147.88	99.06
HOR_2_OL_C15_P1	Olivine	155.45	74.37	51.94
HOR_2_OL_C18_P1	Olivine	82.63	41.06	26.54
HOR_2_OL_C19_P1	Olivine	71.39	33.23	22.01
HOR_2_OL_C25_P1	Olivine	118.50	60.15	38.45
HOR_2_OL_C28_P1	Olivine	151.02	51.77	40.48
HOR_2_OL_C6_P1	Olivine	63.48	30.36	20.90
HOR_3_OL_C10_P2	Olivine	223.25	104.78	69.86
HOR_3_OL_C11_P2	Olivine	171.14	81.19	52.38
HOR_3_OL_C12_P2	Olivine	56.02	21.56	16.72
HOR_3_OL_C13_P2	Olivine	101.79	45.10	27.64
HOR_3_OL_C15_P2	Olivine	162.14	65.72	40.40
HOR_3_OL_C16_P2	Olivine	302.39	139.40	90.36
HOR_3_OL_C3_P2	Olivine	269.28	100.08	78.25
HOR_3_OL_C5_P2	Olivine	166.97	79.64	51.12
SKU_1_OL_C1_P4	Olivine	83.72	38.55	25.55
SKU_1_OL_C2_P3	Olivine	261.98	102.87	75.40
SKU_1_OL_C3_1_P4	Olivine	235.73	113.72	76.41
SKU_1_OL_C3_2_P2	Olivine	65.86	34.15	22.53
SKU_1_OL_C3_3_P3	Olivine	86.41	44.46	27.28
SKU_1_OL_C3_4_P3	Olivine	174.24	77.50	57.29
SKU_1_OL_C4_1_P4	Olivine	199.32	84.99	63.63
SKU_2_OL_C19_P1	Olivine	118.84	47.81	35.58
SKU_2_OL_C8_P1	Olivine	117.24	50.87	37.11
SKU_4_C1_1_OL_P2	Olivine	135.99	66.46	49.42
SKU_4_C3_1_OL_P2	Olivine	190.16	93.31	65.00

**Table S11.** Plagioclase timescale results and uncertainties. Median timescales and  $1\sigma$  errors obtained from the posterior distributions of the Nested Sampling Bayesian inversion conducted on each plagioclase profile.

<b>Profile</b>	<b>Phase</b>	<b>Median (days)</b>	<b>+1<math>\sigma</math> (days)</b>	<b>-1<math>\sigma</math> (days)</b>
HOR_1_C1_P1	Plagioclase	465.54	103.84	110.09
HOR_1_C1_P2	Plagioclase	174.62	38.38	29.53
HOR_1_C1_P4	Plagioclase	392.03	137.70	111.11
HOR_1_C3_P3	Plagioclase	502.49	99.64	106.15
HOR_3_C1_P3	Plagioclase	871.22	109.53	105.47
HOR_3_C2_P1	Plagioclase	1323.84	539.29	311.81
HOR_3_C3_P2	Plagioclase	573.50	29.70	23.70
HOR_4_C2_P1	Plagioclase	2.56	1.40	0.93
HOR_4_C3_P1	Plagioclase	397.04	108.57	86.15
HOR_4_C3_P3	Plagioclase	392.23	104.86	88.29
HOR_5_C1_P1	Plagioclase	24.04	7.43	6.04
HOR_5_C2_P2	Plagioclase	136.87	47.47	40.19
HOR_5_C3_P3	Plagioclase	148.74	51.02	38.66
HOR_6_C2_P1	Plagioclase	150.96	32.72	26.82
HOR_6_C3_P1	Plagioclase	219.27	73.15	63.57
HOR_6_C4_P1	Plagioclase	189.31	29.46	26.42
HOR_7_C1_P1	Plagioclase	613.23	190.96	148.32
HOR_7_C4_P1	Plagioclase	948.08	200.87	207.25
SKU_1_C3_P2	Plagioclase	0.29	0.14	0.09
SKU_1_C3_P3	Plagioclase	164.21	58.77	48.17
SKU_4_C2_P1	Plagioclase	6.19	1.88	1.20
SKU_4_C2_P2	Plagioclase	51.43	17.09	12.71
SKU_4_C3_P3	Plagioclase	0.29	0.20	0.14

## References

- Aigner-Torres, M., Blundy, J., Ulmer, P., & Pettke, T. (2007). Laser ablation ICPMS study of trace element partitioning between plagioclase and basaltic melts: an experimental approach. *Contributions to Mineralogy and Petrology*, 153(6), 647–667.
- Alnæs, M., Blechta, J., Hake, J., Johansson, A., Kehlet, B., Logg, A., ... Wells, G. N. (2015). The FEniCS project version 1.5. *Archive of Numerical Software*, 3(100), 9–23.
- Bindeman, I. N., & Davis, A. M. (2000). Trace element partitioning between plagioclase and melt: investigation of dopant influence on partition behavior. *Geochimica et Cosmochimica Acta*, 64(16), 2863–2878.
- Bindeman, I. N., Davis, A. M., & Drake, M. J. (1998). Ion microprobe study of plagioclase-basalt partition experiments at natural concentration levels of trace elements. *Geochimica et Cosmochimica Acta*, 62(7), 1175–1193.
- Chakraborty, S. (1997). Rates and mechanisms of Fe–Mg interdiffusion in olivine at 980–1300 °C. *Journal of Geophysical Research: Solid Earth*, 102(B6), 12317–12331.
- Chakraborty, S. (2010). Diffusion coefficients in olivine, wadsleyite and ringwoodite. *Reviews in mineralogy and geochemistry*, 72(1), 603–639.
- Cherniak, D. (2002). Ba diffusion in feldspar. *Geochimica et Cosmochimica Acta*, 66(9), 1641–1650.
- Cherniak, D. J., & Watson, E. B. (1994). A study of strontium diffusion in plagioclase using Rutherford backscattering spectroscopy. *Geochimica et Cosmochimica Acta*, 58(23), 5179–5190.
- Costa, F., Chakraborty, S., & Dohmen, R. (2003). Diffusion coupling between trace and major elements and a model for calculation of magma residence times using plagioclase. *Geochimica*

- et Cosmochimica Acta*, 67(12), 2189–2200.
- Costa, F., Coogan, L. A., & Chakraborty, S. (2010). The time scales of magma mixing and mingling involving primitive melts and melt–mush interaction at mid-ocean ridges. *Contributions to Mineralogy and Petrology*, 159(3), 371–387.
- Costa, F., & Morgan, D. (2010). Time constraints from chemical equilibration in magmatic crystals. *Timescales of Magmatic Processes: From Core to Atmosphere*, 125–159.
- Dohmen, R., Becker, H.-W., & Chakraborty, S. (2007). Fe–Mg diffusion in olivine I: experimental determination between 700 and 1,200 °C as a function of composition, crystal orientation and oxygen fugacity. *Physics and Chemistry of Minerals*, 34(6), 389–407.
- Dohmen, R., & Blundy, J. (2014). A predictive thermodynamic model for element partitioning between plagioclase and melt as a function of pressure, temperature and composition. *American Journal of Science*, 314(9), 1319–1372.
- Dohmen, R., & Chakraborty, S. (2007). Fe–Mg diffusion in olivine II: point defect chemistry, change of diffusion mechanisms and a model for calculation of diffusion coefficients in natural olivine. *Physics and Chemistry of Minerals*, 34(6), 409–430.
- Faak, K., Chakraborty, S., & Coogan, L. A. (2013). Mg in plagioclase: Experimental calibration of a new geothermometer and diffusion coefficients. *Geochimica et Cosmochimica Acta*, 123, 195–217.
- Fabbrizio, A., Schmidt, M. W., Günther, D., & Eikenberg, J. (2009). Experimental determination of Ra mineral/melt partitioning for feldspars and <sup>226</sup>Ra-disequilibrium crystallization ages of plagioclase and alkali-feldspar. *Earth and Planetary Science Letters*, 280(1-4), 137–148.
- Giletti, B., & Casserly, J. (1994). Strontium diffusion kinetics in plagioclase feldspars. *Geochim-*

- ica et Cosmochimica Acta*, 58(18), 3785–3793.
- Giletti, B. J., & Shanahan, T. M. (1997). Alkali diffusion in plagioclase feldspar. *Chemical Geology*, 139(1-4), 3–20.
- Holzappel, C., Chakraborty, S., Rubie, D., & Frost, D. (2007). Effect of pressure on Fe–Mg, Ni and Mn diffusion in  $(\text{Fe}_x\text{Mg}_{1-x})_2\text{SiO}_4$  olivine. *Physics of the Earth and Planetary Interiors*, 162(3-4), 186–198.
- Jollands, M., Hermann, J., O'Neill, H. S. C., Spandler, C., & Padrón-Navarta, J. (2016). Diffusion of Ti and some divalent cations in olivine as a function of temperature, oxygen fugacity, chemical potentials and crystal orientation. *Journal of petrology*, 57(10), 1983–2010.
- Kress, V. C., & Carmichael, I. S. (1991). The compressibility of silicate liquids containing  $\text{Fe}_2\text{O}_3$  and the effect of composition, temperature, oxygen fugacity and pressure on their redox states. *Contributions to Mineralogy and Petrology*, 108(1-2), 82–92.
- Logg, A., Mardal, K.-A., Wells, G. N., et al. (2012). *Automated Solution of Differential Equations by the Finite Element Method* (A. Logg, K.-A. Mardal, & G. N. Wells, Eds.). Springer. doi: 10.1007/978-3-642-23099-8
- Miller, S. A., Asimow, P. D., & Burnett, D. (2006). Determination of melt influence on divalent element partitioning between anorthite and CMAS melts. *Geochimica et Cosmochimica Acta*, 70(16), 4258–4274.
- Moore, A., Coogan, L., Costa, F., & Perfit, M. (2014). Primitive melt replenishment and crystal-mush disaggregation in the weeks preceding the 2005–2006 eruption 9 50N, EPR. *Earth and Planetary Science Letters*, 403, 15–26.
- Mutch, E. J. F., MacLennan, J., Shorttle, O., Edmonds, M., & Rudge, J. F. (2019). Rapid



- transcrustal magma movement under Iceland. *Nature Geoscience*, 12(7), 569–574.
- Neave, D. A., MacLennan, J., Hartley, M. E., Edmonds, M., & Thordarson, T. (2014). Crystal Storage and Transfer in Basaltic Systems: the Skuggafjöll Eruption, Iceland. *Journal of Petrology*, 55(12), 2311–2346. Retrieved from <http://dx.doi.org/10.1093/petrology/egu058> doi: 10.1093/petrology/egu058
- Nielsen, R. L., Ustunisik, G., Weinsteiger, A. B., Tepley, F. J., Johnston, A. D., & Kent, A. J. (2017). Trace element partitioning between plagioclase and melt: An investigation of the impact of experimental and analytical procedures. *Geochemistry, Geophysics, Geosystems*, 18(9), 3359–3384.
- Petry, C., Chakraborty, S., & Palme, H. (2004). Experimental determination of Ni diffusion coefficients in olivine and their dependence on temperature, composition, oxygen fugacity, and crystallographic orientation. *Geochimica et Cosmochimica Acta*, 68(20), 4179–4188.
- Spandler, C., & O'Neill, H. S. C. (2010). Diffusion and partition coefficients of minor and trace elements in San Carlos olivine at 1,300 °C with some geochemical implications. *Contributions to Mineralogy and Petrology*, 159(6), 791–818.
- Sun, C., Graff, M., & Liang, Y. (2017). Trace element partitioning between plagioclase and silicate melt: The importance of temperature and plagioclase composition, with implications for terrestrial and lunar magmatism. *Geochimica et Cosmochimica Acta*, 206, 273–295.
- Tepley III, F. J., Lundstrom, C. C., McDonough, W. F., & Thompson, A. (2010). Trace element partitioning between high-An plagioclase and basaltic to basaltic andesite melt at 1 atmosphere pressure. *Lithos*, 118(1-2), 82–94.
- Van Orman, J. A., Cherniak, D. J., & Kita, N. T. (2014). Magnesium diffusion in plagioclase: dependence on composition, and implications for thermal resetting of the  $^{26}\text{Al}$ – $^{26}\text{Mg}$  early

solar system chronometer. *Earth and Planetary Science Letters*, 385, 79–88.

Zhukova, I., O'Neill, H. S. C., Campbell, I. H., & Kilburn, M. R. (2014). The effect of silica activity on the diffusion of Ni and Co in olivine. *Contributions to Mineralogy and Petrology*, 168(2), 1029.